UNIVERSITAT DE BARCELONA

Development of microfluidic devices for cancer cell isolation

Jessica Nathalia Sierra Agudelo

Development of microfluidic devices for cancer cell isolation

Doctoral Thesis

Jessica Nathalia Sierra Agudelo

Prof. Josep Samitier Marti

Prof. Romén Rodríguez Trujillo

UNIVERSITAT DE BARCELONA

Development of microfluidic devices for cancer cell isolation

Doctoral Thesis

Memoria presentada para optar al grado de Doctor por la Universidad de Barcelona Programa de Doctorado en Biomedicina

Autor

Jessica Nathalia Sierra Agudelo

Director

Prof. Romén Rodríguez Trujillo

Tutor

Prof. Josep Samitier Marti

Tesis realizada en el Instituto de Bioingeniería de Cataluña (IBEC)
Barcelona, 2023

UNIVERSITAT DE BARCELONA

"la Caixa" Foundation

Understanding and measuring mechanical tumor properties to improve càncer diagnosis, treatment, and survival: Application to líquid biopsies

Table of contents

Abstract

The emergence of liquid biopsies has been useful for the diagnosis of physiological conditions, inflammatory processes, and especially represents a good alternative tool for non-invasive analysis of tumor-derived materials. Currently, tissue biopsies are still the gold standard for tumor profiling. Nevertheless, this technique presents many limitations that include invasiveness, risk and depending on some anatomical locations is not easy (or even impossible) to obtain. Moreover, it provides a limited picture of the tumor profile, considering that tumors are heterogeneous entities composed of different subpopulations of cells, which display a variability of genetic and epigenetic changes. In this context, liquid biopsies are a cheaper, faster, non-invasive alternative to conventional biopsies, that can be used for personalized cancer therapy.

In a broad sense, liquid biopsy is based on the isolation of biomarkers from the blood that can be used for cancer diagnosis and monitoring. This definition englobes Circulating Tumor Cells (CTCs), circulating tumor DNA (ctDNA) and nanovesicles. CTCs are cancer cells, which leave the primary tumor and enter the bloodstream initiating a process called metastasis. Nevertheless, one of the most relevant challenges in this field involves the processing and analysis of CTCs, due to their low amount in peripheral blood (1 to 100 CTCs per 10^9 blood cells) and high heterogeneity. Furthermore, the approaches for isolating CTCs from blood samples are limited due to high cell contamination rates or substantial loss of cancer cells, and high-cost methods. To overcome these limitations, microfluidic devices have been designed for isolating CTCs based on their intrinsic properties like density, size, deformability, and difference in membrane protein expression.

This project was undertaken to develop microfluidic devices for isolating CTCs based on inertial focusing and affinity binding principle methods. We first developed a spiral microfluidic device that can efficiently separate the CTCs from most of the blood cells by their differences in size by applying a hydrodynamic sorting principle. The CTC output sample is contaminated by the largest leukocytes (~12 to 21 µm) which are in the same size range as the CTCs (~9 µm to 30 µm). The research has also explored the development of microfluidic spiral devices using a 3D printer, in which the geometry dimensions were adapted to remove Leukocytes binding to polystyrene particles functionalized with CD45 antibody, allowing a more CTCs sample purity. Alternatively, second type of microfluidic device known as a Herringbone chip was designed to capture the remaining leukocytes (negative enrichment of CTCs) from the spiral CTC output sample. This device uses an affinity-binding principle based

on a mixed Self Assembled Monolayer (SAM) composed of a Silane-PEG-Biotin, Silane-PEG-OH and CD45-antibody (common antigen for leukocytes).Moreover, the microfluidic platform was optimized for high-throughput blood sample processing including a lysis pre-treatment, guaranteeing a high recovery of CTC and its viability for further analysis.

On the other hand, an electronic circuit was successfully developed using piezoelectric micropumps MP6 controlled by Raspberry PI zero, which allowed to overcome some limitations of traditional syringe pumps, as well as facilitate the use of this platform in a clinical environment. Finally, the clinical proof of concept was initiated with samples from colon cancer patients in collaboration with the Vall d'Hebron hospital.

List of abbreviations

CTCs: Circulating Tumor Cells

EMT: Epithelial to Mesenchymal Transition

CAT: Collective to Amoeboid Transition

MAT: Mesenchymal to Amoeboid Transition.

ECM: Extracellular matrix (ECM)

CPs: Circulating Proteins

ctDNA: Circulating tumor DNA

EVs: Extracelular Vesicles (EVs)

EpCAM : Epithelial Cell Adhesion Molecule

MRD : Minimal Residual Disease

DML : Degassed mold lithography

GASI: Geometrically activated surface interaction

Re: Reynolds number

Rep: Particles Reynolds number

DEP: Dielectrophoresis

FDEP: Dielectrophoretic force

Pdep: Positive dielectrophoresis

nDEP: Negative dielectrophoresis

BrCa : Metastasis in breast cancer

mCRPC: Metastatic prostate cancer

PFS: Progression-free survival

OS: Overall survival (OS)

TNBC: Triple-negative breast cancer

MBC : Metastatic breast cancer

RTK : Receptor tyrosine kinase

MRI: Magnetic resonance imaging

LOC: Lab-on-a–chip

MP: Hydrogel microparticles

FET: Field-effect transistors

HEMT : High electron mobility transistor

RIfS : Reflectometric interference spectroscopy

PDMS: Polydimethylsiloxane

SLA: Stereolithography

FDM: Deposition Modeling

laser-SLA : Laser scanning

PI: Photo-initiators

DLP: Digital Light Processing

DLP: Digital light processing

FBS: Fetal Bovine Serum

RPMI: Roswell Park Memorial Institute Medium

PBS: Phosphate-buffered saline

FACS: Fluorescence-activated cell sorting

DMM: n-Dodecyl β-D-maltoside

Mix-SAM: Mix-Self-assembled monolayers (SAM)

BSA: Bovine serum albumin

CFD: Computational Fluid Dynamics

D_h : Hydraulic diameter

De: Dean number

f_L : Lift coefficient

F_D : Drag force

PCB: Printed circuit board

MSI: Microsatellite instability

CRC: Colorectal cancer

CIN: Chromosomal instability

SCNAs: Somatic copy number alterations

MSS: Microsatellite stable

MCRC: Metastatic colorectal cancer

MAPK: Mitogen-activated protein kinase

ERK: Extracellular signal-regulated kinase

PCR: Polymerase chain reaction

List of Figures

List of Tables

Scope and Thesis Outline

This thesis will summarize the work carried out over the last 4 years in the Nanobioengineering Research Group at the Institute of Bioengineering of Catalonia (IBEC) within the project “Understanding and measuring mechanical tumor properties to improve cancer diagnosis, treatment and survival: Application to liquid biopsies” financed by the banking foundation "la Caixa".

This study aims to contribute to this growing field of research by exploring how to overcome some of the limitations of the only FDA-approved platform for CTC enumeration and other methods described in the literature. Therefore, I will first present in *“Chapter 1”* the current state of research on this topic, starting with the biological principles involved in the formation of CTCs, their key properties, and the main challenges in their recovery. An overview of current methods for separating CTCs and their limitations, as well as manufacturing techniques, will also be provided.

Subsequently, the objectives of the thesis are described in *“Chapter 2”*. This is followed in *"Chapter 3"* by a detailed explanation of the materials and methods used in this research. in *“Chapter 4”,* I explain the results of the design and microfabrication of the microfluidic devices and describe the whole process of their development and characterization using different fabrication techniques such as photolithography, soft lithography and 3D printing.

In *“Chapter 5”,* I describe and analyze the evaluation of a microfluidic spiral device for circulating tumor cell isolation based on computational modeling and an in vitro biomodel. This chapter focuses on the development of a comprehensive computational model for the microfluidic spiral device that allows the approximation of the values of inertial lift forces and drag forces in different channel sections and heights. This enables the optimization of flow and geometry parameters that ensure the balance between inertial lift forces and drag forces for successful separation of CTC cells. The chip shows exceptional experimental results with polystyrene particles and different types of cancer cells correlated with the computational model. Finally, the main features of this microfluidic device as well as its advantages and limitations are highlighted.

In addition, *“Chapter 6”* presents a complementary method that could improve the purity of the CTC sample obtained from the spiral device. Then, the enrichment of circulating tumor cells in liquid biopsies using an improved Herringbone chip is described. Here, I demonstrate

the development of a microfluidic device used for negative enrichment by implementing a mixed self-assembling monolayer (SAM) that allows more stable and controllable surface immobilization of CD45 (common leukocyte antigen). The computational model and experimental characterization allowed us to estimate a factor related to the number of groove sets required to achieve high leukocyte capture rates, depending on the inlet sample..

In *"Chapter 7"* describes a novel low-cost instrumentation applied to liquid biopsies. This chapter presents the design and fabrication of a high-performance electronic platform to overcome the limitations of using conventional instrumentation equipment to evaluate and optimize the performance of spiral microfluidic devices and microfluidic herringbone devices for liquid biopsy applications.

On the other hand, *"Chapter 8"* describes the Low-cost 3D-printed inertial flow microfluidic devices. Throughout this chapter I explore the development and evaluation of spiral microfluidic devices made of 3D printing molds that could help to increase the leukocytes depletion by incubated them with 70 µm diameter microspheres conjugated with Biotin-CD45 antibodies. This sample is processed through the spiral device with a geometry optimized by computational modeling.

The "Chapter 9" identifies future perspectives that include clinical validation of the devices developed during the project using blood samples from colorectal cancer patients. The study includes 15 patients divided into 3 groups: 5 mCRC patients with microsatellite instability (MSI), 5 mCRC patients with a BRAF mutation (V600E) and 5 mCRC patients with a KRAS mutation (G12C). Relevant aspects of the workflow for pre- and post-processing of samples in a coordinated manner between the Gastrointestinal and Endocrine Tumors Group at Vall d'Hebron Hospital and the Nanobioengineering Group at IBEC were optimized and established using a colorectal cancer cell line (SW480 cells) and blood samples from healthy donors as controls. The preliminary test using a sample from a colorectal cancer patient is described. Finally, the future perspectives and limitations of this study are explained.

Finally, in *"Chapters 10 and 11"* a global discussion of the results obtained throughout this thesis is presented, likewise the main conclusions of this work are commented.

Chapter 1

Liquid biopsies based on integrated microfluidic device for early cancer diagnosis

1.1.1 Introduction to cancer biology

Cancer represents one of the leading causes of death worldwide. According to the world health organization (WHO) 10 million deaths in 2020 were caused by cancer, meanly lung, colon, liver, stomach and breast [1] (Figure 1). An increase of 28 million of new cancer cases worldwide is estimated each year by 2040, which is an increase of 54.9% from 2020 and is expected to be higher in males (60.6% increase) than in females (48.8% increase)[2].

One of the greatest challenges is to reduce the cancer mortality, which can be achieved when the cases will be detected and treated early. Thus, when the cancer is diagnosed at an early stage is more likely to respond to the treatment and increase the probability of survival[3].

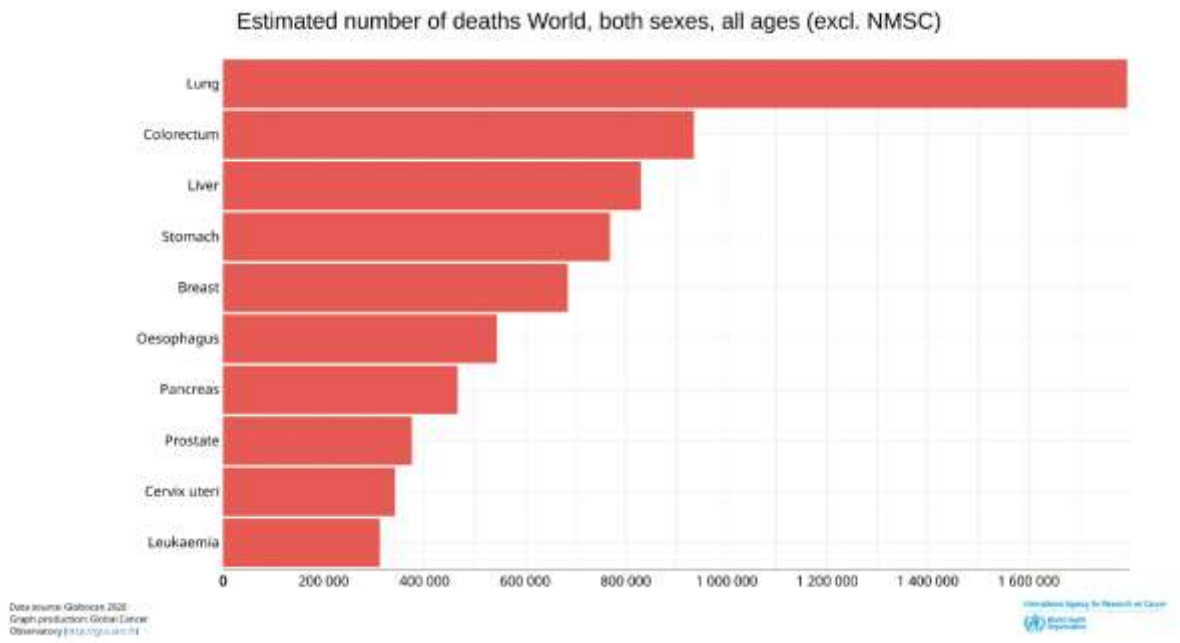

Figure 1. Estimated number of deaths caused by different types of cancer

1.1.2 What is cancer?

The words carcinos and carcinomas were used by Hippocrates to describe non-ulcer forming and ulcer-forming tumors in 460-370 BC. However, the term cancer was introduced by the physician Celsus in (25 BC - 50 AD) [4].

Nowadays, cancer is defined as a group of more than 20 diseases characterized by the uncontrolled division and spread of abnormal cells in the body, which lead the formation of a mass of cells know as tumor[5]. Generally, there are two types of tumors: malignant (cancerous) and benign (non-cancerous) tumors. The benign tumors are composed by cells that do not invade unrelated tissues or organs, but it continues to grow abnormally. By contrast, the malignant tumors are form by cells that invade the basement membrane and other parts of the body. This event occurs by direct extension to near tissues or by metastasizing distant sites which involves the vascular system, lymphatic system or seeding cancer cell in body cavities[6] (Figure 2).

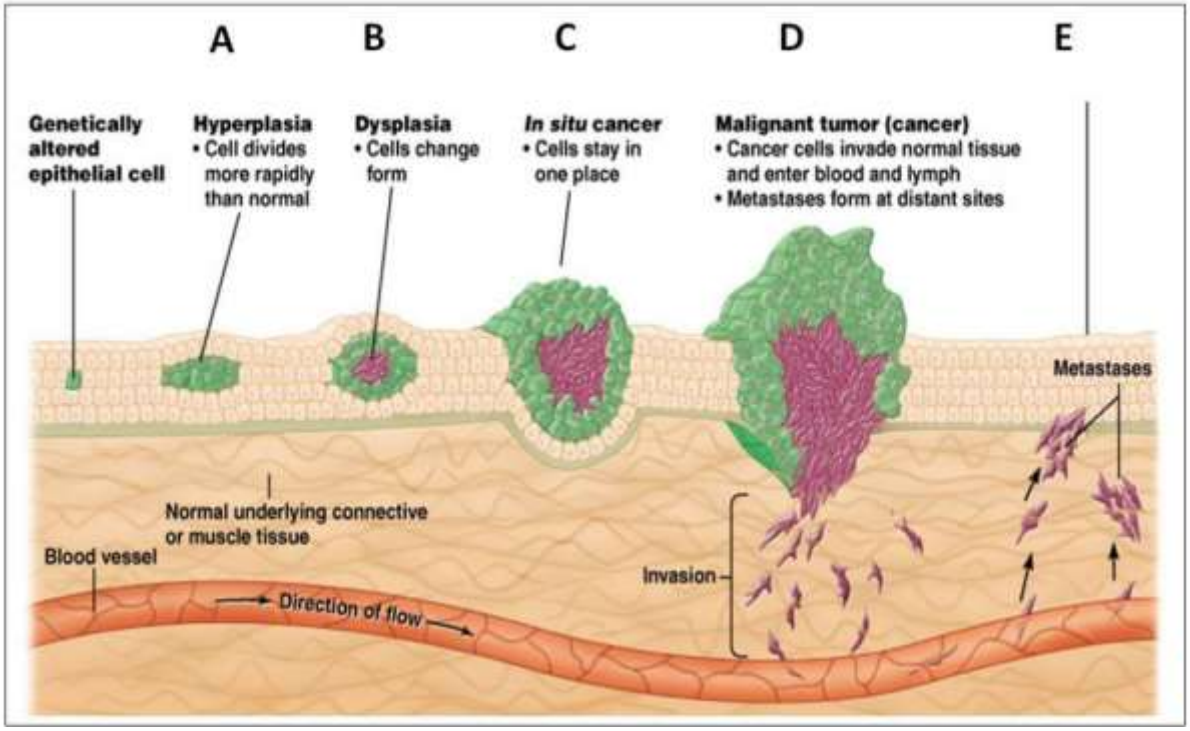

Figure 2. Tumor development processes. **A)** Genetically altered or abnormal cells show uncontrolled and rapid growth. **B)** During the dysplasia the overgrowing cells change their original form from more mature cells to immature cells. **C)** In situ cancer involves the neoplastic lesion where the cells lost their tissue identity and grow without regulation. **D)** Overgrowing cells invade other areas by rupturing basal membrane. **E)** Metastases take place when cancer cells reach to the distant parts across the lymphatic system and blood circulation[7]

It had been previously described that the process of tumor development comprises eight hallmarks which involve the capabilities for sustaining proliferative signaling, evading growth suppressors, resisting cell death, enabling replicative immortality, inducing/accessing vasculature, activating invasion and metastasis, reprogramming cellular metabolism, and avoiding immune destruction[8](Figure 3).

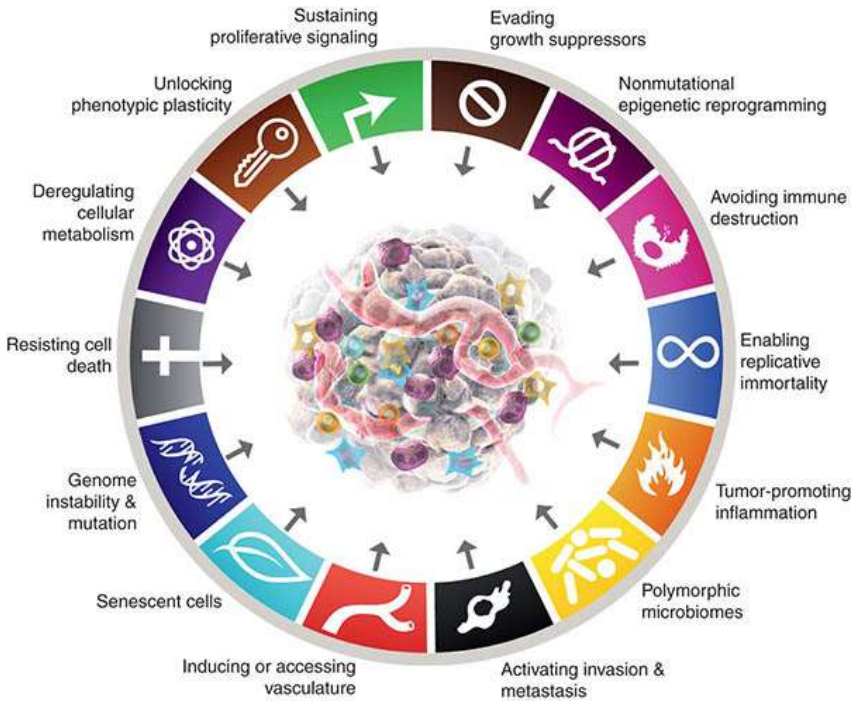

Figure 3. Hallmarks of Cancer. [6]

In this way, the proliferative signaling involves during cell growth and division cycle take place when the growth factor bind the cell surface receptors triggered signaling pathways and regulating the cell cycle. However, cancer cells can realase these signals and adquire proliferative capability through the production of growth factors, which can result in autocrine proliferative stimulation. Alternatively, cancer cells could send signals to stimulate the normal cells which can supply them with growth factors[9,10].

1.1.3 Tumor progression and metastasis

Cancer metastasis is the spread of cancer cells from the primary tumor to other sites in the body, is a major contributor to cancer-related deaths, accounting for about 90% of cancer deaths[11]. Unlike the primary tumor, metastatic cancers are highly incurable and fatal, emphasizing the urgency of understanding and guiding this process, especially in the development of early diagnosis methods that help offer better treatment alternatives.

Current cancer research has primarily focused on early detection and inhibition of tumor growth, leading to better outcomes when diagnosed and treated before metastasis. However, the complexities of the metastatic process hinder successful prevention and intervention. In fact, the metastasis process involves multiple steps (Figure 4)[12]:

1) Local infiltration of tumor cells into the adjacent tissue

2) Transendothelial migration of cancer cells into vessels known as intravasation

3) Survival in the circulatory system

4) Extravasation

5) Subsequent proliferation in competent organs leading to colonization

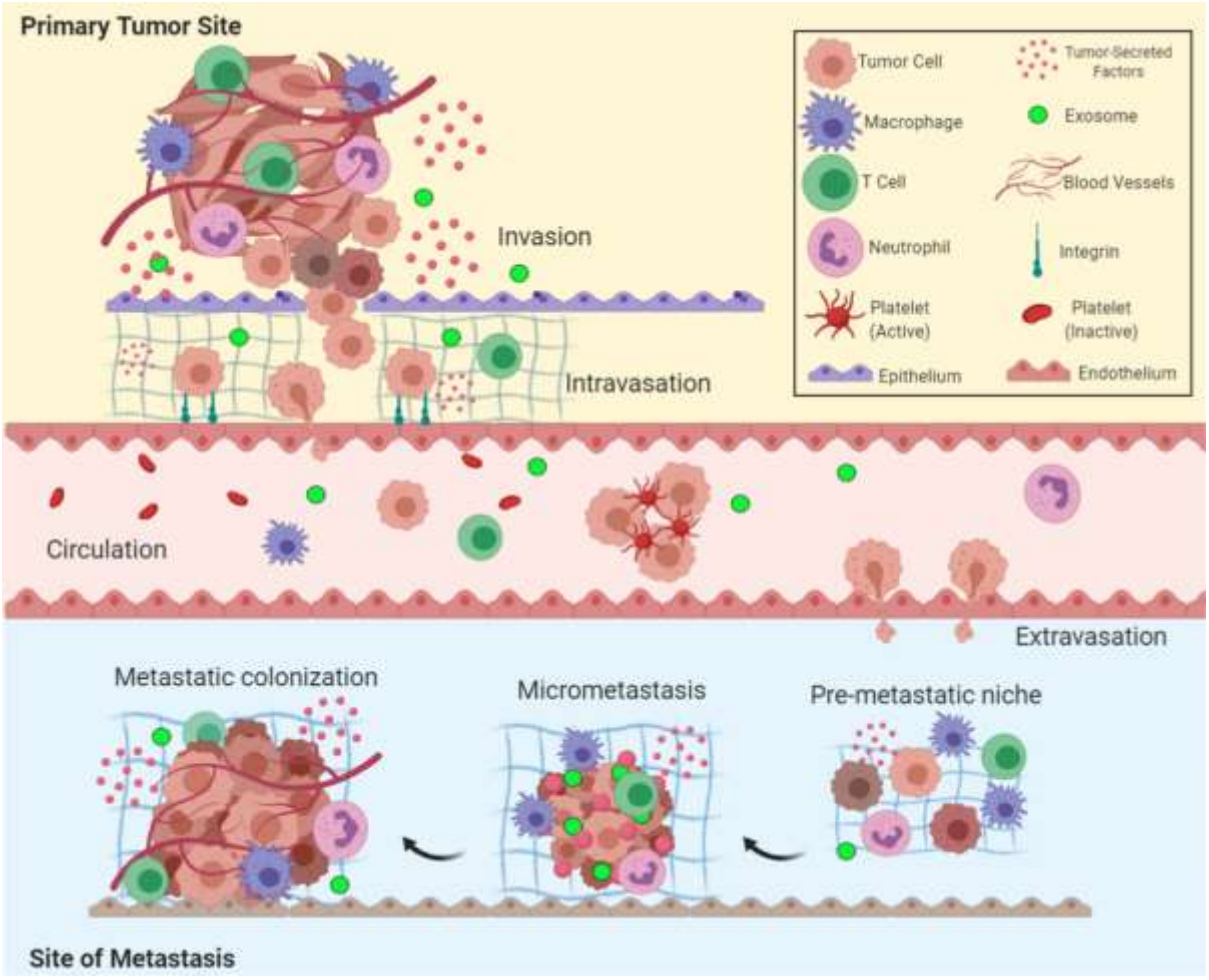

Figure 4. Overview of the metastatic cascade where the five key steps of metastasis include invasion, intravasation, circulation, extravasation, and colonization [13].

On the other hand, metastasis-related genes are stress-response genes involved in inflammation, wound healing, and stress-induced angiogenesis. Understanding these key processes is crucial to developing effective intervention strategies.

1.1.4 Mechanisms of cell invasion

Cancer cells invade other tissues using different methods: Moving collectively as epithelial sheets, detached clusters, as single cells via mesenchymal or amoeboid types[14]. Moreover, these cells undergo plasticity changes during cancer progression, including epithelial to mesenchymal transition (EMT), collective to amoeboid transition (CAT), and mesenchymal to amoeboid transition (MAT)[15].

The EMT is a critical process in cancer progression and metastasis, involving the transformation of cells from epithelial to mesenchymal characteristics. The EMT leads to the loss of E-cadherin, disrupting cell-to-cell adhesion, and promoting the expression of mesenchymal markers like vimentin and N-cadherin[16]. This transition enhances cell motility and invasiveness. Besides, EMT process is linked to stem cell properties, apoptosis resistance, and immune evasion, making it a target for cancer therapies[17]. On the other hand, the reversal process from mesenchymal to epithelial transition (MET), allows mesenchymal cells to regain epithelial characteristics and facilitates colonization at secondary sites.

The second transition known as CAT involves individual cells detaching from clusters and using amoeboid migration, observed mainly in melanoma. In fact, amoeboid cells exhibit reduced interaction with the extracellular matrix (ECM) and can move independently of ECM proteolysis[18].

Finally, MAT represents the third transition and occurs when mesenchymal cells transition into amoeboid cells and has been detected in breast cancer, melanoma, and fibrosarcoma. MAT depends on Rac and Rho/ROCK signaling and is not reliant on protease activities [1920]. Moreover, the tumor microenvironment and regulatory proteins like EphA2 kinase can induce MAT [21]. Therefore, identifying and modulating the factors involved in the plasticity changes previously mentioned, could be possible to develop targeted interventions to inhibit the cancer metastasis effectively.

1.1.5 Collective cell invasion

The collective cell invasion process is a prominent feature in epithelial cancers like breast, endometrial, and colorectal cancers, as well as in melanoma. Three hallmarks define this process:

1) Intact cell-to-cell junctions[22].

2) Coordinated polarity and cytoskeletal activity [23].

3) Remodeling of the extracellular matrix (ECM)[24].

Moreover, there are different types of collective cell invasion such as the monolayer formation, cell strand building for three-dimensional invasion, and detachment of a cell cluster from the initial tumor. Thus, collectively invading cells maintain adherence, tight, gap junctions, and desmosomes, but leader (front) and following (rear) cells exhibit front-rear asymmetry[21]. Rho GTPases and myosin II mediate asymmetric stiffening of actomyosin filaments in tip cells, which differ from following cells in gene expression and morphology. Chemokines and growth factors secreted in paracrine, juxtacrine, or autocrine fashion influence the asymmetry of collectively invading cells[22,25].

It is important highlight the essential role of force generation for collective cell movement, and traction force is provided by substrate-binding integrins in leading cells. Integrin-mediated attachment to the ECM activates cytoskeletal adaptor proteins, facilitating cell motility[25]. Rac and Cdc42 control pseudopodia and filopodia formation, while Rho signaling is more relevant for single-cell movement than collective migration[26].

The third hallmark (ECM remodeling) plays a crucial role in track formation during collective cell invasion, with tip cells secreting MT1-MMP to initiate track formation, while following cells enlarge the track by degrading the ECM and depositing specific components[21,27].

1.1.6 Mesenchymal cell invasion

The term of Epithelial-Mesenchymal Transition (EMT) was first proposed in the late 1960s[28], and was later confirmed in the embryonic lens epithelium of chicks in the 1980s[29]. EMT is a complex process with multiple steps, during which epithelial cells undergo significant changes. They lose their characteristic epithelial features and acquire mesenchymal traits, such as upregulation of mesenchymal marker proteins (N-cadherin, vimentin, and fibronectin) and downregulation of tight- and adherents-junction proteins (E-cadherin and α-catenin)[30,31]. This results in a loss of cell-cell adhesion and polarity, leading to increased cell motility and invasiveness. Ultimately, the cells can digest and migrate through the extracellular matrix (ECM) and acquire motile and invasive characteristics[32].

Extensive research has shown that E-cadherin plays a crucial role in maintaining epithelial cell-cell adhesion, and its repression by transcription factors like Snail, Slug, TWIST, and the ZEB family is a key event in EMT[33–35]. Indeed, EMT is associated with various biological processes, including embryonic development, wound healing, organ development, and cancer progression[36,37]. Some developmental processes involve the loss of epithelial cell polarity, observed in tubulogenesis, branching in the mammary gland, and mesoderm formation, among others[38].

On the other hand, EMT is regulated in temporal and spatial manners to ensure proper cell homing and reversion to non-invasive phenotypes after migration. In cancer, cells undergoing EMT exhibit altered target recognition and activate self-sufficient autocrine loops of growth signals to evade apoptosis[38].

In summary, EMT is a highly complex process with key roles in development, tissue repair, and cancer progression. Its strict regulation is crucial to maintain proper cellular function and prevent abnormal development[39].

1.1.7 Amoeboid cell invasion

The amoeboid mechanism of invasive growth is a primitive and highly efficient mode of migration observed in single tumor cells, resembling the behavior of single-celled organisms like Dictyostelium discoideum[40]. This type of migration is observed in circulating stem cells, leukocytes, and certain tumor cells in breast cancer, lymphoma, lung cancer, prostate cancer, and melanoma[41,42]. Thus, when cells are in amoeboid stage display round or elliptical shapes and exhibit rapid deformability, adapting their shapes to the surrounding extracellular matrix to move through narrow spaces in a compressed form[43,44]. The movement is facilitated by high-speed cycles of cell expansion and contraction with "bleb-like" protrusions of the cell membrane. This process involves the RhoA GTPase and its effector, ROCK kinase, which regulate actin cytoskeleton reorganization[45,46].

Overall, amoeboid migration is composed by changes in cell and nucleus shape and orientation, especially in "soft" matrices. In a "soft" matrix, tumor cells migrate via the amoeboid mechanism due to a weak interaction with the surrounding matrix and the absence of proteolysis at cell-matrix interaction sites. It is important to highlight that this process is characterized by rapid movement, weak cell-matrix interaction, absence of proteolysis, and lack of focal contact. These properties allow tumor cells to achieve high speeds in culture[47,48].

In conclusion, the amoeboid mechanism of invasive growth is an efficient and rapid mode of migration employed by certain tumor cells, providing insights into their behavior and interactions with the surrounding microenvironment.

1.1.8 Tumor heterogeneity and cancer stem cells

Tumor heterogeneity refers to the diverse cell subpopulations within a tumor, showing distinct genetic and phenotypic features leading to varied biological behaviors. This heterogeneity can be present within a primary tumor, its metastases, or among tumors of the

same subtype. Advanced sequencing techniques have revealed increasing prevalence of intra- and inter-tumor heterogeneity[49].

Extensive research has shown the highest grade of multiple sections of tumors when the morphological variations were examinated[50]. Recently, clinicians have observed marked variation in tumor behavior between patients with the same tumor type and within different tumor sites, affecting responses to therapy. Moreover, pharmacodynamics and genetic complexity also contribute to the variability in drug response. Initial evidence of multiple subclones within a tumor came from G-banding karyotyping and fluorescent in situ hybridization (FISH) studies, highlighting chromosomal rearrangements and copy number alterations[51].

On the other hand, the clonal evolution model of cancer development, proposed by Nowell in 1976[52], is based on Darwinian principles of natural selection, where genetically unstable cells accumulate genetic alterations, leading to variant subpopulations. This model, combined with cancer genomic instability mechanisms, contributes to molecular heterogeneity within tumors, increasing the pool of genetic variants for selection. Driver mutations confer a growth advantage, while passenger mutations persist due to their linkage to drivers. Indeed, studies of hematological cancers, brain, breast, and pancreatic tumors support clonal evolution as the basis for tumor progression[52,53]. Sequencing analyses reveal the presence of founding clones in primary tumors, evolving and expanding in relapsed tumors. Thus, both types of mutations (driver and passenger) have implications for cancer therapeutics, as heterogeneous events can determine resistance outgrowth and patient outcomes.

The evidence suggest that tumor heterogeneity is a dynamic state characterized also by spatial and temporal variations, which allow the tumor to adapt to changes in its microenvironment[54]. In some cases, subclones exist in a dynamic equilibrium, leading to unpredictable outcomes and challenges in biomarker strategies. Previous studies demonstrated that clonal cooperativity occur in glioblastoma, where a mixture of mutant and wild-type cells enhances tumor growth through paracrine signaling[55].

Therefore, heterogeneous tumors are related to more complex ecosystems where minor subpopulations can significantly influence overall tumor growth, maintaining their heterogeneity. Subclones occupy different niches within the tumor microenvironment, and their relationships can be competitive, commensal, or mutualistic, contributing to the tumor's survival advantage as a whole[56].

In contrast to the clonal theory the cancer stem cell model proposes that tumors are maintained and propagated by a small subpopulation of cells with stem-like properties (Figure 5)[57]. These cells have “unlimited” proliferation capacity and give rise to various cancer cell

types within the tumor[58]. Thus, metastatic spread is attributed to the dissemination of these cancer stem cells, and resistance to treatment is thought to arise from inherent resistance within this population. Data from previous studies suggest that suggesting that not all tumor cells have the same capacity to induce tumor growth[57]. Later, studies in leukemia and solid tumors identified cell populations with increased tumor-forming ability, supporting the concept of cancer stem cells[59–61].

Previous research has established that the presence of cancer stem cells indicates a role in promoting tumor heterogeneity, as they differ from non-stem cancer cells in various properties such as proliferation rate, migratory behavior, and DNA repair mechanisms[62]. Studies have shown that cancer stem cells can give rise to tumors containing all different cell types of the original tumor, while non-stem cancer cells cannot. The heterogeneity seen in tumors may arise from differentiation of cancer stem cells into different lineages rather than clonal evolution of equal tumor cells[63]. Other studies in melanoma cultures also support the role of cancer stem cells in tumor heterogeneity, as they give rise to tumors containing various lineages expected from the original tumor[64].

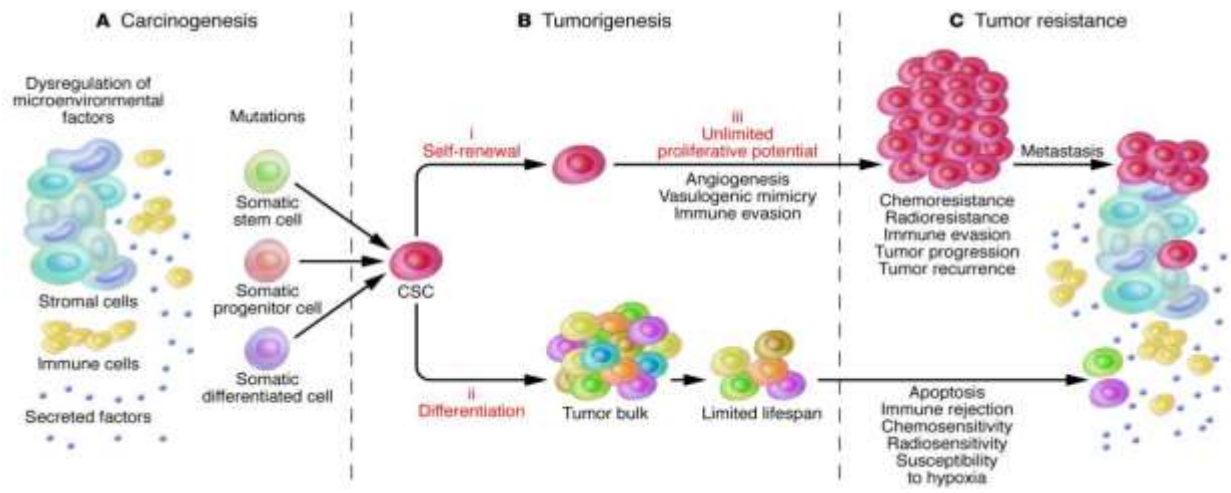

Figure 5. A) Carcinogenesis: Tumors can arise from somatic cells through genetic mutations of cancer-critical genes **B)** Tumorigenesis: CSCs are capable of driving tumorigenesis through 3 features: (i) their ability for long-term self-renewal, (ii) their capacity to differentiate into tumor bulk populations devoid of CSC characteristics, and (iii) their unlimited potential for proliferation and tumorigenic growth. **C)** CSCs exhibit increased resistance to chemotherapeutic agents and ionizing radiation [6566]

1.1.9 What are the circulating tumor cells (CTCs)?

Since 1869, Ashworth discovered the tumor cells in the peripherical blood and proposed the concept of a CTC [67]. These CTCs are cancer cells, which leave the primary tumor and enter the bloodstream initiating a process called metastasis [68]. From the biological point of view, these cells do not bind to the extracellular matrix (ECM) and survive in the bloodstream because of their resistance to apoptotic process known as "anoikis" [69], as well as factors associated with epithelial and mesenchymal plasticity or stem cell-like properties.

As previously explained metastasis is a biological complex process, which involves cell migration, local invasion, intrusion of tumor cells inside the circulation, dissemination, arrest at secondary and primary parts, extravasation at distant parts, colonization and finally the formation of a metastatic secondary tumor clinically detectable (Figure 6) [68,70]. Recent studies indicate the high heterogeneity of CTC population including CTCs clusters individual CTCs , Epithelial CTCs, Hybrid epithelial-Mesenchymal CTCs, mesenchymal CTCs and stem-like CTCs [71]. In fact, it has been found that CTCs clusters show distinct features regarding to individual CTCs, such as phenotype, sign of gene expression and nature [72,73]. Moreover, other studies have revealed that CTCs-clusters may have 100 times more metastatic potential than single CTCs[74]. The presence of CTCs in blood has been recognized in many types of cancer such as breast cancer, colon cancer, lung, prostate among others[75]. Previous clinical studies in patients with breast cancer have correlated the presence of CTCs with an increase in tumor burden, aggressiveness, as well as decreased time to relapse [76]

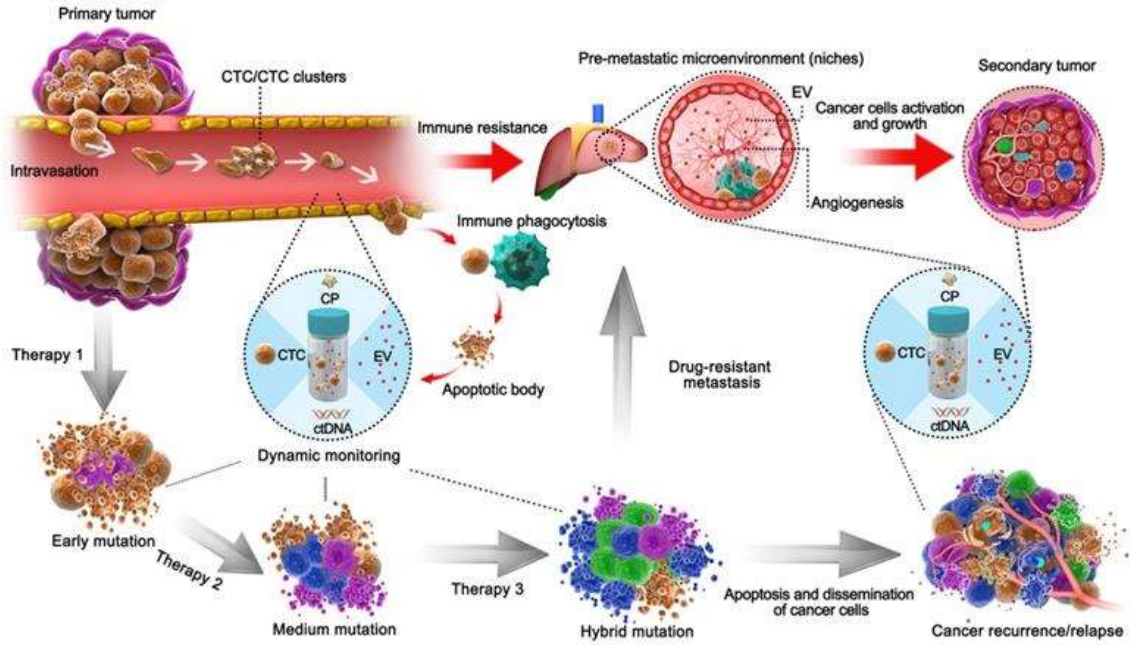

Figure 6. Liquid biopsy and CTCs origin and progression under therapeutic application. circulating proteins (CPs), circulating tumor DNA (ctDNA), circulating tumor cells (CTCs) and Extracellular Vesicles (EVs) enter the bloodstream and can be used to detect minimal tumor generation and monitor tumor heterogeneity. CTCs will be generated by the primary tumor and cooperate with TEPs to survive and enter in circulation as single CTCs or CTCs clusters. Furthermore, EVs represent pre-metastatic scavengers which resist to immune damage and allow metastasis in secondary areas. After target therapy is applied, the drug-resistance cancer cells will proliferate by adaptive evolution. Thus, liquid biopsy allows to predict pre-metastasis or relapse to avoid tumor dissemination. Natural cancer development is represented by the red arrows, meanwhile the development of tumors after therapy is shown by the black arrows. Licensed under CC BY-NC 4.0 International License. The final, published version of this article is available at [77] .

In these circumstances, detection of CTCs that are circulating into the blood stream could be used for early cancer and metastasis detection as well as for monitoring tumor's responsiveness to radio/chemotherapy and developing personalized patient treatments. Some of the diagnostic possibilities that CTCs detection would offer can be summarized as follows [78].

- The presence of CTCs in blood is highly associated with metastatic risk but also indicates primary tumor existence. As it is known that CTCs are present in blood from very early stages of the disease and prior to the appearance of symptoms, a device that allowed detection of CTCs could be used for both determining metastatic risk and early cancer detection.

- It is also known that the number of CTCs present in the blood sample is related to the stage of the patient's disease. Thus, another advantage could be to monitor tumor's responsiveness to therapy. This would be done by running routine blood analysis and comparing the number of CTCs prior and after the treatment.
- Another important issue is tumor heterogeneity, both within a tumor and between the primary tumor and its metastases, which cannot be captured by a simple tissue biopsy. This heterogeneity accounts for the genotypic differences between different regions of the tumor or between the primary and the secondary tumors. It is known that almost all tumors treated with any therapy acquire resistance because of tumor heterogeneity, clonal evolution, and selection[79] .Therefore, liquid biopsy would enable to understand better the phenomena of metastatic drug resistance.
- Tumors are very prone to suffer mutations in their genome, so their molecular profile changes frequently and so does the effective treatment required. Thus, liquid biopsy would allow monitoring the molecular profile of the tumor just by taking periodic blood samples from the patient. Therefore, according to the results obtained the clinicians can find out if the treatment is correct or if it must be adjusted due to mutations.

It is therefore clear that the development of a platform allowing CTCs isolation and detection from blood samples would be a major improvement in the study and treatment of cancer. Nevertheless, the identification of CTC from whole blood is challenging, as the number of CTCs in 1 mL of blood from a cancer patient is only 1 to 100, in comparison with 10^9 hematologic cells [80]. Hence, the traditional methods to isolate cells, like flow cytometry, density gradient centrifugation and immunocapture by magnetic beads do not have enough sensitivity to detect rare cells like CTCs[81].

Despite the high number of scientific publications related to CTC detection, there is only one CTC test approved by the FDA, the CellSearch® system by Menarini Silicon Biosystems [82].This system uses magnetic particles coated with antibodies that bind to the protein EpCAM (epithelial cell adhesion molecule) for quantifying the CTCs in metastatic breast, prostate and colon[83]. In the last few decades, EpCAM (the epithelial cell adhesion molecule) was considered as universal tumor biomarker for epithelial-derived cancer types [84].

Nevertheless, several studies indicate that some CTCs can be EpCAM-negative[85] such as those which had an epithelial-to-mesenchymal transition and mesenchymal origin. Moreover, CTCs isolated from patients display a wide range of EpCAM expression, where a part of these cells are EpCAM-negative[86,87] for instance in some advanced lung cancer [86,88]. This represents one

of the main drawbacks of this platform as well as, it requires expensive equipment and does not allow neither 100% purity nor isolation of viable cells for further culture and studies.

1.1.10 Genetic and molecular characterization of circulating tumor cells

The comprehensive molecular analysis of CTCs through the combination of gene expression, DNA methylation, and mutation analysis with CTC count and phenotypic assessment, enables the detection of minimal residual disease (MRD) up to 4 years before clinically detectable metastasis in breast cancer (BrCa) patients[89,90]. This highlights the potential of liquid biopsy for early therapeutic management. A previous study of 1220 BrCa patients in stage I-III revealed that detecting CK-19 mRNA-positive CTCs predicted early relapse, supporting novel adjuvant therapies[91].Moreover, the prognostic value of EMT (TWIST1) and stem cell (CD24, CD44, ALDH1) markers was explored in EpCAM+ CTCs of 100 early BrCa patients, providing predictive information[92].

On the other hand, it has been detected prostate biomarker in triple-negative BrCa patients[93]. However, it was demonstrated that neoadjuvant therapy eliminated prostate-related gene-expressing CTCs but identified high-relapse-risk PSMA+ CTCs and associated AR-FL-pos and AR-V7-pos CTCs with treatment failure. In early BrCa patients, PIK3CA hotspot mutations were detected in plasma-ctDNA and CellSearch® cartridges before and after treatment. Meanwhile, PIK3CA mutations were more prevalent in cartridges post-treatment. Additionally, a study investigated CD47 and PD-L1 expression in PBMC cytospins from early BrCa patients, detecting a small proportion of CD47+ and/or PD-L1+ CTCs[93,94].

In addition, clinical studies demonstrated that AR-V7 expression in CTCs is associated with better responses to taxane chemotherapy over hormonal therapies in mCRPC (metastatic prostate cancer)[95]. AR-V7 serves as a predictive biomarker for LB, indicating resistance to AR signaling inhibitors. Analytically validated AdnaTest mRNA and Epic nuclear protein assays are used to detect AR-V7 in CTCs, guiding treatment decisions for mCRPC patients. CTC+/AR-V7+ samples have higher CTC counts and biopsy AR-V7 expression, and CTC- and CTC+/AR-V7- patients show detectable AR-V7 protein in tissue biopsies[96,97]. It is important to highlight that using the nuclear-localization of AR-V7 CTC allows to improve the treatment decisions and patient outcomes compared to standard-of-care measures. It is now well established that a transcriptional profile in CTCs serves as an independent prognostic marker and identifies resistance mechanisms in mPCa patients[97].

1.1.11 Implications of circulating tumor cells (CTCs) in clinics

The count of circulating tumor cells (CTCs) can serve as a valuable indicator for predicting progression-free survival (PFS) and overall survival (OS) in various cancer types. In breast cancer, CTC count is a stronger prognostic marker in luminal cancer and triple-negative breast cancer (TNBC) but weaker in HER2+ tumors[98]. Real-time analysis of CTCs enables monitoring of tumor progression during and after treatments. Two clinical trials, NCT01322893 and SWOG0500, provided information on CTC number and breast cancer metastatic sites[99,100]. NCT01322893, a long-term prospective study of metastatic breast cancer (MBC), confirmed the number of metastatic sites as a significant prognostic marker. A prognostic model including CTC count ≥ 5 cells and the presence of CTC clusters improved prediction for PFS and OS. SWOG S0500 study found that the number of CTCs per 7.5 mL whole blood had prognostic value for chemotherapy resistance in MBC patients. Patients with higher CTC counts were more likely to have multiple metastases, especially those with more than 5 CTCs. Additionally, patients with over 5 CTCs or CTC doublets/clusters were prone to develop more visceral metastases. The enumeration of CTCs holds promise as an evaluation tool for therapy efficacy in MBC patients[99,100].

1.1.12 Features of circulating tumor cells and subpopulations

It has previously been observed that CTCs in pancreatic, breast, and colorectal cancers exhibit significant inter-/intra-patient heterogeneity, reflecting disease status and prognosis[101,102]. Morphologically, CTCs display different sizes and shapes, impacting their ability to navigate through capillaries and reach destinations[103]. Phenotypic heterogeneity arises from diverse genomic profiles, influencing drug sensitivity. CTCs are categorized into subgroups based on biomarker status, epithelial/mesenchymal phenotype and aggregation status with distinct genetic and biological characteristics affecting drug susceptibility as is described in Table 1[104].

Heterogeneity of CTC

Heterogeneity Biomarker status		**Genetic Characteristics**	**Biological characteristics**	**Drug responses**
	HER 2+CTC	Receptor tyrosine kinase (RTK) and pro-growth signaling pathways	Higher proliferation rate and lung metastases frequency than HER2- CTCs. The apoptosis rates were similar between HER2+ and HER2- CTCs	HER2+ CTCs were 2-fold more sensitive to the combination of HER2 and IGF1R/EGFR inhibitors.
	HER 2- CTC	Notch and DNA damage pathways		HER2-CTCs were resistant to chemotherapy and sensitive to notch inhibitors compared with HER2+CTCs
Epithelial/mesenchymal phenotype	E-CTC	TFF1, TFF3 Transcriptions enriched.	The number of E-CTCs was less associated with disease progression than that of M-CTCs. EM-CTCs were correlated with the worst prognosis than E-CTCs or M-CTCs. EM-CTCs acquired the strongest stemness and anoikis apoptosis resistance	E-CTCs were presented with lower drug susceptibility than M-CTCs. EM-CTCs were resistant to neoadjuvant chemotherapy.
	M-CTC	TGF-β, FOXC1, WNT signaling pathways. miR-106b and more mutation genes.		
	EM-CTC	miR- 34/SNAI1,miR-200/ZEB, TWIST1,SANAIL1,SLUG and ZEB1		

Aggregation status	Single CTC	Different transcription factors are hypomethylated	Singke CTCs were usually in normoxic status, meanwhile CTC-clusters were hypoxic. CTCs clusters had lower half-life, but stronger capacity of invasiveness and apoptosis resistance than single CTCs. More CTCs-clusters were mesenchymal types instead of epithelial types.	The formation of CTC-clusters could be suppressed by the knockdown of CD44. Plakoglobin or keratine 14. Besides the Na+/K+ ATPase inhibitor ouabain antagonized the maintenance of CTC-clusters
	CTC-Cluster	SERPINE1, FN1 transcriptions Plakoglobin keratine 14 Heparanase Notch-JAG1 signalling		

Table 1. CTCs subpopulations and features. Taken from [105]

1.1.13 Liquid biopsy principles and clinical challenges

Among several techniques, tissue biopsy is still considered the most common cancer diagnosis procedure worldwide, which requires the removal of a portion belonging to the original lesion. In order to determine a patient-specific tailored treatment, the histologic characterization of the fragment is performed. In many instances, however, the patient that is undergoing tissue biopsy can experience some risks, such as tumour sampling near main organs and vessels, lesions located in tricky regions of the brain etc. Imaging techniques are also used in conjunction with tissue biopsies to offer a better profiling of the tumor. These are, however, inadequate for a thorough study of the tumor, in addition to high radiation levels provided by radiology, which might expose the patient to a health problem. Fortunately, this is now evolving, and the oncological community has intensified its emphasis on radiation safety, contributing to advancements in technology, the implementation of new imaging procedures, and reasonable usage criteria to minimize and limit the exposure to radiation. The detection of minimal residual disease (MRD) is considered a main parameter regarding the patient's treatment and monitoring, and non-radiation approaches, including magnetic resonance imaging (MRI) scans, are still inconclusive and inadequate[106].

Therapeutic approaches and patient-tailored treatments are generally established based on the tumor molecular profile. The molecular structure of the tumor, however, changes rapidly through time as a result of a combination of internal and external factors with numerous consequences. The tumor has temporal and spatial heterogeneity[107] and is produced in some cases by stress over certain tumor regions that alter the genomic structure of it[108]. Even inter- and intratumoral convergent phenotypic evolution has been discovered in several regions of the same tumor[109]. The challenge of conducting a single biopsy-based therapeutic intervention and monitoring underestimates the magnitude of the tumor genomics, which is highlighted by its heterogeneity. Moreover, for a more effective tailored diagnosis of cancer, the progression of the tumor must be tracked at several time intervals. Several tissue biopsies, from both primary and metastatic lesion, are taken as the steps to be considered. However, the inherent health hazards, possible surgical complications, and economic considerations are just some of the many pitfalls in the acquisition of tissue biopsies, underlining the pointlessness of performing several biopsies. However, in certain body locations, the threat of metastatic proliferation or cancer "seeding" can be raised by the removal of certain tumors that are unable to be reached through biopsy[110].

As a result, it is important to search for minimally invasive biomarkers so that an early detection technology can be available, with its respective frequent monitoring along with cancer therapy. There has been unprecedented eagerness in the medical community to

explore the molecular environment of solid tumors by a blood draw, a process known as **Liquid Biopsy**. This technique has relevant advantages, including its minimal invasiveness, lower risk, and it has the potential of being analyzed with the use of lab-on-a–chip (LOC)-based platforms with low consumption of reagents, and does not require specialized personnel and expensive equipment for the diagnosis. Several cancer-associated parameters such as the tumour's molecular landscape and MRD among others could be determined by the application of liquid biopsy, which has demonstrated an enormous and valuable potential[111,112]. Lately, liquid biopsies have also gained interest for early diagnosis of tumors, therapeutic guidance, and recurrence monitoring[113]. Figure 7 describes the comparison between tissue biopsy and liquid biopsy.

Liquid biopsy has its origin in the fact that the body fluids contain biomaterials that are originated from different tissues, including cancerous ones. Undeniably, due to the fast evolution of cancer cells, tumor-derived nucleic acids and vesicles can be constantly released into the circulation, and even the whole tumor cells are separated from the primary tumor and enter the blood circulation, which explains the epithelial-mesenchymal transition[114,115]. Thus, detecting and characterizing circulating tumor DNA (ctDNA), exosomes and circulating tumor cells (CTCs), enable clinicians to cross-examine the evolution of different human cancers in a non-invasive way. There is a growing literature that documents how liquid biopsies are informative for detecting and characterizing CTCs[111,112,116–118], ctDNA [111,119–123124–126]and exosomes or extracellular vesicles[122,127,128]. The information extracted from these biological components allows for early cancer detection and real-time monitoring of therapies; identification of therapeutic targets and resistance mechanisms; along with understanding and characterizing of metastasis mechanisms, metastatic relapse or metastatic progression in cancer patients[127,129,130]. Therefore, liquid biopsies will certainly expand in the future as a key diagnostic element for early detection of cancer.

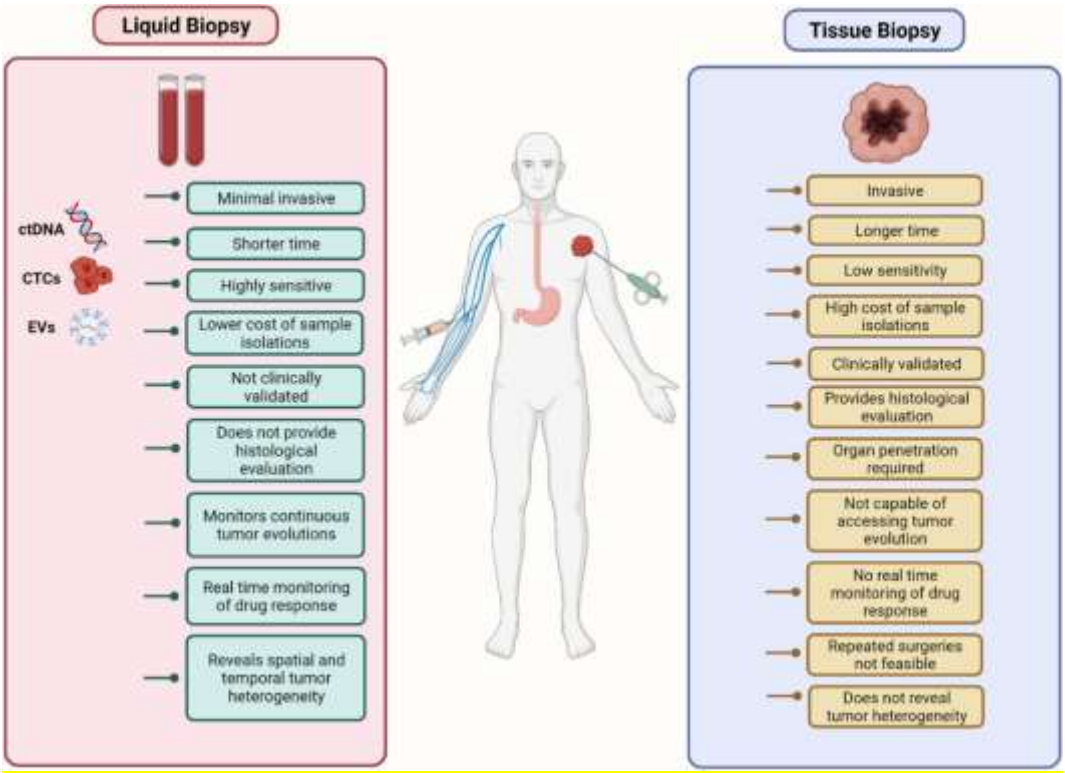

Figure 7. Comparison of traditional tissue biopsy and liquid biopsy. The schematic illustrates the advantages that liquid biopsies have gained over traditional invasive surgical methods over the past decade. Shown here are methods of extracting a test sample which usually includes a small tissue fragment in case of tissue biopsies and blood in LBs. Analytes that are isolated and monitored in LBs include ctDNA, CTCs, and tumor EVs. Taken from: [131]

From a clinical point of view, in order to achieve the successful application of liquid biopsies, some key challenges must be overcome, in particular with reference to the isolation of CTCs, such as:

1. **Low Abundance:** CTCs are extremely rare in the bloodstream, often present at a concentration of 1 in a billion blood cells. This makes their isolation and detection technically challenging and requires highly sensitive methods.

2. Heterogeneity: CTCs can vary greatly in terms of size, shape, surface markers, and genetic characteristics. Developing methods that can capture this heterogeneity accurately is a challenge.

3. Cell Viability: Isolating CTCs while maintaining their viability and functionality is crucial for subsequent analysis. The process of isolation can stress the cells, leading to changes in their gene expression and potential loss of relevant biological information.

4. Contamination: Blood samples contain various other cell types, debris, and substances that can interfere with the isolation process and result in false positives or negatives.

5. Technical Variability: Different methods are used for CTC isolation, including immunomagnetic separation, microfluidics, and filtration. Each method has its own limitations and biases, leading to variability in results between different isolation techniques.

6. Rare Cell Clusters: CTCs can be found as single cells or in clusters. Isolating intact clusters can be more complex, as they may have different properties than individual CTCs.

7. Loss of CTCs: The isolation process itself can lead to a loss of CTCs due to factors like cell adhesion, mechanical stress, and inadequate capture efficiency.

8. Clinical Utility: While isolating CTCs holds great promise for cancer diagnosis, prognosis, and treatment monitoring, the clinical utility of CTC analysis is still being established. The significance of the presence and characteristics of CTCs in relation to disease progression and treatment response is an ongoing area of research.

9. Sample Handling: Proper collection, handling, and storage of blood samples are critical to ensure the preservation of CTCs and minimize pre-analytical variability.

10.Cancer Type Specificity: Different cancer types might release CTCs with distinct properties, making it challenging to develop a universal isolation and detection method.

11. Rare Mutations: Some CTCs might carry important genetic mutations that are present in only a small subset of cells. Detecting these rare mutations requires highly sensitive techniques that can discriminate between normal and mutated DNA sequences.

To overcome these limitations, several microfluidic platforms have also been developed. Indeed, Lab-on-a-Chip (LOC) technologies have been exploited in the recent decades for several biomedical applications such as diagnostics, biochemical assays, and drug discovery among others. Microfluidics and LOC technologies are directly correlated terms since LOC technologies aim to integrate and bring different laboratory processes into the microscale to exploit the advantages that working at this length scale provides. Therefore, these devices are frequently composed of microfluidic elements like microchannels, micropumps, microvalves, etc. to enable processing small (microscaled) amounts of liquid.

Nowadays, most of the analytical and diagnostic assays are done with benchtop equipment in hospitals and/or centralized laboratories which are either operated by trained personnel or composed of chains of automated pipetting robots with the associated increment of power consumption and space demand. Microfluidic LOC platforms arise as an alternative to the

present model of diagnostics since these offer a wide range of new opportunities that can be summarized as [132,133]

- Portability due to its reduced dimensions.
- Higher sensitivity
- Faster results obtaining
- Reduced laboratory space
- Lower cost per test due to less quantity of reagent required.

In addition, apart from those advantages stated above, working at the microscale allows taking advantage of the unique phenomena taking place at such scale:

- Gravitational force loses importance
- Well defined laminar flow
- Controllable diffusion
- High degree of parallelization

Therefore, all the characteristics mentioned before, together with the fact that microfluidic LOC devices have the perfect size for cell manipulation and that they have the possibility to play with well-defined particle forces related to inertial effects[134,135], makes them ideal for building CTCs isolation devices that can be used for liquid biopsies.

1.1.14 Microfluidic-based isolation of CTCs

The application of microfluidic devices to the detection and isolation of circulating tumour cells is quite recent, the firsts scientific works arising towards 2005. The first scientist to create a considerable impact in the field was Prof. Toner and his group at Harvard Medical School with the publishing in 2007 of a research paper [134,135]in which they obtained promising results concerning the isolation of CTCs on a microchip capable of efficient and selective separation of viable CTCs from peripheral whole blood samples, mediated by the interaction of target CTCs with antibody (EpCAM)-coated microposts under precisely controlled laminar flow conditions, and without requisite pre-labelling or processing of samples. At that moment this was revolutionary and encouraged a lot of scientists all with the same purpose of developing a lab-on-chip device to detect and isolate CTCs. If we now look back on that paper, it has become the most cited paper regarding CTCs isolation using microfluidics with almost 3000 citations up to date.

Since then, many other microfluidic devices have been proposed for the separation of CTC from blood. They can be based in microfiltration, deterministic lateral displacement, centrifugation, inertial focusing, affinity-based methods, among others[136–140]

Nowadays, many microfluidic devices have been proposed to separate cells according to their properties like size, density, shape, deformability, or biomarkers expression[132,141,142] The parameters used to evaluate the performance of this technology including purity, recovery rate and cell viability. The purity is associated to the blood cells depletion, which indicates the number of CTCs compared to blood cells. Meanwhile, recovery rate reflects the ratio of targeted cells collected in the CTCs outlet to the total number of CTCs and cell viability indicates if the cells recovered are alive [138,141] Considering the low concentration of CTCs on the blood, it is important to guarantee that all the CTCs are being recovered by the device and that they are viable. Thus, the cells recovered could be used in personalized drug screening [143,144].

Overall, with the emergence of personalized medicine the latest developed devices for CTCs separation are focused on the detection of CTC via label-independent methods, low pre-treatment, large volume of sample processing in a short time, high purity, and possibility to propagate the isolated CTCs [145,146].

1.1.15 Affinity-based methods

The affinity-based microfluidic devices are based on the use of specific antibodies attached on the channels walls to capture target cells. These devices have been developed as positive enrichment techniques when the antibodies are used to directly capture CTCs and negative enrichment techniques if antibodies are used to target blood cells. The first positive enrichment platforms were devices composed by series of posts functionalized with EpCAM antibodies as explained before [147]. Nevertheless, the cells follow the fluid streamlines of the laminar flow, which limit the interaction between the CTCs and the antibody modified surface. To overcome this, herringbone-like structures were proposed[147–150] that promotes fluid mixing in the channel, thus increasing particle-surface interaction. Figure 8 presents a representation of particles trajectories in a rectangular channel and in a channel with a herringbone structure. In Figure 2A the particles follow the fluid streamlines in a rectangular straight channel, while in **Error! Reference source not found.** 2B the herringbone structure promotes a mixing, so the particles move transversally on the channel with more probability to reach the functionalised channel walls.

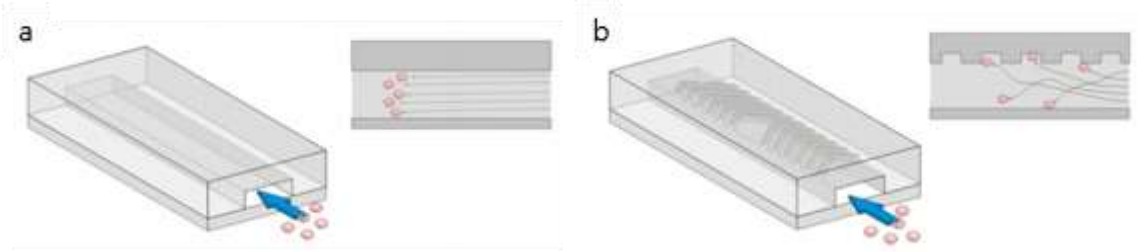

Figure 8. Graphic representation of the particles trajectories in **A)** traditional rectangular channel and in a **B)** Herringbone device. Figure from [148]

Different herringbone-chips were studied for positive-enrichment, including the surface functionalization with different antibodies (Figure 10B,C,D), specific for some cell lines. Some of them have two opposed surfaces with herringbone structures to increase the mixing [140,142,148,150,151] . Moreover, to decrease the non-specific cell adherence Wang et al. proposed a wavy herringbone structure [140]. However, one of the major disadvantages of this system is associated with the difficulty of eluding CTCs after being captured, this process could have an impact on their viability[139] .

Recently, new methods have been developed for improving positive enrichment methods such as hydrogel microparticles (MP) functionalized with EpCAM antibodies, which have the advantages of water-like reactivity, biologically compatible materials, and synergy with various analysis platforms (Figure 9)[48] In this method the hydrogel particles are synthesized using degassed mold lithography (DML), as a result the porosity and functionality of the MPs increase achieving an effective conjugation with antibodies [152]. In addition, the MPs functionalization is based on carbodiimide cross-link chemistry conjugated to antibodies through carboxyl groups. Also, NHS and EDC chemistry was used to covalently attach Neutravidin protein to the carboxyl groups. Finally, biotinylated anti-EpCAM antibodies were used for avidin-biotin reaction [153]. Moreover, other methods based on Immunofunctionalized hydrogels have been successfully developed for capturing circulating tumor cells (CTCs) (Figure 10E)

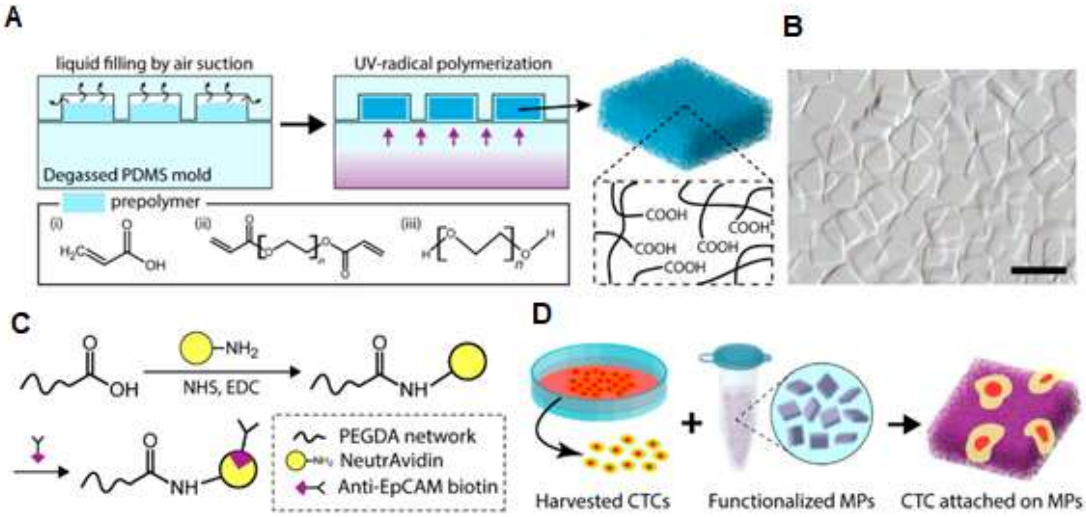

Figure 9. Positive enrichment methods based on hydrogel microparticles (MP) and EpCAM antibodies. **A)** Hydrogel microparticles synthesized by degassed mold Lithography (DML). Thus, UV-induced radical polymerization with prepolymers(i) acrylic acid(ii), polyethylene glycol diacrylate (PEGDA) and (iii) polyethylene glycol (PEG), hydrogel microparticles containing carboxyl groups are synthesized. **B)** Image of polymerized hydrogel microparticles (MP). Scale bar 200µm. **C)** Interaction between avidin protein and biotin allow the anti-EpCAM-biotin conjugation. This principle is based on the reaction between carboxyl groups in the particles and primary amines in NeutraAvidin with the help of N-hydroxysuccinimide (NHS) and N-(3-dimethylaminopropyl)-N'-ethycarbodiimide hydrochloride (EDC). **D)** Circulating tumor cells (CTCs) captured by functionalized hydrogel microparticles with EpCAM antibody. Licensed under CC BY-NC International License [153].

Other studies were focused on increasing the capture efficiency of CTCs, such as the GEDI chip. In this case, the optimization was based on the displacement, size and shape of microposts, as well as, the use of an specific prostate antigen (PSMA)[154].On the other hand, among the commercial methods available, CEE^{TM} microfluidic chip is characterized by randomly located microposts functionalized with streptavidin, which allow to capture targeted CTCs with biotinylated antibodies [155]. Meanwhile, The NanoVelcro CTC chip is composed by silicon (Figure 10A) nanowire substrates (SiNWS) functionalized with EpCAM for CTCs capture[156,157].

All the previous methods have a limitation, though. As mentioned before not all CTC express a specific membrane marker. potentially important CTCs subpopulations like mesenchymal and stem-cell like CTCs would be missed[158] . Besides, the CTCs would need to be eluted after being captured and this process might have an impact on the CTC viability[159,160]. So that, affinity-based techniques based in negative enrichment were proposed.

Negative enrichment of CTCs is an affinity-based method that has the purpose of removing hematopoietic cells by targeting specific antigens that are not expressed by the CTCs as, for instance, CD45 (leukocyte common antigen)[161] For example, CTC-iChip was developed by Ozkumur et al, which eliminate the blood cells based on physical properties and CD45/CD15 expression[162] Hyun et al, proposed a herringbone device for negative enrichment by targeting of leukocytes with the surface immobilized with CD45 after the blood lysis or centrifugation for eliminating the erythrocytes [80] . Another example is the geometrically activated surface interaction (GASI) chip, which was like the Herringbone-chip but with enhanced microvortexing properties aimed at increasing the number of captured leukocytes[162]. Overall, negative enrichment allows the capture of CTCs with low or no expression of EpCAM and the CTCs can be collected intact and viable for subsequently clinical analysis[163] However, as the population of leukocytes in the sample is usually very high, even large depletion rates are not always ensuring good results concerning the purity of the sample. In addition, negative enrichment is used to capture the leukocytes after the blood sample has been already processed to eliminate the erythrocytes, so that, this methodology has potential to be used to complement other techniques by enriching their results in terms of purity.

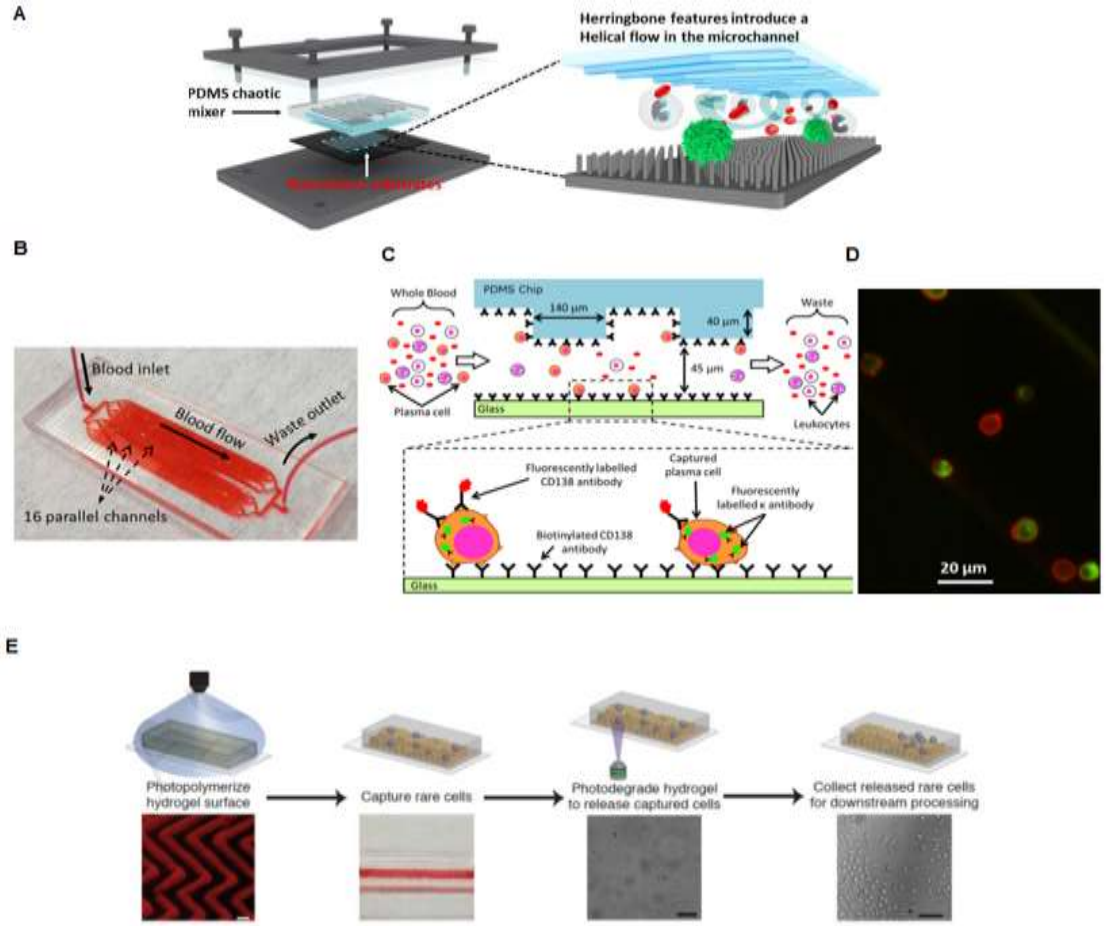

Figure 10. A) NanoVelcro CTC Chip is composed by a patterned silicon nanowire (SiNW)substrate and herringbone features which promote the helical flow in the microchannel improving the interaction between CTCs and anti-EpCAM coated SiNW substrate. Licensed under Creative Commons Attribution 3.0 License (CC BY 3.0). The final, published version of this article is available at[164] **B)** Herringbone microfluidic device composed by 16 parallel microchannels for cells capture**. C)** Schematic representation for capture and analysis of plasma cells in microfluidic device. In this technology the microchannels are coated with biotinylated CD138 antibodies, which capture the cells from the flow. Finally, capture cells are staining with anti-κ immunoglobulin for their identification. **D)**Fluorescence image shows the cells captured from a clinical sample. Red represents the CD138 and green anti-κ immunoglobulin. Licensed under Creative Commons Attribution 3.0 License (CC BY 3.0). The final, published version of this article is available at [165]. **E)**Schematic representation of fabrication and degradation of patterned photodegradable hidrogel films. Thus, a PDMS master is covered with hydrogel and irradiated at 405nm light. Subsequently, a microfluidic herringbone channel is bonded on the top of the hydrogel film. The hydrogel can be degradated under flow condition using irradiation of 365nm light. Finally the CTCs can be collected for further processing . Copyright (2018), Elsevier

Recent evidence suggests however that the entire CD45+ population should not be considered as a discriminant for isolating CTCs from a population of leukocytes, due to some

CTCs displaying expression levels of CD45 and some leukocytes subpopulation such as non-lymphocytes, which show low expression of CD45[166]. To overcome the limitations of employing antibodies, aptamers have emerged as a potential alternative for the isolation of CTCs. These are single-stranded oligonucleotides such as RNA, DNA or peptides that bind to targets such as proteins with a high specificity and sensitivity[167].Moreover, it was also discovered that an in-vitro process called Systematic Evolution of ligands by exponential enrichment (SELEX) allows the synthesis and selection of aptamers in a straightforward manner[166]. In fact, the potential use of aptamers for isolating CTCs has been successfully evaluated with samples spiked with different cancer cell lines and in patients' samples. Based on the previous findings the key advantage of using aptamers for isolations of CTCs is that they can be prepared in different panels targeting several proteins expressed on available cancer cells, for which it is not necessary to know the precise targets[166].

Finally, both negative and positive enrichment methods can be combined with magnetic-activated cell sorting. In this case, magnetic microbeads are coated with the antibodies and a magnetic field is used to attract the target cells bounded to the microbeads[138,168]. However, these devices have limited throughput due to the time needed for the force to act on the particles [168].

1.1.16 Label-free methods

The devices discussed within the previous section has, as a main drawback, the fact that they rely on the expression of a certain biomarker present on the cell membrane. However, this condition is not always satisfied, and this might lead to a loss of CTCs and affect the performance of the device in terms of the recovery rate. As an alternative,

several microfluidic devices have been proposed for the enrichment of CTCs from blood based exclusively on physical properties of the CTCs such as size, density, mechanical plasticity and dielectric properties[169]. Among these methods, the ones that have been more exploited are size-based methods. This methodology considers the difference on size between CTCs , erythrocytes and leukocytes. As was previously indicated, the diameter of CTCs usually ranges from 15 µm to 20 µm [170], erythrocytes are between 6 µm to 8 µm, meanwhile the leukocytes goes from 6 µm to 20 µm, where neutrophils represents between 40% to 75% with diameters that go from 10 µm to 12 µm[171].

1.1.17 Size-based methods

Among size-based methods, one can basically find: filters, in which the sample flow through an array of micro-scale constrictions and inertial microfluidic sorting devices, in which the cells are separated due to size-dependent inertial fluid forces.

1.1.18 Filtering microfluidic sorting devices

Normally, these kinds of devices capture the CTCs as they are bigger and let pass the other cellular components and are classified in three main groups[172]:

1. **Size-exclusion Hydrodynamic chromatography:** Chromatography is a classical technique for separating components of a mixture based on their ability to pass through a column with a porous material. This method is used for separating molecules in a label-free manner[173]. In 2011, Hongshen Ma et al used this principle, but in an opposite behavior for CTCs separation. Thus, dynamic microstructures have the advantages of filtration and hydrodynamic manipulation, wherewith is possible to discriminate cells based in size and deformability, meanwhile the cells are in a continuous flow[172]

On the other hand, an outstanding device designed in the low Reynolds number is known as deterministic lateral displacement (DLD) (Figure 11A,B). In this technology the smaller cells follow the streamlines and pass through and series of posts without net lateral displacement. Meanwhile, the bigger cells change to a different streamline when enter in contact with the pillars and are laterally moved from the original streamline[174]. The evidence from previous studies has been shown the potential of this technology in separating cancer cells from blood with a performance of 80%[175].

2. Pillars: These kinds of devices use an array of micro-posts that form constrictions. Mohamed et al developed a microfluidic device composed by pillars of four successively decreasing clearances from 20 µm to 5 µm[176]

3. Pores: This technology is a membrane with holes which demonstrated a recovery rates higher than 85%.In fact, there are some commercial devices based on this principle such as Rarecells® , Screencell®, and Clearcells®[177–179]. The principle of this technology is based on the force applied to the cells which depends on the flow rate and is related with the deformability of the cells(Figure 11C). Thus, the flow rates and the cross-section of the membrane constrictions are the key parameters that define the efficiency of this kind of devices. Nonetheless, the major disadvantage of this method is the clogging, when it used with whole blood sample and as result the flow rate change. The flow rate modification

triggers a low throughput and change in the limit separation size. Moreover, these microfluidic technologies do not allow recover the CTCs from the membrane for further clinical analysis[139,141].

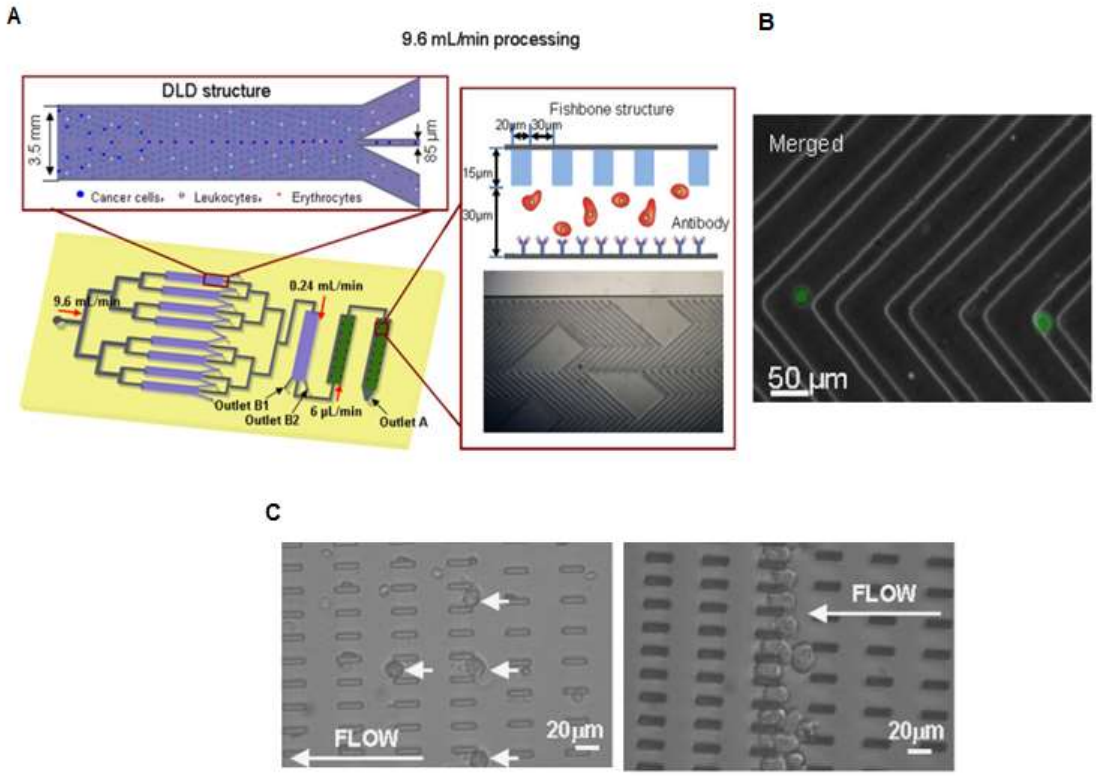

Figure 11. Microfluidic chip composed by a deterministic lateral displacement (DLD) channel with mirrored triangular micropost array. Thus, bigger cells like cancer cells and some leukocytes were concentrated in the middle of the channel, meanwhile the smaller cell such as the erythrocytes and most of the leukocytes follow the streamlines flow direction. Finally the capture channel is a PDMS layer with herringbone structures modified with EpCAM. These structures promoting the capture of CTCs. Copyright (2013), Elsevier **B)** Fluorescent images of cancer cells captured on the chip surface. Cells were stained with Vybrant® DyeCycle™ Green. Copyright (2013), Elsevier . **C)** microfluidic devices for cancer isolation based on cell size and deformability. The images show blood samples spiked with MDA231 cells, where all the blood cells flow freely through the device, but the MDA231 cells were retained between the gaps. Copyright (2009), Elsevier [180]

1.1.19 Inertial microfluidic devices

Among the systems proposed in the literature, microfluidic devices based on the inertial focusing are promising, which could overcome the limitations of other methods that use pillars, porous or labeling approaches with the advantage of achieving a high throughput[181]. Several studies have revealed that in a Reynolds number between stokes flow (Re<<1) and inviscid flow, namely, in a range from 1 to approximately 100, forces from inertial effects appears such as drag forces from Dean flows, shear gradient lift forces, and wall-effect lift forces, which are balanced for achieving the size-based separation[135,182,183].

Overall, the system can be described by the channel Reynolds number (Re) and the particles Reynolds number (Rep) by the follow equations, where ρ_f and μ are the fluid density and dynamic viscosity, U_m is the maximum fluid velocity in the channel, D_h represents the hydraulic diameter and the particle diameter. In a rectangular channel D_h = 2WH /(W + H) , in which W is the channel width and H the channel height

$$Re = \frac{\rho_f U_m D_h}{\mu}$$

Equation 1

$$Re_p = Re_c \frac{a^2}{D_h^2} = \frac{\rho_f U_m a^2}{\mu D_h}$$

Equation 2

In 2007, Di Carlo at el published a pioneer work, in which the inertial focusing was used to control the particles position in microfluidics devices with curved channels according to the particles size. They demonstrated that particles did not follow the fluid streamlines but migrated across them as the inertial forces became significant. The particles position in the microchannel was related to the particles diameter[168].

Traditionally, the inertial lift forces and drag forces are orthogonally on a particle, but in a curved channel a secondary cross-sectional flow start to appear (Dean flows)[184]. Then, the Dean flow triggers that the particles experience a drag force on the same axis as the shear gradient and the wall effect lift forces[168]. Hence, the balance between these forces cause

different equilibrium positions of particles depends on their size. Thus, small particles follow the Dean flow while big particles are under a stronger lift force.

The Dean flow can be described by the Dean number through the Equation 3, in which r is the radius of channel curvature[168].Moreover, inertial lift forces and drag forces can be calculated as indicate the Equations 4 and 6.

$$D_e = R_e\sqrt{\frac{D_h}{2r}}$$

Equation 3

$$F_L = \frac{F_L\,(R_e X_L)\rho U_F^2\, a_p^4}{D_h^2}$$

Equation 4

In equation 4 Re ($Re = \frac{\rho U_F D_h}{\mu}$) represents the channel Reynolds number, μ is the fluid dynamic viscosity, ρ is the fluid density, U_F is the average velocity of the fluid and a_p is the particles diameter. Meanwhile, F_L is the lift coefficient that correspond to a complex function of the Re and the cross-sectional positions of particles X_L.

On the other hand, D_h is the cross-sectional hydraulic diameter represented by the equation 5. Where w and h are the width and height of the microchannel, respectively[185].

$$D_h = \frac{2wh}{w+h}$$

Equation 5

As previously mentioned, Dean Drag Force can be expressed as Equation 6. Where ρ is the fluid density, U_F is the average velocity of the fluid and a_p is the particles diameter. Meanwhile, D_h is the cross-sectional hydraulic diameter and R is the radius of the microchannel[168,185].

$$F_D \propto \rho U_F^2 a_p D_h^2 / R$$

Equation 6

Up to now, several spiral devices have been reported for isolating CTCs from the blood applying inertial forces [141]. As explained before, the separation is based on the difference of size. Thus, the lift force is important for big cells like CTCs, meanwhile is not significant for small cells such as erythrocytes and small leukocytes. The blood cells mainly follow the Dean flow due to the Drag force, and do not focus on certain positions. Finally, the blood cells are located in one device outlet, according to the Dean cycle and the CTCs are focused in another outlet. Some devices developed by previous researchers included a sheath flow inlet to initially confine the blood cells in one wall, so all of them can follow the Dean cycle [141,156,186–188]. Sun et al. proposed a double spiral device with 6 loops and alternation of the flow direction due to a S-turn. The device has 20 a low aspect ratio compared to other devices in the literature (H/W = 0.167) and present one inlet and three outlets [189]. Moreover, spiral design with a trapezoidal cross section were also proposed to generate stronger Dean flow than in a traditional rectangular cross section; this Device is composed by 3 loops and was obtained a recovery rate of 80%[187,190] (Figure 12B) Some years ago, devices with multiplexed setup were proposed to increase the throughput[187] , which are composed by 4 spirals in parallel (Figure 12A) that were stacked forming a multiplexed device with 40 spirals, reaching a throughput of ~ 500 mL/min. The system was tested for separation of Chinese hamster ovary cells (CHO) and yeast[181] . Also, a cascade microfluidic devices were proposed including the integration of more than one spiral [191]. These technologies demonstrated a recovery rate between 80% to 90% and a throughput up to 2 mL/min[192].

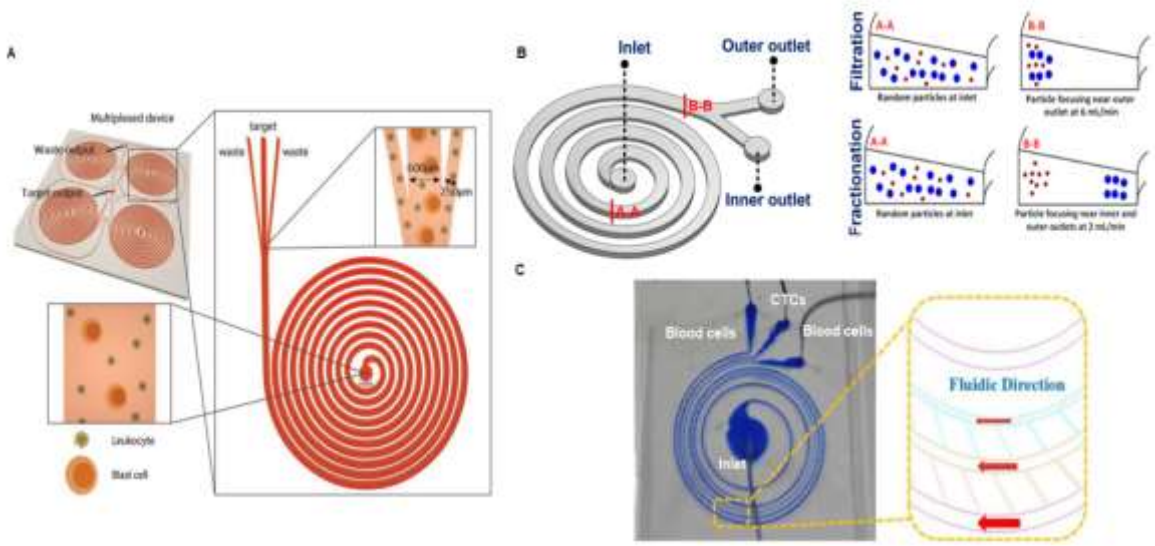

Figure 12. A) Multiplexed spiral device. The device is composed by four inputs in the middle of the sorting unit. The figure shows the CTCs outlet and waste outlets are indicated. Licensed under CC BY-NC International License. The final, published version of this article is available at[193]. **B)** Spiral microfluidic device with trapezoidal cross-section microchannels. The device has two modes: filtration and fractionation. In filtration mode, the particles suspended are trapped and focused near the outer wall under strong vortices. Meanwhile, in the fractionation mode, smaller particles (red) are trapped in Dean vortices and keep near the outer wall, but the bigger particles (blue) are focused near the inner wall. Thus, the particle separation by size is achieved. Basically, changing from one mode to other depends on the magnitude of the hydrodynamic forces inside the microchannels. Licensed under CC BY-NC International License. The final, published version of this article is available at[194].**C)** Representation of triple-microchannel spiral microfluidic chip composed by slits for isolation of CTCs. The three microchannels are interconnected by arrays of slits, which allow that the cells pass from one main microchannel to other through the flow direction. Licensed under CC BY-NC International License. The final, published version of this article is available at [194]

1.1.20 Dielectrophoresis

The dielectrophoresis (DEP) represents a label-free, accurate, fast, low-cost diagnostic technique. This method is based on the dielectric cell properties, due to the cells are electrically neutral but they can be polarized, which depends on their polarity and conductivity. Thus, when the cells are subjected to a non- uniform electric field, a dielectrophoretic force (FDEP) starts to appear, whose magnitude and direction depends on the dielectric properties of the cells, the medium, their size and shape, as well as the frequency of the electric field[195]. It has been reported two types of FDEP, a positive dielectrophoresis (Pdep) which appears when the cell polarization is bigger than the medium.

Thus, the cells move towards the strong electric field region. On the other hand, there is a negative dielectrophoresis (nDEP) that appears if the polarization of the cells is smaller than the medium and therefore the cells move in the opposite direction [195]. This method allows that cells can be differentiated depending on the polarizability (Figure 13A,B).

Currently, microfluidic devices with electrodes embedded that produce the AC electric field have been developed. The benchtop device in the literature presents a recovery rate between 70% and 90%[196]. Alazzam et al demonstrated a yield of 95% by applying this methodology. The main drawback is the low throughput[197].

Therefore, this methodology is used as a complement to the other ones, as the sized based methods. This have been explored by Moon et al. who combines hydrodynamic focusing with dielectrophoresis and obtained 162-fold enrichment of the MCF-7 cells – CTCs cells model over RBCs at a 7.6 mL/h flow rate[198].

In contrast with traditional technologies reported, microfluidics-integrated separation method combined with ODEP represent a novel strategy for complex cell manipulation, which involve suspension, transportation, collection, and purification of cancer cell. This method was validated with 8mL of blood samples with H209 cancer cell clusters, as result an excellent recovery rate up to 91.5% ± 5.6% was achieved[198].

1.1.21 Microfluidic-based detection of CTCs

In general, the CTC separation methods described so far have in common the absence of integrated detection of the isolated tumor cells into the microdevice. Most of the systems, to elucidate the presence of the CTCs, use fluorescent-labeled antibodies specifically attached to the CTC, and the fluorescence label is detected with an external microscope. However, some authors have gone one step further and have combined microfluidic isolation techniques with integrated sensors for CTCs analysis in situ. We have summarized here some representative examples using either electrical, Optical or chemical sensors:

1.1.22 Field-effect transistors (FET) and high electron mobility transistor (HEMT)

Field-effect transistors (FET) are semiconductor components with three terminals (gate (G), source (S) and drain (D))[199].One of the major challenge of using FETs as biosensors is achieving the immobilization of afftinity reagents such as antibodies or aptamers on the open gates[200–202] . Furthermore, Yi-Hong Chen and their colleagues developed a microfluidic device composed by CTC-specific aptamers functionalized on a FET surface and it is composed by a

dual-layer with two inlets and 14 individual trapping chambers. The chip was tested with human colon cancer cell lines (HCT-8), as a CTC model and blood samples spiked with HCT-8 cells. As result, the device was able to capture a maximum of 42 from a total of 1000 cancer cells [203].

Some years ago, Pulikkathodia and colleagues developed a high electron mobility transistor (HEMT), which is composed by a multiplexed sensor integrated in a microfluidic channel to detect colorectal cancer cells (HTC-8)[204].Besides, the rise of impedance spectroscopy represents an excellent tool for label-free characterization of cells, which provides information about electrical cell parameters[205]. Some devices were developed based on this principle,such as the microfluidic device with circular electrodes designed by Nguyen and Jen. This Device was validated with A549 lung CTCs and blood, which was able to discern between the two cell populations based on their different resistivity[206].

1.1.23 Optical and chemical sensors

To date, some optically read out methods and their integartion into microfluidic devices have been designed, which include reflectance spectroscopy, surface plasmon resonance, and evanescent wave sensing, among others. In 2012, Kumeria and collegues reported a microfluidic nanopore reflectometric interference spectroscopy (RIfS) device composed of microchannels and Anodic Aluminum Oxide (AAO) substrate modified with anti-EpCAM for detecting CTCs[207].Thus, when the CTCs binding to the EpCAM antibody on AAO Surface a wavelength shift in the Fabry-Perot interference fringe appears[207].

According to the study provided by Tzu-Keng Chiu et al, the metabolic performance of càncer cells like the production of lactic acid by CTCs represent a promesing approach. This Technology can count the cells by the formation of a micro-droplet and optical transduction of latic acid for cell single detection. Unfortunately, the device can not detect the presence of similar cells like leukocytes[208].

Finally, the metabolic change produced by the CTC that produce a reduction on the surrounding pH was used as a method for differentiating cancer cell lines. The PH studies were performed by potentiometric methods with Ag/AgCl reference electrode and a ZnO working electrode (Figure 13C) Nonetheless, the proposed device was not tested with blood samples[209].

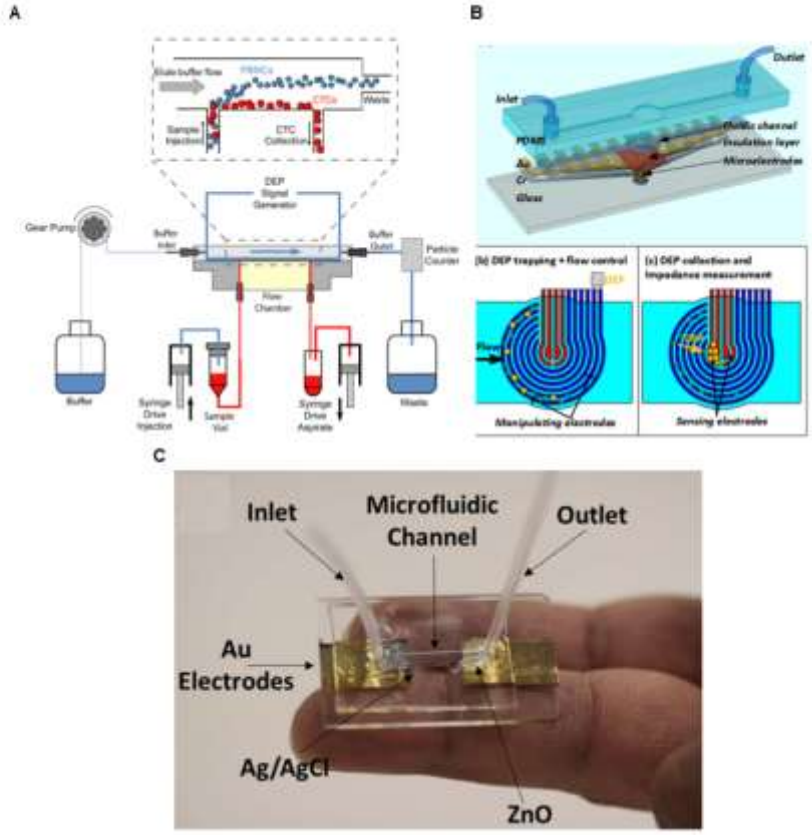

Figure 13. Schematic representation of ApoStream flow chamber. This device applies an AC electric field to the sample and is composed by electroplated copper and gold electrodes on the bottom part of the flow chamber. The sample was introduced into the flow chamber and the cancer cells are collected in the other rectangular port. The principle of separation is based on the DEP forces which pull the cancer cells through the bottom chamber and repel the other cells. **B).** Microfluidic device composed by electrodes, which allow the isolation of cancer cells due to the DEP effect and the difference in cell size. Thus the target cells were trapped onto the sensing electrodes. Finally, the impedance measurements allow to identify the presence of cancer cells. Copyright (2018), Elsevier[210]. **C).** Microfluidic pH Sensor for detection of cancer cells based on the measurements between a silver–silver chloride and zinc oxide electrodes for CTCs recognition in blood. The device detects the cancer cells based on changes of pH in the extracellular environment . Copyright © 2017, American Chemical Society.

1.1.24 Fabrication of microfluidic devices.

Photolithography and soft lithography are prevalent methods for developing microfluidic cell culture or processing devices. UV exposure creates defined microstructures on a photoresist-coated substrate. Cross-linking forms a reusable master for elastomer replication, often PDMS [211,212]. Photolithography, originating from microelectronics, is a technique to create precise microstructures on substrates like silicon[213]. In this process, a silicon wafer is coated with photoresist through spin coating, its thickness determined by spin speed. High-energy UV light cross-links the photoresist, making it soluble or insoluble depending on its type (positive or negative). Microstructures are generated by exposing the photoresist to UV light through a patterned mask. Heat completes cross-linking, and structures emerge by removing exposed (positive) or unexposed (negative) photoresist using a developer solution (Figure 14). The silicon wafer with patterned photoresist becomes a reusable template for soft lithography, commonly using PDMS as an elastomer. PDMS, transparent and non-cytotoxic, is bonded to glass after curing. PDMS's hydrophobicity can lead to air bubbles; rinsing with ethanol and water helps. Though PDMS has drawbacks like molecule absorption, it's useful for prototyping microfluidic devices due to its simple fabrication (Figure 14) [211].

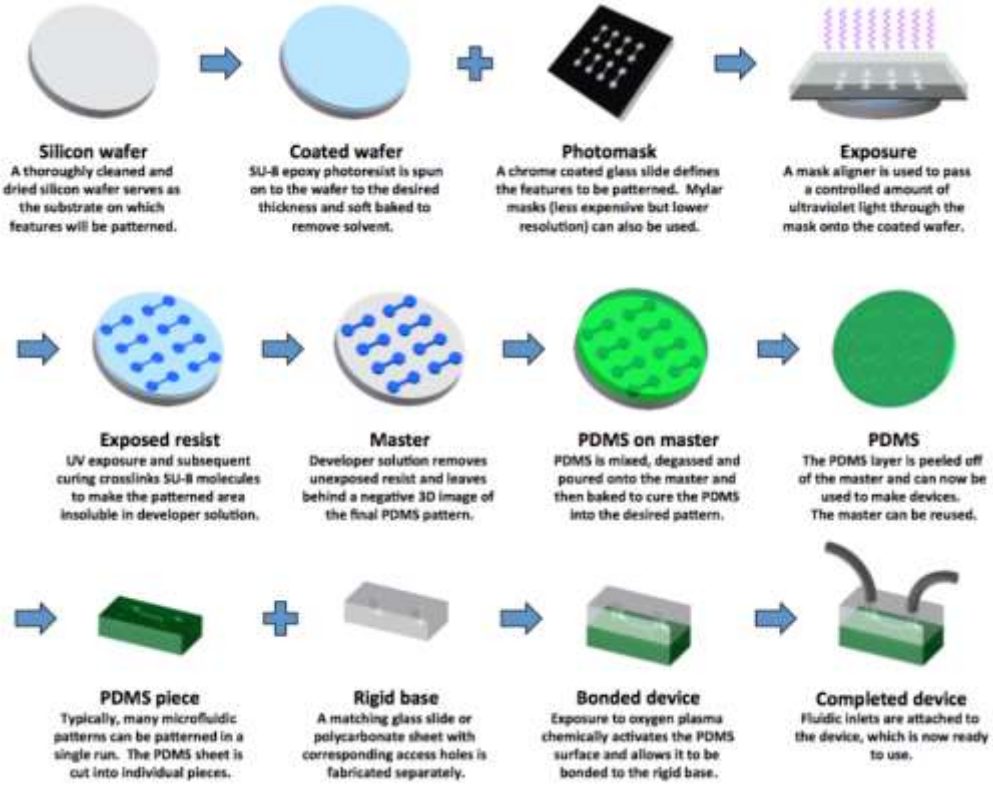

Figure 14. Microfluidic devices fabrication using photolithography and soft-lithography methods [211].

On the other hand, for varying height levels in microfluidic channels, multilayer soft-photolithography is essential[214].Modern techniques like micromilling[214,215], laser micromachining[216], and 3D printing[217–219] offer alternatives but lack resolution compared to photolithography. Multilayer photolithography requires photomask alignment, typically done in cleanrooms, which is costly and inaccessible. An alternative employs a costly motorized micromanipulator and zoom system for aligning layers in a PDMS chip. However, the setup details, protocol, and operation have not been reported[220] (Figure 15).

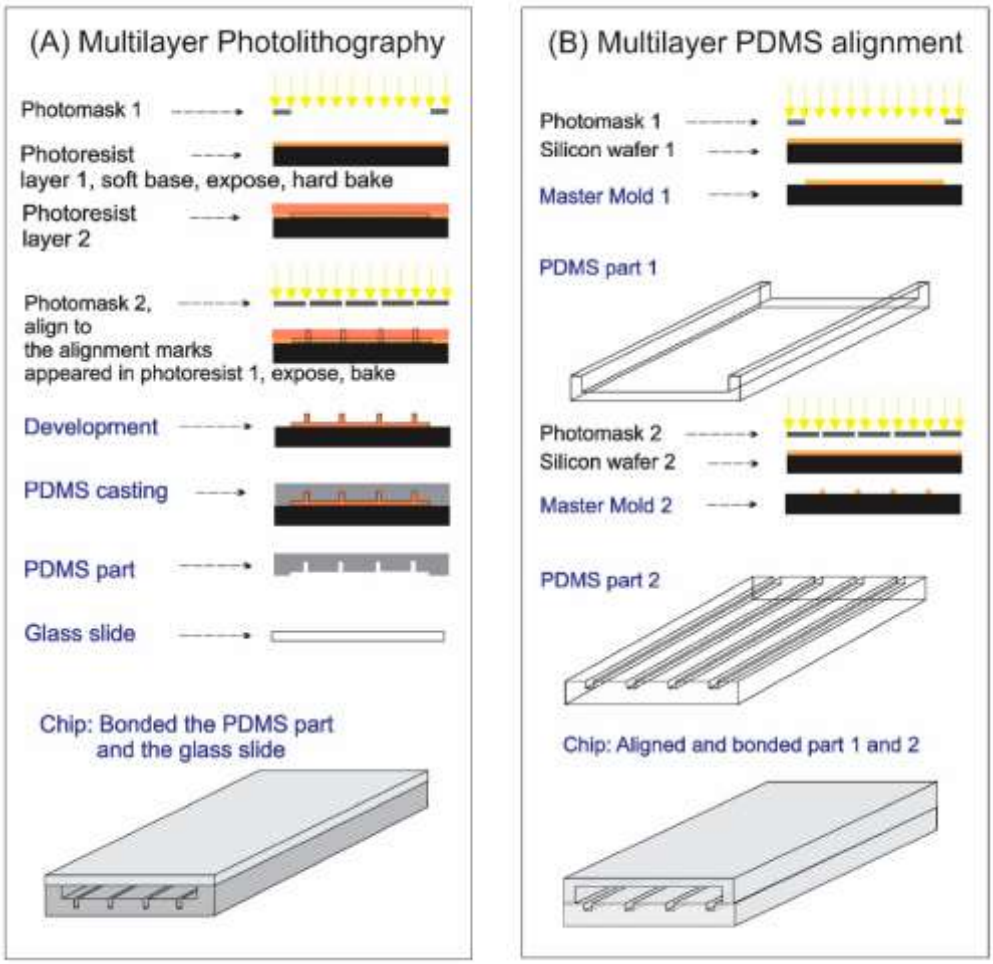

Figure 15. Schematics showing the process flows of fabricating: **A**) the multilayer photolithography approach using a mask aligner to align the photomask number 2 to the marks on the previous exposure photoresist layer (created from photomask number 1); **B**) a multilayer PDMS chip by alignment of two PDMS slabs. Both methods result in the same PDMS structures in the final chip.[221] .

As stated above microfluidic research predominantly employs PDMS and other polymers due to their ease of fabrication, flexibility, cost-effectiveness, and avoidance of issues associated with rigid materials. PDMS, with its appealing properties, serves as a suitable material for rapid prototyping of versatile microfluidic devices across applications. Moreover, PDMS surfaces are inherently hydrophobic due to the presence of repeating –O-Si(CH3)2 groups.

Oxygen or air plasma treatment can render PDMS hydrophilic by introducing silanol (Si–OH) groups and degrading methyl groups. However, plasma-oxidized PDMS gradually reverts to hydrophobicity due to surface reconstruction and non-crosslinked prepolymer components blooming. Sustained hydrophilicity can be maintained by contact with water or polar solvents. PDMS surfaces can react with various silanes (Si–R) bearing functional groups (e.g., NH2, COOH, SH), enabling tuning of hydrophilicity, hydrophobicity, or reactivity. Grafting poly(ethylene glycol)di-(triethoxy)silane creates a permanently hydrophilic surface and reduces protein adsorption. Amino-terminated silanization offers a reactive surface for protein attachment. These modified surfaces can revert to hydrophobicity due to siloxane blooming, which might be counteracted by sol-gel coatings, an avenue yet to be extensively explored.

For irreversible sealing channels in PDMS is simpler compared to glass, silicon, or thermoplastics, as it doesn't require high temperatures, pressures, or voltages. For instance, glass-to-glass or silicon-to-silicon bonding demands high temperatures (~600°C for glass; >800°C for silicon) and voltage (500–1500 V for anodic bonding of glass). PDMS channel sealing can occur under standard lab conditions. Air- or oxygen-based plasma treatment of PDMS and the substrate surfaces enables irreversible bonding between PDMS and materials like glass, silicon, polystyrene, polyethylene, or silicon nitride [222]. Plasma oxidation generates silanol groups on PDMS and –OH functional groups on the other materials. Contact between these treated surfaces creates covalent bonds through siloxane bridges. This process is efficient, reversible sealing at room temperature, which is advantageous for microfluidic device fabrication. In contrast, other materials require intricate methods like adhesive bonding or thermal bonding. The simplicity and versatility of PDMS channel sealing make it a preferred choice in microfluidic device construction[222].

Another notable advantage of PDMS compared to glass, silicon, and rigid plastics lies in its capability to establish reversible conformal contact, known as van der Waals contact, with smooth surfaces. This property enables PDMS devices to be demountable, allowing for repeated sealing without degradation. Demountable microfluidic devices find applications in patterning surfaces with proteins, cells, and biomolecules using fluid flow [223]. Binding assays have been demonstrated using such devices, where antibodies were patterned on a glass substrate by flowing antibody solutions through parallel channels[224,225]. The PDMS device can be peeled off, rinsed, and repositioned perpendicular to the initial channels for introducing antigen solutions. Detection of antibody-antigen complexes occurred at intersections between antibody stripes and channels. PDMS channels can also form reversible seals with silicone (or cellophane) adhesive tapes[226]. Double-sided tape, affixed to a flat plastic or glass slab, provides mechanical stability. Polymer adhesive tapes are flexible and create stronger

yet still reversible bonds with PDMS than other flat surfaces. These tapes accommodate the incorporation of nonsealing functional layers like filter papers and membranes into microfluidic systems[225]. This property enhances the versatility and practicality of PDMS in microfluidic device design and applications.

In addition, PDMS is nontoxic to proteins and cells. It is permeable to oxygen and carbon dioxide, but only slowly permeable to water. It is therefore suitable for biological studies: for example, mammalian cells can be cultured on it directly [227].

1.1.25 3D printing for fabrication of microfluidic devices.

Additive manufacturing, commonly known as 3D printing, offers a promising alternative for microfluidic device fabrication. Unlike traditional methods like injection molding, micromachining, and hot embossing, 3D printing allows for the creation of complex three-dimensional structures layer by layer, providing greater design flexibility. Among the various 3D printing approaches, stereolithography (SLA) stands out as a suitable method for microfluidic devices. SLA employs transparent photocurable resins to build precise microchannels, making it well-suited for microfluidics. In contrast, methods like Fused Deposition Modeling (FDM) present challenges due to the larger filament sizes, limiting the creation of fine microchannels and causing potential leaks[228].

Stereolithography (SLA) originated in 1981 when Dr. Hideo Kodama sought an affordable and rapid 3D modeling method. Charles W. Hull patented the first commercial SLA printer in 1986, founding 3D Systems Inc. to streamline plastic part prototyping. SLA has since evolved, enabling the production of intricate custom geometries beyond its modeling and prototyping origins[228,229]. In the SLA, a vat polymerization technique, selectively solidifies liquid resin layers using UV light. Photo-initiators (PI) in the resin activate polymerization upon UV light exposure, causing curing in exposed areas. This process builds objects incrementally, one layer at a time. SLA encompasses various processes categorized by incident light direction and irradiation method. Light can be applied from above (free surface) or below through a transparent vat (constrained surface). Irradiation occurs through laser scanning (laser-SLA) or by projecting pixelated images (DLP-SLA). An uncommon method employs illumination through an LCD photomask. These SLA processes offer versatile options for 3D printing[229].

On the other hand, Digital Light Processing (DLP) is a vat photopolymerization technique similar to SLA, distinguished by its photocuring process. DLP employs a projector to treat photopolymer resins, using UV light to cure them. Unlike SLA's layered laser scan paths, DLP generates each 2D layer by projecting light onto the liquid polymer. This method has been

utilized to create shape-changing sensors with precision, repeatability, and high accuracy. DLP offers a safer and efficient approach to producing prototypes with excellent resolution[230].

Finally, Digital light processing (DLP) based stereolithography (SLA) offers exciting possibilities for 3D printing microfluidic devices with features under 50 µm. Custom printers and materials have been pivotal in achieving this[231]. To optimize the process, it's crucial to match the optical properties of resins with the light source. Custom resins have been developed for specific applications, such as microfluidic pumps and smaller valves, by carefully selecting photo initiators and absorbers[231,232].

Another promising area is the enhancement of the printer's light source. Utilizing a femtosecond laser, researchers have created high-resolution, movable structures for cell scaffolds and photonic crystals[233]. Programmable lasers have reduced the size of sorting channels, and DLP grayscale techniques have produced compensation patterns for multilayer droplet generators. Custom 3D printers have fabricated microfluidic channels as small as 18 x 20 µm², enabling diverse applications, including chip-to-chip interconnection, active mixers, immunoaffinity monolith capture, and electrophoresis setups for biomarker analysis. These advancements highlight the potential of custom printers and optimized light sources in pushing the boundaries of microfluidic device fabrication[234–236].

Chapter 2

Objectives

2.1 Overall objective

• To develop a lab-on-chip platform for isolating Circulating Tumor Cells (CTCs) as a tool to provide insights into the biology of metastatic cancers, to monitor disease progression and with potential for use in liquid biopsy-based personalized cancer treatment, without the need for invasive tumor biopsies.

2.2 Specific objectives

- To fabricate a size-based separation microfluidic module to achieve depletion of small blood cells (platelets, erythrocytes, and leukocytes with diameters smaller than 12 μm).
- To manufacture an affinity-binding microfluidic module to achieve the selective isolation of CTC from remaining white blood cells. This device will use a negative-enrichment approach consisting of capturing leukocytes for CTCs enrichment.
- To develop an in-vitro biological model of CTC to test the efficiency of the microfluidic devices.
- To automate the operation of microfluidic chips with portable and compact instrumentations for their application in clinical settings.
- To validate the devices with real blood samples from healthy patients spiked with cancer cells of different size
- To validate the devices with real blood samples from colon cancer patients (Clinical proof of concept initiated)

Chapter 3

Materials and Methods

3.1 SPIRAL MICROFLUIDIC DEVICE

3.1.1 1. Spiral Microfluidic Device Description and Fabrication

The current study adopts the design using AutoCAD as shown in Figure 16A. Consequently, the acetate photomask that will be employed during the master manufacturing was also designed in AutoCAD (Figure 16B). The proposed spiral device consists in an inner semi-circular channel with radius $R_1 = 0.42cm$ and external circular channel $R_2 = \left(1.0 + \frac{0.10}{2\pi}\right) cm$ with a rectangular cross section of 500 µm (width), 140µm and 150µm (height) respectively[237] .The channel height was selected based on the computational modeling results. Moreover, the device is composed of two input ports and two outputs. One of the inputs allows the perfusion of the blood sample with the target cells or particles (Figure 16A-"Sample Inlet port"), the other input will allow the perfusion of 1x PBS or sheath flow (Figure 16A-"sheath inlet port"). Finally, through one of the output ports it is possible to collect the sample of cancer cells (CTCs) or enriched particles (Figure 16A "Inner outlet"), while through the other output is discarded the erythrocytes and most of the leukocytes, or particles smaller than 6um (Figure 16A "Outer outlet")

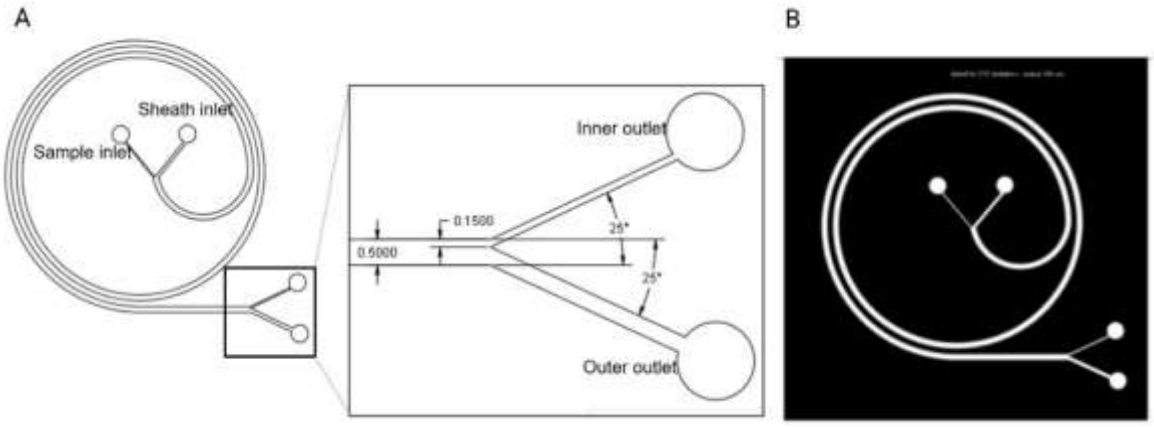

Figure 16. spiral device design in AutoCAD. **B)** Mask designed for the manufacturing of the device. The white features are transparent to UV light to allow polymerizing that part of the resin, meanwhile black is opaque.

Two microfluidic devices were fabricated using the standard photolithography and soft lithography techniques (Figure 17), one with nominal channels height of 150 µm and other of 140 µm. A silicon wafer of 4" inches (10cmX 10cm) was employed as a substrate. The substrate was prepared through a dehydration process on hot plate at 200ºC during 15 min and plasma cleaner for 1 min at High frequency (RF). After, we spin-coated two layers of the photoresin SU8 3050 (MICRO-CHEM). The first layer was spin-coated to 500 rpm-Ac 100 rpm for 30 seconds (first step) and 1900 rpm-Ac 300 rpm for 30 seconds, the second one to 500rpm-Ac 100 rpm (first step) for 10 seconds and 3000 rpm-Ac 300 rpm for 30 seconds (Second layer) to get a channel height of 150µm, and 3500 rpm-Ac 300 rpm for 30 seconds (Second layer) for a channel height of 140 µm . Then, the acetate mask was exposed for 19.7 seconds with I-line filter (Energy = 270 mj/cm^2/ 13,7 mW / cm^2). After the resin diffusion for 5 minutes, the post bake process was performed in two steps (5 min at 65 ºC and 12 min at 95 ºC). Subsequently, the silicon wafer was immersed in SU8 developer for 15 minutes, rinse with isopropanol and dry with N2. Then, the hard bake process was performed for 30 minutes at 95ºC and 10 minutes at 65ºC. Finally, the master device was salinized in a vacuum desiccator for 1 hour with a drop of trichloro (1H,1H,2H,2H-perfluorooctyl) silane (Sigma Aldrich 448931) in a glass or a petri dish. The final microchannels dimensions were verified by interferometer and profilometer.

The microfluidic spiral devices were replicated in polydimethylsiloxane (PDMS, Sylgard 184, Dow Corning). Thereby, the PDMS was first mixed with the curing agent (w/w 10:1) and taken to a vacuum desiccator for approximately 1 hour, until all the bubbles

disappear. Subsequently, the mixture was disposed on top of the Si wafer placed on a petri dish and the remaining bubbles were removed with a plastic pipette. Then, the PDMS was cured at 65ºC for 5h. The cured PDMS was unmolded, cut, and the inlets and outlets holes were punched with a biopsy punch of 1.5mm diameter (Harris Uni-Core). Finally, the PDMS devices were irreversibly bonded to glass slides (Fisher scientific,12392148) using plasma for 30seconds at 30 W and pressure of 0.8Torr (Harrick Plasma Cleaner, USA).

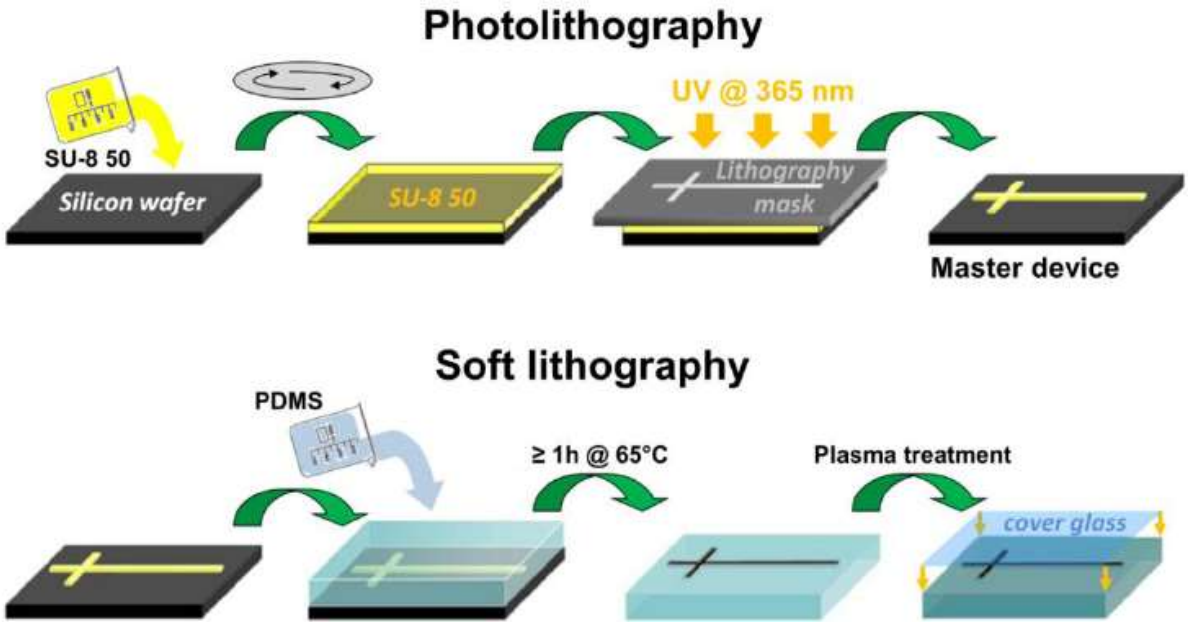

Figure 17. Fabrication of microfluidic devices using photolithography and soft lithography[238].

3.1.2 Computational Modeling

COMSOL Multiphysics® 5.5, a finite element analysis software, was used to evaluate the hydrodynamic and particle trajectories on a spiral device. The spiral geometry was imported from AutoCAD into COMSOL Multiphysics® 5.5 and a tetrahedral mesh refined in Z direction was built with hexahedral elements near the walls. The effect of the spiral geometry was evaluated through the simulations of different channel aspect ratio where four different channel heights were modelled for a CTCs separation limit of 12 µm in size (140, 160, 170 and 180 µm) and channel width of 500µm. For optimizing the separation of smaller CTCs with a size of 10 µm, devices with channels height of 100, 120, 130 and 140 µm were simulated. A new geometry and mesh were built for each case, considering the different dimensions.

Simulations considering the exact dimensions obtaining from fabricated devices were also performed (rectangular channel 152 µm or 138 µm height and 500 µm width).

The simulation developed in this study included a stationary study to calculate the laminar flow with the parameters described in Table 2, followed by a time dependent study to calculate the particles trajectories, in which the solution of the stationary study (velocity, shear stress, etc) was applied. Overall, the fluid was considered in a Eulerian form, Navier-stokes equations were solved for the flow with appropriate defined conditions such as pressure equal to 0 at the outlets, no slip on the walls, the fluid was considered Newtonian with density of 1 g/cm^3 and dynamic viscosity of 0.001 Pa·s. The simulations were performed considering a first order fluid discretization for the velocity and pressure, and quadratic shape function for velocity and a linear shape function for the pressure (P2+P1).

Thus, with the purpose of identifying the optimal operating conditions and design, four different flow rates were simulated to determine the influence of the sheath flow rate in the particle focusing. Thereby, the flow rate of the sample inlet that contains the particles was defined as 100 µL/min and the sheath flow rates studied were: 900 µL/min, 700 µL/min, 500 µL/min and 300 µL/min.

Stationary study

Fluid properties	Density: 1000 kg/m^3 Viscosity: 0.001kg/m.s
Boundary conditions	Sample inlet flow rate: 100 µL /min Sheath flow rates inlet: 900µL/min 700µL/min 500µL/min 300µL/min
Wall conditions	No slip

Table 2. Parameters implemented in the stationary study to evaluate the laminar flow under different sheath flow rates on the spiral device.

Once the laminar flow was calculated, a time dependent study was performed to calculate the particle trajectories. The particles were treated as a discrete phase and for the particle tracing it was used a Langrangian description, based on the solution of the Newton's Second Law of Motion which including the Drag force (Equation 1) and the inertial lift force (Equation 2). The trajectories of different particles sizes were calculated, considering the size of erythrocytes (6 µm), leukocytes (10 µm) and CTCs (11, 12, 13, 15, 17 and 20 µm). The density of all particles

was approximated to the average density of blood (1050 kg/m^3). The number of particles released was arbitrary chosen as is described in Table 3, due to the simulation time and computer power resources required increase when the number of particles increases. In particular, the simulations were performed based on a one-way coupling between the fluid and the particles. Whereby, the particles trajectories were affected by the fluid, but the particles would not affect the fluid and the particle-particle interactions were not considered.

During the calculation it was considered that the particles were under the action of the drag force and a wall-induced lift force. The wall-induced lift force was defined according to the opposed parallel walls. The parameters used in this study are described on Table 3.

Time dependent study

Particles Properties	Density: 1050 kg/m^3
Number of particles and diameter	"Erythrocytes" particles: 6µm "Leukocytes" particles: 10µm "CTCs particles" particles: 11, 12,13,15,17 and 20µm
Forces	Drag force based on Equation 1 Wall-induce lift force based on Equation 2
Time of the study	0 to 3s with a step time of 0.05s
Wall conditions	Bounce

Table 3. Parameters of time dependent study for evaluating the particles trajectories under different sheath flow rates in the spiral device

$$F_D = 6\pi\mu r_p(u - v)$$

Equation 1

Where

μ=The fluid viscosity

r_p=The particle radius

u = The fluid velocity

v =The particle velocity.

$$F_L = \rho\frac{r_p^4}{D^2}\beta\big(\beta G_1(s) + \gamma G_2(s)\big)n$$

$$\beta = \left|D(n \cdot \nabla)u_p\right|$$

$$\gamma = \left|\frac{D^2}{2}(n \cdot \nabla)^2 u_p\right|$$

$$u_p = (I - (nxn)u$$

Equation 2

Where

I *= The identity matrix*

n*= The wall normal at the nearest point on the reference wall*

D*= The distance between the channel walls*

s*= The normalized distance from the particle to the reference wall*

G_1 *and* G_2 *= Dimensionless functions of the normalized wall distance*

3.1.3 Cell culture

Human breast adenocarcinoma cell line, MCF-7 cell line (ATCC® HTB-22™) was used to mimic CTCS (size: 20 µm). Also, Non-small cell lung cancer cell lines were considered to mimic smaller CTCS: A549 (ATCC® CCL-85™-size: 15 µm), H1437 (CRL-5872 – ATCC-size: 15.7 µm) and H460(HTB-177 – ATCC-size: 13.6 µm). The MCF-7(ATCC® HTB-22™), H1437(CRL-5872 – ATCC) and H460(HTB-177 – ATCC) cells were cultured in Roswell Park Memorial Institute Medium (RPMI 1640-Thermofisher Scientific), supplemented with 10% Fetal Bovine Serum (FBS-Gibco, 10270106), 1% l-glutamine (25030, Thermo Fisher) and 1% penicillin-streptomycin (P/S, Invitrogen, 15140). A549 cells (ATCC® CCL-85™),were cultured in DULBECCO'S MEM (Gibco, 41965-039) supplemented with 10% of Fetal Bovine Serum (FBS-Gibco, 10270106) and 1% penicillin-streptomycin (P/S, Invitrogen, 15140). The cells were maintained at 37 °C in

humidified atmosphere containing 5% CO_2, and sub-culture every 3 days using trypsin-EDTA (0.25% Life Technologies, 25200056).

3.1.4 Cell staining

MCF-7(ATCC® HTB-22™), A549(ATCC® CCL-85™), H1437(CRL-5872 – ATCC) and H460 (HTB-177 – ATCC) cells were suspended at a density of 1×10^6 cells/mL in RPMI medium supplemented with 10% FBS (Gibco, 10270106), 1% L-glutamine(25030, Thermo Fisher) and 1% penicillin-streptomycin (P/S, Invitrogen, 15140). Then, 10 µL of CellBrite Green™ or CellBrite Red™ (Cytoplasmic Membrane Dyes-Biotium 30021 and 30023) solution was added per 1mL of cell suspension. The solution was mixed well by flicking the tube. After, the cells were incubated for 20 minutes at 37°C, in dark. Subsequently, cells were pelleted by centrifugation at 500g for 5 minutes. Finally, the supernatant was removed, and the cells were washed by gently resuspending them in warm medium (37°C). The centrifugation and washed steps were repeated two more times.

3.1.5 Chemical blocking of spiral microfluidic surface devices

Chemical blocking on spiral microfluidic devices surface was performed for avoiding the clogging of blood cells in the device output bifurcation. First, the device surfaces were activated using 1 minute of plasma cleaner at 30 W with constant pressure of 0.8Torr (HARRICK-PCD-002-CE). After, the surfaces were cleaned with ethanol 96% (Sigma-Aldrich-159010) and DI H2O. Then, the microfluidic channels were filled with 1mg/mL Silane-PEG-Biotin (PG2-BNSL-3k, NANOCS) and 1mg/mL Silane-PEG-OH (Biopharma PEG Scientific Inc) (ratio 1:1) for 1 hour at room temperature. Finally, the microchannels were rinsed with DI H2O and dried with N2. Figure 18 shows the comparison between the chips with PEG and the absence of blood cells accumulated in the bifurcation, in contrast the chip without PEG the blood cells accumulated in the chip bifurcation.

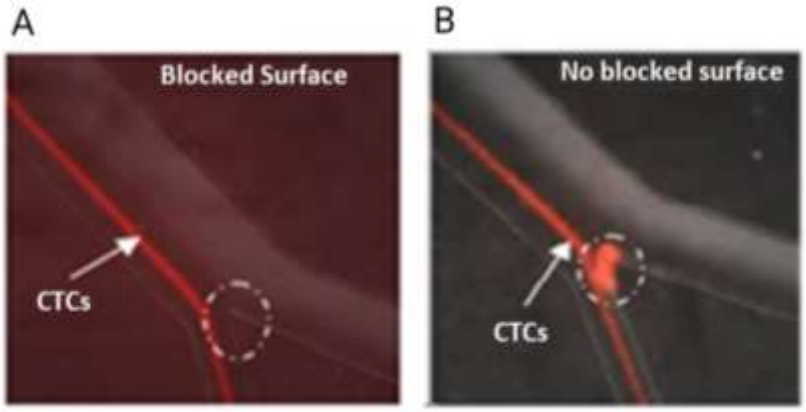

Figure 18. A) Spiral chip surface functionalized without silane-PEG-OH and silane-PEG-Biotin **B)** Spiral chip surface functionalized with silane-PEG-OH and silane-PEG-Biotin

3.1.6 Experiments to optimize and validate the separation efficiency of the spiral microfluidic devices

The devices with nominal heights of 150 and 140 µm were tested and evaluated for different conditions, different inlet samples and different quantification methods, as indicated on table 4. The inlet sample was introduced into the inlet channel (Figure 16- sample inlet port) under a constant flow rate of 100 µL/min. For Experiments 1 to 3, four different conditions of sheath flow (Figure 16-sheath inlet port) were tested: 900, 700, 500 and 300 µL/min. Finally, for Experiments 4 and 5 only sheath flow rates of 900 and 700 µL/min were tested.

Experiment	Device nominal height	Sample	Inlet conditions	Visualization/ quantification
Experiment 1	150 µm	PBS spiked with polystyrene particles of 6, 10, 15 and 20 µm	Sample: 100 µL/min Sheath flow: 300, 500, 700 and 900 µL/min	Fluorescence videos FACS
Experiment 2	150 µm	Blood sample spiked with 30 µm polystyrene particles	Sample: 100 µL/min Sheath flow: 200, 700 and 900 µL/min	Speed camera
Experiment 3	150 µm	Blood sample spiked with MCF-7, A549, H1437 and H460 cells as CTCs model with size ≥12 µm	Sample: 100 µL/min Sheath flow: 300, 500, 700 and 900 µL/min	Fluorescence videos FACS
Experiment 4	150 µm	Lysed blood sample spiked with MCF-7 and A549	Sample: 100 µL/min Sheath flow: 900 µL/min	Fluorescence videos FACS
Experiment 5	140 µm	Blood sample spiked with 10 µm particles as CTCs model	Sample: 100 µL/min Sheath flow: 900 µL/min	Fluorescence videos FACS

Table 4. Experimental design for optimize and evaluate the efficiency of the spiral microfluidic device

3.1.7 Preparation of sample spiked with fluorescent microparticles (Experiment 1)

1mL of PBS 1X was spiked with different concentration of fluorescent polystyrene microparticles (SPHERO^{TM}) that mimic the number of Erythrocytes and Leukocytes in a real blood sample. Particles of 6µm ($5x10^9$ particles/mL) (SPHERO^{TM}Fluorescent particles. FP-10078-2) and 10 µm ($11x10^6$ particles/mL) (SPHERO^{TM} Fluorescent particles FP-10056-2) that represent the erythrocytes and leukocytes were used, respectively. To represent the CTCs, particles of 15 µm and 20 µm ($1x10^4$ particles/mL) of each size were used (SPHERO^{TM} Fluorescent particles FP-10062-2, FP-15056-2).All the samples were diluted 10X in PBS 1X.

3.1.8 Preparation of blood samples spiked with fluorescent Particles (Experiment 2)

Whole blood samples obtained from healthy donors were diluted 2.5X and 10X in sterilized PBS 1X, in order to obtain a hematocrit level of 16% and 4% respectively. The diluted samples were spiked with $1x10^4$ polystyrene microparticles of 30µm per milliliter (SigmaAldrich - 84135-5ML-F).

3.1.9 Preparation of blood samples spiked with breast cancer cells and non-small cell lung cancer cells (Experiment 3)

Whole blood obtained from healthy donors was diluted 10X in PBS 1X for obtaining a hematocrit level of 4%. The sample was spiked with different stained cancer cells as CTCs model (MCF-7-ATCC® HTB-22™, A549-ATCC® CCL-85™,H1437 CRL-5872 – ATCC cells) at different concentrations 10^4 cells/mL, 10^3 cells/mL and 100 cells/mL which represents a final concentration in diluted samples of 1000cells/mL,100cells/mL and 10cells/mL.. The cells were stained as previously described in *"Cell staining"* and independent experiments were carried out for each cell line.

3.1.10 Preparation of lysed blood samples spiked with MCF-7 and A549 cells (Experiment 4)

$1x10^3$ cells/mL of MCF-7(ATCC® HTB-22™) and A549(ATCC® CCL-85™) cells were added in 1ml of whole blood from a healthy donor. The blood was resuspended in 3 mL and 10 mL of VersaLyse Lysing Solution (BECKMAN COULTER life science- A09777). The solution was vortex immediately for 1 second and incubated at least 10 minutes at room temperature (18 – 25°C),

protected from light. After, the sample was centrifuged for 5 minutes at 500 x g at room temperature, the supernatant was removed by aspiration and resuspended in 1 mL of PBS 1X.

3.1.11 Cell viability test

After the lysis processes the viability of MCF-7 cells(ATCC® HTB-22™) was tested with Zombie Violet™ (100 µL PBS 1X + 1 µL Zombie Violet ™ Biolegend-423113). The sample was fixed with paraformaldehyde 8% for 15 minutes and then centrifugated at 500G for 5 min. The supernatant was eliminated, and the cleaning process was repeated one time more with PBS 1X. The analysis of cell death was performed in flow cytometry (FACS).

3.1.12 Cell Sorter

$1x10^6$ MCF-7 cells and $1x10^6$ A549 cells in 250 µL of culture medium were put in a 15 ml falcon. Fluorescent polystyrene microparticles (SPHERO™ Fluorescent particles FP-10056-2) of 10 µm were considered as references for establishing the gate for cell sorter. The sample was recollected in a 15mL falcon with 1 mL of culture medium. The cells sorted were measured by microscope image for determining the size average.

3.1.13 Microfluidic set up for evaluate the performance of spiral microfluidic devices

To assess the performance of the spiral microfluidic device, the samples previously prepared were filled in a 10 mL syringe of 14.57 mm diameter (BD Plastipak Luer-Lock-138432). The samples were pumped through the “sample inlet” (Figure 19A) using a syringe pump syringe pump (Aladdin Programmable Syringe Pump- AL1000-220)(Figure 19B-pump 1), while sheath flow (PBS 1X) was filled in a 20 mL syringe of 19.13mm diameter (BD Plastipak Luer-Lock-138432), and pumped into the device through the “Sheath inlet” (Figure 19B) using a separate syringe pump (Harvard Apparatus PHD 2000) (Figure 4B-pump 2). The syringes were connected to the chip with PEEK luer adapter and 1.5 mm-diameter Tygon tubes of same length (15-30 cm) (Dissolution Accessories-PRPS4194373).Finally, the outlet samples were collected in two Falcon conical tubes of 15mL, through Tygon tubes of 1.5 mm diameter with length of 7cm connected to the chips outlets (Figure 19B). Before starting to collect the outlet samples the chip was stabilized for ~2 min and then ~2 mL of sample was processed. The samples collected at the inner outlet (supposedly CTC enriched) and outer outlet (waste) were analyzed and quantified by flow cytometry (FACS).

To perform the Experiment 2, the microfluidic devices were mounted on an inverted phase contrast microscope equipped with a high-speed camera CCD (Figure 4B-C). The High speed videos recorded at the channel outlets were analysed using ImageJ software. The studies

performed during Experiments 1, 3, 4 and 5 were recorded using Nikon Eclipse Ti2 microscope equipped with EMCCD camera (iXON Ultra DU-897U EMCCD camera (Andor Technology Ltd.) (Figure 19D). The videos were recorded in different sections of the chips for 1 min to verify the correct chip operation. Moreover, in order to determine the number of cancer cells (CTCs) at low concentrations (100cells/mL and 10cells/mL) that are recovered from the inner chip outlet (Figure 19A) videos were recorded during 30 min and processed in image J for quantifying the CTCs recovery rate as describe the Equation 3.

$$\%CTCs\ recovery = \frac{\left((F_1 * t_1) * P_i\right) - N_1}{100}$$

Equation 3.

Where

F_1 = *The sample inlet flow rate (µL/min)*

t_1 = *Total recording time*

P_i = *Concentration of particles per µL*

N_1 = *Number of particles quantifies in the CTCs outlet (Inner Outlet)*

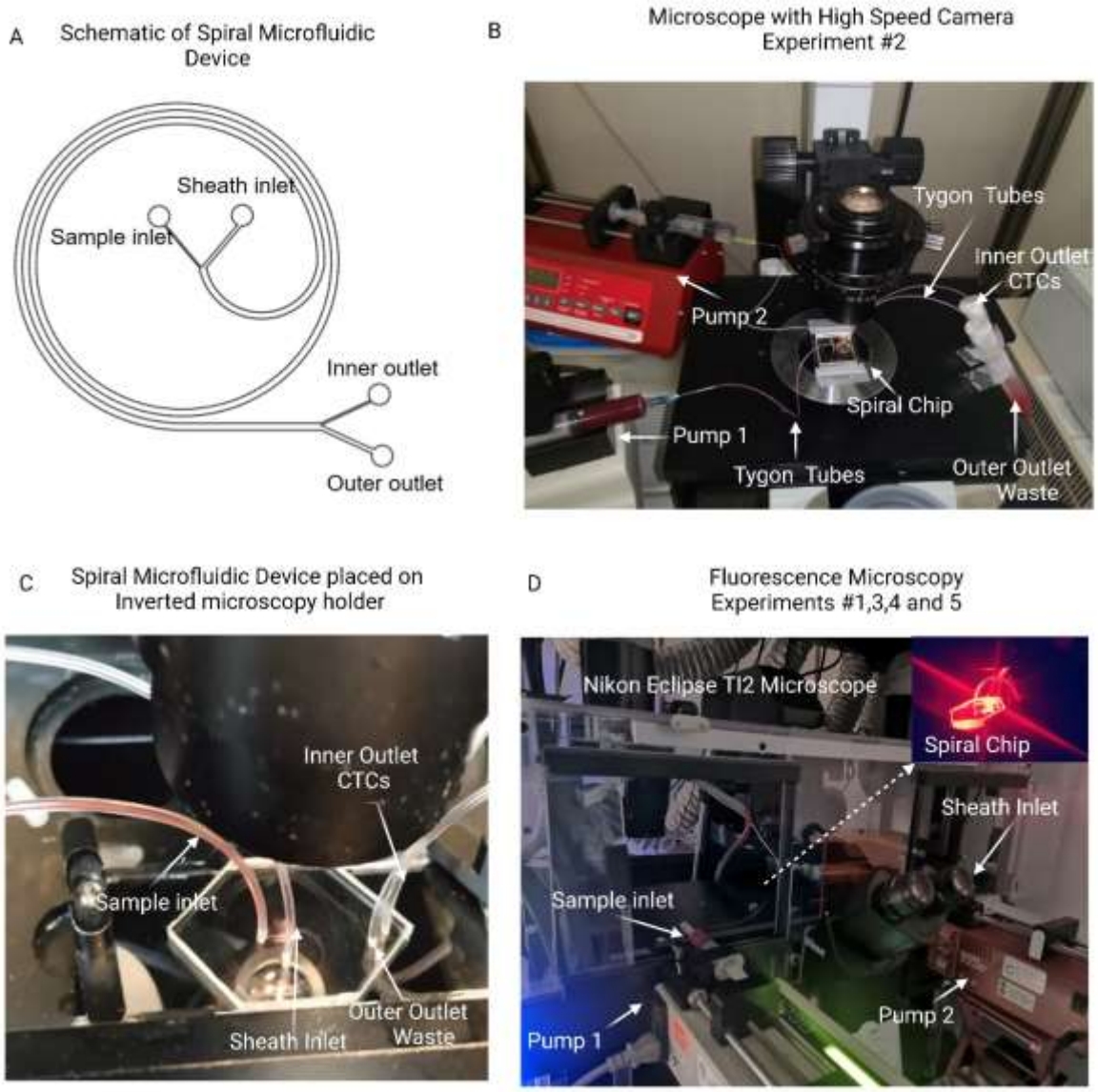

Figure 19. A) Schematic of spiral microfluidic device**. B)** Microfluidic set up for recording high speed videos. Composed by 2 syringe pumps: Pump 1 for blood sample perfusion and pump 2 for PBS 10 (sheath flow perfusion). Two 15mL falcon tubes are connected to collect the samples from the chip outlets**. C)** Spiral microfluidic device placed on the inverted microscope holder. The image shows the detailed connections in chip inlets and outlets

3.2 HERRINGBONE MICROFLUIDIC DEVICE

3.2.1 Herringbone Microfluidic Device Description and Fabrication

The herringbone chip developed in this study was designed in AutoCAD and consists in one inlet that is divided into 4 rectangular channels of 1.2mm * 49.4 mm which are combined in

a single outlet (Figure 20A). The geometry designed is based on the strategy for inducing chaotic mixing under low *Re* number[239]through groove structures on the channel surface. Overall, the nominal dimension of the device corresponds to a rectangular channel height of 50 µm and the groove structures of 45µm, which represent a ratio set to 0.9 between the height of the grooves and the channel. Moreover, the angle between the grooves and the axis to the channel was fixed to 45° and the principal wave vector was equivalent to 2π/100 µm[240]. Finally, two different masks were designed specific for negative resin. The first mask corresponds to the main channel with a thickness of 50 µm, which will be the first layer during the photolithography process. The second mask is the grooves pattern with a thickness of 45µm, which will be second layer in the photolithography process (Figure 20B).

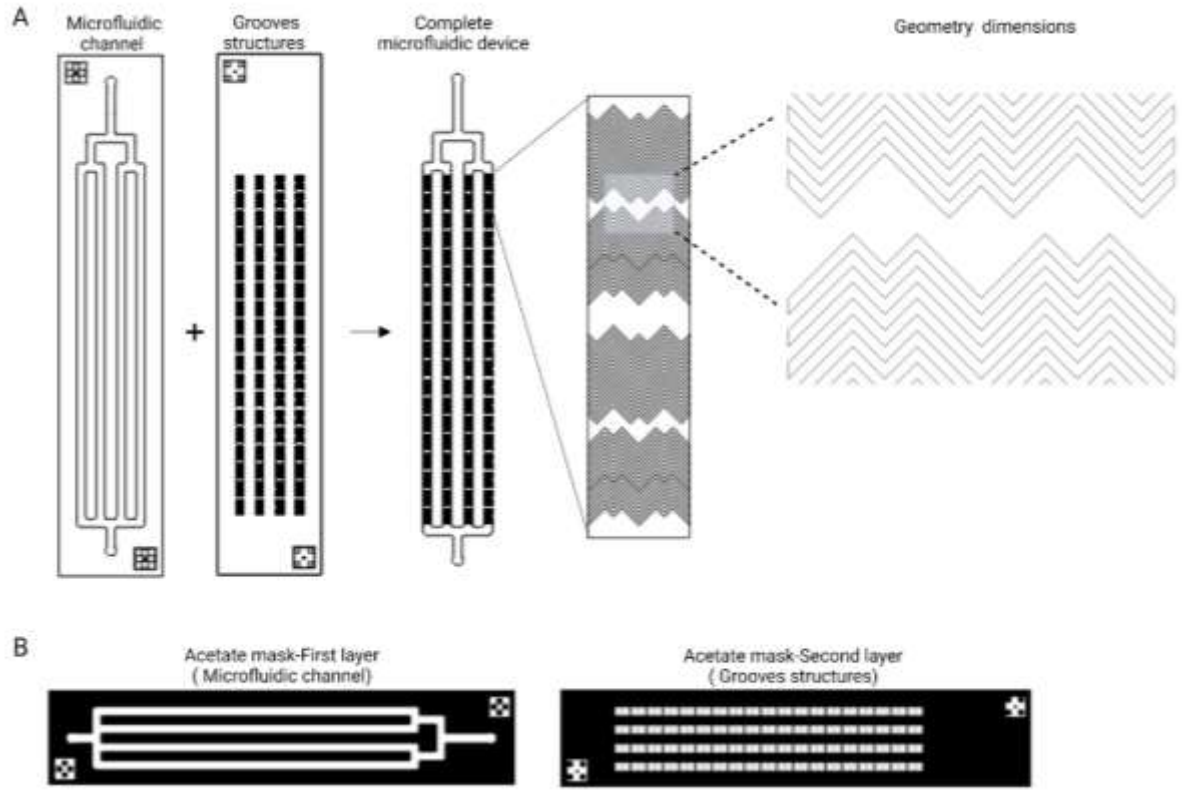

Figure 20. A) Herringbone Microfluidic device design in AutoCAD, composed by Microfluidic channel of 50µm height and groove structures of 45µm height. **B)** Acetate mask with negative polarity for photolithography processes composed by two layers. The first layer for the microfluidic channel and the second layer for the groove structures

The microfluidic Herringbone device was fabricated using the standard photolithography and soft lithography techniques (Figure 21). A silicon wafer of 4" inches (10cmX 10cm) was employed as a substrate. The substrate was prepared through a dehydration process on a hot plate at 200ºC for 15 minutes and plasma cleaner for 1 min at High frequency (RF). After, we

spin-coated two layers of the photoresist SU8 3050(MICRO-CHEM). The first layer was spin-coated to 500 rpm-Ac 100 rpm for 30 seconds (first step) and 3300 rpm-Ac 300 rpm for 30 seconds. After, the pre-soft bake process was performed in two steps (15 min at 95 ºC and a cooldown of 10 min). Then, the acetate mask was exposed for 18.2 seconds with I-line filter (Energy = 250 mj/cm^2/s, 13,7 mW / cm^2). Subsequently, the resin diffusion during 5 minutes and the post-bake process was performed in two steps (1 min at 65 ºC and 5 min at 95 ºC). After, a second layer of the photoresist was spin-coated to 500 rpm-Ac 100 rpm for 30 seconds (first step) and 3500 rpm-Ac 300 rpm for 30 seconds. The pre-soft bake process was performed in two steps (15 min at 95 ºC and a cooldown of 10 min). Afterward, the acetate mask was exposed for 18.2 seconds with I-line filter (Energy = 250 mj/cm^2/s, 13,7 mW / cm^2) and aligned with the first layer. Then, post-bake process was performed in two steps (1 min at 65 ºC and 5 min at 95 ºC). Subsequently, the silicon wafer was immersed in SU8 developer for 15 minutes, rinse with isopropanol and dry with N_2. Then, the hard bake process was performed for 30 minutes at 95ºC and 10 minutes at 65ºC. Finally, the wafer was salinized in a vacuum desiccator for 1 hour with a drop of trichloro (1H,1H,2H,2H-perfluorooctyl) silane (Sigma Aldrich 448931) in a glass or a petri dish. The final microchannel dimensions were verified by interferometer and profilometer.

The devices were replicated in polydimethylsiloxane (PDMS, Sylgard 184, Dow Corning). Thereby, the PDMS was first mixed with the curing agent (w/w 10:1) and taken to a vacuum desiccator for approximately 1 hour, until all the bubbles disappear. Subsequently, the mixture was disposed on top of the Si wafer placed on a petri dish and the remaining bubbles were removed with a plastic pipette. Then, the PDMS was cured at 65ºC for 5h. The cured PDMS was unmolded, cut, and the inlets and outlets holes were punched with a biopsy punch of 1.5mm diameter (Harris Uni-Core). Finally, the PDMS devices were irreversibly bonded to glass slides (Fisher scientific,12392148) using plasma for 30seconds at 30 W and pressure of 0.8Torr (Harrick Plasma Cleaner, USA).

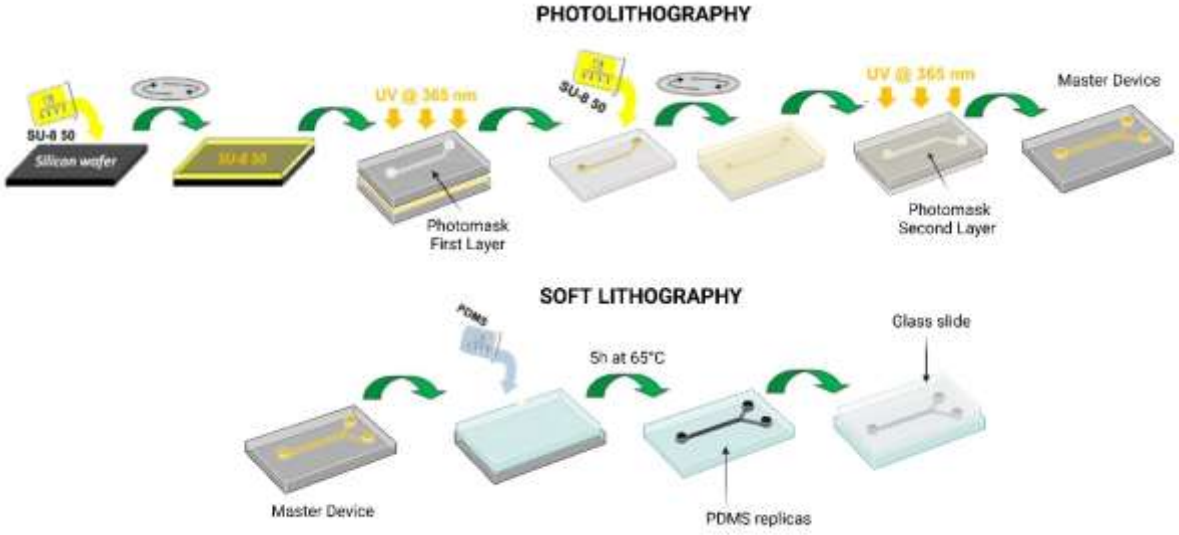

Figure 21. Fabrication of Herringbone devices by photolithography and soft lithography.

3.2.2 Computational modeling

COMSOL Multiphysics® 5.5 was used to evaluate the hydrodynamic and particle trajectories on the herringbone device. The device geometry previously described was imported from AutoCAD. In this study, we did two simulations to further validate the flow rate that will be used in the experimental stage. Thus, a stationary simulation was run to calculate the laminar flow, where the fluid was considered to have the water properties. Subsequently, a time dependent study was done to calculate the particles trajectories which represent the leukocytes and the CTCs inside the device. In addition, the wall condition on the particle tracing mode was set to freeze the particle if it touched the wall, as well as the Drag force and wall – induced lift force were set to act on the particles. In overall, the parameters were defined as indicated in Table 5. Nevertheless, the simulations are limited to study the particle interaction with the surface without consider the antibody efficiency capture, which will represent a bias of the particle capture efficiency between the computational modeling and the experimental stage.

Stationary study for laminar flow	**Fluid properties**	**Density: 1000 kg/m3** **Viscosity: 0.001 kg/m.s**
	Boundary Conditions	Inlet flow rate: Simularion 1: 2.5 µL/min Simulation 2: 5 µL/min Outlet: P=0
	Wall condition	no slip
Time dependent study for particle tracing	Particles	Density: 1050 kg/m3 Diameter: 10µm Number of particles : 100
	Forces	Drag Force Wall-induce lift force
	Wall condition	Freeze

Table 5. Parameters in the COMSOL Multiphysics simulation for herringbone device.

3.2.3 Cell culture

Human breast adenocarcinoma cell line, MCF-7 (ATCC® HTB-22™) was cultured in Dulbecco's modified Eagle Medium (DMEM- Gibco, 41965-039), supplemented with 10% FBS (Gibco, 10270106), 1% L-glutamine (25030, Thermo Fisher) and 1% penicillin-streptomycin (P/S, Invitrogen, 15140). Acute myeloblastic leukemia, Kasumi-1 (ATCC® CRL-2724™)(CD45+), J45.01 (ATCC® CRL-1990™)(CD45-) and lymphoblast-like cell line, Su-DHL-4 (ATCC® CRL-2957™) cell lines were cultured in Roswell Park Memorial Institute Medium (RPMI 1640-Thermofisher Scientific) supplemented with 10% FBS (Gibco, 10270106), 1% L-glutamine (25030, Thermo Fisher) and 1% penicillin-streptomycin (P/S, Invitrogen, 15140).The culture was maintained at 37 °C in a humidified atmosphere containing 5% CO_2. The cells were sub-culture every 3 days, using Trypsin-EDTA (0.25% Life Technologies, 25200056)

3.2.4 Western Blot

Kasumi-1(ATCC® CRL-2724™), J45.01(ATCC® CRL-1990™) and MCF-7 (ATCC® HTB-22™) cells were seed in a 6-well plate (800.000-1.500.000 Cells). After 48h, cells were centrifuged at 1000g for 5 minutes, resuspended in 200 µL of RIPA Buffer (150 mM NaCl, 5mM EDTA, 50mM Tris, 1%Triton x-100, 1%SDS, 1 pill Protease inhibitor) for 30 minutes in ice. Then, the samples were centrifuged 10 minutes at maximum speed (16.100 g) at 4°C. The supernatant was stored at -80°C. Subsequently, for running the gel: 800mL of running buffer 1x (Tris-SDS) was prepared. The Protein samples were also prepared: 6.67 µL of loading buffer, the volume to had around 10 µg of protein (calculated with the BCA Protein quantification Kit) and MiliQ water for a final volume of 20 µL. After, the samples were incubated 10 minutes at 96°C to denaturalize the proteins. Then, SDSPAGE gel was put in the bucket and the tank was filled with the running buffer. 20 µL samples were loaded along with the protein ladder. the gel was run at 50V until the samples did the transition between the stacking and the running parts of the gel. For immunostaining, the membrane was washed in TBS for 5 minutes, blocked for 1 hour using 50mL of Tris-buffered saline, Tween® 20 detergent (TBS-T) with 2.5g of powered-milk, After, it was washed with TBS-T, and incubated with the primary antibody CD45 D9M8I XP® Rabbit mAb (Cell Signaling) overnight at 4ºC. The next day, the membrane was washed three times with TBS-T for 10 minutes. The secondary antibody was incubated during 1hour at room temperature. Then, the membrane was washed three times with TBT-T for 10 minutes and detected using ECL substrate (Bio-Rad) and a LAS4000.

3.2.5 Validation multicellular tumor spheroid by the cyclo-rgDfK(TPP) peptide as a CTCs model

Annexin V/Propidium Iodide cell death assay cells were plated in 12-well plates incubated with different concentrations of cyclo-rgDfK(TPP) (IrisBiotech LS-3920) (5 µM, 10 µM, 20 µM, 30 µM and 40 µM) for 24 hours and 5 µM for 6 hours, 4 hours and 2 hours. After, the medium of each well was collected in eppendorfs(1mL). For the negative control 250 µL of trypsin (TrypleExpress trypsin-Thermo Fisher) for 1- 2 minutes. The cell suspension was collected in eppendorfs. After, the samples were centrifuged at 1000g for 5 minutes. Then, the supernatant was aspirated and 250 µL of the annexin V (1/2000) and Propidium iodide (1/2000) was added to the cells. The samples were analyze by flow cytometry. The chemical structure and cyclo-RGDfK(TPP) peptide-based biochemical method is described in Figure 22.

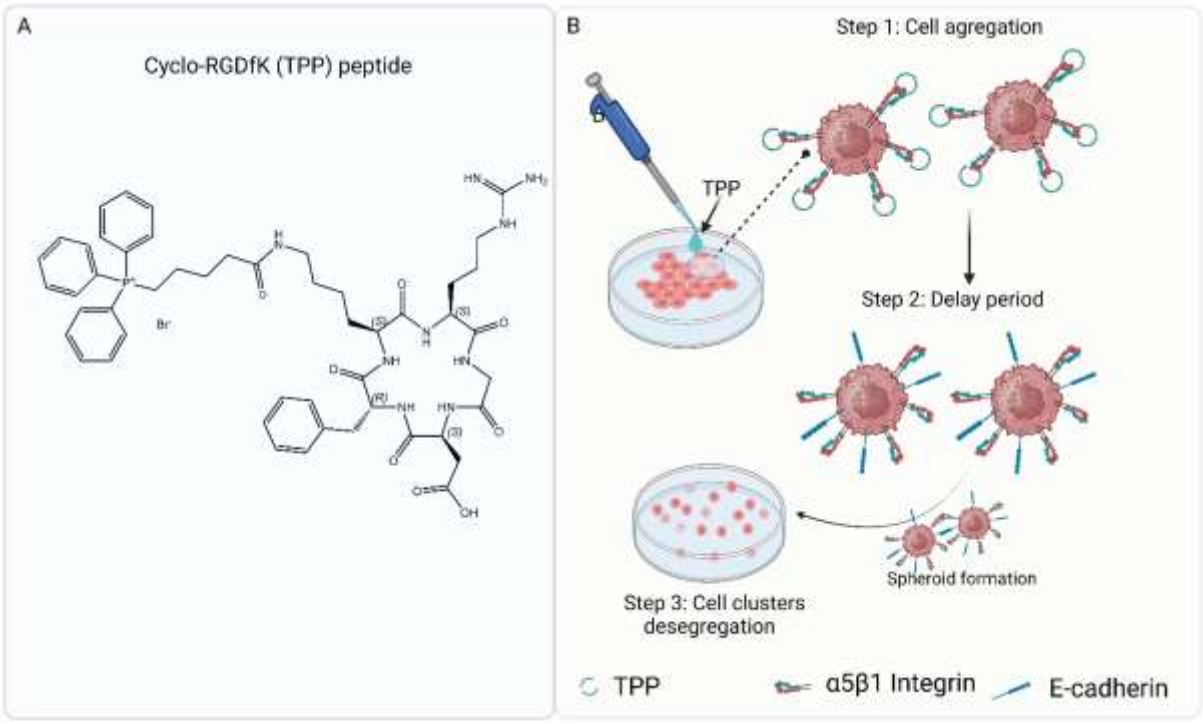

Figure 22. A) Chemical structure of Cyclo-RGDfK (TPP). **96** Formation of multicellular spheroids (MCTS) using cyclo-RGDfk(TPP) peptide-based biochemical method. During step 1 take place the formation of loose cell aggregates via α5β1 integrin- cyclo-RGDfk(TPP). Then, in step 2 starts a delay period for E-cadherin expression and accumulation. Finally, before the formation of MCTS the cluster are desegregated in single cell for testing the Herringbone device (step 3).

3.2.6 Cell staining

MCF-7(cyclo-rgDfK(TPP) (ATCC® HTB-22™) cells as CTCs model and Kasumi-1 (ATCC® CRL-2724™) cells as leukocyte model were suspended at a density of 1×10^6 cells /mL in complete cell media. Then, 10 µL of CellBrite Red™ and CellBrite Green™ (Cytoplasmic Membrane Dyes-Biotium) solution was added per 1mL of MCF-7(cyclo-rgDfK(TPP) cells and Kasumi-1 cells, respectively. The cells were mixed well by flicking and incubated for 20 minutes at 37°C, in the dark. Subsequently, the cells were pelleted by centrifugation at 500g for 5 minutes. Finally, the supernatant was removed, and the cells were washed by gently resuspending them in warm medium (37°C). The centrifugation and wash were repeated two more times and the cells were resuspended at the final concentration (10.000 cells/mL of MCF7(cyclo-rgDfK(TPP) cells and 100.000 cells /mL of Kasumi-1)

3.2.7 Chemical surface modification

Herringbone microfluidic device was functionalized by a mix-self-assembled monolayer (Figure 23). First, the chip surfaces were activated by using plasma for 1 minute at 30 W and pressure of 0.8Torr (Harrick Plasma Cleaner, USA). The surfaces were cleaned with ethanol 96% and DI H2O. After, the microfluidic channels were filled with Silane-PEG-Biotin (NANOCS-PG2-BNSL-3k) (1mg/mL) and Silane-PEG-OH (1mg/mL) (Biopharma PEG Scientific Inc) (Ratio 1:1) for 1 hour at room temperature (Figure 23). Then, the microchannels were rinsed with DI H2O and dry with N2. Subsequently, the microchannels were filled with neutravidin for 15 minutes at room temperature (0.2 mg/mL- Thermo Scientific™) in DHBS (HEPES- buffered saline-HBS containing 20Mm HEPES, pH 7.5 and 100mM NaCl; Tris-buffered saline (TBS) containing 20mM TRIS, PH 7.4, 100mM NaCl) and 0.1% n-Dodecyl β-D-maltoside (DDM-SigmaAldrich). Subsequently, the microchannels were washed with DHBS or DBTS buffer with 0.1% DDM. After, the channels were filled with 10 µg /mL of biotinylated CD45 antibody (Miltenyibiotec) incubated for 30 minutes. Then, it was washed with PBS1X. The surfaces were blocked with 1%BSA in PBS 1X for 1 hour at room temperature. After, the surfaces were washed with DHBS or DTBS with 0.1 DDM buffer and PBS 1X. All the functionalization processes were performed filling the 1mL syringes with the respective solution and pumped through the Herringbone microfluidic device using a syringe pump (Aladdin Programmable Syringe Pump- AL1000-220 (Figure 8). The flow rate for the processes fixed in 20 µL/min. The validation of the surfaces functionalized was performed by Fluorescence and confocal images. Thus, the presence of mix-SAM in PDMS and glass surfaces was verified by 0.2 mg/mL Neutravidin Oregon Green 488 (Thermo Fisher Scientific) and Goat Anti-Mouse IgG H&L Alexa Fluor 488 (Thermo Fisher Scientific). The images were analyzed using ImageJ

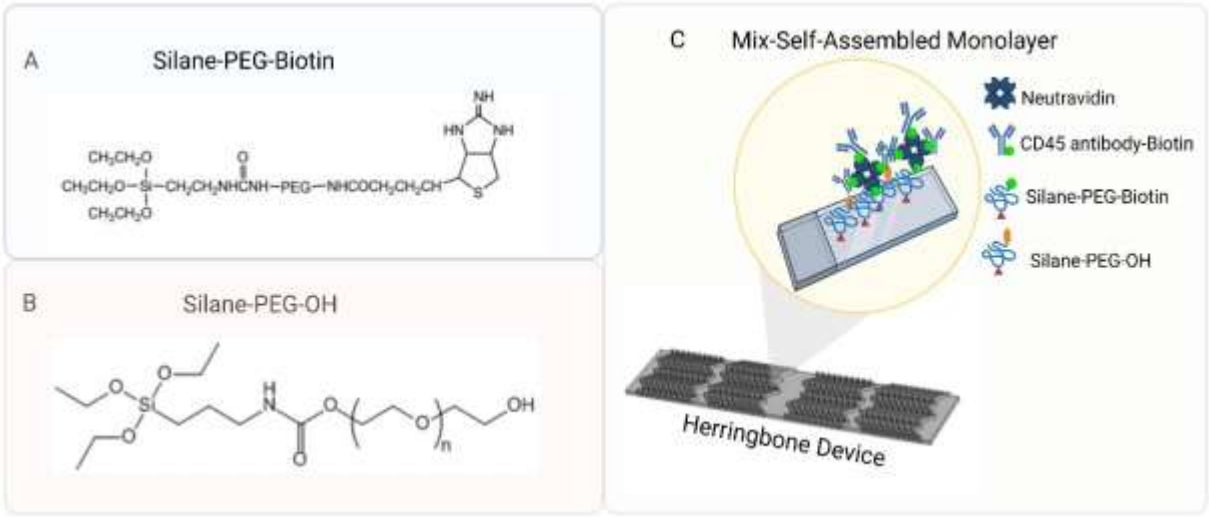

Figure 23. A) Chemical structure of silane-PEG-Biotin **B)** Chemical structure of Silane-PEG-OH **C)** Schematic representation of the herringbone surface (PDMS and glass) functionalized with the Mix-Self-Assembled Monolayer composed by Silane-PEG-OH, Silane-PEG-Biotin, CD45 antibody-Biotin and Neutravidin.

3.2.8 Herringbone Fluidic setup and characterization with cell lines

Herringbone device was tested with MCF-7(cyclo-rgDfK(TPP)) (10.000 Cells/mL) as CTCs model and Kasumi-1 as Leukocytes model (100.000 cells/mL). The sample was filled in a 1 mL syringe, connected to the chip with PEEK luer adapter and 1.5 mm-diameter Tygon tubes of same length (7 cm) (Dissolution Accessories-PRPS4194373). The sample was pumped through the microfluidic device using a syringe pump (Aladdin Programmable Syringe Pump- AL1000-220) under a flow rate of 20 µL/min for 1 hour and washed during 15 min. Two samples were processed through two different chips, one of them without the mix-SAM as negative control and the other with the mix-SAM as positive control. The samples collected from the chip outlet and the sample without process through the device were analyzed by flow cytometry. Kasumi-1 cells and MCF-7 cells anchored on the chip surface were visualized by microscopy (Nikon Eclipse Ti2) (Figure 24)

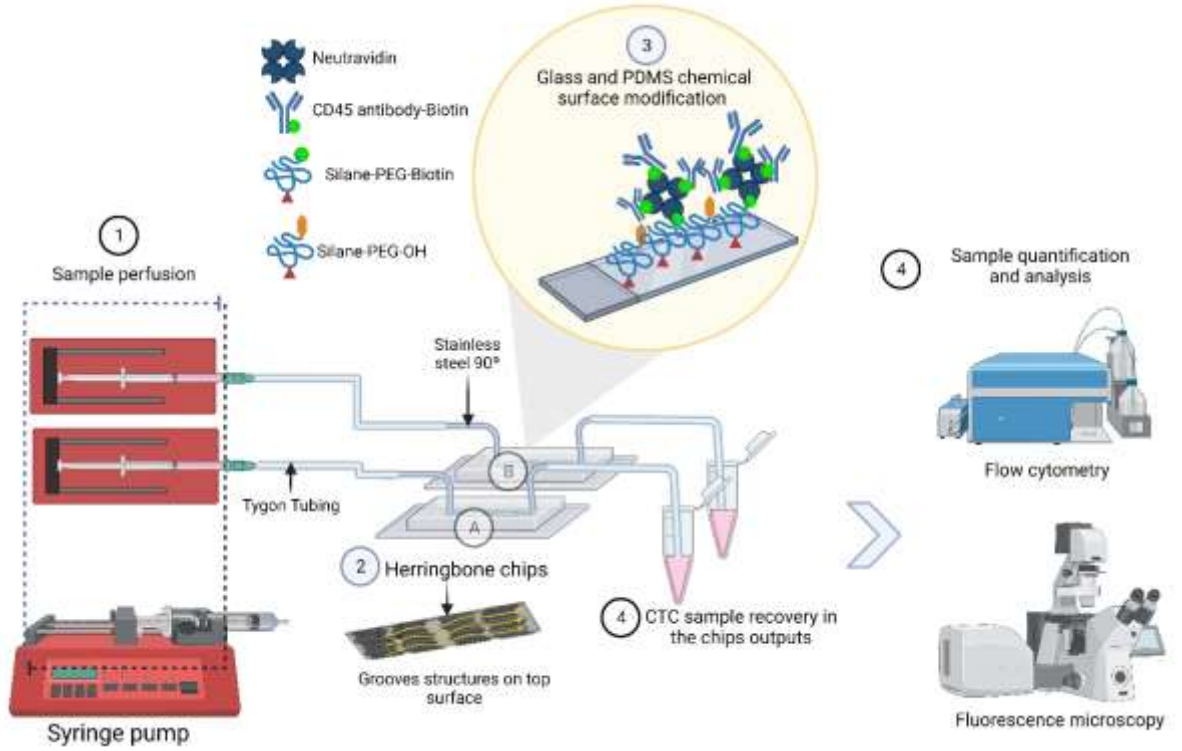

Figure 24. Microfluidic setup for purifying CTCs from blood samples with a micro vortex microfluidic chip. (1) Connection of syinge pump and perfusion of blood samples in 2 chips at the same time. **A)** Herrigbon chip with mix-SAM (C+) and **B)** Herringbone chip without SAM (C-). (2) schematic representation of grooves structures on top of the chip which allow localized mixing of the sample (3) Glass and PDMS surface modify with a mix-SAM (4) The CTCs sample is recovered in the chips outputs and quantify by FACs and the cells attached on the chip surface are analysed by Fluorescence microscopy (4).

3.2.9 Device characterization with blood samples obtained from spiral microfluidic devices

Blood samples from healthy donors spiked with $10x10^4$ MCF-7(cyclo-rgDfK(TPP)) cells as CTCs model were processed through a spiral microfluidic device. The sample was diluted, filled in a 10 mL syringe, and pumped through the spiral microfluidic device using a syringe pump (Aladdin Programmable Syringe Pump- AL1000-220) while sheath flow (PBS 1X) was filled in a 20 mL syringe and pumped into the device using a separate syringe pump (Harvard Apparatus PHD 2000). The flow rate for the blood sample was fixed at 100 µL/min and sheath flow 900 µL/min. The device was mounted on an inverted phase contrast microscope equipped with a high-speed camera CCD. The sample output was processed using the herringbone device for depleting Leukocytes. During the present study 4 chips were

employed under different conditions to assess the capture efficiency and its correlation with the chip geometry: 1 chip without grooves structures and mix-SAM, 1 chip without grooves structures and with mix-SAM, 1 chip with grooves structures but without mix-SAM, 1 chip with both grooves structures and mix-SAM. The output samples were analyzed and quantified by Flow cytometry (FACS) and videos. Figure 25 is a detailed schematic representation of the entire microfluidic setup.

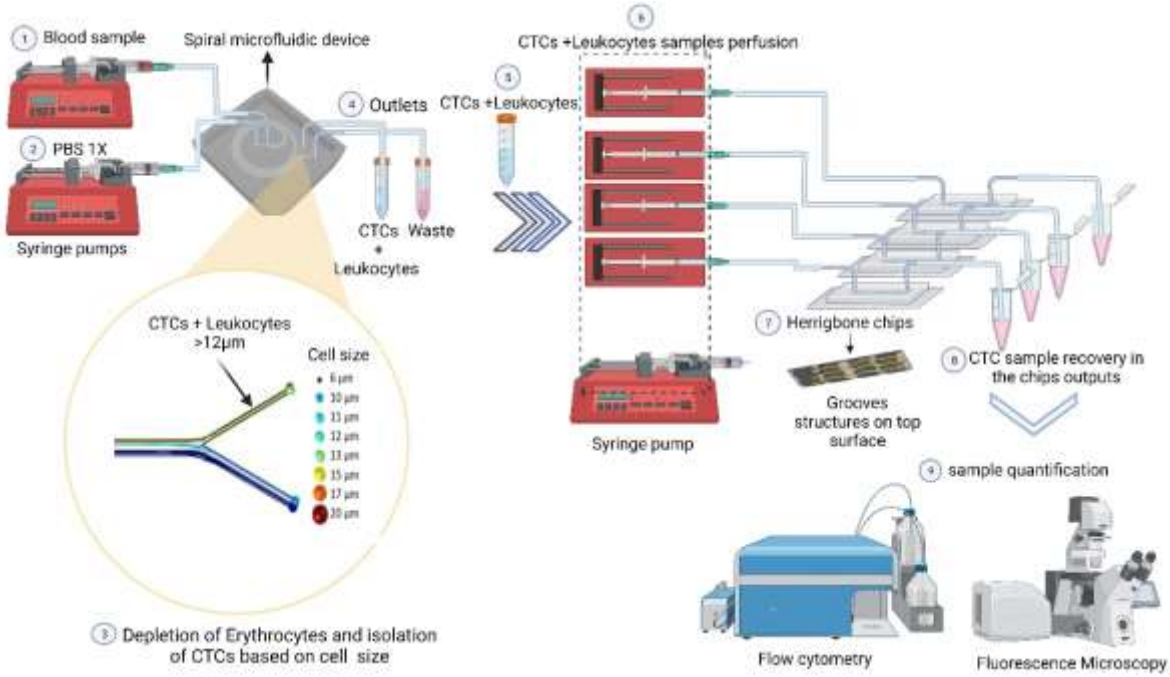

Figure 25. Microfluidic setup for pre-Erythtrocytes depletion and post-depletion of leukocytes. (1)(2) First a spiral microfluidic device composed by two inlets and two outlets separates cells >12µm, which allows the depletion of erythrocytes through one of the outlets (cells <12µm) (3). Meanwhile, the CTCs contaminated by leukocytes bigger than 12µm take the other outlet (4). (5) The CTCs+Leukocytes sample collected is processed through the herringbone chip. (6,7) Four samples can be processed at the same time through four Herringbone chips using a Syringe pump. (8) The samples collected from the outlet of the chip are analysed and quantified by Flow cytometry and Fluorescence microscopy (9).

3.3 Low-cost fluidic set-up for a whole CTCs enrichment system

3.3.1 Flow electronic circuit platform design and fabrication

The flow platform was fabricated using micropumps MP6-OEM (Bartels Mikrotechnik GmbH), two mp-low drivers (Bartels Mikrotechnik GmbH) controlled by Raspberry Pi zero. A custom-built PCB composed by two-layer board was designed in Autodesk EAGLE (Figure 26). Molex connectors (Molex FCC 39532045-Bartels Mikrotechnik GmbH) were used for connecting the

components to the PCB. In addition, two check valves (BT-mp-cv Bartels Mikrotechnik GmbH) and two mp-dampers (Bartels Mikrotechnik GmbH) were connected to the micropump outlets.

The Raspberry Pi touch screen and Raspberry Pi Camera 12.3MP IMX477 Sensor were connected to Raspberry Pi Zero, and a portable microscope XPD-101 expedition (Bresser) was also included in the platform. Python was the programming language used to implement Raspberry Pi and its external devices. Finally, the flow rates were validated using cell culture media measured in intervals of 60 minutes. The experimental curve was compared with the reference values given by pump's manufacturer. The resulting calibration equation was used in the code.The casing was designed in AUTOCAD Schematic of flow platform circuit.

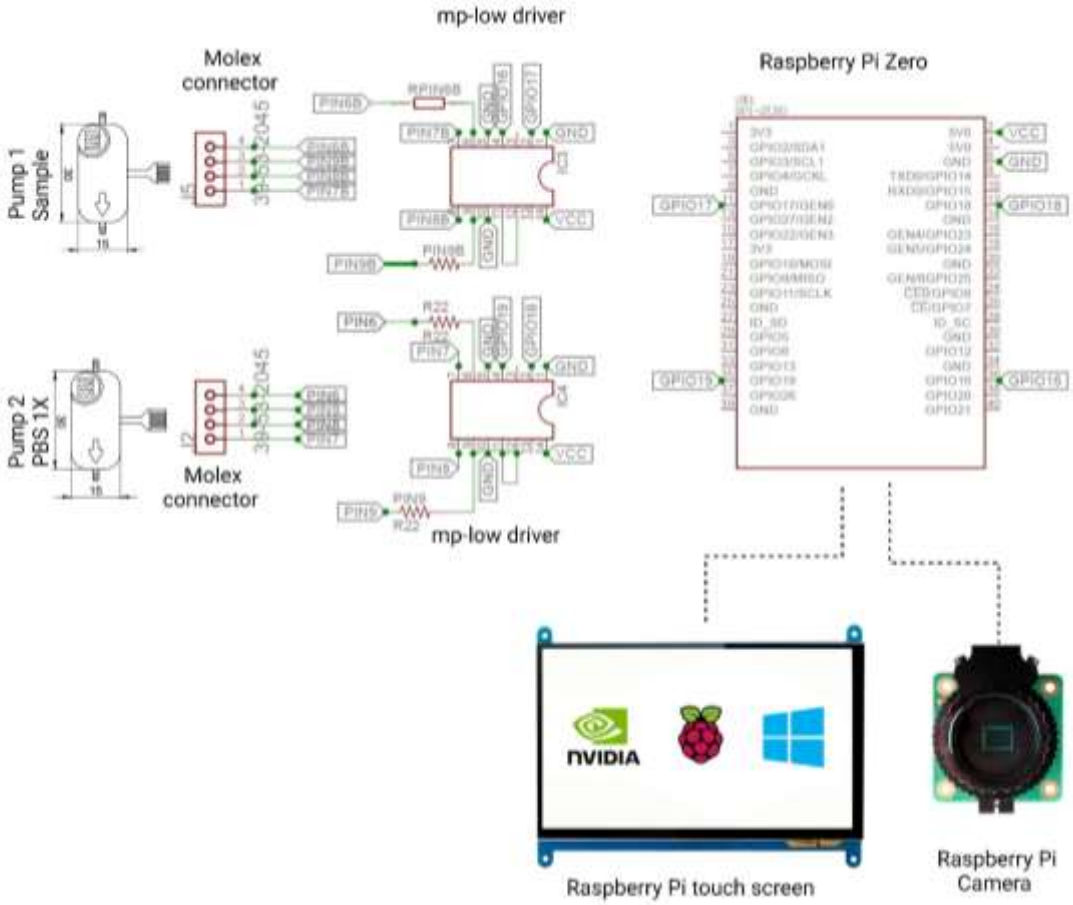

Figure 26. Schematic representation of electronic circuit design for flow platform

3.3.2 Cell culture

Human breast adenocarcinoma cell line, MCF-7 cell line (ATCC® HTB-22™) was used to mimic CTCS (size: 20 µm). Also, Non-small cell lung cancer cell lines were considered to mimic smaller CTCS: A549 (ATCC® CCL-85™-size: 15 µm). The MCF-7(ATCC® HTB-22™) cells were cultured in Roswell Park Memorial Institute Medium (RPMI 1640-Thermofisher Scientific), supplemented with 10% Fetal Bovine Serum (FBS-Gibco, 10270106), 1% l-glutamine (25030, Thermo Fisher) and 1% penicillin-streptomycin (P/S, Invitrogen, 15140). A549 cells (ATCC® CCL-85™),were cultured in DULBECCO'S MEM (Gibco, 41965-039) supplemented with 10% of Fetal Bovine Serum (FBS-Gibco, 10270106) and 1% penicillin-streptomycin (P/S, Invitrogen, 15140). The cells were maintained at 37 °C in humidified atmosphere containing 5% CO2, and sub-culture every 3 days using trypsin-EDTA (0.25% Life Technologies, 25200056).

3.3.3 Cell staining

MCF-7(ATCC® HTB-22™), A549(ATCC® CCL-85 cells were suspended at a density of 1×10^6 cells/mL in RPMI medium supplemented with 10% FBS (Gibco, 10270106), 1% L-glutamine(25030, Thermo Fisher) and 1% penicillin-streptomycin (P/S, Invitrogen, 15140). Then, 10 µL of CellBrite Green™ or CellBrite Red™ (Cytoplasmic Membrane Dyes-Biotium 30021 and 30023) solution was added per 1mL of cell suspension. The solution was mixed well by flicking the tube. After, the cells were incubated for 20 minutes at 37°C, in dark. Subsequently, cells were pelleted by centrifugation at 500g for 5 minutes. Finally, the supernatant was removed, and the cells were washed by gently resuspending them in warm medium (37°C). The centrifugation and washed steps were repeated two more times. Finally, the cell suspension was diluted to achieve the cell concentrations used in the experiments: 1000 cells/mL,100 cells/mL and 10 cells/mL.

3.3.4 Cell viability test

The viability of MCF-7 cells (ATCC® HTB-22™) collected through the spiral device using micropumps was tested with Zombie Violet™ (100 µL PBS 1X + 1 µL Zombie Violet ™ Biolegend-423113). The samples collected from the spiral device and micro-pump outputs were fixed with 8% paraformaldehyde for 15 minutes and then centrifugated at 500g for 5 min. The supernatant was eliminated, and the cleaning process was repeated one time more

with PBS 1X. The analysis of cell death was performed by flow cytometry (FC). The settings stablished in flow cytometry for quantifying and analyzing the data are described in Figure 27.

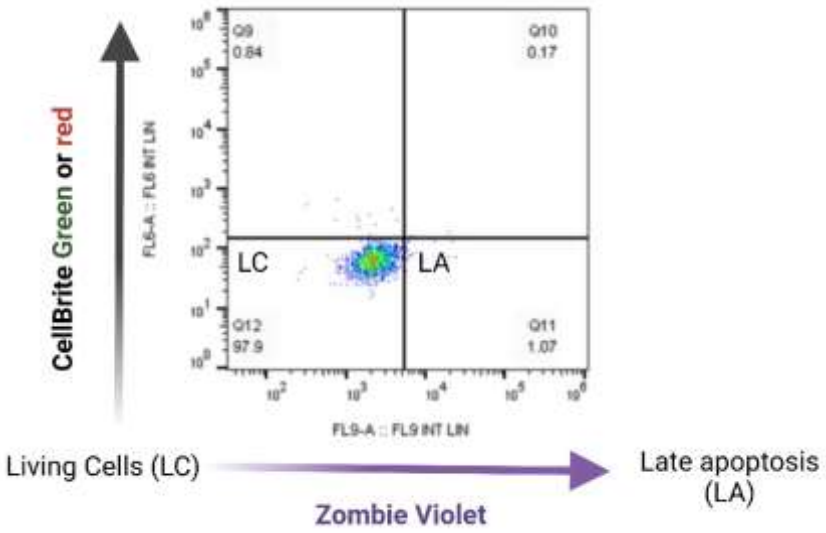

Figure 27. Flow cytometry analysis of cell death assay. X axis corresponds to the cells incubated with Zombie Violet. The fluorescent dye that is non-permeant to live cells (LC), meanwhile the cells with compromised membranes are permeant to the dye (LA). Y axis represents the cancer cells stained with CellBrite red or green.

3.3.5 Blood sample preparation spiked with MCF-7, A549 cells and Fluorescent particles as CTCs model

Whole blood obtained from healthy donors was diluted 10X in PBS 1X for obtaining a hematocrit level of 4%. The sample was spiked with $1x10^4$cells/mL, of MCF-7, A549 cells labelled as described in section "Cell staining". Moreover, blood sample was spiked with 20µm particles as a CTCs model (SPHERO™ Fluorescent particles FP-15056-2) and diluted 10X in PBS 1X (final concentration 100 and 10 particles/mL)

3.3.6 Microfluidic set up for evaluate the performance of spiral microfluidic devices

To assess the performance of the spiral microfluidic device of the samples prepared as previously described and using the flow electronic circuit platform. The samples (Blood and PBS 1x) were put in a 50mL reservoirs. The blood sample were pumped through the chip inlet A applying an SRS-signal and voltage 125Vpp with a frequency of 41Hz (3300 µL/min) (Figure 13). Meanwhile the sheath flow (PBS 1X) was perfused through the inlet B and the parameters were set to 150 Hz and voltage of 125 Vpp (7700 µL/ min) (Figure 28). Finally, the outlet samples were collected in two Falcon conical tubes or reservoirs of 50mL, through Tygon tubes of 1.5 mm diameter with length of 7cm connected to the chips outlets (Figure 28). Before starting to collect the outlet samples the chip was stabilized for ~2 min and then complete sample was processed. The samples collected at the inner outlet (supposedly CTC enriched) and outer outlet (waste) were analyzed and quantified by flow cytometry (FACS). In addition, videos recorded in different sections of the chips for 1 min to verify the correct chip operation.

To perform the experiments with 100 and 10 particles of 20 µm diameter, the microfluidic devices were mounted on an inverted Nikon Eclipse Ti2 microscope equipped with EMCCD camera (iXON Ultra DU-897U EMCCD camera (Andor Technology Ltd.) (Figure 28). Videos were recorded during 30 minutes at the channel outlets and analysed using ImageJ software. Equation 1 was applied for quantifying the CTCs recovery rate.

$$\%CTCs\ recovery = \frac{\left((F_1 * t_1) * P_i\right) - N_1}{100}$$

Equation 1.

Where

F_1 *= The sample inlet flow rate (µL/min)*

t_1 *= Total recording time*

P_i *= Concentration of particles per µL*

N_1 *= Number of particles quantifies in the CTCs outlet (Inner Outlet)*

Figure 28. Complete microfluidic set up evaluated inside of Nikon Eclipse Ti2 microscope

3.4 3D printing spiral microfluidic device

3.4.1 Spiral Microfluidic Device Description and Fabrication

The spiral microfluidic device was designed in AutoCAD. The geometry dimensions were adapted based on the simulations in COMSOL MULTIPHYSICS® and the capabilities of the 3D printed. The proposed spiral device consists in an inner semi-circular channel with radius R_1=0.42cm and external circular channel R_2=(1.0+ 0.10/2π)cm with a rectangular cross section of 1400 µm (width), 560µm (height) respectively. Moreover, the device is composed of two input ports and two outputs. One of the inputs allows the perfusion of the sample that contain the particle binding to the leukocytes spiked with the CTCs (Figure 29-"Sample Inlet port"), the other input will allow the perfusion of 1x PBS or sheath flow (Figure 29-"sheath inlet port"). Finally, through one of the output ports it is possible to collect the sample of cancer cells (CTCs) or enriched particles (Figure 29"Outer outlet"), while through the other output is discarded the particles bonded to the leukocytes (Figure 29 "Inner outlet") (Figure 29)

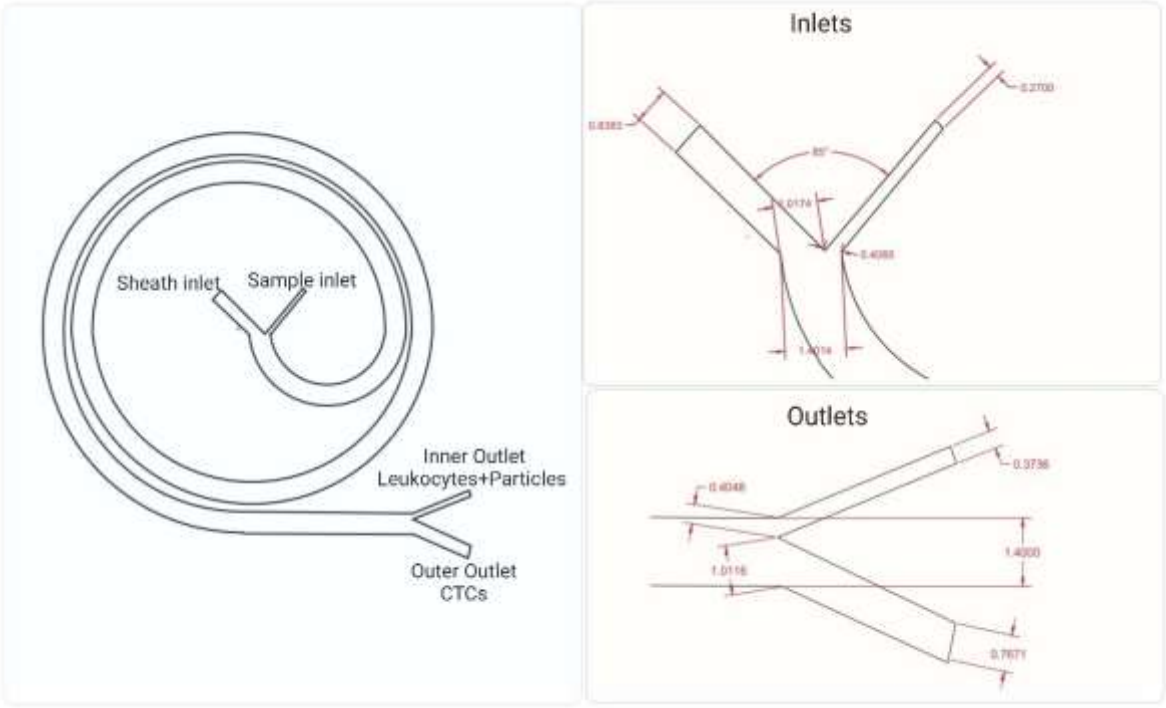

Figure 29. Schematic representation of spiral microfluidic device designed in AutoCAD

The 3D mold was printed using the DLP 3D Printer Microlay equipped with a HD direct light projector (385nm wavelength). The acrylic resin tank was filled with SolusArt Grey V3.0 resin and the design was upload to the MicroForm software. Once, the 3D printer finished the process, the mold was detached from the platform. The excess of resin from the printed piece was removed and washed with ResinAway sonicating for 5 minutes. Then, the printed piece was dried with the N2 gun and put it under a UV light during 30 minutes. Finally, the 3D mold was salinized in a vacuum desiccator for 1 hour with a drop of trichloro (1H,1H,2H,2H-perfluorooctyl) silane (Sigma Aldrich 448931) in a glass or a petri dish. The final microchannels dimensions were verified by profilometer.

The microfluidic spiral devices were replicated in polydimethylsiloxane (PDMS, Sylgard 184, Dow Corning). Thereby, the PDMS was first mixed with the curing agent (w/w 10:1) and taken to a vacuum desiccator for approximately 1 hour, until all the bubbles disappear. Subsequently, the mixture was disposed inside the 3D mold and the remaining bubbles were removed with a plastic pipette. Then, the PDMS was cured at 85ºC overnight. The cured PDMS was unmolded and the inlets and outlets holes were punched with a biopsy punch of 1.5mm diameter (Harris Uni-Core). Finally, the PDMS devices were irreversibly bonded to glass slides (Fisher scientific,12392148) using plasma for 30seconds at 30 W and pressure of 0.8Torr (Harrick Plasma Cleaner, USA).

3.4.2 Computational Modeling

COMSOL Multiphysics® 5.5, a finite element analysis software, was used to evaluate the hydrodynamic and particle trajectories on a spiral device. The spiral geometry was imported from AutoCAD into COMSOL Multiphysics® 5.5 and a tetrahedral mesh refined in Z direction was built with hexahedral elements near the walls. The effect of the spiral geometry was evaluated through the simulations of different channel aspect ratio where four different channel heights were modelled for a Leukocyte depletion limit of ≥70 µm and considering the 3D printed capabilities (420µm, 500µm, 520 µm and 560µm). A new geometry and mesh were built for each case, considering the different dimensions. Simulations considering the exact dimensions obtaining from fabricated devices were also performed (rectangular channel 560µm height and 1400 µm width).

The simulation developed in this study included a stationary study to calculate the laminar flow with the parameters described in Table 6, followed by a time dependent study to calculate the particles trajectories, in which the solution of the stationary study (velocity, shear stress, etc) was applied. Overall, the fluid was considered in a Eulerian form, Navier-stokes equations were solved for the flow with appropriate defined conditions such as pressure equal to 0 at the outlets, no slip on the walls, the fluid was considered Newtonian with density of 1 g/cm^3 and dynamic viscosity of 0.001 Pa·s. The simulations were performed considering a first order fluid discretization for the velocity and pressure, and quadratic shape function for velocity and a linear shape function for the pressure (P2+P1).

Thus, with the purpose of identifying the optimal operating conditions and design, the particle Reynolds number(Re_p) and channel Reynolds number (Re_c) were estimated to be equivalent to the spiral device previously reported by Hou et al., 2013 (Equation 1 and 2). Then, the flow rate of the sample inlet that contains the particles was defined as 700 µL/min and the sheath flow rates was stablished as 6300µL/min.

Stationary study

Fluid properties	Density: 1000 kg/m^3 Viscosity: 0.001kg/m.s
Boundary conditions	Sample inlet flow rate: 700 µL /min Sheath flow rates inlet: 6300µL/min
Wall conditions	No slip

Table 6. Parameters implemented in the stationary study to evaluate the laminar flow under different sheath flow rates on the spiral device.

$$Re_c = \frac{\rho v Dh}{\mu}$$

Equation 1

Where

$\rho =$ *Density of the fluid*

$v =$ *Average flow velocity*

$Dh =$ *Hydraulic diameter*

$\mu =$ *Kinematic viscosity of the fluid*

$$Re_p = Re_c(\frac{a}{Dh})^2$$

Equation 2

Where

Re_c=

$a = Particle\ diameter$

$Dh = Hydraulic\ diameter$

Once the laminar flow was calculated, a time dependent study was performed to calculate the particle trajectories. The particles were treated as a discrete phase and for the particle tracing it was used a Langrangian description, based on the solution of the Newton's Second Law of Motion which including the Drag force (Equation 1) and the inertial lift force (Equation 2). The trajectories of different particles sizes were calculated, considering the size of Leukocytes binding to the beads (≥70 µm) and CTCs (20 µm and 30µm). The density of all particles was approximated to the average density of blood (1050 kg/m^3). The number of particles released was arbitrary chosen as is described in Table 2, due to the simulation time and computer power resources required increase when the number of particles increases. In particular, the simulations were performed based on a one-way coupling between the fluid and the particles. Whereby, the particles trajectories were affected by the fluid, but the particles would not affect the fluid and the particle-particle interactions were not considered.

During the calculation it was considered that the particles were under the action of the drag force and a wall-induced lift force. The wall-induced lift force was defined according to the opposed parallel walls. The parameters used in this study are described on Table 7.

Time dependent study

Particles Properties	Density: 1050 kg/m^3
Number of particles and diameter	"Leukocytes" particles: 70 and 100µm "CTCs particles" particles: 20 and 30µm
Forces	Drag force based on Equation 3 Wall-induce lift force based on Equation 4
Time of the study	0 to 3s with a step time of 0.05s
Wall conditions	Bounce

Table 7. Parameters of time dependent study for evaluating the particles trajectories under different sheath flow rates in the spiral device

$$F_D = 6\pi\mu r_p(u - v)$$

Equation 3

Where

μ=The fluid viscosity

r_p=The particle radius

u = The fluid velocity

v =The particle velocity.

$$F_L = \rho \frac{r_p^4}{D^2} \beta\big(\beta G_1(s) + \gamma G_2(s)\big)n$$

$$\beta = \left|D(n \cdot \nabla)u_p\right|$$

$$\gamma = \left|\frac{D^2}{2}(n \cdot \nabla)^2 u_p\right|$$

$$u_p = (I - (nxn)u$$

Equation 4

Where

I = The identity matrix

n= The wall normal at the nearest point on the reference wall

D= The distance between the channel walls

s= The normalized distance from the particle to the reference wall

G_1 and G_2 = Dimensionless functions of the normalized wall distance

3.4.3 Preparation of polystyrene streptavidin particles

Polystyrene particles of 70 µm conjugated with streptavidin (SPHERO^{TM}SVP-800-4) were washed before use to remove the 0.02% NaN_3 added as a preservative. First, the particles were resuspended by gently shaking the vial to obtain a homogeneous suspension. Then,400 µL from the vial was added to a 2mL Eppendorf tube. After, the tube was placed in a centrifuge at 1000g for 20minutes. The supernatant was removed by aspiration, avoiding touching the particle pellet with the pipette tip. Subsequently, the pellet was resuspended in 1mL of buffer solution (10 mM Tris-HCl (pH 7.5), 1 mM EDTA and 2.0 M NaCl). Finally, the washing step was repeated and resuspended in 1mL of PBS1X with CD45-Biotin (1:100) (Human Clone 5B1 - LOTE 5190918251 de Miltenyi Biotec). The particles were incubated 30 minutes at room temperature with gentle rotation. The particles coated with the biotinylated antibody CD45 were centrifuged two times at 1000g for 20 minutes with PBS/BSA. Figure 30 describes the preparation of streptavidin polystyrene particles for the spiral device characterization.

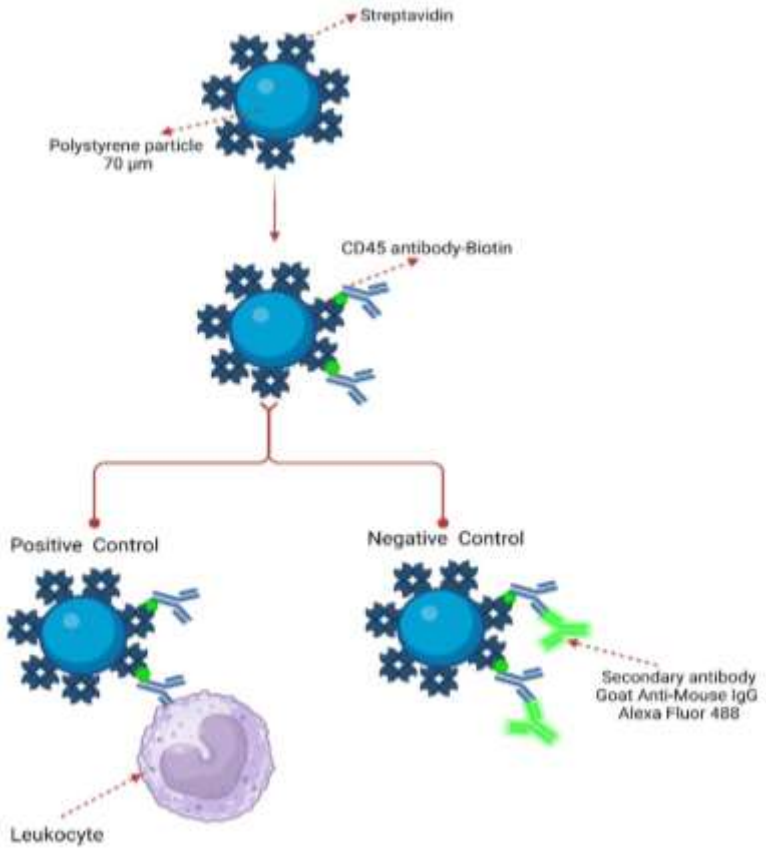

Figure 30. Schematic of streptavidin polystyrene particles prepared for spiral device performance characterization.

3.4.4 Characterization of spiral device with polystyrene particles binding to CD45-antibody

The particles coated with the biotinylated antibody CD45 were centrifuged at 1000g for 20 minutes and resuspended in 1mL of PBS1X with Goat Anti-Mouse IgG H&L Alexa Fluor 488 (1:100) (Thermo Fisher Scientific). The particles were incubated for 30 minutes at room temperature with gentle rotation. Thus, the presence of CD45 antibody on the particles surface was checked by fluorescence microscopy (Nikon Eclipse Ti2). Moreover, particles incubated only with secondary antibody was considered as a negative control.

The sample recovered from the first spiral device with a channel height of 152µm was stained with Hoechst (1:10.000) (Thermofisher -33342) and incubated with the particles coated with the biotinylated antibody CD45 for 30 minutes with gentle rotation (Figure 31-Stage 1). Subsequently, the sample was processed through the second spiral device with a channel height of 560µm. The Leukocytes binding to the polystyrene particles were checked by fluorescence (Nikon Eclipse Ti2) and quantify using Image J (Figure 31-Stage 2). Also, the sample collected from the CTCs outlet was quantifies by Flow cytometry following the processes referred in previous section .

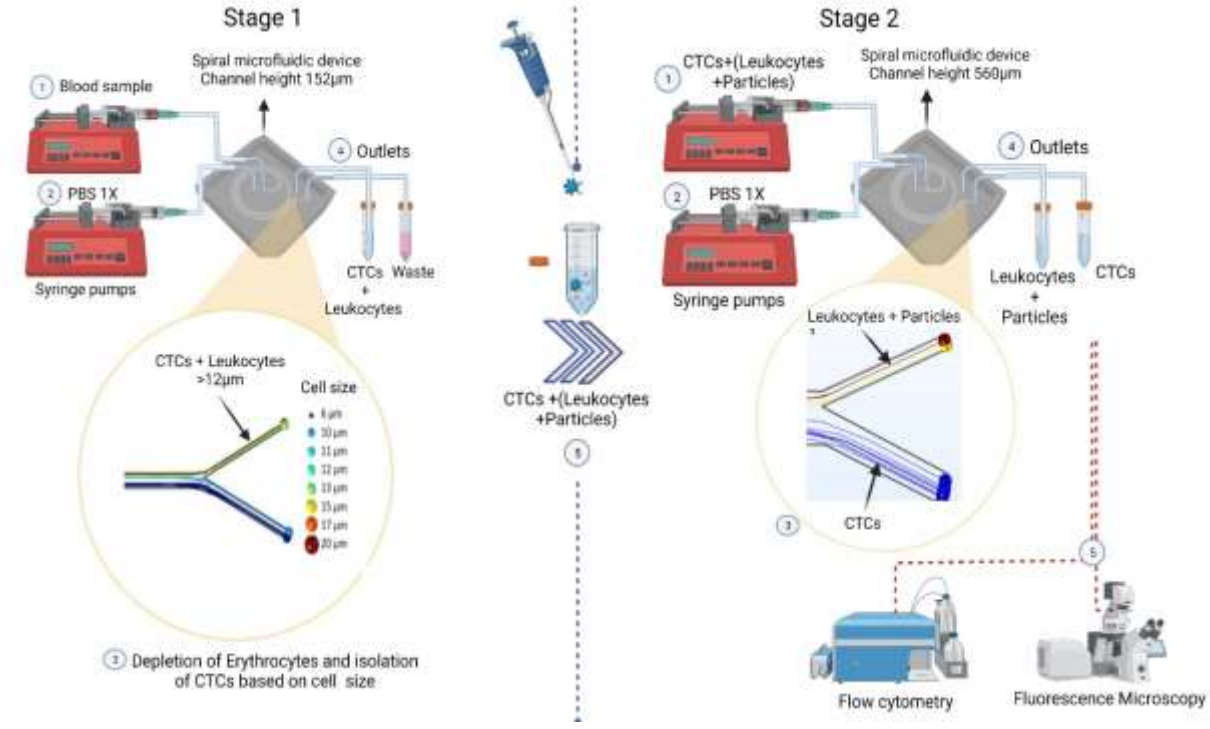

Figure 31. Microfluidic setup for pre-Erythrocytes and leukocytes depletion. Stage 1: (1)(2) First a spiral microfluidic device composed by two inlets and two outlets separates cells >12µm, which allows the depletion of erythrocytes and smaller leukocytes through one of the outlets (cells <12µm) (3).

Meanwhile, the CTCs contaminated by leukocytes bigger than 12µm take the other outlet (4). (5) The CTCs+Leukocytes sample collected is incubated with polystyrene particles conjugated with CD45-Biotin. Stage 2: Second spiral microfluidic device composed by two inlets and two outlets separates cells >70µm, which allows the depletion of leukocytes bonded to the particles through the inner outlets. Meanwhile, the enriched CTCs take the other outlet (4). (5) The samples collected from the outlet of the chip are analyzed and quantified by Flow cytometry and Fluorescence microscopy

3.5 Flow cytometry analysis and quantification of separation efficiency using microfluidic devices

To quantify the enrichment ratio between the blood sample and sorted cancer cells (CTCs), flow cytometry (FACS) analysis was performed in Experiments 1,3,4 and 5. Once the samples with a concentration of $1x10^4$ particles or cells/mL were prepared and processed through the spiral devices as previously described in section *"Microfluidic set up for evaluate the performance of spiral microfluidic devices"* . Those were collected from each outlet (Inner outlet: CTCs, outer outlet: Waste), incubated with CD45-Alexa647 (1:1000 CD45 Antibody (35-Z6) Alexa Fluor® 647 – Santa Cruz) or Brilliant Violet 421™ anti-human CD45 Antibody (1:1000 Biolegend) during 30 minutes at room temperature. After, the samples were washed 2 times with PBS1X centrifugated at 500G for 5 min and fixed with 200 µL of 8% paraformaldehyde (PFA) (wt/vol) for 15 minutes. Subsequently, 800 µL of N2 buffer (1.7M TRIS Base, 1.25 M Glycine, pH 9.1) was added to neutralize the PFA 8%. Finally, Flow-Check Pro Fluorospheres (Beckman Coulter- nominal concentration of 106 fluorospheres/mL) were added in the sample (dilution 1:10) for quantify the number of cells collected apply the Equation 1. Samples without pass through the spiral device were considered as a control for quantifying the ratio of CTCs recovery. During the acquisition of the data, the gates were established according to the forward scattering angle and secondary scattering angle in order to separate the particles or cell populations as the Figure 32 shows. The CTCs recovery rate was quantified according to Equation 2, meanwhile the depletion of Erythrocytes and Leukocytes was calculated based on Equation 3 and the enrichment ratio according to Equation 4.

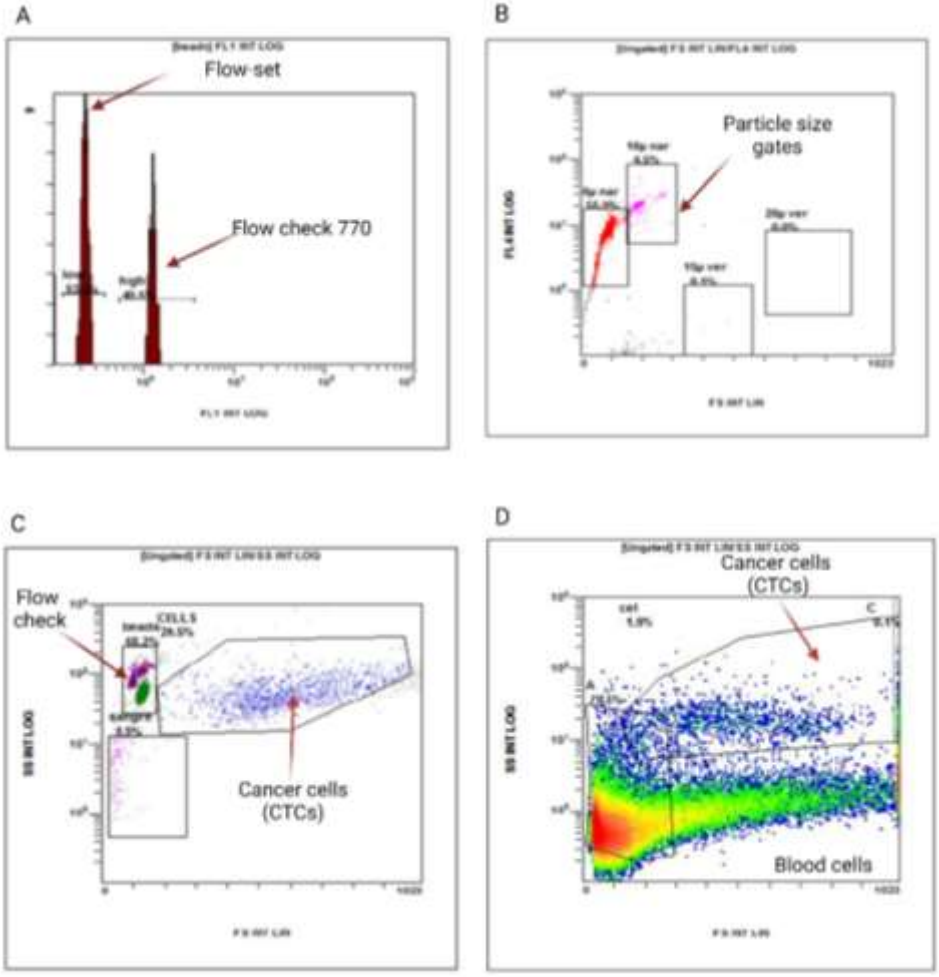

Figure 32. Flow cytometry gates configuration **A)** Flow cytometer alignment verification fluorospheres composed by FLOW-CHECK 770 (7 µm) and FLOWSET 770 (6 µm). **B)** Particle size gates separate by diameter of 6µm, 10µm,15 µm and 20µm. **C)** Cancer cells gate (CTCs model) and flow check fluorospheres gate. D) Blood cells gate composed by erythrocytes and smaller leukocytes. Cancer cells (CTCs) and leukocytes with the similar diameter

Meanwhile, to quantify the depletion rate of Kasumi-1(ATCC® CRL-2724™) that represent the Leukocytes population, the samples collected from the Herringbone chip outlet composed by Kasumi-1(ATCC® CRL-2724™) and MCF-7(cyclo-rgDfK(TPP) (ATCC® HTB-22™) cells, which were previous stained as described in section *"Cell staining"* were analyzed by flow cytometry (FACS). Thus, the samples recovered from the chip output were fixed with paraformaldehyde 8% for 15 minutes. Then, the sample was centrifugated at 500G for 5 min. The supernatant was eliminated, and the cleaning process was repeated one more time. Finally, Flow-Check Pro Fluorospheres (Beckman Coulter- nominal concentration of 106 fluorospheres/mL) were added in the sample (dilution 1:10) for quantify the number of cells collected apply the

Equation 1. Samples without passing through the herringbone device were considered as a control for quantifying the ratio of CTCs recovery and depletion of Leukocytes. During the acquisition of the data, the gates were established according to the forward scattering angle and secondary scattering angle in order to separate the cell populations as the Figure 33 shows. The CTCs recovery rate was quantified according to Equation 2, meanwhile the depletion of Leukocytes was calculated based on Equation 3 and the enrichment ratio according to Equation 4.

On the other hand, to quantify the depletion of leukocytes during the device characterization with blood samples obtained from spiral microfluidic devices, the samples were incubated with BV421-CD45 (Biolegend) for 20 minutes at 4°C. Then, cells were centrifuged at 500g for 5 minutes. The supernatant was removed, and the cells were washed with PBS 1X. The process was repeated two more times. Finally, the sample was fixed with paraformaldehyde 8% for 15 minutes. Then, the sample was centrifugated at 500G for 5 min. The supernatant was eliminated, and the cleaning process was repeated one time more. Also, Flow-Check Pro Fluorospheres (Beckman Coulter- nominal concentration of 106 fluorospheres/mL) were added and the quantification process was performed as previously described. During the acquisition of the data, gates were also established. The CTCs recovery rate, depletion of Leukocytes and enrichment ratio were calculated applying Equations 2, 3 and 4.

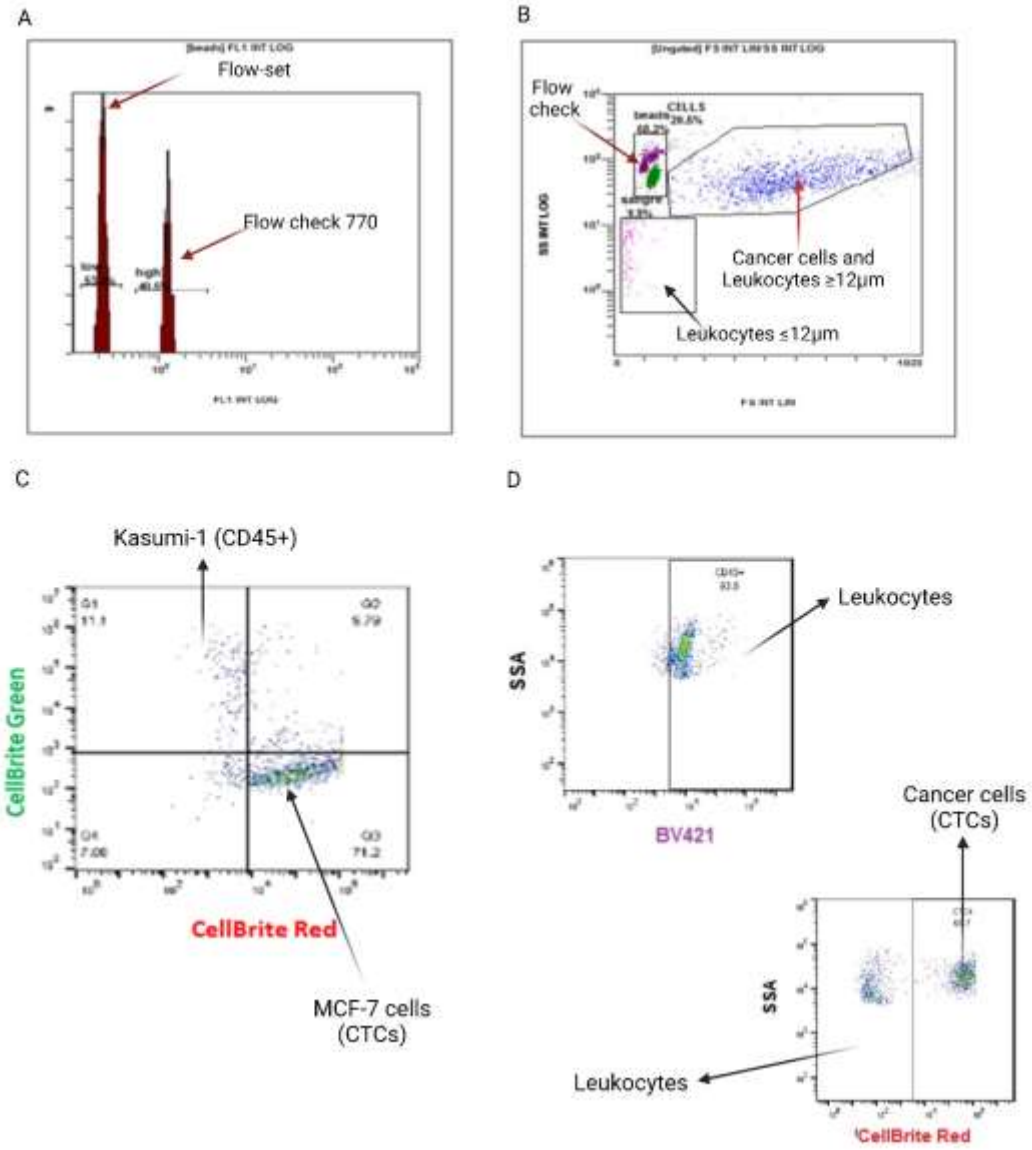

Figure 33. Flow cytometry gates configuration **A)** Flow cytometer alignment verification fluorospheres composed by FLOW-CHECK 770 (7 µm) and FLOWSET 770 (6 µm). **B)** Cancer cells (CTCs model), Leukocytes and flow check fluorospheres gates. **C)** Gates for analyse the sample recovered from the chip outlet composed by Kasumi-1 and MCF-7 cells stained with Cellbrite Red (X axis) and Cellbrite Green (Y axis), respectively**. D)** Gates of sample recovered from chip outlet where MCF-7 cells were stained with Cellbrite Red (X axis-Right image) and Leukocytes with BV421 CD45 (X axis-left image).

$$Absolute\ Count\ \left(\frac{Cells}{\mu L}\right) = \left(\frac{T_C}{T_P}\ x\ F_P\right) x V_T$$

Equation 1

Where

T_C *= Total Number of Cells Counted*

T_P *= Total Number of Fluorospheres Counted*

F_P *= Flow-Count Fluorospheres Assayed Concentration*

v_T *= Total volume processed (µL)*

$$CTCs\ recovery\ rate\ (\%) = \left(\frac{C_R}{C_i}\right) x100$$

Equation 2

Where

C_R *= Total Number of isolated cancer cell lines*

C_i *= Total Number of spiked cancer cell lines*

$$Leukocytes\ or\ Erythrocytes\ depletion\ rate\ (\%) = \left(\frac{N_{Inlet} - N_{CTC\ outlet}}{N_{Inlet}}\right) x100$$

Equation 3

Where

N_{Inlet}*= CTCs spiked in the inlet*

$N_{CTC\ outlet}$ *= CTCs recovered from Inner outlet*

$$Enrichment\ ratio\ (\%) = \left(\frac{\frac{N_{CTC\ Outlet}}{N_{CTC\ Inlet}}}{\frac{L_{Outlet}}{L_{Inlet}}}\right)$$

Equation 4

Where

$N_{CTC\ outlet}$ *= CTCs recovered from Inner outlet*

$N_{CTC\ Inlet}$ *= CTCs spiked in the inlet*

L_{outlet} *= Leukocytes recovered from inner outlet*

L_{Inlet} *= Leukocytes in the blood sample inlet*

3.6 Blood sample obtention

Blood samples were obtained from healthy volunteers and acquired from the Blood and Tissue Bank in Barcelona (up to 36h from its extraction). Blood samples were used as controls with previous approval of the committee on research ethics with medicines and commission of research projects of the Vall d'Hebron University Hospital.

Chapter 4

Design and microfabrication of the microfluidic devices

Photolithography has represented one of the microfabrication methods used to date. This technique is based on the exposure of light in a photoactive material which is subject to a chemical reaction to form a liquid-solid transition [241]. The advantages of this technique are mainly the spatial control of light and the high resolution of the microfluidic structures or molds. However, some limitations have been reported: lower sealing quality, chemical invariability of the surface, absence of other materials and related photoresists that can be used instead of traditional silicon[242].

On the other hand, most of the research in microfluidic devices is carried out in PDMS and other polymers. The PDMS has several attractive properties that make it suitable as a material for rapid prototyping of microfluidic applications, such as

- Optical: Transparent material, UV cutoff, 240nm
- Mechanical: Conforms to surfaces, allows actuation by reversible deformation which facilitates release from molds
- Thermal: Can be used to insulate heated solutions
- Interfacial: Replicas release easily from molds
- Permeability: Contains aqueous solutions in channels, allows gas transport through the material
- Toxicity: Can be implemented in vivo and supports mammalian cell growth

However, the fabrication of microfluidic devices using lithography and soft-lithography represents a complex process, whereby the use of 3D printing has emerged as an alternative for rapid and low-cost prototyping of microfluidic devices when the dimensions of the channels meet the capabilities of each particular printer.

In this chapter, we describe the design and manufacture of the microfluidic devices for liquid biopsy applications developed during this thesis.

4.1.1 Numerical modelling of spiral microfluidic device

A computational model was developed to characterize and optimize the device design for the separation of particles in curved microfluidic channels according to their size. The device consists of a spiral channel with rectangular cross-section, with two inlets and two outlets. In one inlet is introduced the sample with particles of different sizes, ultimately blood sample with CTCs. In the other inlet is introduced the sheath-flow, that helps to focus the particles. It is expected that the CTCs would be collected in one outlet and the blood cells in the other one. Figure 1A illustrates the spiral device geometry, the tetragonal mesh constructed and the refinement in Z direction, used to get more details on the Dean Flow.

As has been reported in curved channels, the influence of centrifugal forces in the radial direction results in the formation of two counter-rotating vortices across the channel cross-section, known as Dean Flow.

Based on the theoretical assumptions previously mentioned, we modelled the separation of particles in a spiral channel in COMSOL Multiphysics. The simulations of the laminar flow considered a fluid with the properties of water. The density and viscosity of PBS (Phosphate Buffered Saline) can be approximated to the water properties, but blood properties are quite different, starting from its non-Newtonian behaviour. However, as the blood was 10 times diluted in PBS, the assumption of considering this fluid with the properties of water is acceptable.

First, the laminar flow was solved considering a linear discretization for the velocity and pressure (P1+ P1). However, the particle trajectories did not match the experimental results. Then, the discretization was raised to P2 + P1, by using a quadratic function to solve the velocity and a linear one to solve the pressure. The element order or the order of the shape function directly affects the number of freedom degrees and the precision of the solution. Thus, the accuracy of laminar flow simulations was improved by increasing the discretization (Appendix A-Supplementary Figure 45).

Furthermore, in the simulation we also observed the Dean Flow effects on a transversal plane as indicated in Figure 34A (red line). The in-plane velocity magnitude was plotted in this plane together with the in-plane velocity vectors. The in-plane vectors indicate two symmetrical recirculating zones in the upper and bottom part of the channel, characteristic of the secondary Dean flow (Figure 34A). Figures 34A shows a comparison of the different sheath flow rates considered (300 µL/min, 500 µL/min, 700 µL/min and 900 µL/min), meanwhile the

blood sample flow rate was fixed to 100 µL/min. The results show that the Dean velocities decreased as the sheath flow decreased, due to the reduction of the Reynolds number (Figure 34A). Then, it would be expected that the particles would be more affected by the Dean flow in the cases where the sheath flow rates are higher: 700 µL/min and 900 µL/min (Figure 34A).

After the stationary solution for the flow was obtained, the particles trajectories were calculated in a time-dependent study. The simulations were done considering a one-way coupling between the fluid and the particles, which means that particles trajectories were affected by the fluid but the particles did not affect the fluid and the particle-particle interactions were not considered. In practice, these interactions might affect the cells trajectories. However, as the total volume of cells in comparison to the fluid volume is on the range of 0.4 to 1% (due to the dilution), the one-way coupling is a good approximation.

The equilibrium position for each particle was calculated along the microfluidic device. The particles' lateral migration depends on the drag force and lift force. The balance between these two forces generates different equilibrium position of the particles depending on their size. The lift force is stronger for bigger particles ($F_L \sim a_p^4$) while the small particles are mainly affected by the drag force, which allows being able to separate them, since they take different outputs in the microfluidic device.

The particles were first focused on the inner wall of the spiral channel, pushed by the sheath flow. Subsequently, when the sheath flow rate was 700 and 900 µL/min particles between 6µm to 11µm (erythrocytes and leukocytes) move according to the Dean flow. After, these particles moved away from the inner wall until they got focused on the outer wall. Meanwhile, the particles from 12 µm to 20 µm that represent the largest leukocytes (~15 to 21 µm) and the CTCs (≥12 µm) experience strong inertial lift forces, avoiding them from migrating under the influence of Dean drag, therefore coming out from the inner outlet. Figures 34B shows a zoomed image of the trajectories of the particles in the chip output, considering four conditions studied for sheath flow rate (900, 700, 500 and 300 µL/min) and the particle size indicated previously.

Further analysis showed that the Dean Flow and the inertial lift force were not strong enough to focus the particles and direct them to the expected outlet under flow rates equal to 300 µL/min and 500 µL/min. Whereby, the results show that 67% and 33% of 6µm particles under 300 µL/min and 500 µL/min will contaminate the CTCs outlet. Moreover, 50% and 100% of 10 µm particles took the CTCs outlet under 300 µL/min and 500 µL/min respectively (Figure 34B). Likewise, the results suggest that for sheath of 700 µL/min the smaller particles (6µm) were closer to the left wall and a lower contamination would be expected on the CTC outlet (33%), as well recovery of all CTCs is expected(>12µm) (Figure 34B). Meanwhile, smaller particles of

6µm and 10µm are not expected to contaminate the CTC sample under a flow rate of 900 µL/min, and 100% of the particles that mimic the CTCs (>12µm) could be recovered (Figure 34B). Our findings revealed that the best flow conditions are a sheath flow of 900 µL/min and blood sample flow rate of 100 µL/min for achieving a high efficiency CTCs recovery rate (100%), high depletion of erythrocytes (100%) and 100% depletion of leukocytes around 10 um, which represents the lymphocyte population that comprising 25% of the total population of leukocytes[243]. These data must be interpreted with caution because the simulations does not consider the particle-particle interaction and it is limited by the number of particles included, for which it is expected to obtain variations in the rates of recovery of CTCs and contamination of blood cells. However, the results obtained from the simulations allow us to conclude the general dynamics of the particles under different flow parameters and select the most appropriate ones that allow the recovery of the greatest possible number of CTCs in a real sample.

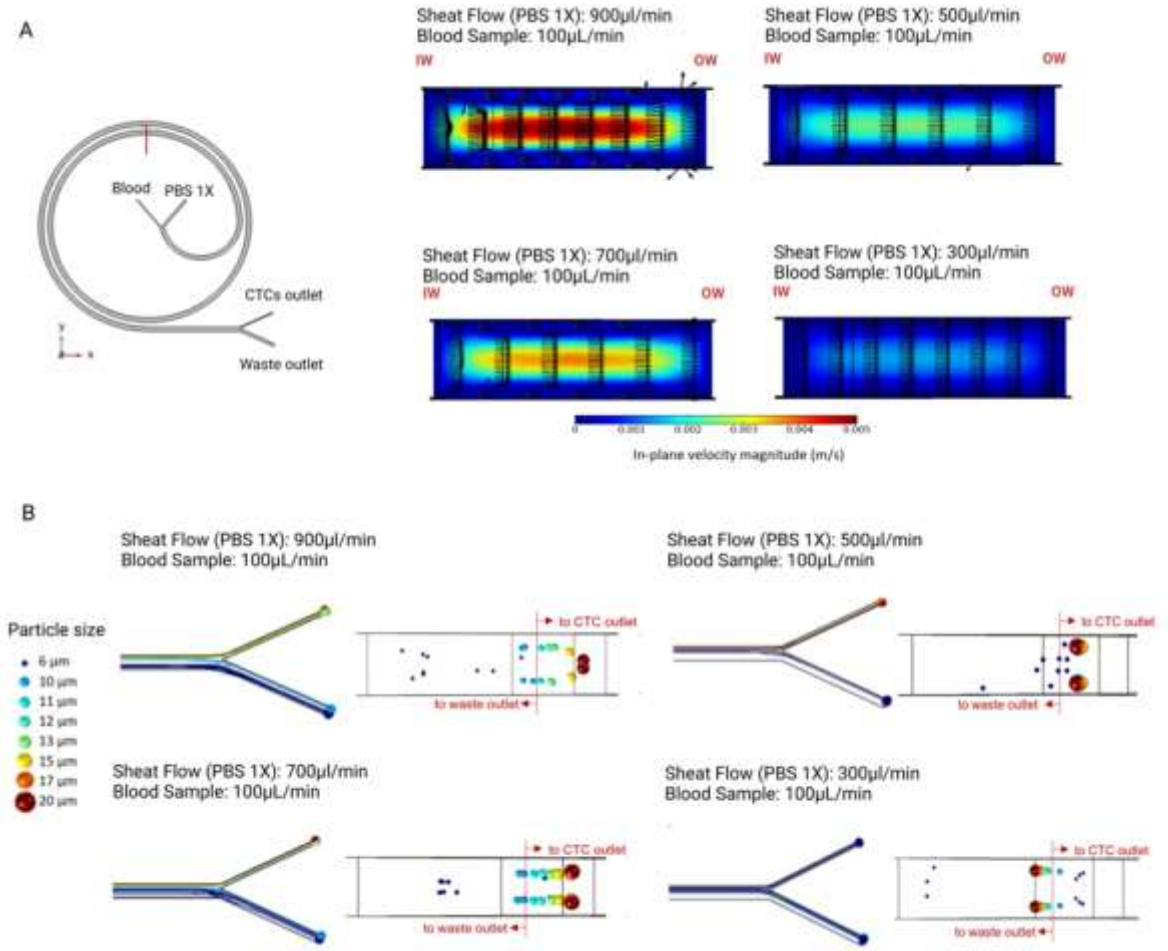

4.1.2 Figure 34. A) Selected transversal plane (Red line). In-plane velocity profile with in-plane velocity vectors for inlet sample flow rate of 100 µL/min and sheath flow rate of 900 µL/min, 700 µL/min, 500 µL/min and 300 µL/min, respectively. IW and OW indicate inner wall and outer wall, respectively. B) Detail of the different particle sizes trajectories in the chip outlets (CTCs and waste) according to the sheath flow rate (900 µL/min, 700 µL/min, 500 µL/min and 300 µL/min, respectively) and particles position before the bifurcation (right images)

Computational simulations of the spiral device with different channel heights

Previous studies revealed the presence of CTCs with a mean size of around 12.4 µm in patients with breast cancer, 16 µm for patients with metastatic lung cancer. However, a broad size range were found within single patients, with CTCs from 10 µm to 22.5 µm[244] [245246] Hence, the channel height of the device could be tuned to recover CTCs of different size and optimize the separation efficiency. Simulations of the spiral device with different channel heights (140, 160, 170 and 180 µm) were performed. The influence of the aspect ratio on the device

operation was evaluated considering the optimized flow conditions (sample flow rate of 100 µL/min and sheath flow rate of 900 µL/min).

Figure 35 shows the particles trajectories in the output for each channel height, where it is observed that if the channel height decreases the cut size of the particles also decrease. Thus, in the device with a height of 140 µm the particles of 10 µm take the inner outlet (CTCs outlet). Devices with a channel height of 150, 160, 170 and 180 µm showed a particle cutting size of 12, 13, 14 and 15 µm, respectively. In addition, the simulations also demonstrated the compromise between recovering small CTCs (10 µm) and increasing the blood cell contamination on CTCs outlet. This parameter is evaluated on the device through the lateral distance between the blood cells and the CTCs. Wherewith, if the blood cells are far from the CTCs position, low contamination in the CTCs output would be observed. Meanwhile, if the lateral distance between blood cells and CTCs is short, higher contamination and lower CTCs recovery would be obtained. Figures 35A and B show most of the erythrocytes (blue particles) were located close to the outer wall but some were located close to bifurcation, especially for 140 µm. In this case, the contamination on the CTC outlet with erythrocytes would be expected to be higher (90%) than in the microfluidic channel with 150 µm or 160 µm of height(See figure 35 A,B,C).

Considering the contamination in the CTC outlet, the condition in which the erythrocytes were closest to the outer wall and more distant from the CTCs, was the one with the channel height equal to 160 µm (Figure 35C), allowing the recovery of CTCs as small as 13 µm. Meanwhile, a device with a channel height of 150 µm allows to recover CTCs of 12 µm or higher (Figure 35B, F). Finally, for heights of 170 and 180 µm, the erythrocytes were more dispersed and particles of 13 and 14 µm would take the waste outlet. For these cases, a lower recovery rate would be expected for small CTC around (Figure 35D,E,F).

As previously was mentioned the absence of erythrocytes contamination in channels with heights of 150 µm, 160 µm and 170µm must be interpreted with caution because the simulations does not consider the particle-particle interaction. Therefore, it is expected that at the experimental level some variations in the rates of recovery of CTCs and contamination of blood cells will be obtain. However, the results obtained from the simulations allow us to decide the most appropriate channel dimensions to achieve the best performance possible for recovering CTCs bigger than 12µm which corresponds to 150µm

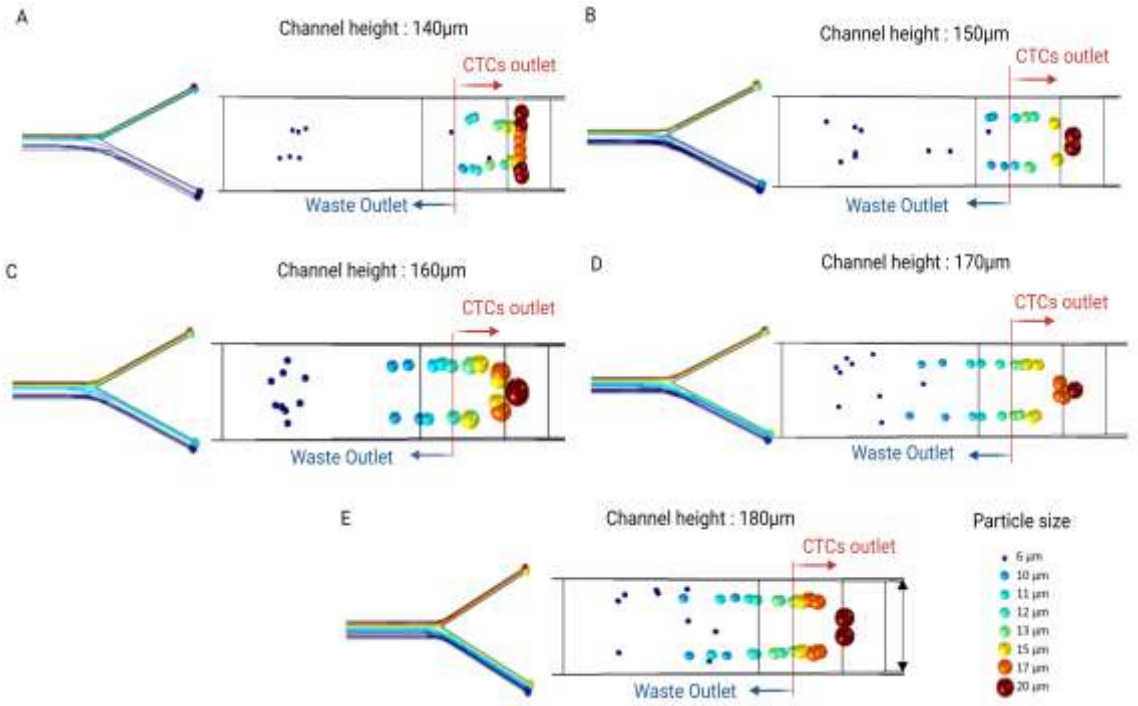

Figure 35. Particles trajectories in the output of the spiral (Left images) and particles position plotted in a transversal plane 0.5 mm before the bifurcation for inlet sample flow rate of 100 µL/min and sheath flow rate of 900 µL/min according to the channel height (right images): 140 µm **(A),** 150 µm **(B)**, 160 µm **(C)**, 170 µm **(D)** and 180 µm **(E).**

To date, several studies have investigated the heterogeneous CTCs size from cancer patients, highlighting the morphological difference between commercial cancer cells and cancer cells from patients. One analysis performed by Wujun Zhao (2019) found small CTCs from Non-Small Cell Lung Cancer (NSCLC) patients with size from 9.73±3.11 µm up to 10.98±3.41 µm[247]. This size is on the same range of reported leukocytes diameter, around 10.58±2.27 µm[248]. Previous simulations in COMSOL Multiphysics® revealed that with a channel height of 140µm it is possible to recover CTCs starting at 10µm (Figure 355A). In addition, we performed simulations considering different channel heights (100 µm, 120 µm, 130 µm and 140 µm) , with the aim to know the separation limit of the device for each design and consider the suitable height range during the fabrication processes. The results revealed that the suitable channel height for isolating 10 µm cells would be 140 µm (Appendix A-Supplementary Figure 46).

Overall, the computational model of inertial focusing on spiral devices for cell separation previously performed, ratify the reported studies developed by Wu et al and Yeh et al [249,250]. who demonstrated the efficiency of inertial forces in isolate small cells from larger cells. In

fact, similar results for other microfluidic numerical and experimental simulations were obtained regarding to the velocities values (near-zero in the wall, and maximum 0.9m/s in the channel center), where the imbalance of force between the higher velocity flow near the outer wall and the lower velocity flow near the inner wall generated counter-rotating vortices[251–253].

4.1.3 Photomask Desing of spiral microfluidic device

The photomask represents one of the key elements in the fabrication of microfluidic devices using the photolithography method for obtaining the desired master. Therefore, it is crucial to design the mask accurately depending on the resin to be used in the manufacturing of the master if it is negative or positive. In our case, the selected resin was SU8 which was negative that means the microfluidic pattern in the mask has to be transparent to UV light in order to polymerize that part of the resin (Figure 36B). Thus, the final master is composed by hills with the shape of the spiral microfluidic device. The designing of the mask was carried out using AutoCAD with the exact geometry of the device previously optimized by computational modeling in COMSOL MULTYPHYSICS® (Figure 36A).

On the other hand, it is important to highlight that based on the dimensions of this device the acetate photomask type was selected since the smallest dimension of the desired device was 150 µm.

4.1.4 SU8 master manufacturing of spiral devices

First, the fabrication process involves the pretreatment of the Si wafer surface putting on the hot plate at 200°C for 15 minutes with the aim to dehydrate its surface. Afterwards, it undergoes a plasma oxidation for 1 minute which allows removing all the organic matter from the surface of the substrate[254].

Then, the SU8 was poured on the Si wafer previously placed on a spin coater. It is important to consider that there are different types of SU8 resins depending on the thickness of the coating layer, in our case the target was 150 µm. According to the MicroChem protocols of manufacturing, SU8 2100 seems to be the best option since it can reach thicknesses ranging from 90 to 230 µm depending on the speed of the spinner[255]. The protocol was followed into detail to obtain the best possible outcomes.

However, numerous resin adhesion problems were encountered. Therefore, the SU8 3050 resin was selected, which presents good adhesion characteristics of the substrate and a thickness ranging from 45µm to 100µm. Considering the above, the process was divided into

2 layers to achieve a total height of 150µm of the microchannel. Thus, the resin was extended by applying the spin cycles as indicated in Table 8. After, each layer a post bake process was carried out to evaporate the solvent component of the resin so that it densifies. This procedure consists of put the master in a leveled hot plate for 30min at 95°C followed by a cooldown for 5 minutes at room temperature.

Number of Layer	***Theoretical thickness***	***Spin coater parameters***
First layer	85µm	Step 1 : 10 "sec. – 500 rpm Ac 100 rpm Step 2: 30 "sec. – 1900 rpm Ac 300 rpm
Second layer	55µm	Step 1: 10 "sec. – 500 rpm Ac 100 rpm Step 2: 30 "sec. – 3000 rpm Ac 300 rpm

Table 8. SU8 3050 spreading cycles parameters for spiral microfluidic device.

Subsequently, the Si wafer is ready for alignment and exposure where the critical parameters to be optimized were the exposure energy, the intensity of the mask aligner and the exposure time(Figure 36C). Those parameters are strictly correlated to Equation 1.

$$Pd = \frac{I}{t}$$

Equation 1.

Where Pd is the power density (mJ/cm^2)/s, I corresponds to the intensity (mW/cm^2) and t is the time (s). In this case the optimal exposure energy for achieve a total thickness of 150 µm is $270\,\frac{\mathrm{mJ/cm^2}}{\mathrm{s}}$. Moreover, knowing the intensity of the mask I-liner and type of photomask that is acetate, which represents the power density ($13{,}7\,\frac{\mathrm{mW}}{\mathrm{cm^2}}$) it was possible to calculate the exposure time as indicated in Equation 2.

$$t = \frac{270\,\frac{\mathrm{mJ/cm^2}}{\mathrm{s}}}{13{,}7\,\frac{\mathrm{mW}}{\mathrm{cm^2}}}$$

$$t = 19.7\ s$$

Equation 2

Then, after the exposure process a post bake step is performed (5’ min – 65ºC + 12’ min – 95ºC), which is a common method for stabilizing the printed features to provide optimum performance at etch (Figure 36D) . Finally, the development of the resin to see the microfluidic pattern is performed using the specific developer from MicroChem for 15 minutes. Afterwards, to eliminate the remaining SU8, the substrate is rinsed with IPA and finally dried with N2 gas gun. The final master composed by 4 spiral microfluidic devices is shown in Figure 36E. The correct formation of the microfluidic channels was verified under the microscope (Figure 36F). In addition, it was confirmed by the interferometer and profilometer that the height of the microfluidic channels was 152µm (Figure 36H).

4.1.5 Soft-lithography of spiral microfluidic devices.

Polydimethylsiloxane (PDMS) replicas were performed from the master previously created. In our case as the microfluidic structures in the master was hills, the PDMS replica obtained is composed by valleys. However, to make PDMS replicas, the master was subjected to a treatment with fluorinated silane vapors to passivate its surface, thus the PDMS does not remain permanently anchored to the master's surface. In overall, the process consists of putting the master into a vacuum desiccator for 1 hour with a drop of trichloro (1H,1H,2H,2H-perfluorooctyl) silane in a petri dish. Subsequently, the 80gr of PDMS was mixed with cross-linker to start the polymerization reaction in a proportion of 1:10. The obtained mixture was put into a vacuum to eliminate all the air for approximately 30 minutes. Then, the master was placed into a petri dish and the mixture was poured onto the top of the master. The thickness of the device was around 5 mm to tolerate the relative high pressures and stress.

Once the PDMS was completely solidified, it was de-molded from the master and the inlets and outlets were opened. Finally, these resulting replicates were carefully cleaned by sequential washings with water, soap and sonication for 5 minutes with ethanol. This ensured that the surfaces were clean enough to bond with the glass. Moreover, the glass slides were subjected to sequential cleaning steps soon with ethanol, acetone and isopropanol.

Finally, the PDMS devices and glass slides were subjected to oxygen plasma treatment for 30 seconds, in order to improve the affinity between these two surfaces. The irreversibly bonded device is shown in Figure 3G.

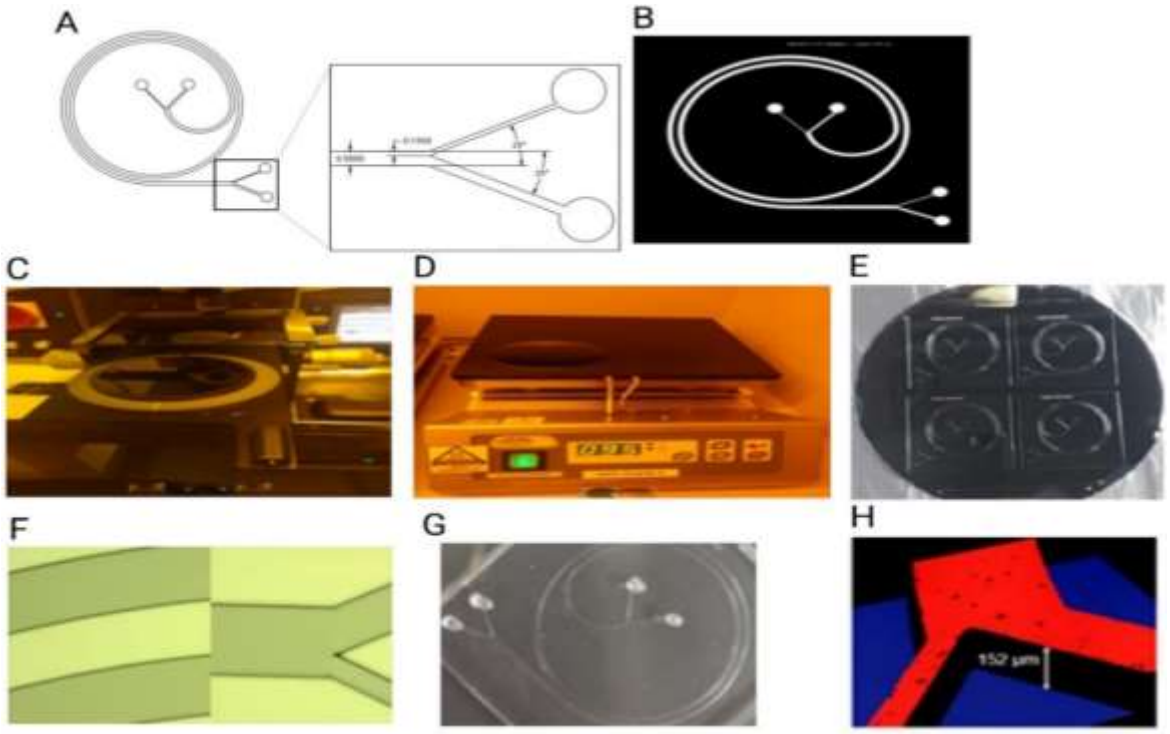

Figure 36. Process of photolithography. **A)** AutoCAD Schematic of the spiral device composed by two inlets (Blood sample input and PBS 1X) and two outlets (Waste and CTCs outputs), microchannels of 500 mm (width) x 150 µm (height)), outlet split to 150 µm for CTCs outlet near to the inner wall and 350 µm for waste outlet near to the outer wall. **B)** Acetate mask with opaque regions in the desired pattern is used to illuminate a light-sensitive photoresist. **C)** UV light Exposure with acetate I-line filter on the positive photoresist. **D)** Hard bake after the develop step. **E)** Master fabricated by soft lithography in a Silicon wafer and Photoresin SU8 3050. **F)** Optical validation of the correct development of microfluidic channels for subsequent replication in PDMS. **G)** Final PDMS replica of the spiral chip bonded to glass slide. **H)** Master characterization using interferometer and profilometer, respectively. A channel height of around 152µm was obtained

4.2 Numerical modelling of Herringbone microfluidic device

Simulations in COMSOL Multiphysics® 5.5 were done to evaluate the flow mixing behavior caused by the grooves . Since the aspect ratio of the herringbone is large and the device is composed of repetitive units (76 set of grooves), a section with 4 sets of grooves was selected for the simulation (Figure 37).

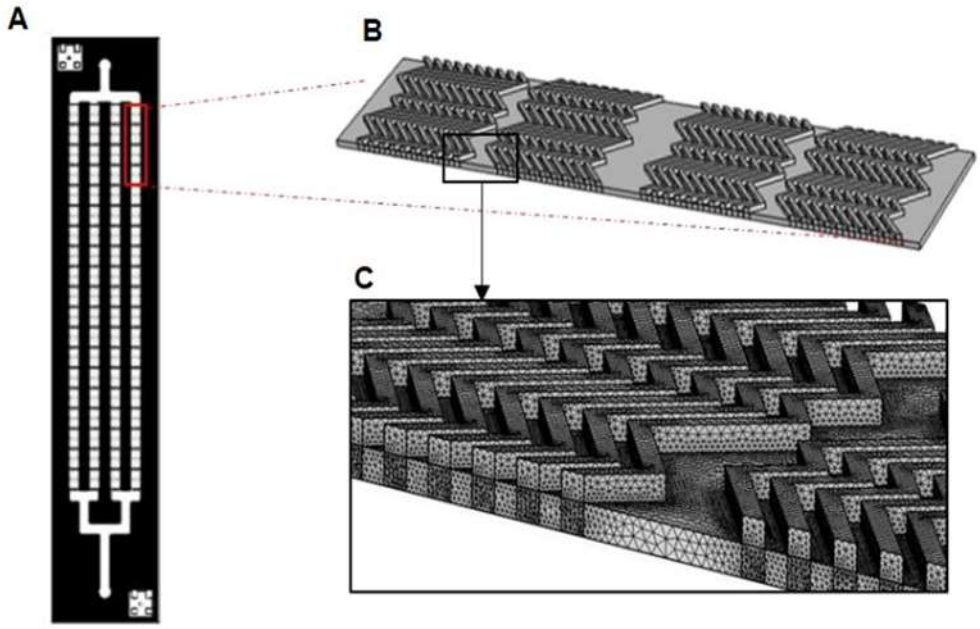

Figure 37. (A) Herringbone device designed in AutoCAD®. **B)** geometry of the domain used in COMSOL Multiphysics simulation equivalent to the first 4 sets of grooves. **C)** detail of the mesh built in COMSOL Multiphysics

In order to assess the flow rate influence in the mixing inside the device, two simulations were performed considering inlets of 2.5 and 5 µL/min in this section . The velocity profile indicates that part of the flow penetrates in the grooves region. The streamlines highlight the mixing behavior induced by the grooves (Figure 38). This mixing is fundamental to increase the leukocytes' probability of interacting with the antibodies that are immobilized on the device walls. In the absence of the grooves, the cells would tend to go straight following the fluid streamlines because of the low Reynolds number. Table 9 describes the parameters considered for the computational model.

Stationary study for laminar flow	Fluid properties	Density: 1000 kg/m^3 Viscosity: 0.001 kg/m.s
	Boundary Conditions	Inlet flow rate: Simulation 1: 2.5 µL/min Simulation 2: 5 µL/min Outlet: P=0
	Wall condition	no slip
Time dependent study for particle tracing	Particles	Density: 1050 kg/m^3 Diameter: 10µm Number of particles : 100
	Forces	Drag Force Wall-induce lift force
	Wall condition	Freeze

Table 9. Parameters in the COMSOL Multiphysics simulation for herringbone device design

The simulation considers that the leukocyte that touches the wall would be captured. In practice, this interaction is not 100% efficient, because it also depends on the kinetics of the interaction between antibody and CD45. Therefore, the immobilization of leukocytes efficiency in the simulation should be seen as a maximum (ideal) value that considers the hydrodynamics of the device.

The increase of the flow rate in the device contributes to the increase in the total velocity but is insufficient to improve the mixing (Figure 38). The calculation of the leukocytes trajectories confirms that 44% of them enter in contact with the grooves surface under a flow rate of 2.5µL/min (11% of each set of grooves). Meanwhile, 46% for a flow rate inlet of 5 µL/min (11.5% of each set of grooves) (Appendix C-Supplementary Figure 47). If the same efficiency is considered to the remaining 72 set of grooves that composed the one microfluidic device

and without considering the antibody capture efficiency 36 sets of grooves are enough for achieving a total immobilization of each 100 leukocytes entering.

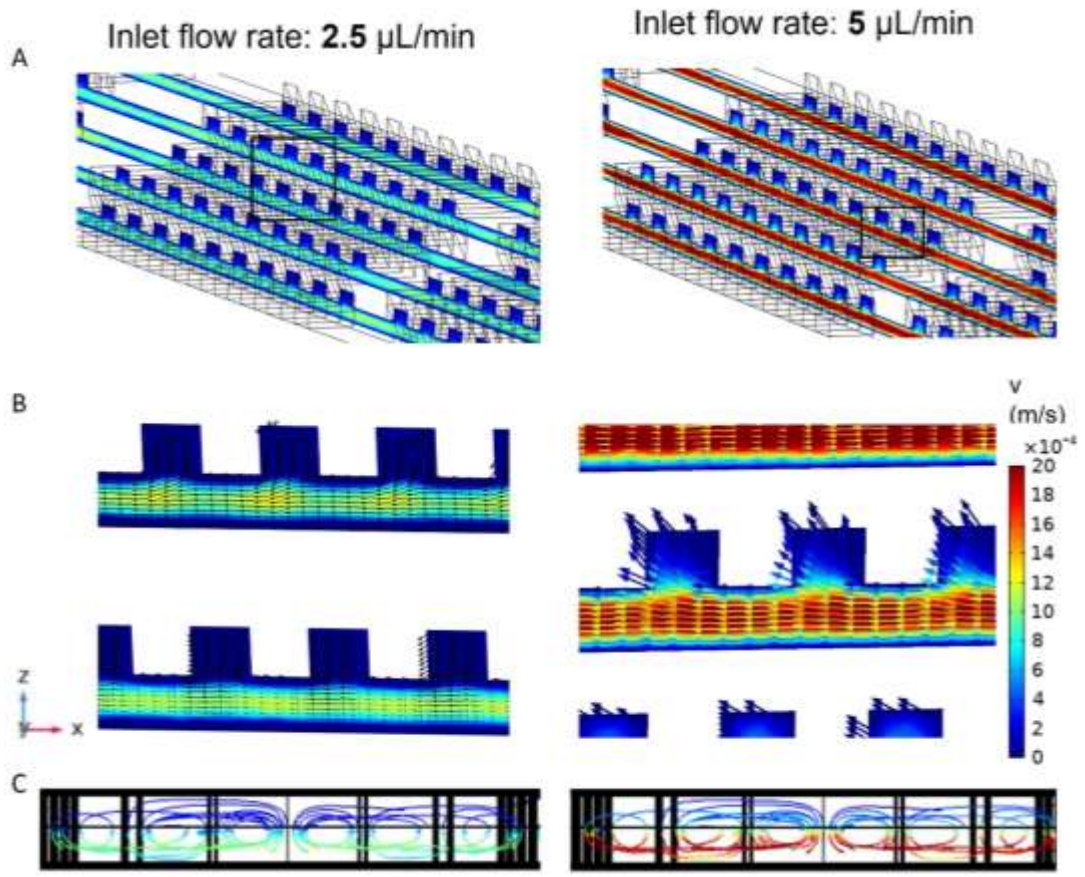

Figure 38. Simulation results for the herringbone device with inlet flow rates of 2.5 µL/min . **A)** Velocity profile at selected planes, **B)** detail of the normalized velocity vectors at the zoomed region indicated in the red square on Figure A**. C)** transversal view (xz) of the device with the fluid streamlines in one channel of the herringbone device colored with the velocity magnitude.

4.2.1 Photomask designing of herringbone microfluidic device

The fabrication of the photomask was carried out following the same procedure previously described for the fabrication of the spiral microfluidic device master. However, in this case the Herringbone device has two structures with different heights, on the one hand the microfluidic channel with a theoretical height of 50µm (Figure 41A-left) and the herringbone pattern of 45µm (Figure 41 B-Right). Therefore, the design of two specific masks was required to use negative resin SU8 and those were carried out using AutoCAD with the exact geometry

of the device previously optimized by computational modeling in COMSOL MULTYPHYSICS® (Figure 41B).

4.2.2 SU8 master manufacturing of Herringbone devices

The first step in the fabrication process involves the pretreatment of the Si wafer surface putting on the hot plate at 200°C for 15 minutes with the aim to dehydrate its surface. Afterwards, it undergoes a plasma oxidation for 1 minute which allows removing all the organic matter from the surface of the substrate[254].

Then, the SU8-3050 was poured on the Si wafer previously placed on a spin coater. Considering the above, the process was divided into 2 layers to achieve heights of 50µm and 45 µm for the channel and the herringbone structures respectively. Since this process required obtaining 2 different heights, an optimization curve was carried out with the SU8-3050 in order to establish the correct spin parameters. Based on previous experimental works developed in MicroFabSpace at IBEC, the calibration curve obtained is shown in Figure 39, which considers different thickness range and the required rpm values in the spin coater.

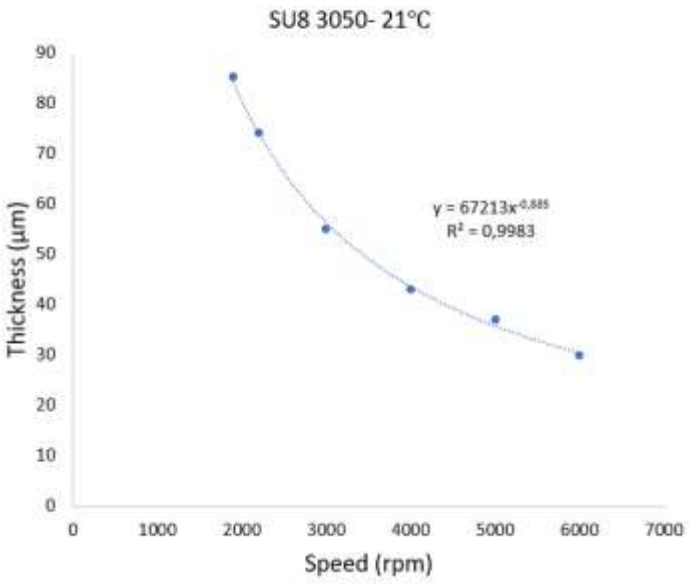

SU3050	
Speed (rpm)	Thickness (µm)
1900	85
2200	74
3000	55
4000	43
5000	37
6000	30

Figure 39. SU-8 3050 optimization thickness

Considering the equation obtained from the curve the theoretical rpm value for achieving a height of 45 µm and 50µm corresponds to 3800µm and 3500 µm, respectively. Since one of the critical steps is to reach the correct height in the second layer that corresponds to the

grooves structures, the spin and exposure parameters were optimized as is shown in Figure 40.

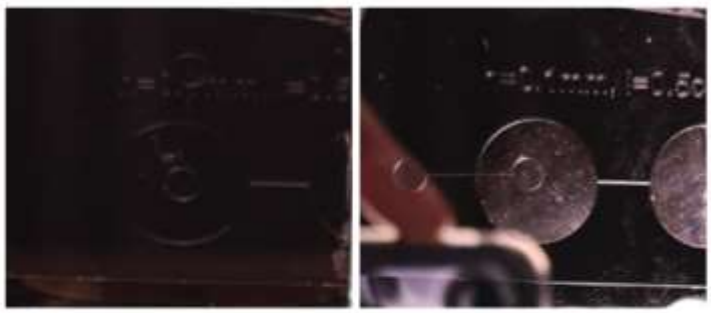

SU8-3050	
Speed (rpm)	Thickness (µm) Second Layer
2500	61
3000	51
3500	45

Figure 40. SU-8 3050 optimization of two layers

Considering the previous optimization, the resin was extended by applying the spin cycles for the first layer that corresponds to the microfluidic channel as indicated in Table 10. After, a pre-soft bake process was carried out to evaporate the solvent component of the resin so that it densifies. This procedure consists of putting the master in a leveled hot plate for 15min at 95°C followed by a cool down for 10 minutes at room temperature. Then, the UV light exposure was calculated using the same equation indicated in the spiral microfluidic device (Equation 1).

$$t = \frac{250\,\frac{\mathrm{mJ/cm^2}}{\mathrm{s}}}{13{,}7\,\frac{\mathrm{mW}}{\mathrm{cm^2}}}$$

$$t = 18.2\ s$$

Equation 3.

After the exposure process a post bake step is performed (1 min – 65ºC + 5 min – 95ºC), which is a common method for stabilizing the printed features to provide optimum performance at etch. Subsequently, the second SU8 layer which corresponds to the grooves structures was extended by applying the spin cycles described in Table 10 flowed by a pre-soft bake process for 15 min at 95ºC.

Number of Layer	*Theoretical thickness*	*Spin coater parameters*
First layer *Microfluidic channel*	50µm	Step 1 : 10 "sec. – 500 rpm Ac 100 rpm Step 2: 30 "sec. – 3300 rpm Ac 300 rpm
Second layer *Grooves structures*	45µm	Step 1: 10 "sec. – 500 rpm Ac 100 rpm Step 2: 30 "sec. – 3500 rpm Ac 300 rpm

Table 10. SU8 3050 spreading cycles parameters for Herringbone microfluidic device.

Then, the Si wafer is ready for alignment and exposure using the same parameters previously calculated in Equation 3 ($Pd = 13{,}7\,\frac{\mathrm{mW}}{\mathrm{cm}^2}$,$I = 250\,\frac{\mathrm{mJ/cm}^2}{\mathrm{s}}$, $t = 18.2\ s$). It is very important to highlight that the mask that contains the grooves has alignment patterns on the corners that are used as a guide to align them with the microfluidic channel that corresponds to the first layer of SU8 (Figure 8A). After the exposure process a post bake step is performed (1 min – 65ºC + 5 min – 95ºC), which is a common method for stabilizing the printed features to provide optimum performance at etch.

The development of the resin to see the microfluidic pattern was performed using the specific developer from MicroChem for 10 minutes. Afterwards, to eliminate the remaining SU8, the substrate is rinsed with IPA and finally dried with N2 gas gun. The final master composed by 4 Herringbone microfluidic devices is shown in Figure 2C. The correct formation of the microfluidic channels was verified under the microscope (Figure 41E). In addition, it was confirmed by the interferometer and profilometer that the height of the microfluidic channels was 53µm and 44 µm for the grooves structures (Figure 41F,G). Finally, a hard bake process was performed putting the master inside the oven at 150ºC with an upward heating ramp and keep it 30 seconds. Afterwards the master was cooled in a descending temperature ramp until reaching 65ºC.

4.2.3 Soft-lithography of Herringbone microfluidic devices.

The Polydimethylsiloxane (PDMS) replicas were performed from the master previously created following the same process in the fabrication of the spiral microfluidic device. In overall, the process consists of putting the master into a vacuum desiccator for 1 hour with a drop of trichloro (1H,1H,2H,2H-perfluorooctyl) silane in a petri dish. Subsequently, the 80gr of PDMS was mixed with cross-linker to start the polymerization reaction in a proportion of 1:10. The obtained mixture was put into a vacuum to eliminate all the air for approximately 30 minutes. Then, the master was placed into a petri dish and the mixture was poured onto the top of the master. Once the PDMS was completely solidified, it was de-molded from the master and the inlet and outlet were opened. Finally, these resulting replicates were carefully cleaned by sequential washings with water, soap and sonication for 5 minutes with ethanol. This ensured that the surfaces were clean enough to bond with the glass. Moreover, the glass slides were subjected to sequential cleaning steps soon with ethanol, acetone and isopropanol. Finally, the PDMS devices and glass slides were subjected to oxygen plasma treatment for 30 seconds, to improve the affinity between these two surfaces. The irreversibly bonded device is shown in Figure 41D.

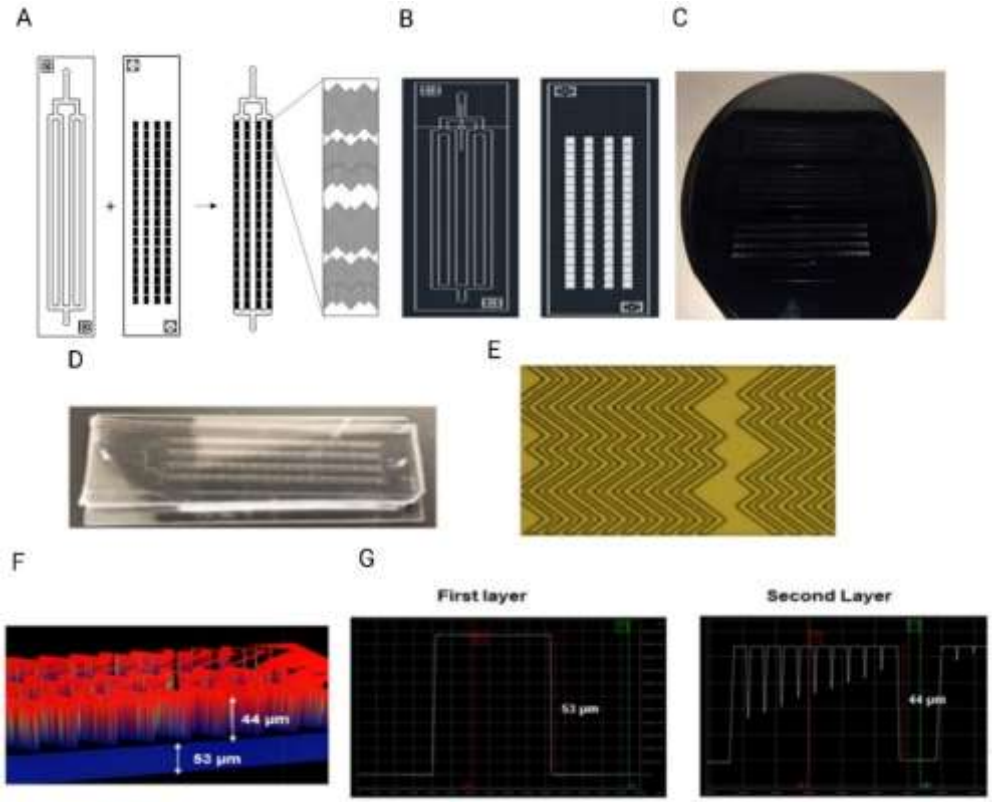

Figure 41. Process of photolithography. **A)** AutoCAD Schematic of the Herringbone chip composed by microfluidic channel (Image on the left) and grooves structures (Image on the right). The union of these two structures form the final device (Image on the right). **B)** Two acetate masks with opaque regions in the desired pattern is used to illuminate a light-sensitive photoresist. **D)** Plasma bonding step for permanently bond the PDMS chip to the glass slide. **E)** Optical validation of the correct development of microfluidic channels for subsequent replication in PDMS **F,G)** Master characterization using interferometer and profilometer, respectively. A channel height of around 53µm (first layer) and 44µm for the grooves structures (second layer) were obtained.

4.2.4 Design of 3D printing spiral microfluidic device for CTC separation

According to our previous results, one of the main challenges of using spiral microfluidic devices for CTCs isolation, is the contamination of the sample with leukocytes that have similar size of CTCs. Therefore, with the device previously described in the *chapter 5* is possible to recovered CTCs samples contaminated with larger leukocytes, which range in size from approximately ~12 to 21 µm[162,186]. To address this issue, we proposed designing a second spiral inertial device to capture remaining leukocytes, thus achieving negative enrichment of CTCs sample output recovered. This can be accomplished by using beads coated with antibodies that trap leukocytes expressing the characteristic CD45+ receptor. The size of the beads can be chosen to define the discrimination limit of the device based on the size of the isolated CTCs or cell aggregates. By using this affinity-binding principle, the device can effectively filter out the larger leukocytes, resulting in a more accurate CTC sample for further analysis.

Considering that the separation ratio depends on the height of the channel, the Equation 1 and 2 were used to calculate the separation diameter, as well as, Reynolds number of the particle and fluid were estimated to be equivalent to the values from the previous validated spiral device with 152 µm channel height[186].

$$a_p/\mathrm{D_h} > 0.07$$

Equation 1

$$\mathrm{Re_p} = \mathrm{Re}\frac{a_p^2}{\mathrm{D_h^2}} = \frac{\rho_\mathrm{f}\mathrm{U_m}a_p^2}{\mu\mathrm{D_h}}$$

Equation 2

In these formulas, $\mathrm{D_h}$ represents the hydraulic diameter, and a_p represents the diameter of the particle or "particles+leukocytes", $\mathrm{Re_p}$ is the Reynolds number of the particle, Re is the Reynolds number of the fluid, ρ_f and μ are the fluid density and dynamic viscosity and U_m is the maximum fluid velocity in the channel.

This device was designed in AutoCAD based on the layout shown in Figure 42. The dimensions were set to be fabricated using a 3D printer, where the gap between the channels must be

minimum 500µm for achieving the proper 3D structure , the channel height higher than 520 µm and the channel width 1400µm. Overall, this device is composed by two inputs, including a diluted blood sample previously processes by the spiral device fabricated by standard lithography that allows the depletion of red blood cells and the smaller white blood cells and the second inlet for the PBS1X sheath flow, as well as two outputs, consisting of CTCs and beads + leukocytes. The spiral design enables precise control of flow rate and pressure, allowing for efficient concentration of CTC reducing the leukocytes contamination. By using this cutting-edge microfluidic technology, it could be possible to improve the purification of CTCs from blood samples.

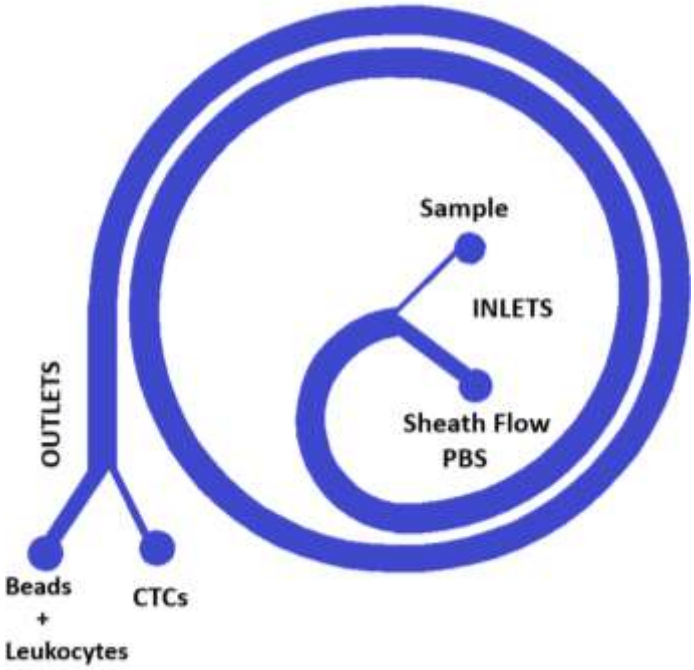

Figure 42. Single spiral device designed in AutoCAD.

Overall, the proposed method consists of having a purified sample of CTCs by using two microfluidic spirals. The CTCs sample obtained from the first spiral device is incubated with 70 µm particles coated with CD45 antibodies. Then, it is introduced through the “sample inlet” port from the second 3D spiral device (Figure 42). Thus, the sample composed by CTCs and particles-anchored leukocytes flows through the spiral, which is subjected to centrifugal forces, and causes the migration of the CTCs towards the outer wall of the spiral while the other components such as particles-anchored leukocytes move towards the center. This separation is then facilitated by the device's two outputs, with the CTCs being directed towards one output while the particles and leukocytes are directed towards the other. This

design could allow to improve the purification process of CTCs from blood samples, which can then be used for various diagnostic and therapeutic applications.

Before fabricating and testing the device a numerical analysis was executed using COMSOL Multiphysics 5.6. The geometry of the spiral channel used in the simulations was created in Auto CAD and imported into COMSOL. The geometry was then extruded for different heights based on the capabilities of the Microlay 3D printer(420 µm, 500 µm, 520 µm, 560 µm), as well as, the custom 3D printer developed in the Nanobioengineering research group at IBEC (550 µm, 600 µm, 700 µm and 800 µm)[256].To simulate how particles behave inside the spiral, the Computational Fluid Dynamics (CFD) module and Particle Tracing module were used. The CFD module enables simulating a continuous flow field inside the device, and the Particle Tracing module was used to solve several discrete trajectories. Hence, the device was utilized to simulate and monitor the actions of CTCs and "Leukocytes+Particles" which is expected to have a total size higher than 70 µm. Hence, the size threshold was ranging from 50 to 60 microns to eliminate bead-trapped leukocytes measuring between 70 µm and 100 µm.

The simulations of the laminar flow demonstrated the Dean Flow effect on a transversal plane as indicated in Figure 43A (Blue line). The in-plane velocity magnitude was plotted in this plane together with the in-plane velocity vectors. As a result, the in-plane vectors indicate two symmetrical recirculating zones in the upper and bottom part of the channel, characteristic of the secondary Dean flow (Figure 43B-E). Figures 10B-E show a comparison of the different channel height considered, meanwhile the sample flow rate was fixed to 700 µL/min and the sheath flow to 6.300 µL/min. The results show that the Dean velocities increase when the cross-sectional area of the channel also increase, leading to a stronger Dean force. This enhanced Dean force leads to more efficient separation of particles, resulting in a higher separation ratio.

After the stationary solution for the flow was obtained, the particles trajectories were calculated in a time-dependent study. The simulations were done considering a one-way coupling between the fluid and the particles. The equilibrium position for each particle was calculated along the microfluidic device, and as explained in previous chapters, it is expected that the balance between the drag and lift force generates different equilibrium position of the particles depending on their size. Thus, the lift force is stronger for the "Particles+leukocytes", meanwhile the CTCs are mainly affected by the drag force, which allows being able to separate them, since they take different outputs in the microfluidic device. The results demonstrated that the optimal channel heights to achieve an efficient separation are between 520 µm to 600 µm (Figure 43D, Table 11).

Height of device (µm)	Separation diameter (µm) by equation 1	Separation diameter (µm) simulated in COMSOL
550	55.3	65
600	58.5	75
700	65.3	90
800	71.3	100

Table 11. Description of Height of spiral devices for separation of beads >50µm

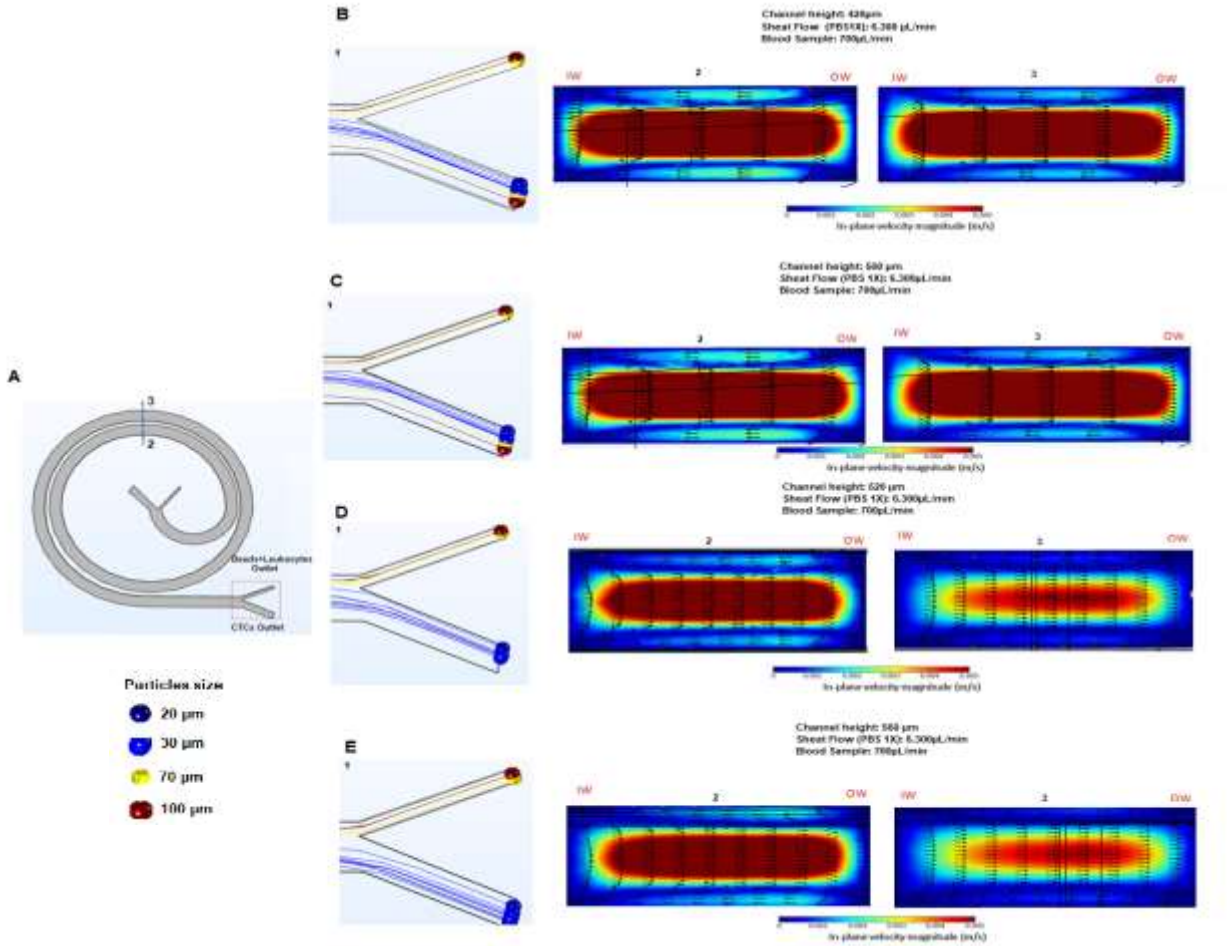

Figure 43. Results obtained in COMSOL. The figure shows a 2D view of a COMSOL simulation of the spiral microfluidic device with particles of different sizes introduced into the system, represented by different colours. The simulation is used to analyse the behaviour of the particles as they flow through the spiral channel. By tracking the trajectories of the particles, the efficiency of the device in separating particles of different sizes can be studied

4.2.5 Fabrication of spiral microfluidic devices molds using 3D printer

The 3D mold was designed in AutoCAD covered the requirements for achieving a suitable 3D printing cast using the commercial 3D printer Microlay (Figure 44A,B). After some tests, it was defined that the minimal gap between the curve microchannels must be 500 µm in order to obtain a proper 3D structure. Moreover, the walls of the cast should be 3mm thick and the height of 5mm (Figure 44A).

The cast mold was fabricated using Solus Art Grey Resin, which traditionally has been designed for miniatures, high resolution prototypes and developed for producing the smoothest surface quality. In overall, once the printing is finished and the 3D mold is removed from the platform, the excess of resin was eliminated using " ResinAway pre-wash, stirring it with a glass rod and after sonicating for 5 minutes. The printed piece was dry with N2 gun and put it under the UV light for 30 minutes.

Once the mold was obtained (Figure 44C), the manufacturing process ended with its silanization which consists of one minute of plasma cleaner at 30 W with constant pressure of 0.8 Torr. After, the activation surface, a drop of Trichloro(1H,1H,2H,2H-perfluorooctyl) silane ($CF_3(CF_2)_5CH_2CH_2SiCl_3$) was deposited on top of a glass slide or a petri dish inside a vacuum desiccator for one hour. Afterwards, to create the PDMS replicas, the 3D printed mold was covered with PDMS with a ratio of 10:1 of curing agent and left on the oven at 85 °C overnight. After unmoulding the PDMS (Figure 44D), the replicas were washed with soap, water, and ethanol, as well as the glass slides which were cleaned with ethanol, acetone, and 2-Propanol. Finally, the cleaned PDMS and glass were activated 30 s with the plasma cleaner at 30 W and pressure of 0.8 Torr, and the two parts were bonded.

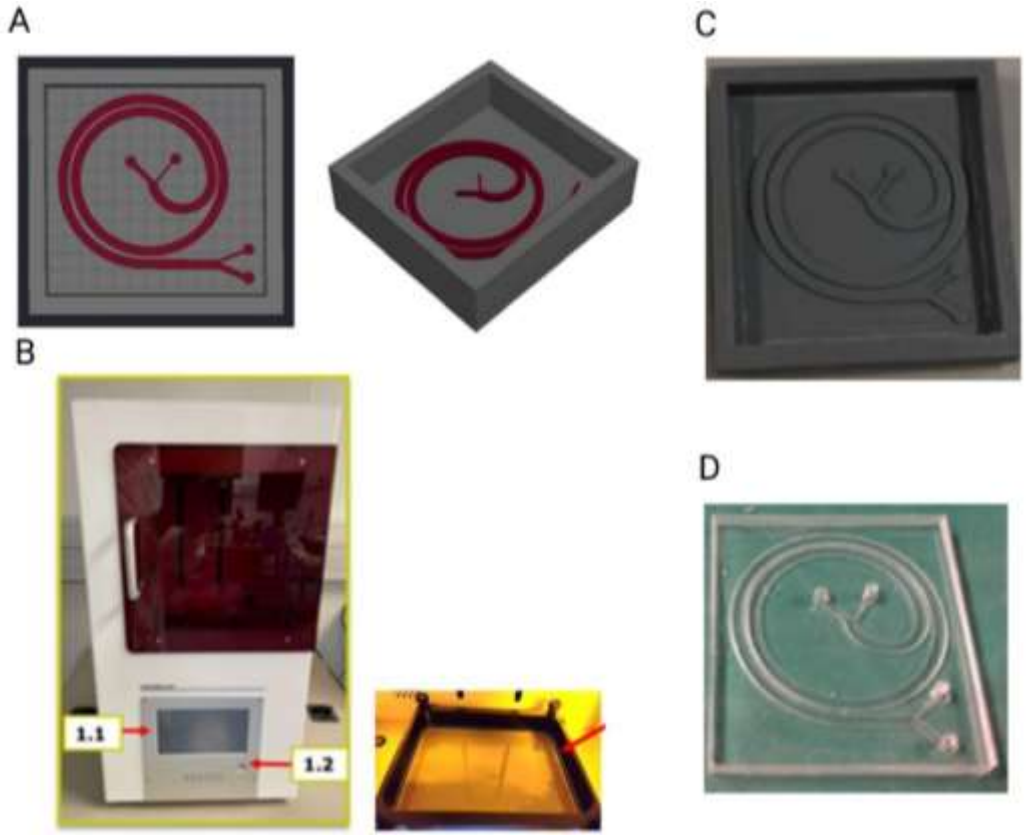

Figure 44. Master fabrication by 3D printing. **A)** Spiral device designed using AutoCAD® and 3D modelling of spiral microfluidic master using AutoCAD®. **B)** Solus DLP 3D Printer printing the spiral master**. C)** Spiral microfluidic master fabricated by 3D printing. **D)** PDMS replica from de 3D printed master.

Chapter 5

Assessment of a microfluidic spiral device for circulating tumour cell isolation based on computational modelling and in-vitro biomodel

As described above, current approaches for isolating CTCs from blood samples are limited due to high blood cell contamination rates, substantial loss of cancer cells, and high-cost methods. To overcome these limitations, microfluidic devices have been designed for isolating CTCs based on their intrinsic properties like density, size, deformability and difference in membrane protein expression [257–259]. The use of microfluidic platforms for CTC enrichment and liquid biopsies presents several advantages such as low cost, portability, they require a significant lower volume of sample and reagents (of the order of microliters) and reduce the human error [260].

On the other hand , to overcome the limitations of affinity-based techniques for positive enrichment of CTCs, hydrodynamic sorting techniques were proposed. They separate the cells according to physical properties, like size and deformability, and present the advantage that no labelling is needed, being able to achieve high throughputs, high purity, and the possibility to culture the isolated CTCs[261,262]. Among them, inertial focusing devices have received a lot of attention as a method for isolating CTCs from blood cells based on the difference of size[138,168,181–183]. Usually, the diameter of CTCs is between 15 µm and 20 µm [263]. On the other hand, the erythrocytes are biconcave discs with average diameter between 6 to 8 µm, meanwhile Leukocytes have a diameter range of 6 – 20 µm whereof 40% to 75% are neutrophils that have a diameter between 10 µm to 12 µm [264].

The inertial microfluidic devices make use of hydrodynamic forces for particle separation such as inertial lift (FL) and Dean drag forces (FD), that arise in microfluidic devices with curved channels. On these devices particles do not follow the fluid streamlines, but migrate across them. Depending on the particle diameter, they achieve different equilibrium positions enabling particle separation [265].

The design of microfluidic systems that allow the separation of cell populations efficiently is a complicated problem to approach analytically. Therefore, numerical simulations can be used as a powerful tool for clarifying particle dynamics inside the microfluidic devices. One of its greatest advantages is the possibility to test different designs before its fabrication, as well as optimize operational parameters as was demonstrated in *"Chapter 4"*.

In this study, we carried out computational fluid dynamics (CFD) simulations of a spiral device based on the finite element method. Several parameters were tested in the simulations in order to optimize the design of the device and the operational conditions for separating CTCs from the blood, like height of the channel and fluid velocity (See *"Chapter 4"*). The computational results were confirmed with experiments in which the spiral device was tested with fluorescent polystyrene microparticles, and blood samples spiked with CTC model cells (MCF-7, H1437, H460 and A549). Other parameters like CTC concentration and blood sample dilution were assessed experimentally.

Our results revealed a high depletion of erythrocytes (99.9%) and leukocytes (80%) and a high enrichment efficiency of CTCs with different sizes (15µm and 20µm) between 80% to 96%. In addition, it was possible to obtain a viable sample of CTCs in solution for subsequent analysis, avoiding the limitations of the only commercial method available and validated by the FDA to isolate CTC based on the expression of EpCAM.. Moreover, the simulations also helped in the design of a device to separate small CTCs, with diameter of 10 mm. The separation efficiency of this device was also validated experimentally.. Contrasting these results with previous studies such as those carried out by Warkiani and colleagues[266,267]. Here we described in detailed how the computational modelling can provide advantageous tools for developing more accurate spiral devices for separating cell target populations based on their size (from 10 µm or 12 µm) and the influence of different variables that have an impact on the device performance such as, the haematocrit level, flow rate parameters, involve intermediate steps during the sample processing like blood lysis. Overall, the use of numerical simulations could pave the way to improve the parameters used in microfluidic systems, reducing time in experiments and costs associated with their development, together with obtaining the optimal efficiency of the device

5.1 Fundamental aspects of inertial focusing and numerical modelling of inertial microfluidic devices

The inertial microfluidics devices operate in an intermediate Reynolds number range, from 1 to approximately 100. In this range, inertial effects start to be relevant, in addition to the viscous effects [260]. A neutrally buoyant rigid particle placed in this device will be transported by the fluid (drag force) and migrate transversally to the direction of the flow due to the effect of two opposed forces: 1) the wall effect lift force, which push the particles away from the wall, and 2) shear-gradient-induced lift force, that direct the particles towards the walls [265,268]. According to the shape of the device there are some equilibrium positions in which the particles are focused. Critical conditions for a particle with diameter a_p to reach the inertial focusing are [269]:

$$a_p/D_h > 0.07$$

Equation 1

and

$$Re_p = Re\frac{a_p^2}{D_h^2} = \frac{\rho_f U_m a_p^2}{\mu D_h}$$

Equation 2

in which D_h the hydraulic diameter, Rep is the Reynolds number of the particle, Re is the Reynolds number of the fluid, ρ_f and μ are the fluid density and dynamic viscosity and U_m is the maximum fluid velocity in the channel.

In devices with curved channels the fluid has recirculation. zones transversally to the direction of the flow, called Dean flow, which is caused by the inertia of the fluid itself. In this devices, the particles' equilibrium positions depend on its size.

The Dean flow can be described by the Dean number.

$$D_e = R_e \sqrt{\frac{D_h}{2r}}$$

Equation 3

in which r is the radius of channel curvature.

If the De < 50, the Dean flow consist of two counter recirculation zones in the transversal direction of the main flow.

In a serpentine or spiral channel, the curvature induces a shear gradient lift force, directing the particles away from the centre of the channel. As the particles move towards the wall, they also experience a wall-induced lift force, which repels the particles from the walls. The lift forces and the Drag forces act upon the particles making them reach an equilibrium position when the opposite forces cancel out each other [265,269].

Drag force in the Stokes regime is given by the equation:

$$\mathrm{F_D} = 3\pi\mu a_p(\mathrm{u} - u_p)$$

Equation 4

in which u is the fluid velocity, and u_p is the particle velocity.

The lift force can be calculated by

$$F_L = \frac{f_L\,(R_e x_p)\rho U_F^2\, a_p^4}{D_h^2}$$

Equation 5

In which f_L is the lift coefficient that correspond to a complex function of the Re and the cross-sectional positions of particles x_p and U_F is the average velocity of the fluid.

The ratio between lift force and Drag force has a third power dependence with the particle's diameter $\left({F_L}/{F_D}\;\alpha\; a_p^3\right)$. Then, bigger particles are more prone to focusing than the smaller

ones at same Re[183]. The small particles follow the Dean flow while big particles are under a stronger lift force. The result is that particles move to different equilibrium positions according to its diameter[265].

There is not a single formula for the lift coefficient that is applied for all conditions. Among the inertial forces' models proposed, the Saffman lift force showed that spherical particles moving in a viscous liquid would suffer a lift force perpendicular to its rotational and translational velocity vectors. The result is that if the particle had a smaller velocity than the fluid, it would be pushed towards the channel central line. Meanwhile, If the particle had a bigger velocity than the fluid it would be directed towards the walls [270]. Furthermore, Asmolov proposed a model for lateral migration of particles in a 2D confined flow in a wide range of Re. This model considers a lift coefficient that depends on Re and on the particle lateral position [271]. Later, the model was expanded for 3D flow[272].

Among the most used commercial CFD software COMSOL Multiphysics is the only one that provides a formula for calculating the inertial forces. It is important to consider that this formula is not accurate for all conditions[273]. Thus, the inertial lift force is calculated based on equation proposed by Ho and Leal[274].

$$F_L = \rho \frac{r_p^4}{D^2} \beta \left(\beta G_1(s) + \gamma G_2(s)\right) n$$

Equation 6

$$\beta = \left| D(n \cdot \nabla) u_p \right|$$

Equation 7

$$\gamma = \left| \frac{D^2}{2} (n \cdot \nabla)^2 u_p \right|$$

Equation 8

$$u_p = (I - (n * n))u$$

Equation 9

in which I is the identity matrix, n (dimensionless) is the wall normal at the nearest point on the reference wall, D is the distance between the channel walls, s is the normalized distance from the particle to the reference wall, G1 and G2 are dimensionless functions of the normalized wall distance

5.2 Experiment with fluorescent polystyrene particles of different sizes (Experiment 1)

As a first assessment of the separation efficiency of the spiral device, we developed experiments with an inlet sample that consisted of PBS spiked with fluorescent particles of 6 µm and 10 µm as blood cell models (erythrocytes and leukocytes), and particles of 15 µm and 20 µm as CTCs model. The concentration of these particles was selected to represent a blood sample diluted 10x. The conditions in this experiment are equivalent to the assumptions made for the simulations: a Newtonian fluid spiked with rigid and spherical particles that do not deform. The same flow rates simulated for the sheath flow (PBS 1X) were tested (300 µL/min, 500 µL/min, 700 µL/min and 900 µL/min) and the flow rate for the particles sample was fixed to 100 µL/min. The particle trajectories inside the chip were analysed by fluorescence microscopy FACS and compared with the simulations in COMSOL Multiphysics® (Appendix D-Supplementary Figure 53, Figure 48B). There is a good agreement between the simulations and the experiment, confirming that the condition for a higher isolation of CTCs (15 and 20 mm particles) and a higher depletion of particles smaller than 10 um is the one with sheath flow rate of 900 uL/min (Fig 48). The results obtained by Flow Cytometry demonstrated that, in this condition, 93±1% of the particles of 6 µm and 77±5% of particles of 10 µm are collected in the waste outlet, which would correspond to a high depletion of blood cells, Meanwhile, particles of 15 µm and 20 µm, representing the CTCs, would be isolated on the CTCs outlet with an efficiency of 94±1% and 96±4%, respectively (Appendix D-Supplementary Figure 54).

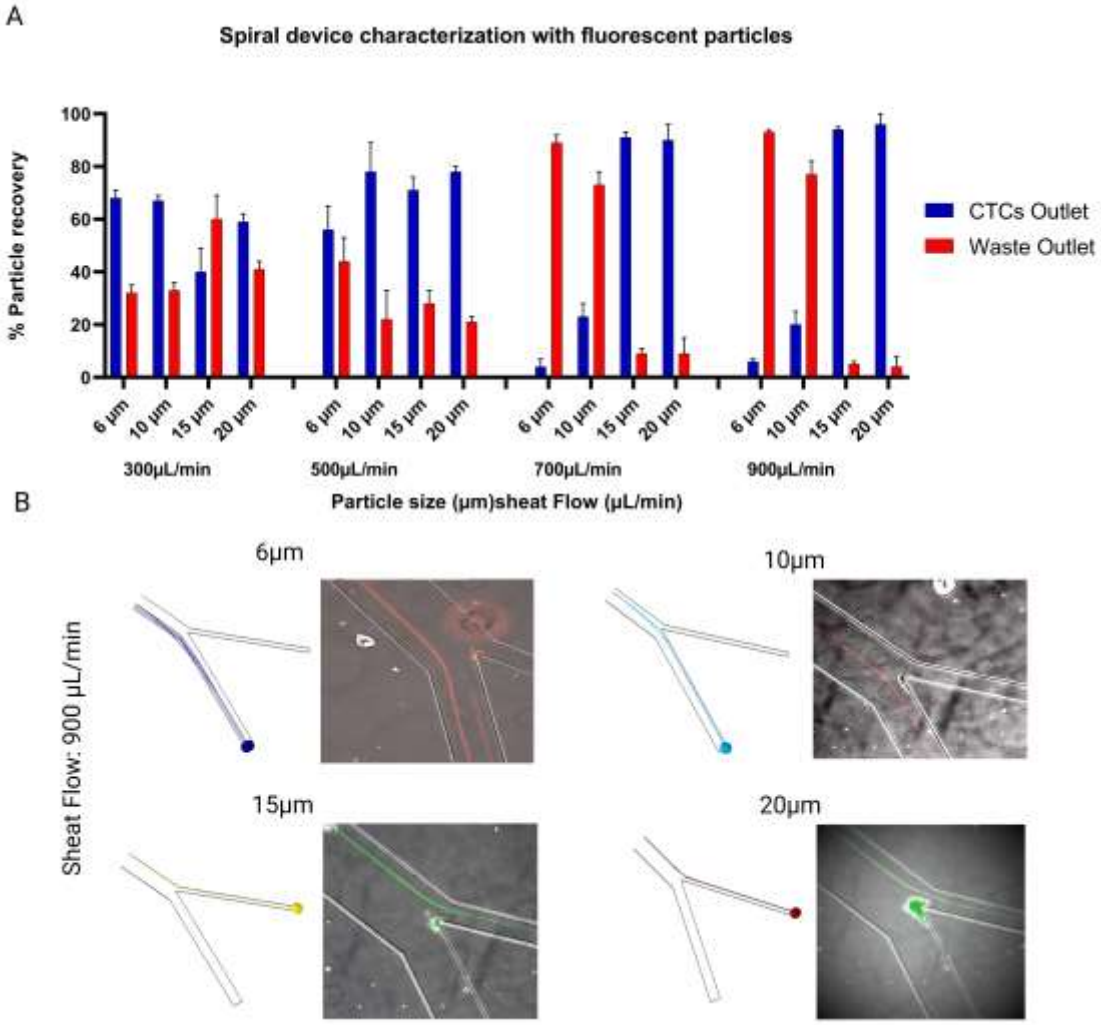

Figure 45. Spiral device characterization with fluorescent particles of 6 µm and 10 µm as Erythrocytes and Leukocytes models respectively; and particles of 15 µm and 20 µm as CTCs models. **A)** Histogram plot indicating the polystyrene particles recovered in the CTCs output and Waste output to four different sheat flow rates :300 µL/min, 500 µL/min, 700 µL/min and 900 µL/min, where the sample flow rate was fixed at 100 µL/min. **B)** Comparison of the particles trajectories in the chip output between the simulations in COMSOL Multiphysics® (left images) and experiments perform with polystyrene fluorescent particles of different sizes (6µm,10µm,15µm,20µm)(right images). Scale bar 100.Values and error bars represent mean ± S.E.M (n = 3).

5.3 Effect of blood concentration on cell focusing (Experiment 2)

When feeding a sample of whole blood in this kind of device, the intense cell-cell interactions could pose problems on its separation efficiency, a part of the non-Newtonian rheology properties of blood such as deformation-rate dependency, viscoelasticity and yield stress [275]. Therefore, the dilution of blood represents an alternative step for achieving high separation rates. To determine the effect of blood concentration on focusing and high depletion rates of blood cells, as well as high recovery of CTCs, we first carried out experiments with blood samples from healthy donors diluted 2.5X and 10X in PBS spiked with 30 µm-diameter particles as CTCs model (Figure 49E-L).

First, we verified that the device performs well also with whole blood samples. The images acquired indicate that with sample inlet of 100 µL/min and sheath flow rate of 900 µL/min, most blood cells are directed towards the waste outlet and particles of 30 µL towards the CTC outlet. Images were taken in different locations of the device, in which was possible to see the focalization of the blood cells. They are first push by the sheath flow towards the outer wall, then smaller blood cells migrate along with the Dean vortices towards the inner wall, and back to the outer wall, where they exit (Figure 49A-D).

The experiment was done for three different flow rates of PBS 1X (200 µL/min, 700 µL/min, 900 µL/min) and the flow rate for the blood sample was fixed to 100 µL/min (Figures 49E-J). The conditions were analysed qualitatively using a speed camera and considering the correct focusing of most blood cells in the outer wall and the recovery of CTCs (30 µm particles) in the inner wall (Figure 49K,L), for a sheath flow rate of 900 µL/min.

The images acquired revealed that the width of the focused blood is wider when the concentration of blood increase. Figure 49J shows how our spiral microfluidic channel can focus almost all the blood cells (erythrocytes and leukocytes) into a narrow stream near the outer wall when the inlet sample is more diluted (10X). Meanwhile, Figures 49 E,F,J,H and I show the processing capacity of our device or saturation limit. With a sample diluted 2.5x ,the wide cell stream start to increase until fulfil the entire outer outlet and part of the inner outlet, demonstrating an unsatisfactory focusing. This phenomenon happens because the increase in concentration reflects in more cells that tend to migrate towards the same equilibrium position, which increase the cell-to-cell interaction and finally results in the sample defocusing.

Moreover, the results demonstrated the influence of the flow rates in achieve the best separation efficiency, since the cells are affected by the inertial lift force (F_L) and dean drag force (F_D), and as a consequence the cells migrate towards the varied lateral equilibrium

positions according to the employed flow rates. Thus, the cells were not fully focused due to the weak FL and FD under flow rates of 200 µL/min for PBS 1X ,and 100 µL/min for blood sample (Figure 49 E,H). Besides, the increased flow rates up to 700 µL/min was translated in a significant improvement of the focusing performance, and most of the blood cells were detected towards the outer output. However, there was a small amount of blood cells entering in the inner output (Figures 49F,I). Finally, Figure 49J revealed that the best condition for achieving a high focusing performance, reducing the amount of blood cells in the inner output correspond to a flow rate of 900 µL/min for the PBS 1X, and a diluted blood samples 10X under a flow rate of 100 µL/min.

Previous studies demonstrated how the extremely high cell concentration of undiluted blood make the cell separation impossible caused by the intense cell-cell interactions[276] .Moreover, the relatively high viscosity of undiluted blood would increase the difficulty of sample transportation and introduction. Despite, a higher degree of dilution would lead to better separation, this results in an increase of processing time[276] . Di Huang and colleagues reported a dilution of blood 100x in their experimental characterization and a throughput of 400 µL/min. In contrast, our study demonstrated that extremely higher dilution is not necessary to achieve optimal results, since a blood dilution of 10x lead a proper cell separation and blood cells depletion with a throughput of 100µL/min. Finally, our findings are consistent with the previous work of Bo-Wen Li et al, where 4% of haematocrit (10 fold dilution) was required for guarantee a correct cell distribution in the channel, and in consequence a higher cancer cell recovery and blood cells depletion rates[277]

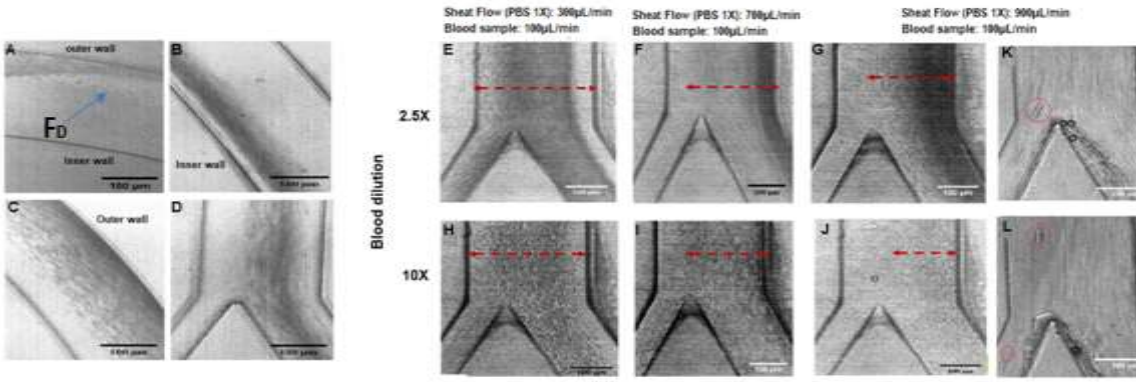

Figure 46. Principle of CTC isolation using spiral microfluidic device with polystyrene particles of 30µm. **A)** Once the blood sample and the PBS 1X were pumped through the outer and inner inlets of the spiral device, the influence of Dean drag forces (FD (blue arrow)) starts to appear (A). Subsequently, the erythrocytes migrate along with the Dean vortices across the inner wall **(B),** and back to the outer wall again **(C, D).** The 30 µm-diameter particles experience an additional inertial lift force and keep them along the inner wall, thus the separation is achieved **(K,L). (E-L)** Optimization of conditions for the best focalization of blood cells across the inner wall. The blood sample was diluted 2.5 and 10 times. Three different sheat flow rates were tested (300 µL/min(E,H), 700 µL/min(F,I) and 900 µL/min **(G,J)** with a blood sample flow rate fixed to 100 µL/min. The best blood focalization effect was achieved under a sheat flow rate of 900 µL/min **(K,L).**

5.4 Device validation with human blood spiked with breast cancer and non-small-cell lung cancer cells as CTCs model (Experiment 3)

Since the separation of CTCs continues to be a challenge, given the limitations of the existing methods, from not considering the heterogeneity of the CTCs, the impossibility of processing large volumes of blood, loss of viable CTCs, among others, it is crucial to isolate the maximum number of cancer cells in blood. Thus, we tested the spiral device with diluted blood sample spiked with cells of different sizes such as MCF-7 (20µm), A549 (15 µm) and H1437 (15.7 µm) in a concentration of $1*10^4$ cells/mL (final concentration in diluted sample: $1*10^3$ cells/mL). The results were analysed by flow cytometry (Supplementary figure 5) and demonstrated a recovery of the CTCs of 93.7±8.6%, 92.9±9.8% and 96.7±3% for MCF-7, A549 and H1437 cells, respectively, with a sheath flow rate of 900µL/ min (Figure 50A). The trajectory of the cells at the chip output was verified by image (Figures 50D). Moreover, it was achieved a high erythrocytes' and leukocytes depletion (99.9±0.01% and 84±1.87% respectively) under a sheat flow 900 µL/min (Figure 50B).

As mentioned previously it is crucial to isolate the maximum number of CTCs for downstream assays due to their low concentration in real blood sample from cancer patient (1-100 CTCs). Therefore, the device was tested for isolating CTCs with a lower concentration in a diluted sample (final concentration of 100 cells/mL and 10 cells/mL). The results revealed that the separation efficiency was 97.70±2.9%, 86.7±1.2% and 92.5±4.8% for MCF-7, A549 and H1437 cells respectively in a samples with 100 CTCs/mL (Figure 3C). Furthermore, 80.25±12.6%, 71.5±1.3% and 85.9±7.0% of MCF-7, A549 and H1437 cells were recovered in a sample spiked with 10 CTCs/mL (Figure 3C). Overall, these results indicated a high recovery rates of cancer cells with different size regardless the expression levels of EpCAM. Furthermore, we confirmed the optimal flow rates for achieving a high depletion rates of blood cells (PBS 1X: 900 µL/min and blood sample: 100 µL/min).

Consistent with the literature, there are three distinct advantages of the spiral devices that make it beneficial for clinical and research objectives: 1) The CTCs collected are in suspension and not immobilized on the chip surfaces like in others positive enrichment methods, which facilitate the downstream manipulation and analysis. 2) The platform could be potentially more sensitive than competing immune-based platforms since the CTC isolation is tumour antigen-independent. 3) Relative high purity in the enrichment samples, enable a leukocytes depletion up to 4log[187,278] . Thus, the high specificity of our CTCs isolation device could allow greater accuracy during genome sequencing and mapping. 4) This study demonstrated that could be possible separate small CTCs (<12µm) implemented modifications in the channel dimensions. In fact, this could open new perspectives for the implementation of a system of depletion of blood cells and recovery of CTCS in a sequential way that contains spirals with different channel ratios.

The findings exposed in this study broadly supports the work of other studies performed by Warkiani et al [267], who based on FACS analysis of the samples recovered from the spiral microfluidic device, reported a high cancer cell recovery (>85%), enrichment ratio of 10^9 fold (over RBCs) ,10^3 fold (over leukocytes) and high cell viability (98%) [278] .In contrast, our findings reveal an improvement in the throughput (6ml/hr) compared to the of 3mL/hr reported by them. Thus, we successfully introduced a high throughput blood separation method based on ‘‘Dean Flow Fractionation (DFF)’’, where the use of an additional sheath buffer in our spiral device facilitates the Dean migration of RBCs in a controlled manner under a haematocrit of 4%, which differs from other reported to be 20-25%[266] .

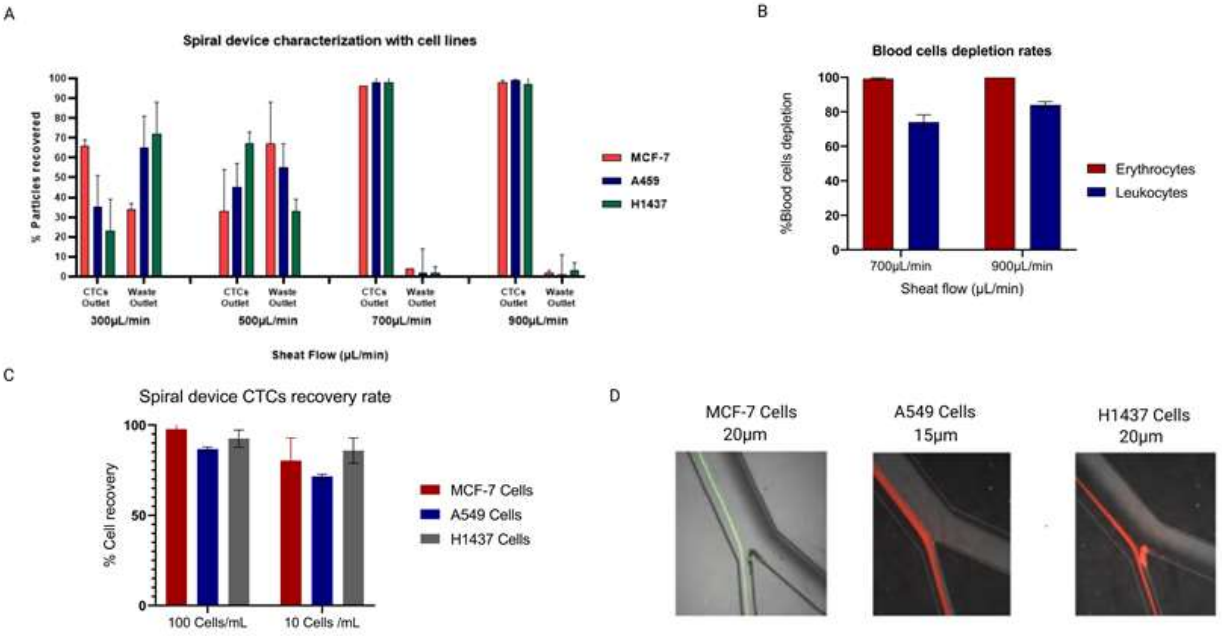

Figure 47. Validation of CTCs isolation using the spiral microfluidic device with breast and lung cancer cells. **A)** Histogram plot indicating a high cell separation efficiency >90% with a sheat flow rate of 900µL/min in a diluted blood sample 10X spiked with a final concentration of $1*10^3$ cells/Ml of MCF-7, A459 and H1437 cell lines. Values and error bars represent mean ± S.E.M (n=3). **B)** Histogram plot indicates the depletion of Erythrocytes of 99.1 ±0.49% and 99.9 ± 0.01% under a sheat flow of 700 µL/min and 900 µL/min. Depletion of leukocytes of 74± 4.30% and 84±1.87% under sheat flow of 700 µL/min and 900 µL/min. Values and error bars represent mean ± S.E.M (n=3). **C)** Cell separation efficiency around 92.5±2.9%, 86.7±1.2% and 95.5±4.8% for diluted blood sample 10X spiked with $1*10^2$ cells /Ml. The recovery rate in samples with a final concentration of 10 CTCs/mL was 80.25 ±12.6%, 71.5±1.3% and 85.9±7% for MCF-7, A549 and H1437 cells respectively. Values and error bars represent mean ± S.E.M (n=3). **D)** The correct targeting of blood cells and the recovery of CTCs models (MCF-7, A549 and H1437 cells) were verified by microscopy.

5.5 Device validation with lysed human blood spiked with breast cancer and non-small-lung cancer cells as CTCs model (Experiment 4)

With the purpose of improving yield, target cell purity, throughput and facilitate the sample analysis by flow cytometry, we modified the method for blood sample processing including a lysis step before passing the sample for our device. This cell lysis pre-treatment step reduces the number of erythrocytes, therefore is possible to reduce the cell dispersion caused by the cell-cell interaction. A major advantage of this method is the possibility of processing more blood volume in less time.

To validate this method, we performed a cell viability test, to know the effect of lysis on the viability of our target cell population (CTCs model). It is fundamental to guarantee the cell viability of CTCs, as it could allow to perform models like organoids for drug screening in personalized therapies. The cell viability was evaluated in flow cytometry with Zombie Violet which is an amine-reactive fluorescent dye permeant to the cells with compromised membranes. Supplementary Figures 4C show in quadrant Q2 the dead cell population from MCF-7 cells without lysis and dyed membrane. Meanwhile, Figure 51D shows the MCF-7 cells dead in quadrant Q2 after lysis and combined with blood in Figure 51E. Overall, these results indicate a cell death (CTCs model) of around 3% regarding the negative controls (Figure 51A). Therefore we could consider that lysis procedure does not affect cell viability (cell viability ~90%-95%).This finding is consistent with that of Warkiani et al , who reported the collection of viable CTCs, allowing downstream studies assays including cells culture[279]

The lysed blood sample spiked with MCF-7 and A549 was processed on the device without any dilution. It is important to note that with the whole blood lysis procedure, 86.7±1.04% of red blood cells are eliminated, which reduces contamination in the CTCs output sample and avoids making dilutions of the initial sample (Figure 51 B,C,F). The recovery obtained was 86.0±4% for A549 and 89.6±3.1% for MCF-7 cells (initial concentration of 10^4 cells/mL in the sample). In addition, the depletion of erythrocytes was around 99.99±0.001% for a lysed blood sample. This level of depletion is equivalent to the depletion of erythrocytes for an inlet sample of whole blood diluted 10X. It was also found that 86.79±1.04 % of leukocytes were removed from the samples.

Nonetheless, our system displays some limitations since in the operation of the spiral the sheath fluid that is used for influencing the particle focusing, creates a larger collection of volume to the chip outlet. Despite, that the throughput can be improved if the blood sample is lysed instead of diluted, our results revealed a reduction of 7% and 4% of the A549 and MCF-7 cancer cells isolated from lysed sample compared with a diluted sample (Figure 51B). A possible explanation for this might be related with the extra centrifugation steps required during the lysis process, which can influence the loss of the target population. These results are consistent with the total cell loss due to lysis and centrifugation reported by Warkani et al (8%)[278,279] . Despite the loss of cancer cells, there is a slight improvement in leukocyte depletion of 3% when the blood sample is lysed compared to the diluted sample (Figure 51D).

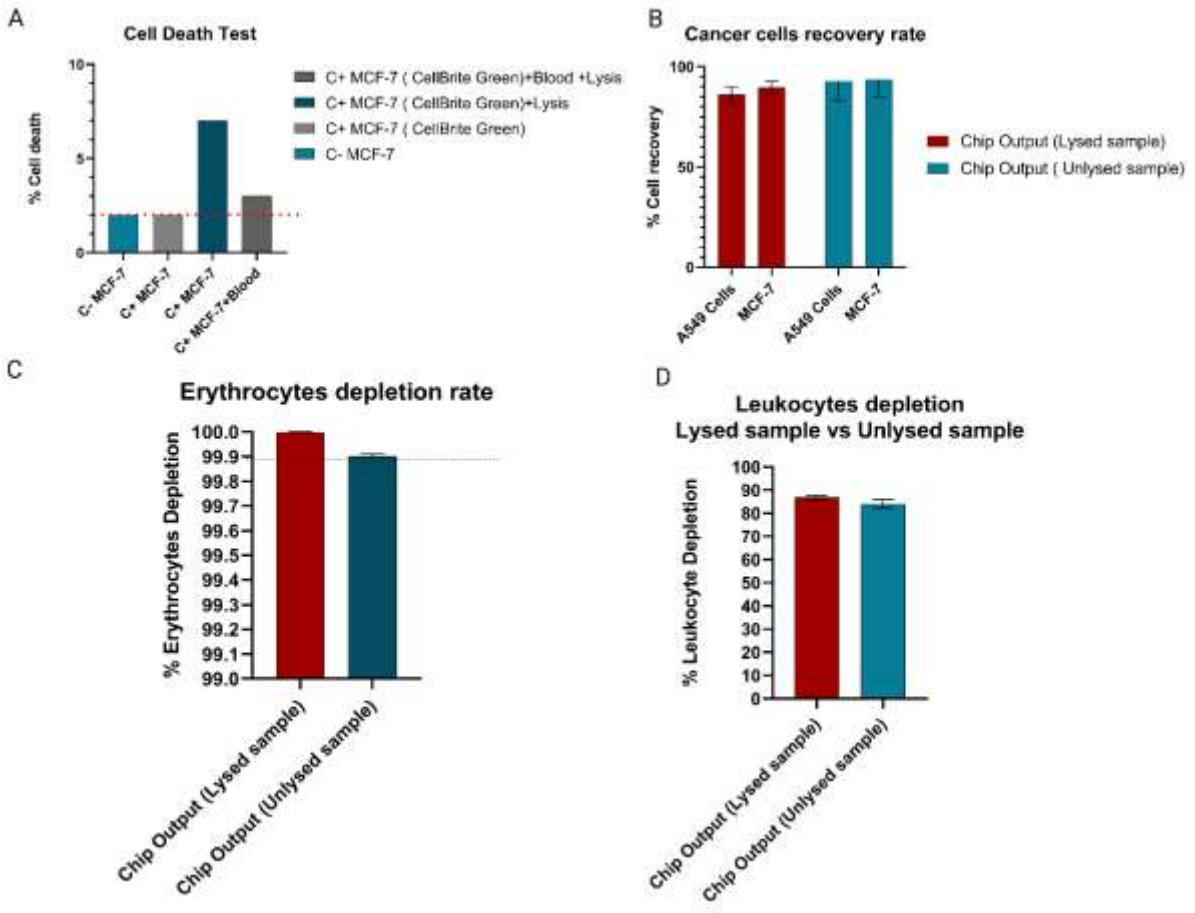

Figure 48. A) Cell viability test after blood lysis. Histogram plot shows a cell death less than 7% in all conditions. The first two bars (blue and gray) represent cell death (~2%) of the samples considered as a negative control without lysis (MCF-7 cells unlabelled and stained with CellBrite Green). The blue bar shows the cell death of MCF-7 cells after lysis (~7%), this mortality is reduced when combined with the blood sample (~3%) (dark blue bar). **B)** Cancer cells recovery rate from blood samples lysed vs unlysed (diluted 10X) processed through the spiral microfluidic device. A549 cancer cells 86±4% vs 92.9 ±9.8%, MCF-7 cancer cells 89.6±3.1% vs 93.7±8.6%. **C)** Erythrocytes depletion rate from lysed vs unlysed blood samples processed through spiral microfluidic devices. 99.999±0.001% vs 99.9±0.001%. D). Leukocytes depletion from lysed vs unlysed samples processed through spiral microfluidic devices. 86.79±1.4 vs 84±1.87%. For all the figures values and error bars represent mean ± S.E.M (n = 3).

Thus, it was possible to fabricate a spiral microfluidic device with a channel height of 140 µm. A sample of whole blood diluted 10x and spiked with fluorescent polystyrene particles of 10 µm was processed on the device. These particles were successfully recovered in the CTC outlet, while in the previous 152 µm device they would go to the waste outlet) (Figure 52). For the device of 140 µm height there is a trade off in terms of isolation of small CTCs and

contamination level of the outlet sample, due to the intrinsic principle of separation by size and the overlap between small CTCs and leukocytes .

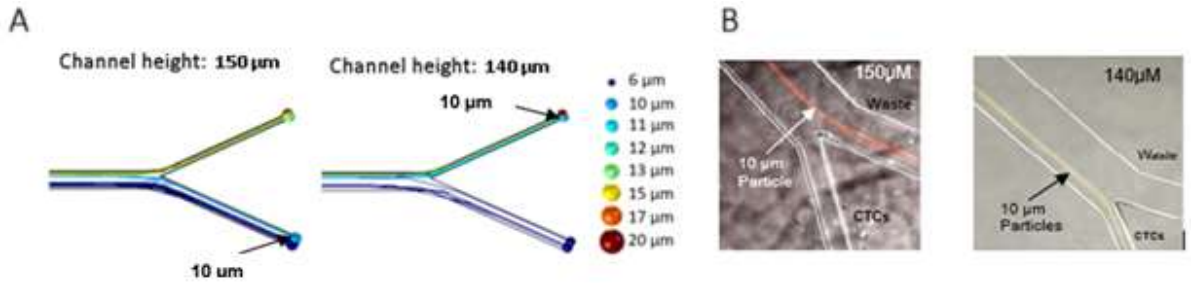

Figure 49. A) Comparison of Numerical modelling between spiral microfluidic device with a channel height of 150µm vs 140µm for the isolation of small CTCs (10µm). **B)** Separation of 10 µm Fluorescent particles in a microfluidic spiral device with a channel height of 150 µm vs 140µm.

5.6 Discussion

This study provides a comprehensive assessment of Inertial separation of Circulating tumor cells (CTCs) from leukocytes and erythrocytes in a spiral microchannel. The use of this device displays a big potential as a label free isolation method with a high CTC recovery rate (>80%) and high blood cells depletion (99.9±0.01% and 84±1.87% respectively). In this study the trajectories of different size particles determined by numerical simulation in COMSOL MULTIPHYSICS were successfully compared and validated with images obtained with a microscope in an experimental set up using fluorescent beads with different sizes as CTCs and blood cells (6 µm, 10 µm, 15 µm and 20 µm). Moreover, the computational model was validated by experiments with blood samples from healthy donors spiked with breast cancer (MCF-7, 20µm) and different non-small lung cancer cells (A549 and H1437 cells).

Different simulations were done to optimize the operational conditions and the channel height according to the desired cut size of CTCs. The sheath flow rate's effect was also evaluated experimentally, confirming the results from the simulations. They revealed a higher CTCs recovery rate (of around 93.7±8.6%, 92.9±9.8% and 96.7±3% for MCF-7 (20µm), A549 (15 µm) and H1437 (15.7 µm) cells, respectively) under flow rates of 900 µL/min for PBS 1X and 100 µL/min from 10x diluted sample. Moreover, the experiments with fluorescent particles of 15 µm and 20 µm as the CTCs model demonstrated high recovery rates of 94% and 96%, which is similar to the rates obtained with cancer cells. In contrast, a high throughput could be achieve including a blood lysis as a previous step to the separation in the spiral microfluidic device. Nevertheless, this leads to losing up to 7% of the target cancer cells, which could be compensated by an increase in leukocyte depletion.

Finally, we demonstrated how the computational modelling of spiral microfluidic devices for CTCs separation could be applied to define the best geometry of the device and operational conditions to achieve the highest efficiency depending on the target cell population. In addition, this device could be used to isolate even small CTCs that do not express EpCAM, and otherwise could not be separated in CTC label-dependent commercial approaches.

Chapter 6

Enrichment of circulating tumor cells in liquid biopsies using an enhanced Herringbone chip

In recent years, several microfluidic devices have been developed for isolating CTCs from blood based on their difference on size, deformability, dielectrophoresis, affinity chromatography and magnetic forces[280,281]. In fact, one of the most effective system for CTCs separation is based on affinity techniques which can be used as a positive enrichment, when antibodies are used to capture CTCs, or negative enrichment, if antibodies are used for targeting blood cells[280,282]

Negative enrichment display some advantages over the traditional cell purification methods such as efficient processing of complex fluids, minimal damage of target cells as well as the potential to support live cells [147,282,283]. The negative enrichment method is used to capture leukocytes subsequent to blood lysis, in which the erythrocytes are previously eliminated. One of the devices reported was the herringbone-chip, whose principle of operation is based on promoting a chaotic mixing at low Reynolds number (Re) ($0<Re<100$)[284] through microstructures that can disrupt the streamlines of the laminar flow. Consequently, there is greater cell-surface interaction with the anchored antibody in the chip surface[80,163].

Traditionally, the surface of microfluidic devices have been functionalized with avidin or engineered avidin such as streptavidin, neutravidin or nitrividin, and a biotinylated antibody specific for the target cells[285,286]. However, this kind of surface modification has some drawbacks, in particular its variable affinity, which affect the sensitivity and reproducibility due to non-specific binding[287]. In order to overcome this limitation, self-assembled monolayer (SAM) has been used to allow more stability and controllable surface immobilization[288]. SAM immobilization facilitates building block surfaces with advantageous characteristics such as the attachment of molecules through covalent bonding [289],

spontaneous formation by the immersion of the substrate in a solution containing the precursor molecules, stability enhancement , and high binding strength[290,291] . Moreover, the incorporation of Poly-Ethylene Glycol (PEG) chains into SAM reduces or eliminates the non-specific absorption of proteins[292] and lowered the background. The steric hindrance on the cell attachment could be reduced with the use of spacers with a surface-attaching head group and a protein-binding tail group [293] .

Our work is focused on the negative enrichment of CTCs, based on the affinity binding principle. This device should be used as a second stage in the CTCs purification, for instance after lysis or erythrocyte depletion using another type of microfluidic device. In the proposed platform we delve in the development and characterization of a SAM that aims to overcome some limitation of traditional surface modification. Cell models were used for recapitulating the main features of CTCs and leukocytes in the characterization of the microfluidic device.

Figure 55 shows a schematic of the experimental microfluidic setup connected to the micro vortex chip which is composed by a syringe pump that allows dispensing the sample in 4 chips simultaneously using 1 mL syringes at the flow rate parameters optimized in the simulation (20µL/min) (Figure 1 (1) and (2)). The glass and PDMS are chemically modified by a mix-self assembly monolayer (SAM) composed by silane-PEG-Biotin, Silane-PEG-OH, Neutravidin and a biotinylated antibody CD45 (Figure 55 (3)). The samples in the outputs are collected in Eppendorf and quantified by FACS (Figure 55 (4)).

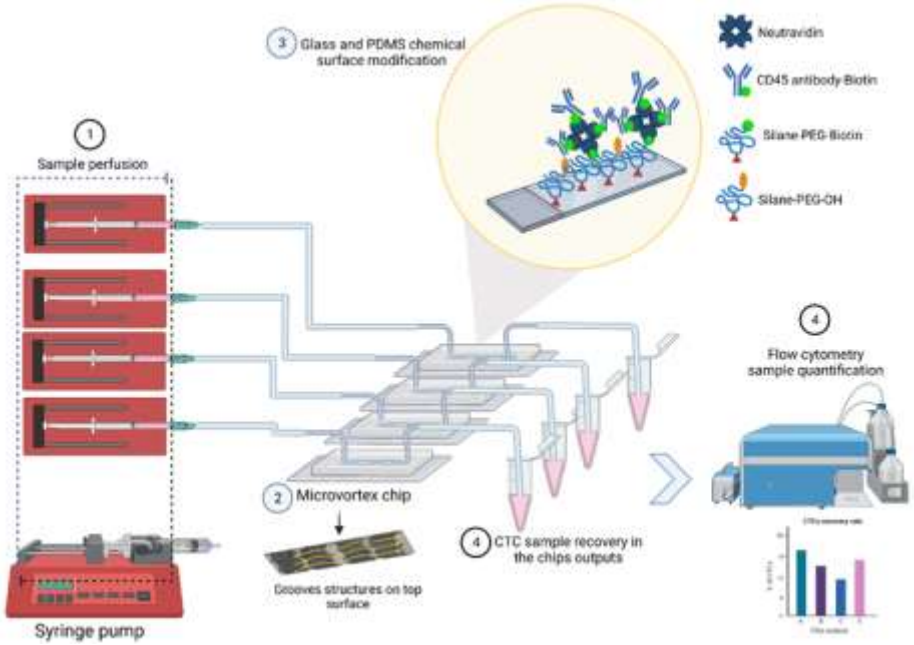

Figure 50. Microfluidic setup for purifying CTCs from blood samples with a micro vortex microfluidic chip. (1) Connection of syringe pump and perfusion of blood samples in 4 chips at the same time (2)

schematic representation of grooves structures on top of the chip which allow localized mixing of the sample (3) Glass and PDMS surface modify with a mix-SAM (4) The CTCs sample is recovered in the chips outputs and quantify by FACs (4)

6.1 Cell line models for Herringbone characterization

To demonstrate the efficiency of the herringbone chip for catching Leukocytes (CD45+ cells), we first select two cell models that mimic the Leukocytes and CTCs, respectively. The cell line considered as leukocyte model was selected based on key features such as a high and stable expression of CD45 (common membrane protein in leukocytes), non-adherent cells characteristics and similar diameter as leukocytes; ~20 µm. Based on previous literature report we select and verified the CD45 expression levels in different cell lines by flow cytometry (J45_01_P1 (passage 1), J45_01_P5 (passage 5), Su-DHL-4, Kasumi-1 and MCF-7 as a negative control). The results revealed that Kasumi-1 cell line display a stable and high expression level of CD45 (Figure 56A,C.Appendix E-Supplementary Figure 61). Furthermore, CD45 expression levels in Kasumi-1 cells were also validated by western blot (Figure 56B).

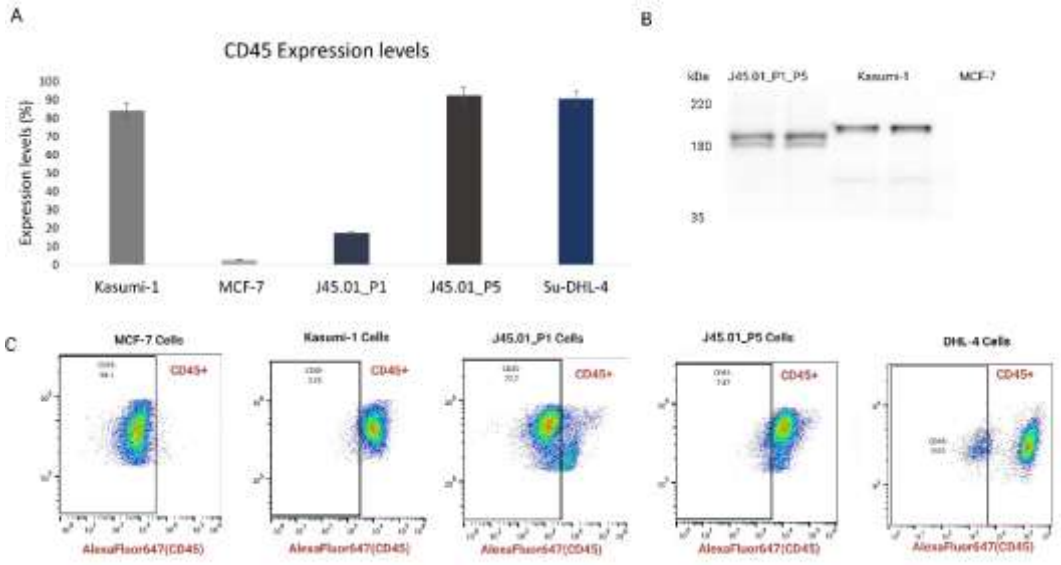

Figure 51. Validation of CTCs and Leukocyte cell models. **A)** The histogram plot shows the expression levels of CD45 in Kasumi-1, J45.01_P1, J45.P5 and Su-DHL-4 cells verified by Flow cytometry, the MCF-7 cells were considered as a negative control. **B)** Western Blot of CD45 expression levels in Kasumi-1 cells. MCF-7 cells were considered as a negative control. protein molecular weights are indicated on the left of the graph**. C)** Flow cytometry analysis shows low expression levels of CD45 in MCF-7 and J45.01_P1; high expression levels of CD45 in Kasumi-1, and J45.01_P5 cell lines. A clear subpopulation of negative CD45 is also observed in the SU-DHL-4 cell line. All samples were incubated with AlexaFluor647 CD45

On the other hand, the CTCs cells model was selected based on their size (~20 µm), and also in the absence of CD45-(negative), and non-adherent cells characteristics. Thus, we used a widely reported cell model based on the formation of multicellular tumor spheroid by the cyclo-rgDfK(TPP) peptide [294,295]. The addition of this peptide to a monolayer culture cause the self-assembly into loose cell aggregates through interaction with alpha-5 beta-1 integrins. Then, the tumor spheroids are disgregated into single cells to perform the experiments.

In addition, we tested the toxicity of cyclo-rgDfK(TPP) peptide in the MCF-7 cells through an annexin V/ propidium iodide apoptosis assay (Figure 57 A,B). The results revealed a cell death between 15% to 20% at 24 h of incubation with different peptide concentrations (5 µM , 10 µM ,20, µM ,30 µM , 40 µM) (Figure 57 A,B).Subsequently, we decided to reduce the peptide concentrations and incubation times, observing a cell death around 7% in all conditions. Considering the results, the suitable CTC model for validating the Herringbone chip and the integrated final microfluidic platform correspond to the MCF-7(5µM-cyclo-rgDfK(TPP)) cells with the peptide incubation for 2h (Figure 57 C,D, Appendix E-Supplemented Figure 62)

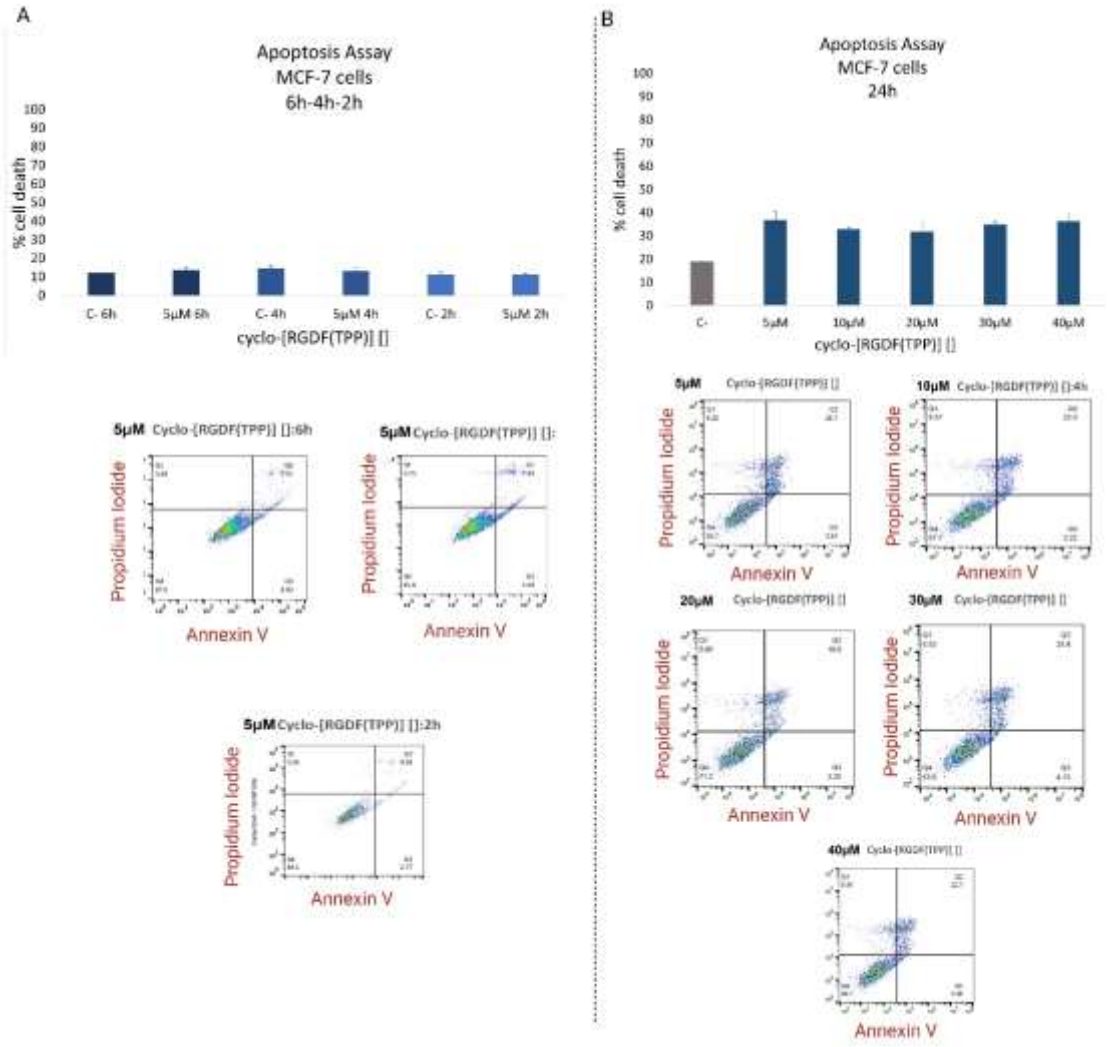

Figure 52. Cell models for Herringbone Characterization. A) CTC model based on multicellular tumor spheroid by the cyclo-rgDfK(TPP) peptide. Quantification of cell death by Annexin V/Propidium Iodide apoptosis assay. The histogram plot shows the cell death caused by different concentrations of cyclo-rgDfK(TPP) incubated for 24h around 15% to 20% regarding the negative control. C) The histogram plot the cell death caused by 5 µM of cyclo-rgDfK(TPP) incubated during 6h,4h and 2h. (B-D) Flow cytometry results of Annexin V/Propidium Iodide apoptosis assay with different concentrations of cyclo-rgDfK(TPP) and incubation times. The images show the expression level of Annexin (X axis) increasing for early apoptotic stage and Propidium Iodide (Y axis) increasing for Necrotic cells. When these two markers are increasing, the expression levels represent the cells in the late apoptotic stage. Thus, cells located in LC area represent the living cells, the EA, LA and NC areas correspond to cells entering in early apoptosis, late apoptosis and Necrotic cells, respectively.

6.2 Characterization of Self-assembled monolayers (SAM) for capture Leukocytes(CD45+):

The CTCs enrichment through a Herringbone device is based on an affinity binding principle, where the device surfaces (PDMS and Glass) is functionalized with a mixed Self-assembled monolayer (SAM) composed by Silane-PEG-Biotin, Silane-PEG-OH and CD45-antibody (common antigen for leukocytes), considering its advantages reported in the literature over the traditional Streptavidin-based system such as covalent binding of biomolecules through a strong interaction between Silane group and PMDS-glass chip surfaces, suppress the non-specific binding of charged molecules to the functionalized surfaces and long term stability[293,296–299](Figure 58). Moreover, the surface coverage was calculated and demonstrated that the chip could allow to capture 4.265.100 leukocytes (Appendix E-Supplementary Figure 63 and Appendix F- Supplementary Equation (1))

The validation of the correct modification of the surfaces with the SAM was carried out optically by fluorescence and the fluorescence intensity (AFU) was also quantified and compared between the conditions. First, one chip without SAM immobilization was considered as a negative control to identify and eliminate the PDMS autofluorescence, as a result the AFU was zero (Figure 58A, Appendix E-Supplementary Figure 63). Then, the fluorescence intensity levels where compared between the surfaces modified with only Neutravidin Oregon green (Figure 58 C Appendix E-Supplementary Figure 63) and including the linker composed by Silane-PEG-Biotin and Silane-PEG-OH (Figure 58D, Appendix E-Supplementary Figure 63). The results show an increase of 70% and 46% in the intensity levels of fluorescence in the glass and PDMS surfaces respectively, which were immobilized with the linker compared with the chip immobilized only with Neutravidin (Figure 58 A,C, Appendix E-Supplementary Figure 63).

Finally, the fluorescence levels where quantified in the surfaces composed by the linker (Silane-PEG-Biotin and Silane-PEG-OH), Neutravidin and biotinylated-CD45 antibody. Figure 7E demonstrate that the biotinylated-CD45 antibody was successfully immobilized on the surfaces composed by the linker and Neutravidin, in contrast the negative control without biotinylated-CD45 antibody confirm the absence of fluorescence signal (Figure 58 B). Moreover, the AFU quantification revealed a decrease of 25% in the fluorescence levels in the Glass surface with the linker and the biotinylated-CD45 antibody compared with the surfaces with only Neutravidin and the linker (Appendix E-Supplementary Figure 63) .

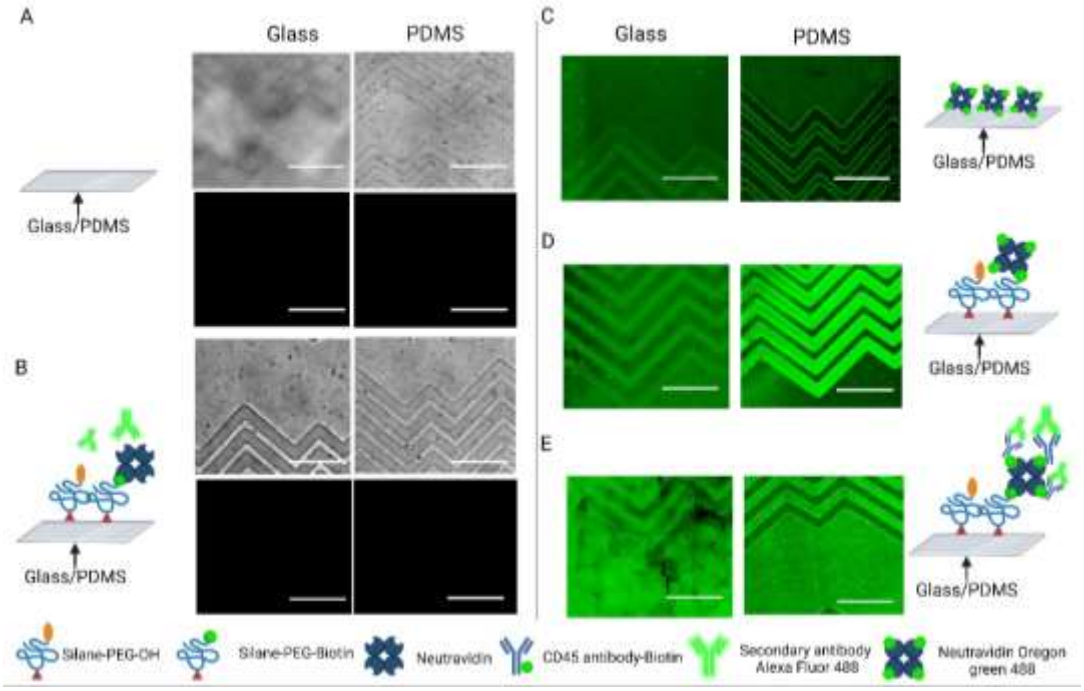

Figure 53. Characterization of Surfaces functionalization by fluorescence. **A)** Optical characterization of glass (images on the left) and PDMS (images on the right) surfaces (Negative control). **B)** PDMS and glass surfaces functionalized with Neutravidin Oregon green 488. . **C)** Glass and PDMS surface-functionalized with mixed-SAM (Silane-PEG-Biotin and Silane-PEG-OH), neutravidin and a secondary antibody Alexa Fluor 488 for validating the absence of CD45 antibody**. D)** Glass and PDMS surfaces functionalized with mixed-SAM (Silane-PEG-Biotin and Silane-PEG-OH), validated through the presence of Neutravidin Oregon green 488. **E)** PDMS and glass surfaces functionalized with mixed-SAM, Neutravidin and Biotinylated CD45 antibody. The presence of the CD45 antibody was validated by a secondary antibody Alexa Fluor 488.Scale bars 20 µm.

6.3 Characterization of Herringbone chip for CTCs model enrichment:

Once the verification of the correct chemical modification of the chip surfaces (PDMS and glass) was carried out, some experiments were performed to determine the efficiency of the set of grooves for capture leukocytes model (Kasumi-1 cells) and the recovery of CTCs model (MCF-7-cyclo-rgDfK(TPP) cells). Then, 10.000 MCF-7(cyclo-rgDfK(TPP) Cells/mL and 100.000 Kasumi-1 cells/mL were mixed in cell culture media, passed through the Herringbone device under the same flow rates previously simulated (10 µL/min and 20 µL/min)and the samples collected from the outlet of the chip were analyzed by FACS and quantified (Appendix E-Supplementary Figure 64).

The results revealed that a high percentage of CTCs model and Leukocyte model were recovered using a flow rate of 20µL/min from one chip without mix-SAM and 76 set of grooves(96±1% and 76±14% respectively) (Figure 59B). Comparing this result with the cells recovered from the chip immobilized with the SAM and 76 set of grooves, 39±7% of Leukocytes were recovered (Figure 59B), which suggest that 61±7% of leukocytes model were captured by the mix-SAM inside the Herringbone chip with 76 grooves structure (0.8% in each set of grooves) and the glass surface (Figure 59B). .

Moreover, 85±7% of CTCs model were recovered from the chip outlet indicating that 15±7% of cells can be unspecifically attached on the chip surfaces or were missed during subsequent sample preparation steps for flow cytometric analysis. Figure 59B shows the increase in the number of Kasumi-1 cells captured by the mix-SAM in the herringbone surface compared with the low unspecific binding of cells in the Herringbone chip without mix-SAM. Together these results suggest the efficiency of one herringbone chip in enhancing the enrichment CTCs model:leukocytes rate from 1:10 to 1:5 which represents a purity of 50% in 76 set of grooves.

On the other hand, the percentage of CTCs and Leukocyte cells model were recovered using a flow rate of 10µL/min from one chip with SAM and 76 set of grooves(70±16,3% and 50±6,5% respectively) and without SAM as negative control (100% and 93.15±6.85)(Figure 7B). Thereby, 50±6,5% of Leukocytes were recovered from the chip immobilized with the SAM and 76 set of grooves, (Figure 59B), which suggest that 50±6,5% of leukocytes model were captured by the SAM inside the Herringbone chip with 76 grooves structure (0.7% in each set of grooves) and the glass surface. Under this flow condition the recovery rate of CTCs model was reduce into 15%±16,3% compare with the percentage of cells isolated with a flow rate of 20µL/min.

Finally, correlating the estimation of the computational model (without considering the capture efficiency of the mix-SAM) with the experimental data obtained with cell lines and blood sample from healthy donors spiked with CTCs model (considering the capture efficiency of the mix-SAM) it was possible to estimate a factor of 14.30 using cell lines as a model and 20.3 when blood is processes through one herringbone chip. These factors are associated with the actual percentage of leukocyte captured on the surfaces (Figure 59C). Therefore, this model could help to estimate experimentally the amount of set of grooves or chips needed to capture a given number of leukocytes at the input.

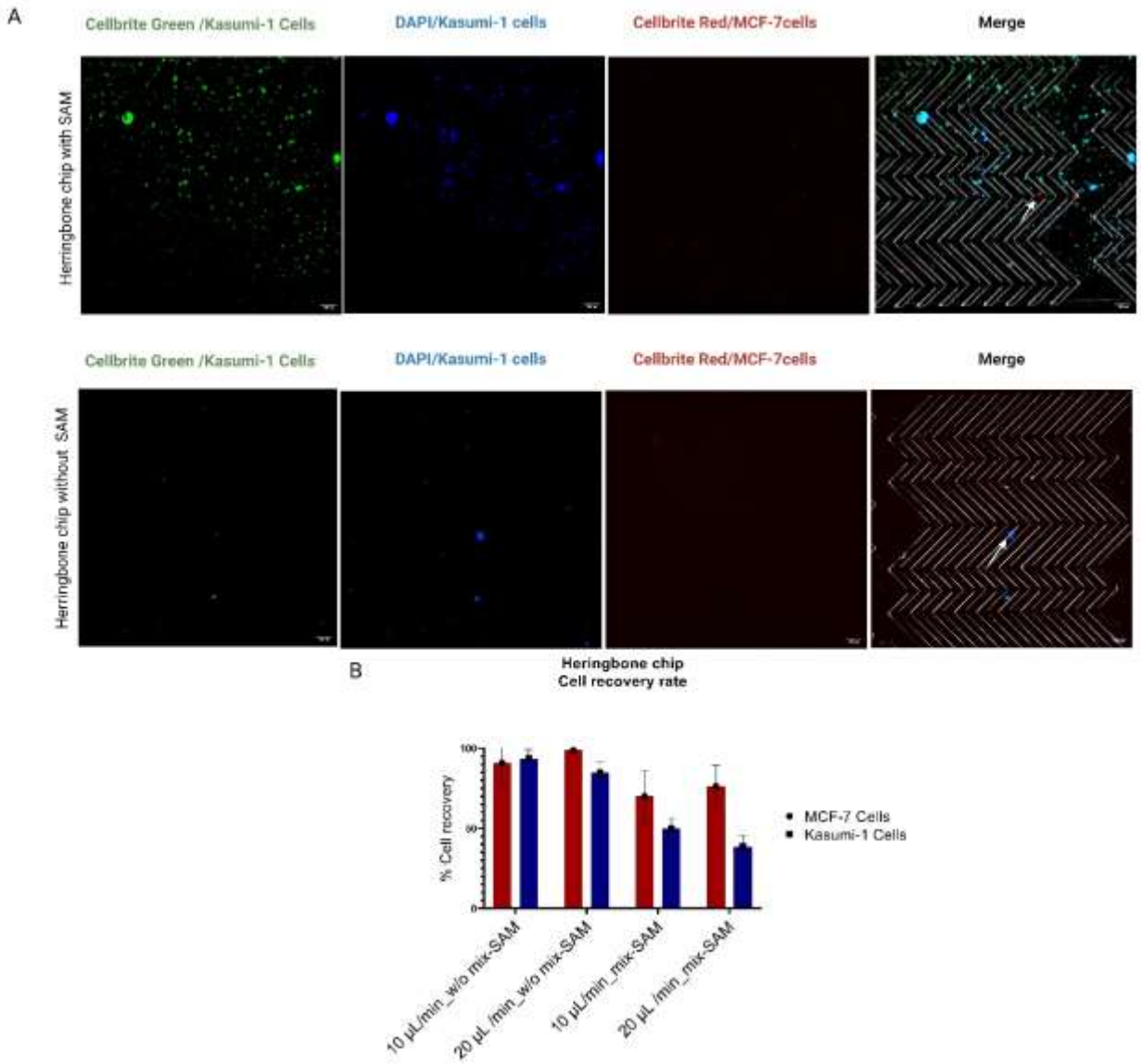

Figure 54. Efficiency of Herringbone device with 76 set of grooves tested with Leukocyte and CTCs cell models. **A)** Optical validation of Kasumi-1 cells (Leukocytes model) stained with cellbrite Green for cytoplasmic membrane, DAPI for nucleus. MCF-7 cells (CTCs model) were stained with Cellbrite red for cytoplasmic membrane. The images in the upper part show the cells anchored in the herringbone chip with the SAM and flow rate of 20µL/min, and the white arrow indicates the non-specifically anchored CTC cell model. The images at the bottom show little cell adhesion on the chip without SAM. The white arrow indicates the non-specific anchoring of leukocyte model. Scale bar 100 µm**. B)** Cell recovery (CTCs and Leukocytes cell models) from chips output with a flow rate of 10 µL/min and 20µL/min. The blue bars represent the sample recovered from one chip with 76 set of grooves output without SAM analyzed by flow cytometry. A high percentage of CTCs and Leukocytes were recovered (96±1% and 76±14% respectively). The red bars represent the sample recovered from the chip output with SAM 85±7% CTCs and 39±7% Leukocytes were recovered. Values and error bars represent mean ± S.E.M (n = 3).

6.4 Characterization of Herringbone chip for CTCs model enrichment with blood control samples

The Herringbone chip was tested with blood samples spiked with $1*10^3$ (MCF-7-cyclo-rgDfK(TPP) cells/mL as CTCs model previously purified by a spiral microfluidic device. Then, this outlet sample was processed through the Herringbone chip with a flow rate of 20µL/min in order to capture the leukocytes that contaminate the CTC sample.

The samples recovered from chips outlet with 76 set of grooves and analyzed by FACS revealed that 43±0.90% of leukocytes were capture in the chip surface immobilized with the SAM (<1% in each set of grooves).Moreover, 80±3.6% of CTCs model were recovered, which indicates that 20% are unspecifically anchored on the chip surfaces or are lost during sample preparation for FACS analysis. Despite, no decrease in the unspecific capture of CTCs in the chip surface immobilize with the SAM was detected (Figure 60B) compared with the chip without SAM, lose 20% of CTCs is compensated by an increase of 75% in leukocyte capture compared to the chip without SAM (Figure 60B).

Moreover, the results highlight the importance of grooves structures that guarantee the mixing of the cells and increase the probability that the Leukocytes interact with the antibody and are captured. Figure 8A-Herringbone chip with SAM/no grooves, shows the low capture of leukocytes in a chip without the grooves structures and the surface immobilize with the SAM. In addition, the flow cytometry results demonstrated that only 6±8.4% of Leukocytes were immobilized in the chip without grooves (Figure 60B), in contrast 43±0.90% of leukocytes where captured in the chip with 76 grooves structures (Figure 8A-Herringbone chip with SAM,B), which represents an increase of 86% in the capture efficiency when 76 set of grooves are included inside the microfluidic channel. Thereby, the enrichment ratio CTCs:Leukocytes was improved from 1:2 to 1:1 which is translate into 50% of CTCs purity for each 76 set of grooves in herringbone chip with a mix-SAM immobilized on the surfaces.

In addition, a cell viability test was performed to evaluate the percentage of viable CTCs recovered from one herringbone chip. The samples were evaluated by flow cytometry and demonstrated a high cell viability of 93%±0,12 which guarantees its use for subsequent molecular analysis (Figure 60C, Appendix E-Supplementary Figure 65).

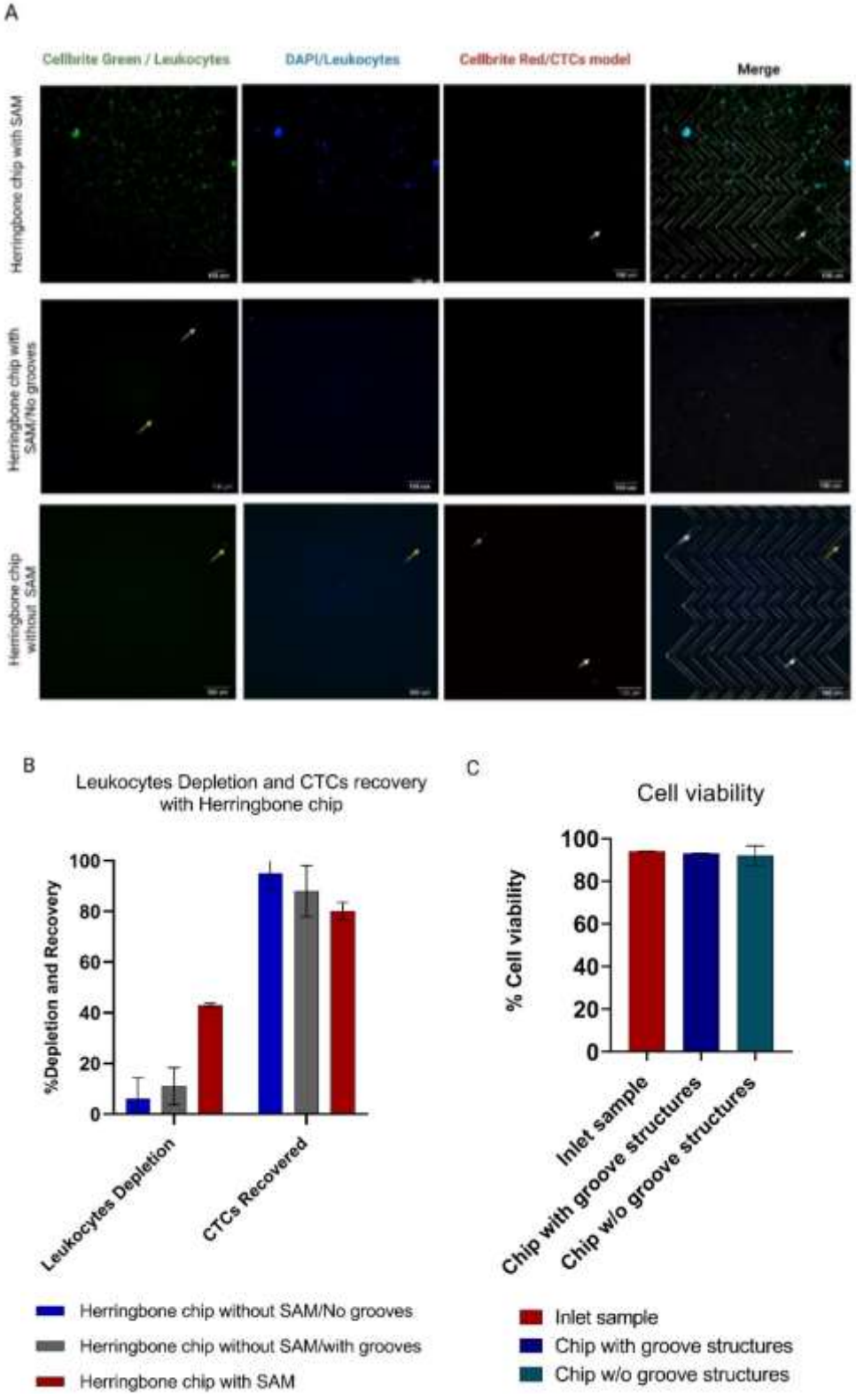

Figure 55.Characterization of Herringbone chip for CTCs model enrichment: Herringbone chip with 76 grooves tested with a sample pre-processed by a spiral microfluidic chip. **A)** Top image: Fluorescence

microscopy images of Herringbone chip with grooves structures and with its surface immobilized with mixed-SAM. Middle image: Fluorescence microscopy images of Herringbone chip without grooves structures and with its surface immbolized with mixed-SAM. Bottom Image: Fluorescence microscopy images of Herringbone chip with grooves structures and without mixed-SAM.Leukocytes capture on the chip surfaces were stained with Cellbrite Green and DAPI for nucleous, MCF-7-cyclo-rgDfK(TPP) cells as CTCs model were stained with Cellbrite Red. Yellow arrows show the Leukocytes adhered to the chip surfaces , and white arrows indicate the CTCs model adhered to the chip surfaces.**B)** The histogram represents the depletion of leukocytes in the chips (negative controls: chips without grooves structures (6±8.4%) or without SAM (10.6±7.4%). Positive control: Chip with grooves structures and SAM (43±0.9%). In addition, it represents the recovery of CTCs model in the chip without SAM and/or grooves structures (95±6.2% and 88±10.1%), as well as with SAM (80±3.5%%). Scale bar 100 µm. Values and error bars represent mean ± S.E.M (n = 3). **C)** Cell viability test of samples recovered from chip with grooves and without grooves . Values and error bars represent mean ± S.E.M (n = 3).

6.5 Discussion

Nowadays, the development of microfluidic technologies for purifying Circulating tumor cells (CTCs) from blood samples represents a challenge, especially to reach a high depletion yield of leukocytes and preserved the viability of the rare cancer cells recovered via label-independent methods, which can potentially be used for subsequent molecular analysis and eventually functional characterization.

In fact, there is only one CTC test approved by the FDA, the CellSearch® system by Menarini Silicon Biosystems[300] .This system uses magnetic particles coated with antibodies that bind to the protein EpCAM (epithelial cell adhesion molecule) for quantifying the CTCs in metastatic breast, prostate and colon[301]. In the last few decades, EpCAM (the epithelial cell adhesion molecule) was considered as universal tumor biomarker for epithelial-derived cancer types[302]. Nevertheless, the discovery of the CTCs heterogeneity and the existence of EpCAM-negative cancer cells[303] has revealed one of the major limitations of this method. To overcome this limitation, we proposed a CTCs enrichment method based on a negative principle which avoid use biomarkers and provide a sample of viable CTCs in solution for further analysis

In our model, we recreate one of the key features of the CTCs related to the E-cadherin expression, and the loss of its expression in association with the epithelial-mesenchymal transition (EMT) that occurs during tumor metastasis[304] . Our results revealed that we successfully recreated this property for the correct optimization of the microfluidic device. Thus, we recreated the non-adherent properties of the CTCs based on the formation of multicellular tumor spheroid by the cyclo-rgDfK(TPP) peptide, guaranteeing cell viability higher than 90% (Figure 57). The implementation of this model for the characterization and

optimization of the herringbone chip with cell lines, allows to reduce the vias in the results caused by the tendency of attachment of the cancer cell lines to the microfluidic device surfaces. In contrast, previous studies related to the use of herringbone chips for liquid biopsy characterized by cell lines, did not use an appropriate model to emulate the CTCs[305]. Furthermore, traditionally this type of microfluidic chip has been used as positive enrichment where the CTCs are captured on the chip surface instead of capturing the leukocytes.

On the other hand, we successfully implemented a chemical surfaces functionalization with a mix-SAM composed by organosilanes with poly(ethylene glycol) (PEG), which created a relatively hydrophilic surface that did not adsorb proteins or other biological species[306–308]. In our case , the presence of Silane-PEG-OH was used as a blocking agent to reduce the non-specific binding of the CTCs on the chip surfaces. In addition, the reduction of 25% in the fluorescence intensity on the surface functionalized with the mix-SAM, the CD45 antibody and the secondary antibody (Figure 58, Supplementary Figure 63), confirm that in heterogeneous interactions with an excess of target capture interact with a limited concentration of capture probe on the surface[309]

Our results revealed that between 80±3.6% and 85±7% of CTCs model cells were recovered from the chip outlet (1000 cells/mL), which demonstrated the potential of the silane-PEG-OH in reduce the unspecific binding in 76 set of grooves under a flow rate of 20µL/min as well as the capability of this device of providing viable cancer cells in solution for further analysis (>90%).Therefore it is not necessary to carry out extra steps for the collection of CTCs from the chip surfaces, and can be used for all types of cancer regardless of EpCAM expression levels.. These results highlight the advantages of our system compared to other previously reported technologies such as the microvortex-generating herringbone-chip developed by Shannon L. Stott, where 79% ± 4.5% of 5000 PC3 prostate cancer cells per militer were captured in the device surfaces, which implies that subsequent trypsinization or lysis must be done to collect the cells[310].In addition to being limited to capturing CTCs based on EpCAM expression levels.

The computational model developed in this study highlight the impact of the grooves structures in create the localized mixing with an increase in the velocity profile when the flow rate is increased from 10µL/min to 20 µL/min. (Figure 38).Despite, that no significant differences were found in the percentage of particles that enter in contact with the surfaces under 10 µL/min and 20 µL/min, an increase of 11% in the leukocytes immobilization efficiency experimentally, revealed that localized mixing under an increase in the velocity profile could improve the probability that the leukocytes move towards the functionalized surfaces of the devices and be captured. In contrast, the key role of the grooves in the leukocytes capture was ratified experimentally where in absence of the 76 set of grooves in

a channel functionalized with a mix-SAM the cells tended to go straight and only 6±8.4% of leukocytes were capture in the chip surfaces.

In addition, the computational model supported together with the experimental characterization, allows us to estimate the number of grooves required to guarantee the capture of the total population of leukocytes that contaminate the sample of CTCs that are collected at the output chip. In this way, our results reveal that to eliminate all the leukocytes that contaminate a sample of blood spiked with CTCs model previously diluted and preprocesses to remove the erythrocytes, 228 sets of grooves are required, which is equivalent to 3 herringbone chips. In fact, two different factors were calculated experimentally in this study, one from cell lines (14.30) and the other from a blood sample (20.3). These factors could serve as support for the computational model to achieve a real approximation of captured cells using a certain amount of set of grooves from different types of samples as a source (cell lines or blood). It is worth noting that the difference between these two factors may be associated with the different characteristics of the samples that may influence the results of the capture efficiency. Since, in the first part of this study cell lines were used to recreate the targeted model (Leukocytes), with which there is a more homogeneous population in the expression levels of CD45 (Kasumi-1). Meanwhile, when leukocytes from blood samples are used, there is a heterogeneous population in terms of CD45 expression levels. This fact has been supported by previous studies, where it was demonstrated that the expression of CD45 was the highest on lymphocytes (279,369±101,409), intermediate on monocytes (52,398±15,192), and the lowest on granulocytes (26,890±7,856)[311]

Finally, the depletion obtained from 76 set of grooves employing a bloodsample, can be translate into CTCs sample purity of 50%. Comparing this results with those ones obtained by Shunqiang Wang and colleagues, who reported a purity with the grooved-HB chip and the wavy-HB chip of 36.7% ± 2.2% vs. 25.6% ± 1.7% and 39.4% ± 4.3% vs. 25.7% ± 2.1%,respectively under different shear rates conditions[312] ,with our method is possible to improve the purity over 10%. In fact, we provide an strategy for potentially achieve a complete depletion of leukocytes and in consequence have more chance of increasing the purity of the CTCs sample.

Overall, this negative enrichment approach is advantageous not only because it leads to unbiased detection of CTCs regardless of EpCAM expression levels, but also produces intact tumor cells free of attached biomarkers, eliminating potential artifacts in subsequent studies. Although, the depletion of leukocytes through immunocapture on functionalized surfaces is not practical to be used in high blood volumes directly. The use of negative enrichment

methods accompanied by the prior depletion of red blood cells opens new avenues for their potential application in clinical practice

Chapter 7

Low-cost instrumentation for whole cancer cell isolation in liquid biopsies

Traditionally, experimental setups are composed by syringe pumps or peristaltic pumps and microscope for checking the correct working principle of microfluidic devices. Although, syringes or peristaltic pumps offer benefits such as precise fluid volumes, high speed, and ease to use. But they often come with high costs, limited programmability, and restricted fluid dispensing volumes in the case of syringe pumps. Moreover, these pumps do not facilitate scalable solutions[313,314] . Despite the numerous approaches developed to address some of the limitations of current pump systems like open-source syringe pumps, low-cost syringe pumps and pump system based on braille display as an actuator[313,315–319], none of these systems overcome the limitations for using in spiral microfluidic devices.

Nowadays, the development of open-source platforms for medical applications has opened new ways to design more flexible, low cost and portable diagnostic tools using microfluidic devices. In fact, with a small version of a computer capable of performing task effectively that allow to install open-source operating systems, and the creation of compact micropumps able to transport a very small quantity of liquid or gas have given rise to the possibility of manufacturing compact, easy-to-use, and low-cost medical diagnostic tools.

To overcome some of the limitations previously exposed, we proposed to integrate spiral devices into a low-cost, portable, and versatile electronic flow control platform, which can serve as a model for advanced diagnostic platforms based on microfluidic technology

7.1 Low-cost instrumentation set-up for a whole cell detection diagnostic system.

In microfluidic applications, syringe pumps have traditionally been used to modulate a small amount of liquid flow. However, when used in spiral microfluidic devices for liquid biopsies, they require large and complex setups, as shown in Figure 66, and have several drawbacks such as:

1. The traditional pump do not allow the recirculation of the sample multiple times.

2. The syringe must be frequently refilled for processing large blood volumes, which leads to the loss of circulating tumor cells (CTCs) as the flow stabilizes following the replacement of the sheath flow syringe.

3. The blood sample tends to settle in the syringe, requiring continuous rotation to ensure a homogeneous mixture.

4. The setup takes up a significant amount of space and is not portable, making it challenging to fit easily in clinical laboratories

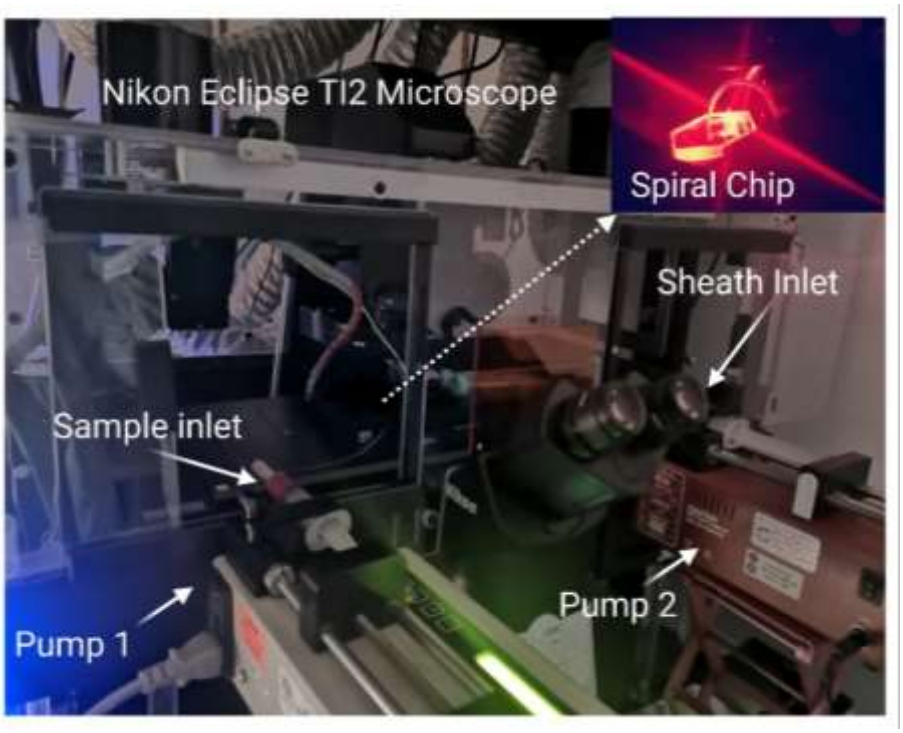

Figure 56.Traditional microfluidic set-up for isolating CTCs using a spiral device. The system is composed of two syringe pumps, two reservoirs connected to the outlet of the microfluidic channel and one microscope.

To address the limitations of traditional syringe pumps for liquid biopsies in microfluidic devices, a flow compact circuit has been developed using commercial piezoelectric micropumps (Bartels MP6), which are controlled by a Raspberry Pi zero microcontroller and python 3.8[320,] .The GPIO library was used to control the PWM signal generated through the raspberry Pi Zero. Thereby, the frequency of the PWM was modulated to control the flow rate of each pump, and a library was created to generates constant flow rates (Q1 and Q2) for each micropump independently, as well as the code allowed to specify the duration (T in sec) when each micropump is activated. Figure 67A and B show the schematic of the electronic circuit and the Printed circuit board (PCB) designed in Eagle®

In overall, micropumps are piezoelectric in combination with passive check valves. Thus, a piezo ceramic put on a coated brass membrane is deformed when voltage is applied. Then, the medium is displaced out of the pump chamber below. The check valves on both sides of the pump chamber define the flow direction. [321]By using piezoelectric pumps, this flow control circuit offers several advantages over traditional syringe pumps. For instance, piezoelectric pumps do not require a separate syringe, thus eliminating the need for frequent filling and reducing the loss of CTCs. Moreover, the compact size and portability of the piezoelectric micropump setup make it more convenient for clinical laboratories. Therefore, the printed circuit board (PBC) of the flow electronic circuit was designed using EAGLE, as shown in Figures 67A and B. Moreover, the casing was created in AutoCAD and printed using a 3D printer Ender 3 PRO (Figure 67C), as well as, the first electronic prototype is shown in Figures 67D and E.

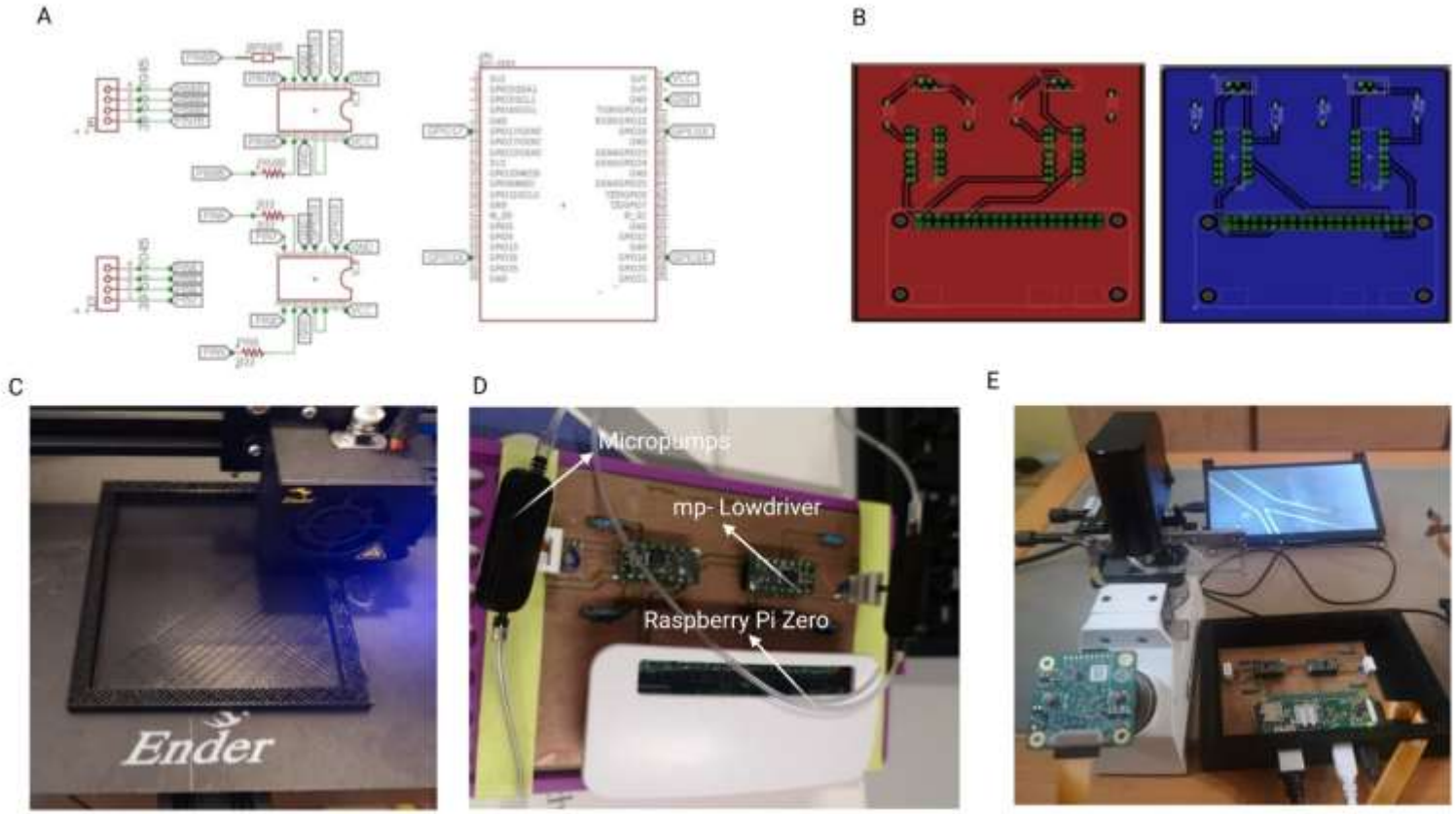

Figure 57.**A)** Schematic representation of the electronic circuit designed in Eagle **B)** Printed circuit board (PCB) composed by two layers designed in Eagle **C)** Fabrication of casing made by 3D printing **D)** First prototype of PCB electronic circuit composed by Raspberry pi Zero, 2 micropumps and 2 Low-drivers **E)** First circuit prototype composed by portable microscope and raspberry Pi camera.

On the other hand, the circuit is composed of a small driving circuit (mp-Lowdriver) for mp6 micropumps, useful for low flow rate applications (8 µl/min up to 4.000 µl/min) and high amplitude resolution. These micropumps display some drawbacks such as high pulsation of the flow and the lifetime around 5.000 hours. Nevertheless, these disadvantages can be overcome by integrate mp-dampers in the system which allows to reduce pulsations in the flow generated by the micropump, and consequently, a more stable flow rate is achieved (Figure 68B and Appendix F- supplementary Figure 70 and Supplementary Table 12). Finally, the circuit has a passive check valve (mp-cv) that prevents the medium or blood from flowing back when the pump is switched off. Although pumps can be sterilized to prevent cross-contamination by autoclaving for 20 minutes at 121°C and 10% of EtO, it is more cost-effective to replace them weekly if they are manufactured on a large scale than to undergo repeated sterilization procedures [322]. To address other limitations of conventional set-ups a small microscope (XPD-101 expedition Bresser) was adapted to raspberry pi camera (Raspberry Pi Camera 12.3MP IMX477 Sensor), shown in Figure 3A. This camera has been controlled with the Raspberry Pi zero at the same time and will allow to visualize and monitor the blood cells focalization towards the waste outlet using real samples from patients with cancer, which won't be stain with a fluorescent biomarker and the correct functioning of the chip can only be evaluated through the visualization of the depletion of blood cells as shown in Figure 68C (white arrow). Overall, the system exhibits various features that augment its programmability, portability, and affordability, ultimately enhancing its versatility and adaptability to clinical laboratories.

Figure 58.**A)** Portable biocompatible flow platform composed of Raspberry Pi Camera 12.3MP IMX477 Sensor, micropump circuit, Raspberry Pi touch screen and one small microscope (XPD-101 expedition Bresser). **B)** Micropump circuit composed of two small micropumps and two mp low-drivers controlled by one Raspberry Pi Zero, two mp dampers and check valves. The system has inlet and outlet reservoirs that can be filled without shutting down the system and allows sample recirculation**. C)** The depleted blood cells can be recorded and visualized in real time in Bright field.

7.2 Validation of cell isolation system with blood samples spiked with cancer cells as CTCs model.

The operation of micropumps was evaluated with a single spiral microfluidic device made of PDMS and based on the work previously reported in "*Chapter 5"* . Thus, the spiral device was tested with 10X diluted blood samples from healthy donors spiked with a final concentration of 1.000 cells/mL of different sizes such as MCF-7 (20µm) and A549 (15 µm). The sample was perfused through the inlet A of spiral microfluidic device using the portable biocompatible flow platform applying an SRS-signal and voltage 125Vpp with a frequency of 41Hz (3300 µL/min), as shown in Figure 69A. Meanwhile the sheath flow (PBS 1X) was perfused through the inlet B, as seen in Figure 69A, and the parameters were set to 150 Hz and voltage of 125 Vpp (7700 µL/ min). Furthermore, some mp-dampers were included in the electronic circuit to reduce the effect of pulsation on the flow, which affects the separation efficiency, as shown in Figure 69B. Figure 69C shows the reduction of flow pulsation, which leads to the flow

stability and the hydrodynamic focalization of blood sample through the outer wall, being one of the key parameters for the larger CTCs (>12um) undergoing inertial focusing. Moreover, passive check valves were added to prevent the medium from flowing back when the pump is switched off.

On the other hand, the samples recovered from the outlet A (Figure 69A-CTCs outlet) were analyzed by flow cytometry and revealed a recovery efficiency of 80±4% for MCF-7 cells and 95±4% for A549 cells (Figure 69D, H and I). In addition, the system enables 97.5±1.89% and 83.4±3.6% depletion of erythrocytes and leukocytes respectively (Figure 69E). Further analysis of the cell viability of the CTCs outlet demonstrated that the micropump and the spiral microfluidic devices allow to recovery cells with a high viability of 93±0.12% and 94±0.23% respectively, as shown in Figure 69F, which can be used for subsequent downstream analyses.

Our finding suggests that our system could achieve an increase in the cancer cells recovery rate of 10±4% compared with the previous results reported by Warkiani et al. In contrast, the leukocytes depletion rates differ from the values reported by Warkiani et al by a reduction of the leucocytes depletion of 17%. An implication of the finding exposed is the throughput of the platform in terms of blood processing, which is equivalent to 3.3mL/10min[323].Despite not being consistent with those reported by Warkiani in lysed blood samples (7.5 mL/10 min), it represents an improvement over the data reported by Hou and colleagues using samples with high hematocrit of 20–25% (3 mL/h) [323].

Finally, the complete system was tested with a low concentration of 20 µm particles as a CTCs model (100particles/mL and 10particles/mL) in diluted 10X human blood samples. In particular, the quantification of the recovery CTCs model sample was performed by videos since the correct analysis by flow cytometry was limited to the low cell concentration. Therefore, the results showed a recovery of 80±11.2% and 87±4.3% for 100 particles/mL and 10Particles/mL, as shown in Figure 69G and 69J. Here, it could be expected similar recovery rates for low concentrations will be obtained with cancer cells. Nevertheless, a bias should be considered due to other cells properties that can alter the separation yield like the cell deformability[324].

Overall, the results demonstrates that this instrumentation platform is suitable for spiral microfluidic devices used for the separation of particles or cells with different diameter and allows its potential application in liquid biopsy to recover a high rate of CTCs, with a greater flexibility and scalability compared to traditionally used pump systems. Moreover, this system displays some advantages as a label free or independent antigen method, since the CTCs are collected in solution which could be cultured for subsequent analysis, as well as, the possibility of not using intermediate steps such as blood lysis that could promote the loss of

CTCs. However, some drawbacks must be considered, such as the loss of smaller CTCs. This could potentially be solved by integrating different spirals in series with different separation ratios.

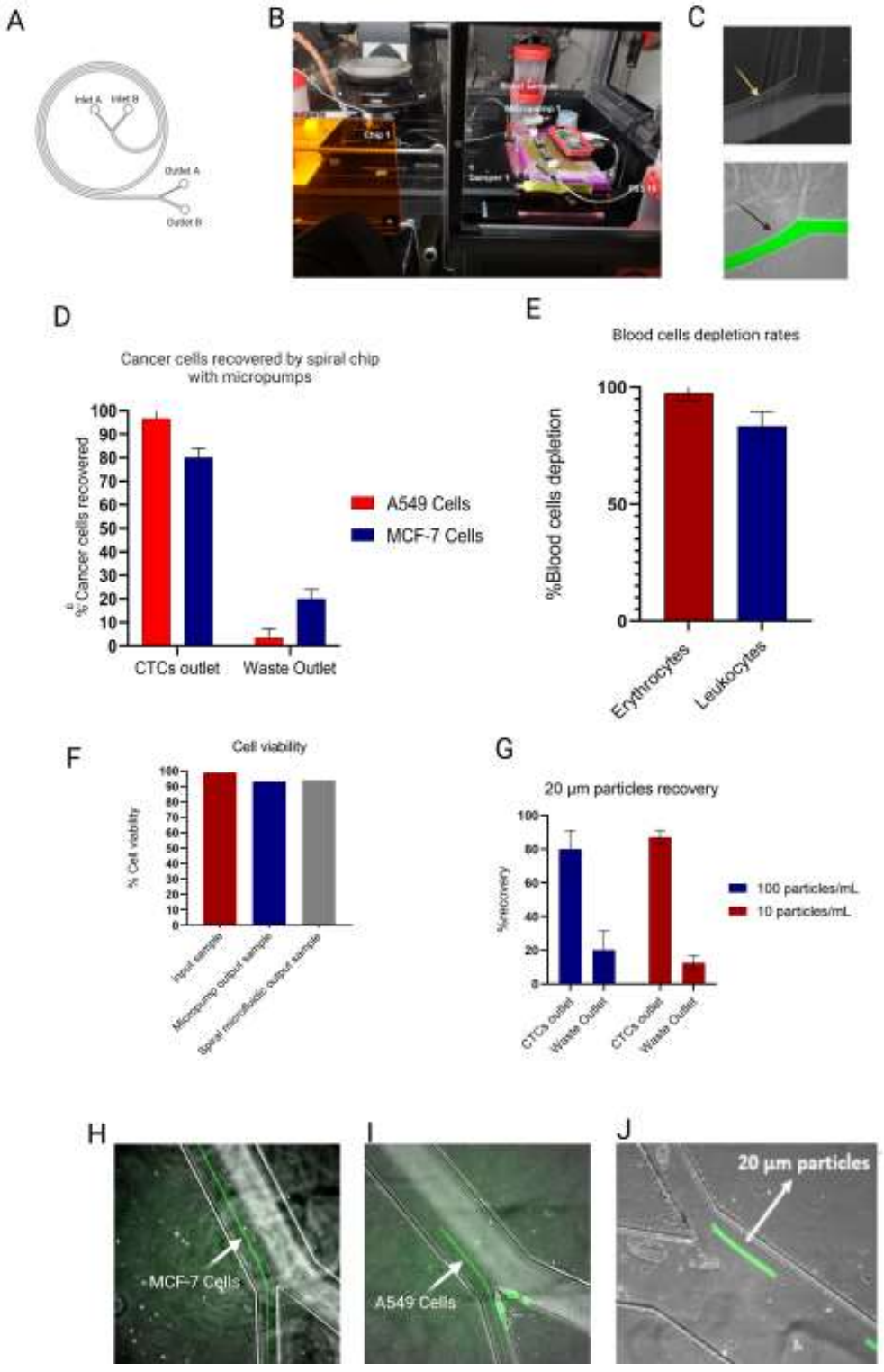

Figure 59. Portable flow platform tested with blood samples from healthy donors spiked with cancer cells lines. (A) schematic representation of spiral microfluidic device composed by inlet A (10x blood sample), inlet B (PBS 1x), outlet B (waste), outlet A (CTCs outlet). (B)circuit composed of two

micropumps, mp-low drivers programable by a Raspberry pi Zero, mp-damper and passive check valves (mp-cv). (C) Hydrodynamic non-focalization of blood sample because of pulsation on the flow (yellow arrow) vs sample focalization of sample with mp-dampers included (black arrow). (D) Recovery efficiency of A549 and MCF-7 cells by spiral chip using micropumps. Values and error bars represent mean ± S.E.M (n = 3). (E) Depletion rates of blood cells. Values and error bars represent mean ± S.E.M (n = 3). (F) Cell viability test of cancer cells passing through the micropumps and spiral microfluidic device. The bars represents the average. G) Recovery rates of low concentration of 20µm particles as a CTC model. Values and error bars represent mean ± S.E.M (n = 4). (H-J) Separation of cancer cells (MCF-7 and A549 cells) and 20 µm particles stained in green.

7.3 Discussion

The current research showed the successful development of a low-cost fluidic platform using micropumps, Raspberry and coding in open-source software (Python). This platform offers multiple advantages over traditional syringe-based perfusion systems, such as the processing of large sample volumes, it allows the creation of closed flow circuits for sample recirculation, and it is a compact and portable system that does not require the use of large microscopes.

Surprisingly, it was found that using this platform higher flow rates are required to obtain high efficiencies in the separation of cancer cells as CTCs models (3300 µL/min and 7700 µL/ min, for blood and PBS 1X respectively) using spirals with 152 µm channel height. Likewise, the high depletion rates of erythrocytes and leukocytes cells equivalent to those obtained using syringe pumps (97.5±1.89% and 83.4±3.6%), reveal not only the potential application of this compact system, but also offer the advantage of increased throughput to 3.3mL/10min compared to previously reported studies (3mL/h)[142]. This could speed up the processing of real blood samples from cancer patient. Despite these promising results, questions remain about the efficacy of these platforms using real samples from cancer patients, which will be the next phase of the project to be developed in the Nanoengineering group at IBEC.

Finally, considering all the results from the two different spiral microfluidic devices, we propose that it could be possible achieve a total leukocyte depletion up to 91% and a maximum cancer cells recovery up to 95%, which would represent an increase in the cancer recovery rate compared to the results reported by Warkiani et al ([323]).

Chapter 8

Low-cost 3D-printed inertial flow microfluidic devices

The emergence of 3D printing has led new manufacturing methods for microfluidic devices adapted to medical applications. Specifically, it has been shown that the development of Stereolithography (SLA) 3D printing has enabled the design of microfluidic devices with dimensions that are particularly useful for concentrating and purifying CTCs from blood samples[256].

Among the commercial technologies available, the SLA 3D printing Microlay created for dental applications, has demonstrated its potential for the development of microfluidic devices molds. This technology offers some advantages over others 3D printers in the market, such as supply the same amount of UV energy dosage on each layer, the internal radiometer can auto calibrate the amount of energy before each layer, as well as it is able to print with a resolution of 65 µm in the horizontal XY plane and 50 µm in the vertical Z plane up to 10 µm. Overall, 3D printing has proven to be a versatile and cost-effective method for microfluidic channel fabrication.

Finally, lithography has represented one of the most prominent methods for the fabrication of microfluidic devices. However, it is limited to acceptable aspect ratios; otherwise, the channels may collapse after fabrication[325]. Therefore, with this technique, it would not be possible to manufacture spiral microfluidic devices with a high channel aspect ratio, which will allow the implementation of new methods to achieve a higher purified CTC sample. On the other hand, SL 3D printing allows creating microfluidic devices with features that enhance CTCs separation, which potentially could enable more effective purification.

During this thesis, we have successfully manufactured microfluidic devices molds using 3D printing, which enables the creation of complex structures and features that are challenging to achieve using other fabrication methods. This demonstrates the potential of 3D printing as a powerful tool for creating microfluidic channels and devices for cell detection and isolation applications [256]

8.1 3D printing layouts for microfluidic cell isolation and detection obtained by Stereolithography.

Based on the geometry previously validated by computational modeling (Figure 71A,B), 3D printing molds were fabricated using Microlay 3D printer and SolusArt Grey resin (Figure 71C). This resin offers some advantages for the development of molds for microfluidic applications, such as supports 10 slices, fast dry to cut down on post curing times, great mechanical performance, low shrinkage for excellent dimensional accuracy and stability and withstands high temperatures for mold making.

Once the mold was printed, it was silanized to be able to make PDM replicas. The salinization process consisted of one minute of plasma cleaner at 30 W with constant pressure of 0.8 Torr. With the activated surface, a drop of Trichloro(1H,1H,2H,2H-perfluorooctyl) silane ($CF_3(CF_2)_5CH_2CH_2SiCl_3$) was deposited on top of a glass slide or a Petri dish inside a vacuum desiccator for one hour. Afterwards, to create the PDMS replicas, the 3D printed mold was covered with PDMS with a ratio of 10:1 of curing agent and left on the oven at 85 °C overnight. After unmolding the PDMS, the next step was to wash the PDMS replicas with soap and water, and ethanol, as well as the glass slides which were cleaned with ethanol, acetone, and 2-Propanol. Finally, the cleaned PDMS and glass were activated 30 s with the plasma cleaner at 30 W and pressure of 0.8 Torr, and the two parts were bonded. The final device was tested with Fluorescein to check the absence of leakage between the microchannels (Figure 71D-G). The result was a microfluidic device with the architecture of the 3D printed configuration.

On the other hand, with the development of a custom 3D printer in the Nanobioengineering group, it has been possible to use transparent resins to manufacture molds for spiral microfluidic chips and closed spiral microfluidic channels [256] (Appendix G).

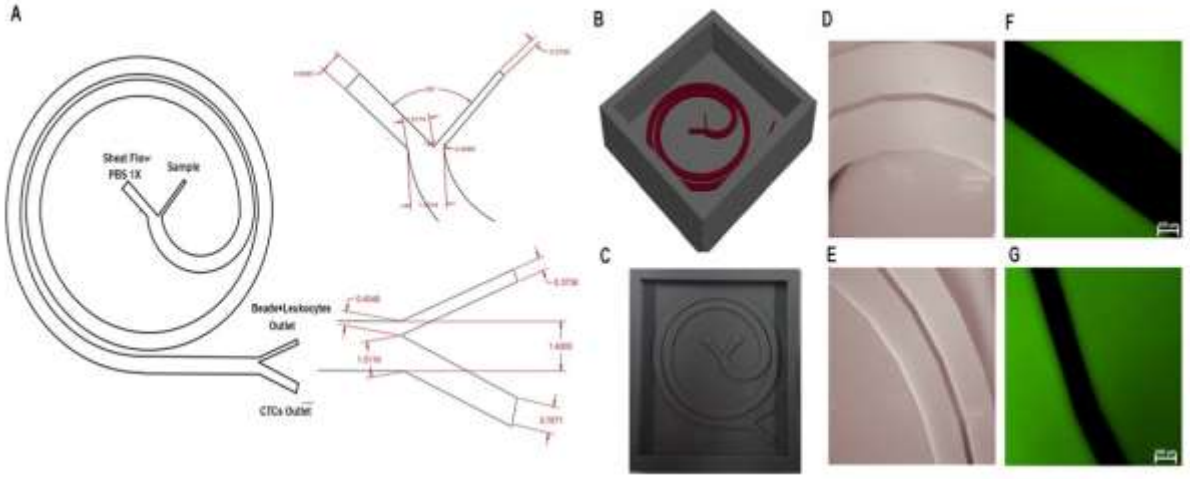

Figure 60. Design and manufacture of spiral device. Overview of the spiral microfluidic device for leukocytes-particles depletion. A) Schematic of the spiral device composed by two inlets (Blood sample input and PBS 1X) and two outlets (CTCs outputs and Beads+Leukocytes Outlet), microchannels of 1.4 mm (width) x 560 µm (height)), outlet split to 373 µm for "particles+leukocytes" outlet near to the inner wall and 767 µm for CTCs outlet near to the outer wall. B) Master designed in AutoCAD C) Master fabricated by 3D Printing. D-E) Optical validation of the correct development of microfluidic channels for subsequent replication in PDMS. F-G) Microfluidic spiral device stained with Fluorescein show a good bonding between glass and PDMS.

8.2 Characterization of spiral device with 70 µm particles-Leukocytes and 15 µm particles as CTCs model

Therefore, as previously mentioned, new enrichment methods are needed to purify CTCs and reduce the leukocyte background, which is a key requirement for performing cancer gene mutation analysis using contamination-sensitive technologies, such as real-time polymerase chain reaction (PCR) and next generation sequencing [326,327]. For that purpose, the single 3D spiral device previously developed could help to increase the leukocyte depletion. For this, a blood sample without cancer cells was processed through another spiral device as previously described in chapter 5. The sample obtained from CTCs outlet, which would correspond to the leukocytes that could contaminate the CTCs sample, was incubated with 70 µm diameter microspheres conjugated with Biotin-CD45 antibodies and secondary antibody as a control (Figure 72A-C). The surface antibody coverage and the total number of particles required to maximize the leukocyte capture was calculated based on the assumption that in heterogeneous interactions with an excess of target capture interact with a limited concentration of capture probe on the surface, estimated to be around 30%[328] (Appendix H)

The results revealed that around 48% of leukocytes were captured by the beads (Figure 72 D, E). Moreover, through the capture of microscope fluorescent images was possible to demonstrated that most of the 70 µm particles without leukocytes bonded could be separated and take the “Leukocytes+beads outlet” (Figure 72H). It may be the same case for the particles with the leucocytes bonded, since the total size of the particles would be bigger, and as the simulation results demonstrated that this device allows separate particles bigger than 70µm. Limitations in the quantification of 70 µm particles recovered were encountered using flow cytometry due to clogging caused by the particles size and recording videos due to the time recording time possible per sample . Despite the limitations exposed the number of 70 µm particles recovered were quantified by microscopy, and the results shows a recovery rate of 75±17% (Figure 72I). Moreover, particles of 20 µm as CTCs model were pass through the spiral and as result 100% were successfully recovered (Figure 72F,G)

Hence, based on the preliminary optimization based on the percentage of leukocytes captured by the beads, as well as, the separation of the particles observed by microscope images; we hypothesize that this device could separate smaller particles which correspond to cancer cells or CTCs (>12µm) from streptavidin particles coated with CD45 and leukocytes. Nonetheless, further work is needed to develop reliable quantification methods for the easy implementation of this system and the validation of the complete system with blood samples spiked with cancer cells, as well as blood samples from cancer patients.

Finally, thanks to the devices developed is not needed to perform extra sample centrifugations, which increases the risk of losing CTCs. In contrast, our system could represent a new approach to CTC separation by combining inertial forces microfluidic devices, antibody binding approaches, and 3D printing methods that have not been widely reported until now, which could allow higher leukocyte and erythrocyte depletion rates.

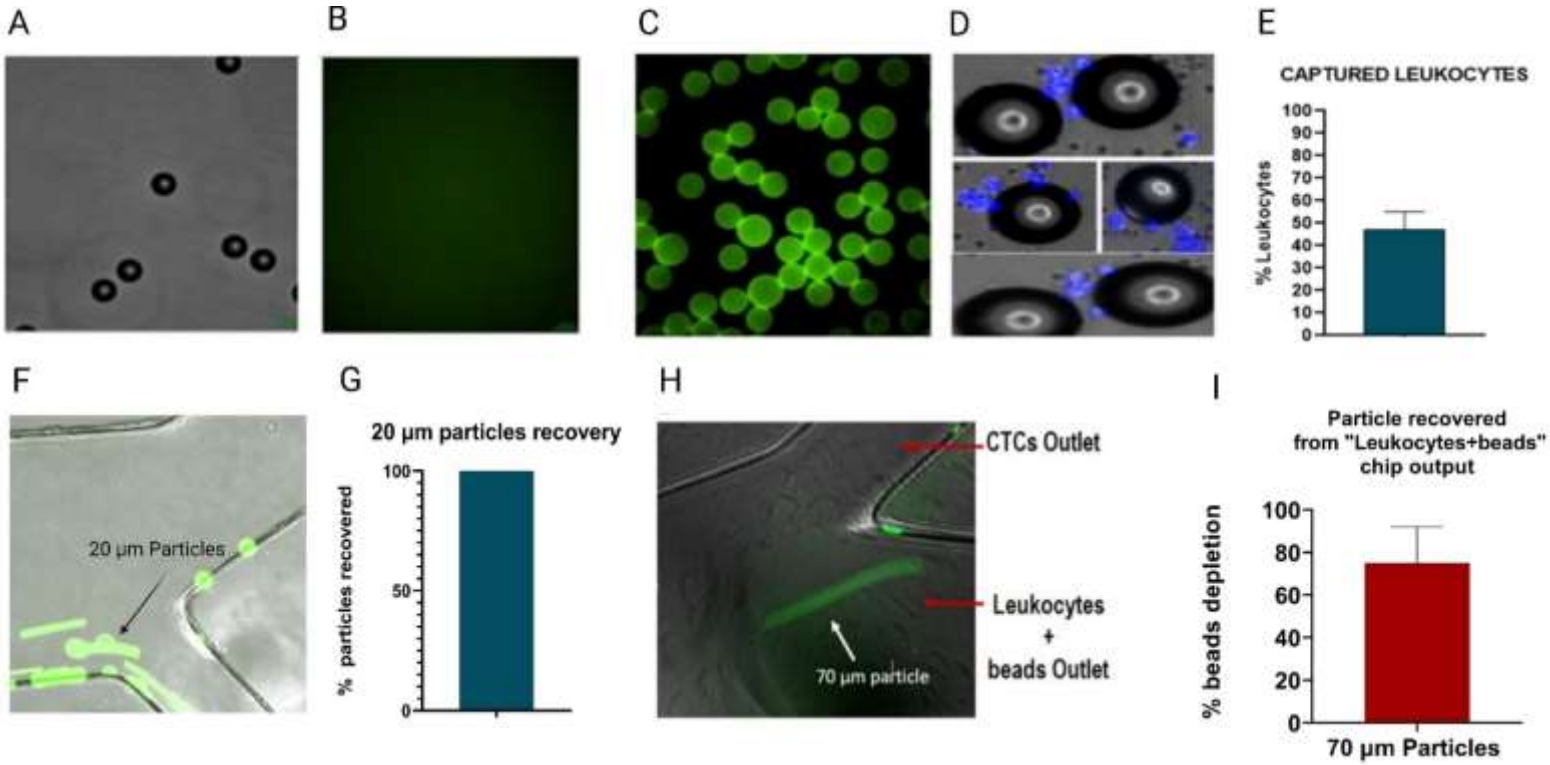

Figure 61. Characterization of polystyrene particles binding to CD45-antibody: **A)** Polystyrene particles of 70um in Bright field (BF). **B)** Negative control for Biotin-CD45. **C)** Polystyrene particles binding with biotin-CD45 antibody and secondary antibody AlexaFluor 488. **D).** Polystyrene particles are binding with leukocytes (nucleus stained in blue). **E)** Microscopy images of 70µm particles (green) focalized through of outer wall. **F)** Quantification of particles binding to leukocytes with an efficiency around 48%.G) Quantification of 70µm depleted from the sample (75±17%). Values and error bars represent mean ± S.E.M

8.3 Discussion

Nowadays, the additive manufacturing or 3D printing has become a powerful tool for rapid prototyping of microfluidic devices for medical applications, allowing to reduce costs and production times compared to traditional lithography. However, the use of this technology is limited to the minimum manufacturing dimensions depending on the printer used. However, we managed to successfully manufacture spiral molds for liquid biopsy applications with a novel approach, compared to other similar devices reported to date for the depletion of leukocytes and obtain a sample of purified CTCs.

The results of this study showed the potential application of 3D printing in the fabrication of functional microfluidic devices based on the principle of inertial forces for liquid biopsy applications. The most important finding was the validation of the computational model with particles of 70µm and 20µm as target models in the 3D device, where up to 75±17% of bigger particles functionalized with CD45 antibodies were separated and 100% of small particles as CTCs model were recovered. In addition, the preliminary evaluation of the method for anchoring leukocytes in particles with CD45 antibodies could open new approaches for leukocyte depletion from CTC populations using microfluidic spiral devices. However, even though the maximum leukocyte capture efficiency was 48%, a study with more focus on maximizing the capture efficiency is therefore suggested.

These findings may be somewhat limited by the characteristics of the microfluidic setup implemented with syringe pumps, since this device requires high flow rates to guarantee the correct separation of the target particles or cells (700 µL/min and 6,300 µL/min), and with these traditional perfusion systems, the maximum sample volume possible to process is limited to the size of the syringe used, as well as it is not possible to recirculate the sample through the device. Therefore, our study also included the development of a low-cost fluidic platform that seeks to overcome the limitations of traditional microfluidic setups as was described in “Chapter 7 “.

Chapter 9

Future perspectives

Further experiments, using a broader range of blood samples from cancer patients, could shed more light on the potential usability of the microfluidic devices and the low-cost fluidic platform developed during this study in a real clinical environment. Therefore, it was proposed to carry out a study with blood samples from 15 patients with colorectal cancer. This clinical study was evaluated and approved by the Ethics Committee for Research with Medicines of the Vall d'Hebron University Hospital.

The cohort was divided into three groups according to the following phenotype:

1) 5 mCRC patients with microsatellite instability (MSI)

2) 5 mCRC patients with a BRAF mutation (V600E)

3) 5 mCRC patients with a KRAS mutation (G12C).

In Spain, Colorectal cancer (CRC) represents the second most common cancer. Moreover, it is the leading cause of cancer death in women, and the second leading cause of cancer death in men[329]. According to the international agency for research on cancer, colorectal represents the 3rd most common cancer worldwide[330]. In 2020, more than 1.9 million new cases of colorectal cancer and more than 930.000 deaths were estimated[330] (Figure 75). It is predict that by 2040 the cases will increases to 3.2 million per year, which represents an increase of 63%; as well as the death could increase of 73% per year[331].

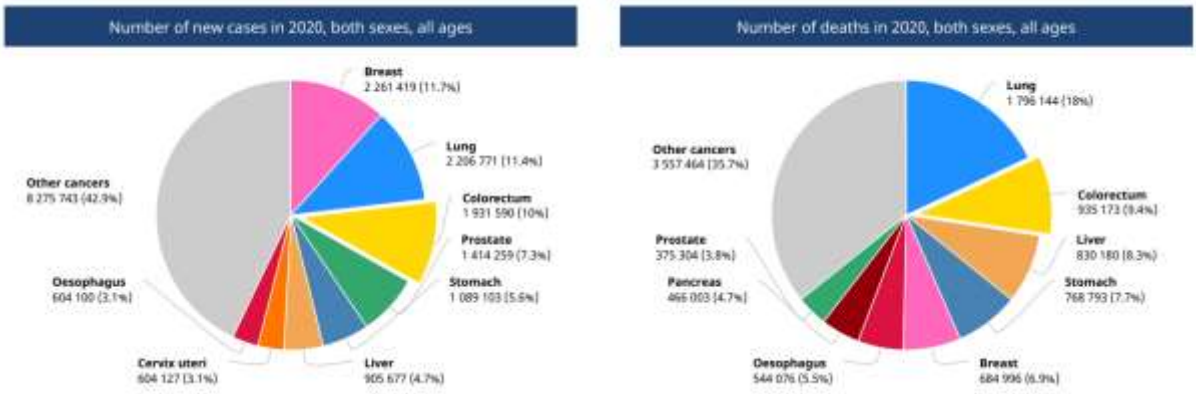

Figure 62.Colorectal cancer statistics worldwide in 2020.Taken from: [330]

CRC is a heterogeneous disease characterized by different pathways of carcinogenesis and display different molecular landscapes that reflect the histopathological and clinical information. Based on a wide of genomic and transcriptomic characterization studies, the CRC has been classifies into three major groups[332]:

1. Hypermutated cancers which corresponds ~16% with microsatellite instability (MSI), caused by defective mismatch repair due to MLH1 silencing via promoter hypermethylation.

2. Ultra mutated cancers (3%) with DNA polymerase epsilon or delta 1 exonuclease domain mutations, including the malfunctioning enzyme which introduce incorrect nucleotides during the DNA replication.

3. Chromosomal instability (CIN) represents ~84% and include a high frequency of DNA somatic copy number alterations, which is a consequence of the combination of oncogene activation such as KRAS and PIK3CA, as well as tumor suppressor gene activation like APC, SMAD4 and TP53.

On the other hand, the second classification was proposed based on the CRC expression profiling data from different studies. This classification divide the CRC into 4 groups associated with different patients outcomes[333].

1. CMS1 (MSI-immune, 14%) included CRC hypermutated due to dMMR with MSI and MLH1 silencing and accordingly CpG island hypermethylation phenotype-high (CIMP-high) with frequent BRAF mutations, and a low number of somatic copy number alterations (SCNAs).

2. CMS2 (canonical, 37%)

3. CMS3 (metabolic, 13%)

4. CMS4 (mesenchymal, 23%)

Finally, there is a residual unclassified groups with a mixed features that corresponds to 13% of the cases.

9.1 Patients Samples Phenotype

9.1.1 Microsatellite instability (MSI)

From the perspective of the patient phenotype, the microsatellite instability (MSI) is a clonal change in the number of repeated DNA nucleotide units in microsatellites, which is translate to genomic hypermutability and deficient mismatch repair in tumors, caused by the inactivation of one of the four mismatch repair genes (MMR): *MSH2, MLH1, MSH6*, and *PMS2* [334,335] (Figure 76).On the other hand, 15%-20% of all colorectal cancers (CRCs) display MSI or abnormal Immunohistochemistry (IHC), which often refers to microsatellite instability (MIN) pathway[336]. Meanwhile, the remaining 80% to 85% of CRCs corresponds to microsatellite stable, but most of them are characterized by chromosomal instability (CIN pathway)[337].

A number of cross-sectional studies have demonstrated the implementation of biomarkers from blood as a non-invasive method for CRC screening, specially during the early stages[337]. Some of the markers evaluated were:

1. Proteins (hemoglobin) [338–340].

2. Deoxyribonucleic acid/DNA from intact cells or blood circulation (including methylation markers)

3. Ribonucleic acid/RNA (messenger RNA, non-coding RNA and microRNA)[341–343]

4. Genes (mutation)[344].

5. Low molecular weight metabolites (volatile organic compounds)[345].

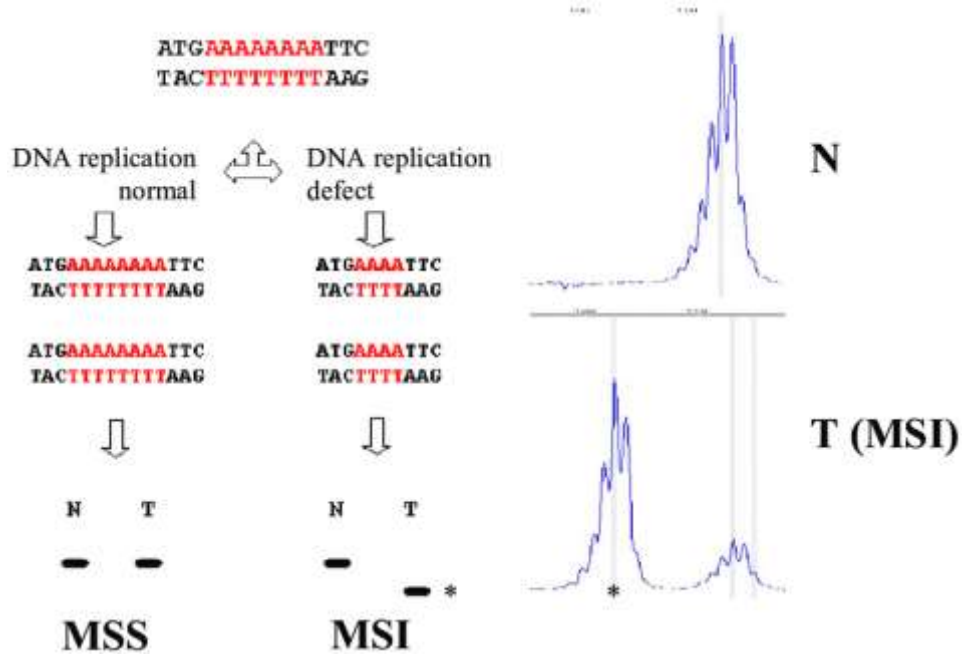

Figure 63.Microsatellite instability (MSI). When the tumor cells have normal MMR system the size of the microsatellite is the same in DNA isolated from normal (N) and from tumor (T) cells, which corresponds to microsatellite stable (MSS) tumor. But a defect in MMR leads a change in the size (in most cases becomes shorter) when comparing N with T DNA. This represents a microsatellite unstable (MSI) tumor. Asterisks in the graph indicate the microsatellite unstable tumor DNA fragment[346].

On the other hand, the benefits of liquid biopsy over the conventional tissue-based biopsies MSI testing includes rapid detection, non-invasive procedure, high concordance rate with tissue biopsy-based detection, high specificity, precision, and sensitivity; as well as, the ability to monitor genetic heterogeneity and the potential to enhance utility to help direct the clinicians beyond targeted therapies including immunotherapies[347,348].

In recent years, CTCs have emerged as a new approach in MSI research, due to they allow structural evaluation, molecular stratification of cancer phenotype and elucidate the tumor heterogeneity in CRC[349–351]. In 2020, studies performed by Toh et al revealed the relationship of MSI with the increase of CTCs release in intra-operative and post-operative stages[352]. Therefore, intact CTCs are a heterogeneous population of tumor cells with potentially resistant clones, also that means that the CTCs contain additional DNA information which could be scan all the MSI loci compared to the Circulating tumor DNA (CtDNA)[353]. Figure 77 shows the possible sources of DNA for MSI testing in liquid biopsy.

Other studies have revealed interesting finding such as the detection of MSI in some CTCs but no in the tumor[354], somatic mutations detected in CTCs are associated with CRC prognosis (ref), CEACAM5mRNA-positive CTCs from blood was identify as an adverse prognostic factor

correlated with poor clinical outcome in mCRC patients with MSI-high tumors[355]. Those findings highlight the clinical relevance of CTCs analysis to further predict the diseases outcome based on the CTCs count.

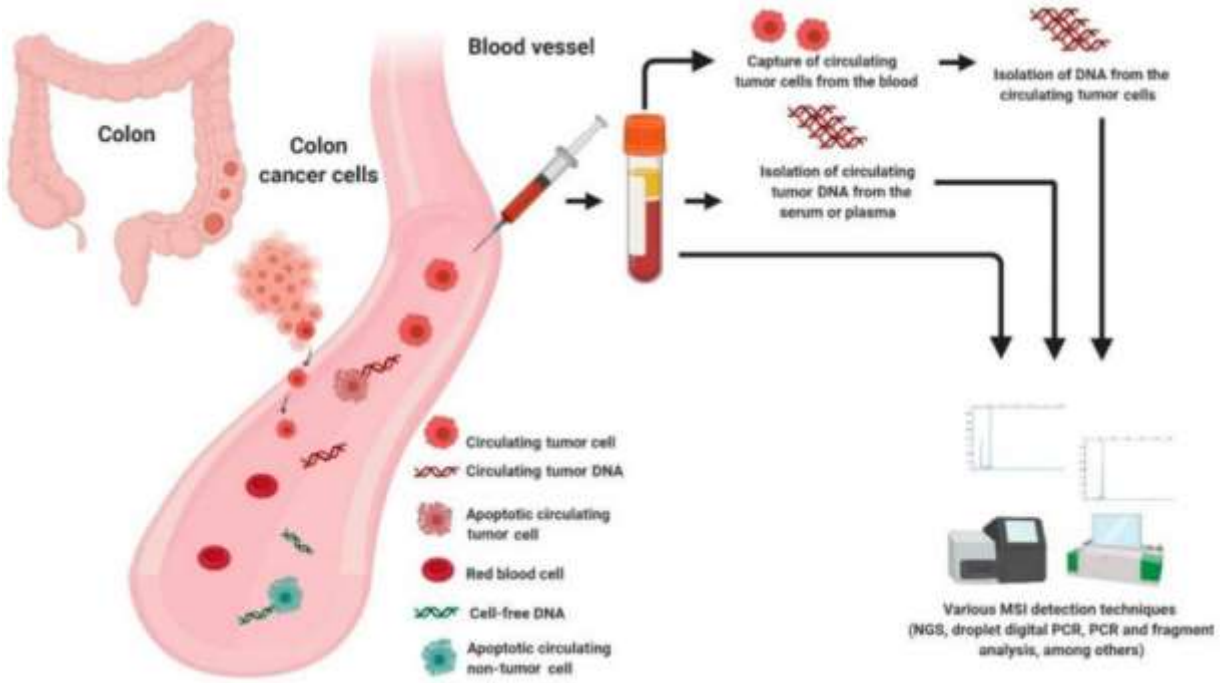

Figure 64.Possible sources of DNA for MSI testing in liquid biopsy.

9.1.2 BRAF mutation (V600E)

The *BRAF*^{V600E} represents between 8 to 10% of metastatic colorectal cancer (mCRC) patients and is recognize as a poor prognostic factor with a survival lower than 20 months[356].BRAF is known as a serine-threonine kinase playing a key role in the mitogen-activated protein kinase (MAPK)/extracellular signal-regulated kinase (ERK) signal transduction cascade (Figure 78). Its mutation causes an unsuitable activation of the pathway that leading an uncontrolled cell proliferation, migration, and angiogenesis[357].

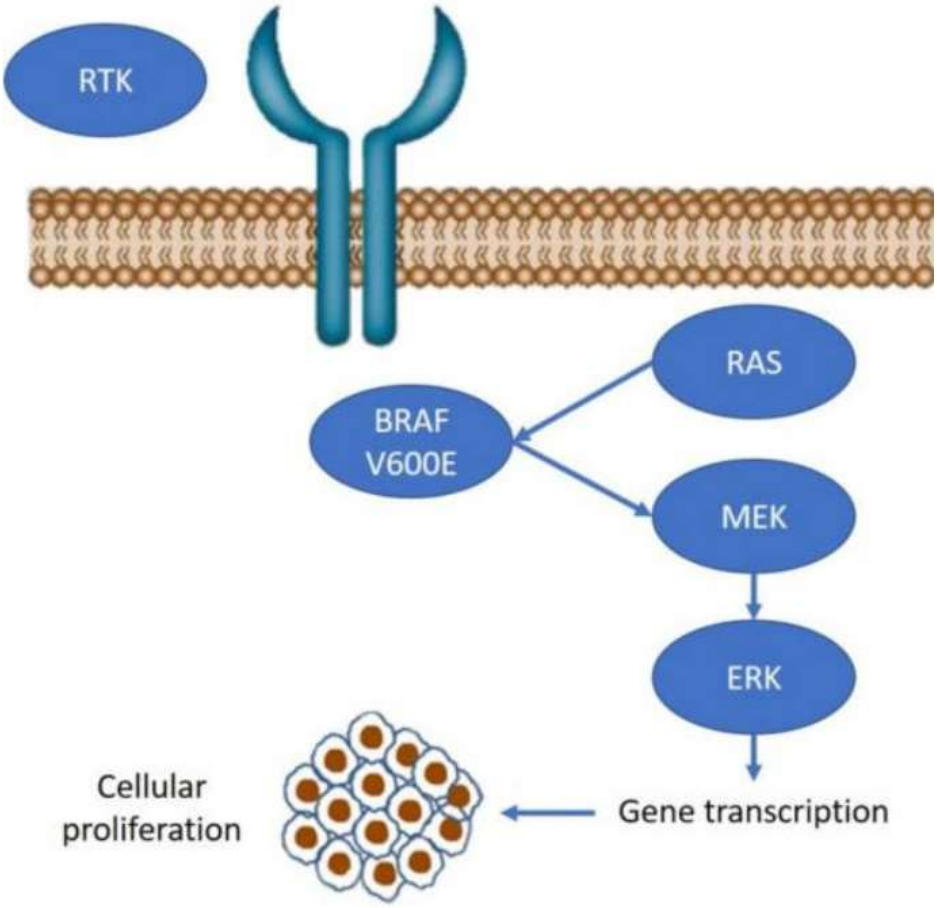

Figure 65. Mitogen-activated protein kinase (MAPK) pathway in BRAF V600E-mutated metastatic colorectal cancer (mCRC). RAS activates the RAF family proteins (ARAF, BRAF, and CRAF). Activated RAF proteins caused the phosphorylation and activation of MEK1/2 proteins, which subsequently phosphorylate and activate ERKs, which finally lead the cell growth.

9.1.3 KRAS mutation (G12C)

Kirsten rat sarcoma (KRAS) is a mutated oncogene in CRC, which is present in approximately 40% of all CRC cases. This activation caused the activation of the KRAS protein, which acts a a molecular switch to stimulate downstream signaling pathways, including cell proliferation and survival and leading the tumorigenesis process[358]. Activating mutations in KRAS are responsible to anti-EGFR therapy resistant in metastatic colorectal cancer (mCRC)[359,360]. Figure 79 shows the KRAS signaling pathway and relevant inhibitors.

On the other hand, previous studies that analyzed the KRAS mutations in CTCs and the KRAS status in matched with primary tumor, revealed the concordance of KRAS status between CTC

and primary tumors of 71%[361]. Existing data have demonstrated the clinical significance of CTCs in different stages of CRC including an early diagnosis, staging and prognosis[362,363].

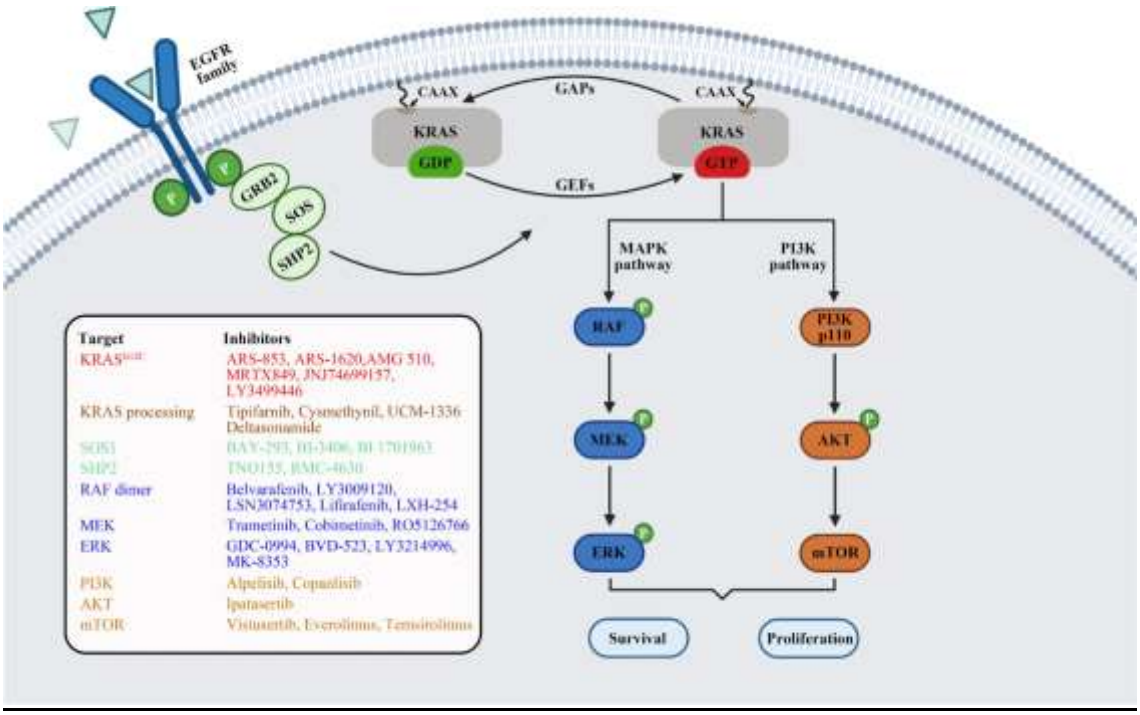

Figure 66.KRAS signalling pathway and relevant inhibitors of each node. After the activation of receptor tyrosine kinase, GRB2 combines with the guanine nucleotide exchange factor SOS and then interacts with KRAS protein that is attached to the cell membrane, thereby promoting KRAS activation. Intrinsic KRAS GTP-GDP cycling is regulated by GEFs and GAPs. Once *KRAS* is mutated, this cycle is disrupted, allowing mutant KRAS protein to accumulate in an active state and thereby persistently activating downstream MAPK and PI3K signalling cascade, resulting in cell proliferation and survival. Some KRAS inhibitors are listed in the box, which were developed to target each node of the KRAS signalling pathway and then evaluated in preclinical or clinical studies[364].

Traditionally, KRAS and BRAF mutations have been routinely detected in primary and metastatic colorectal cancer (CRC) cells, but rarely in CTCs. Nonetheless, the detection of mutations in CTCs could help to elucidate the mutational differences between tumor cells at local sites and distant metastases, which could improve the treatment outcomes [365].

Previous studies based on PCR sequencing for mutations of KRAS, BRAF and PIK3CA genes in CTCs shown similar mutations compared to tumor biopsies for 77.8% of patient samples. However, additional mutations were detected in CTCs[366]. Moreover, it has been demonstrated that CTCs counts differ significantly between patients with colorectal polyps

and those with nonmetastatic CRC[367]. Finally, the analysis of the metabolic profile of CTCs has demonstrated the potential for achieving an early diagnosis and differential diagnosis[368].

9.2 CTCs culture from patient samples

More recent attention has focused on the developments of CTC lines from cancer patients with metastatic CRC. Thus, the CTCs have been growing exposed to the conditions that promote the survival of self-renewing cells and maintaining their self-renewal and multilineage differentiation properties[369]. Fanny Grillet et al reported three CTC lines (CTC41,CTC44 and CTC45) from patients without chemotherapy with metastatic CRC (stage IV). Then, the cells were grown as spheres in suspension to promote the survival of cancer stem cells (CSCs) (Figure 80A). Moreover, it was demonstrated that the CTCs lines generated were able to initiate tumors when those were injected them subcutaneously in the flank of nude mice (Figure 80B,C).

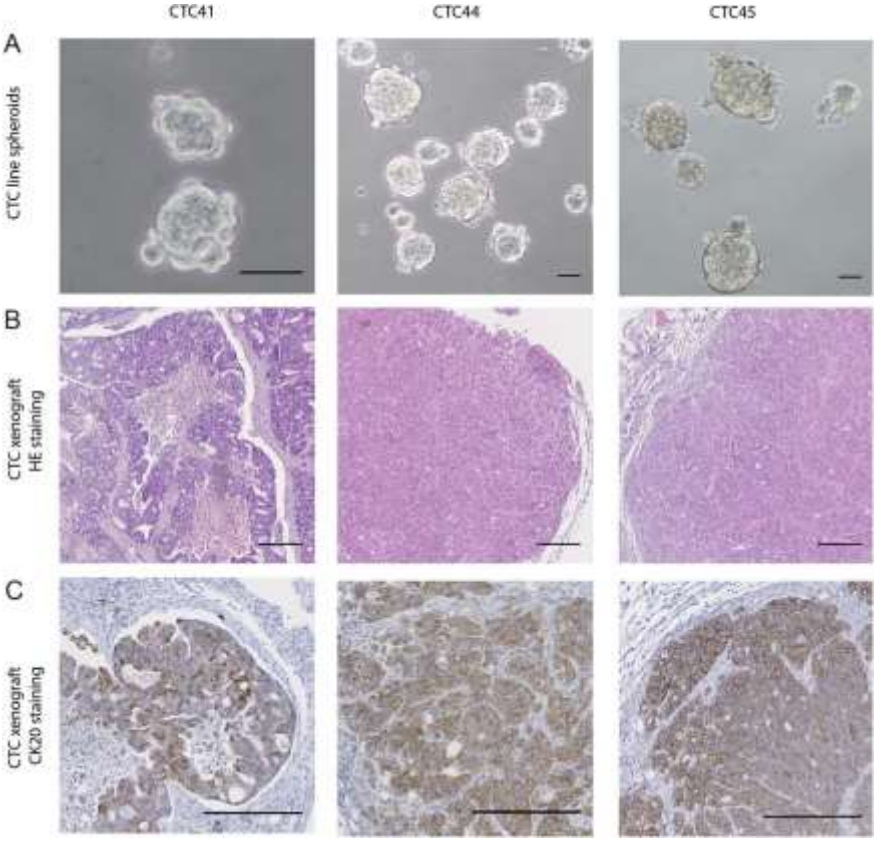

Figure 67. A. Spheroids formed by diffente circulating tumour cells (CTC41, CTC44 and CTC45) (scale bar 50 µm). B. H&E staining on tumours following subcutaneous injections of CTC lines into nude mice (scale bar 250 µm). C) CK20 staining on tumours following subcutaneous injections of CTC lines[369].

9.2.1 Workflow for pre-and post-processing of samples

The present study involved the optimization of the workflow for the pre-processing and post-processing of the blood samples from CRC patients between the Stem cells and cancer group lead by Dr. Hector G. Palmer at Vall d'Hebron University Hospital (VHIO) and the Nanobioengineering research group at Institute for Bioengineering of Catalonia (IBEC).

The workflow consists of 2 days. On the first day, 10mL of blood is collected in EDTA tube at Vall d'Hebron University Hospital with prior informed consent of the patient. The sample was sent to the IBEC the same day of the collection or maximum 36h post collection at room temperature. At day 2, the blood sample was processes through the spiral microfluidic device developed as was described in Chapter . The isolated CTCs collected from the microfluidic chip outlet (CTCs outlet) suspended in special cell culture media at 4°C was sent to VHIO. Once the sample collected arrived to the VHIO, it was cultured in Matrigel by Dr. Jordi Martinez Quintanilla. During the subsequent weeks of culture, follow-up was performed to assess the potential formation of organoids from the cultured CTCs. Figure 81 shows the experimental circuit overview.

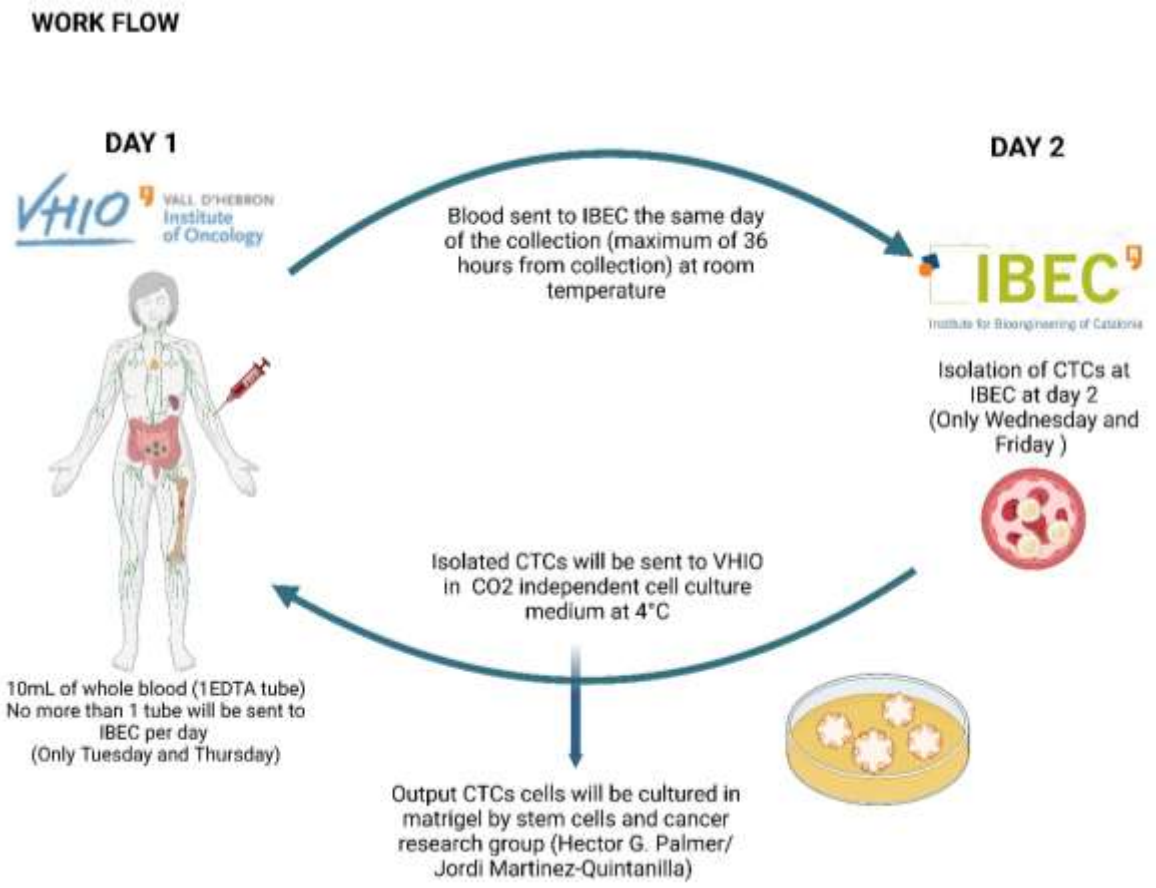

Figure 68.Workflow overview for the blood samples processing between VHIO and IBEC.

9.2.2 Workflow optimization with a blood sample from healthy donors and colorectal cancer cell line

In a coordinated manner between the Gastrointestinal and Endocrine Tumors Group at Vall d'Hebron Hospital and the Nanobioengineering Group at IBEC the sample processing circuit were optimized and established using a colorectal cancer cell line (SW480 cells) and blood samples from healthy donors as controls.

First, 10mL of blood sample from healthy donors was spiked with 100 SW480 cells/mL as CTCs model. 1mL of blood sample was diluted 10X using special cell culture media (8ml de $C0_2$ independent cell culture media supplemented with 2ml de FBS (20% FBS), 40µl Primocin (1/250), 10µl of 10mM de inhibidor de RhoKinase Y-27632 (1/1000) or lysis for increasing the throughput. As described in previous chapters, the blood sample is perfused through the " Sample inlet port". Meanwhile, the other input is used for perfused PBS1X or

sheath flow ("sheath inlet port"). However, in this case, PBS1X was not used as sheath flow, but the special cell culture media $C0_2$ independent supplemented as previously described was use. Moreover, in this case, the cancer cells were not stained and only the focalization of blood cells were checked as a critical mark of the proper chip functioning. Figure 82 describes the overall methods for processing the blood samples through the spiral device.

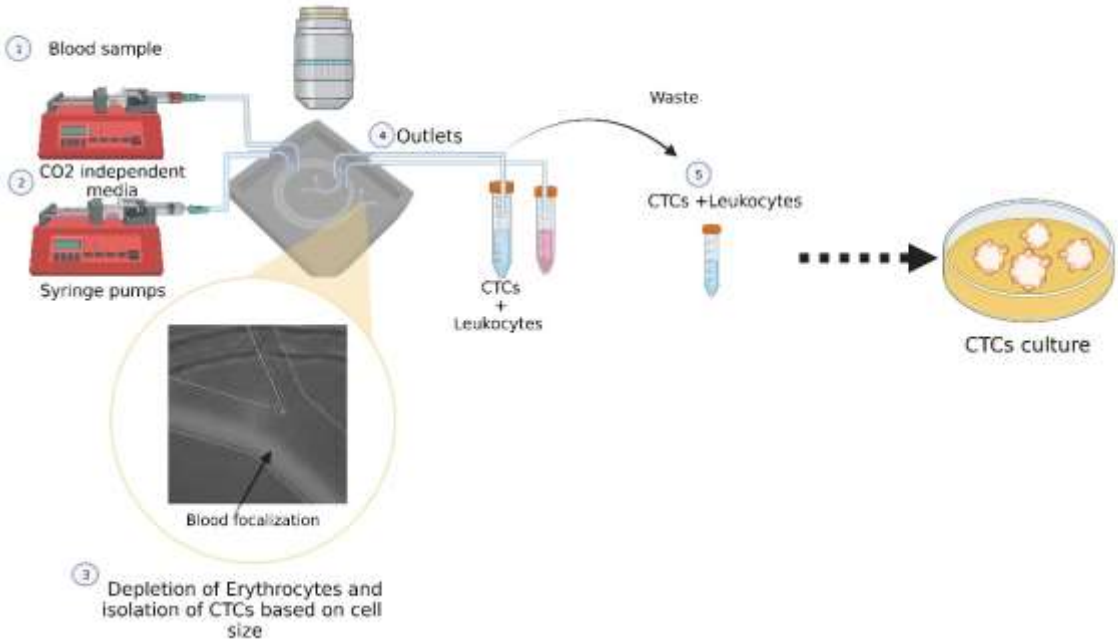

Figure 69.Schematic representation of the microfluidic setup for the processing of patient samples. 1) Syringe pump for perfusion of blood sample diluted in CO2-independent medium or lysate. 2) Syringe pump for perfusion of CO2-independent media. 3) The focalization of the blood sample is checked by microscopy in Bright Field (BF). 4) The samples are collected in the chip outputs (CTCs+ Leukocytes and waste (blood cells)). 5) The CTCs sample collected is cultured in Matrigel.

On the other hand, it is important highlight that the traditional cell culture media is composed by sodium bicarbonate as the primary buffer, because of that a carbon dioxide (CO_2) rich atmosphere of five to ten percent in air is required to maintain the in vitro environment at physiological pH, that means it does not allow work outside of the CO_2 regulated atmosphere for extended periods of time because of the extreme fluctuations in pH, which can affect the cellular functions[370]. Moreover, our experimental conditions required keep the cells alive not only during their separation through the spiral microfluidic device, but also during its transportation up to the Hospital. Therefore, in our method we used a CO_2 Independent media (with or without phenol red), which contains a unique buffering system composed of mono and dibasic sodium phosphate and ßglycerophosphate. Thus, this kind of media has been formulated with components that enhance the cellular production and utilization of

CO_2, then an external source of CO_2 is not required for the maintenance of CO_2 dependent cellular functions[371].

Moreover, adding ROCK inhibitor Y-27632 (Rho-associated coiled coil protein kinase or ROCK)) to our method allows to prevent the apoptosis of isolated CTCs, increases their survival rate, cell adhesion, proliferation, planting efficiency and enhance the colony formation efficiency, as well as, increases post-thaw cell survival and post-passaging cell viability[372,373]. The Rho kinase is the major downstream effector for the small GTP-binding protein Rho, and is involved in various biological processes including cell mitosis adhesion, cytoskeletal adjustments, muscle cell contraction, tumor cell invasion, among others[374].

The results revealed that our system can successfully isolated the SW480 CRC cells, with a high depletion rate of Erythrocytes demonstrated by the focalization of blood through the waste output recording by video (Figure 83A, Supplementary video 1), as well as, the sample collected from each outlet revealed clear differences (Figure 83B). Finally, the samples collected from the “CTCs chip outlet” were centrifuge for 5 minutes at 600g and successfully seeding. After 16 days post seeding was possible to visualized that the cells grow correctly (Figure 83 C). Therefore, it demonstrated that the collected cells were viable for subsequent cultivation.

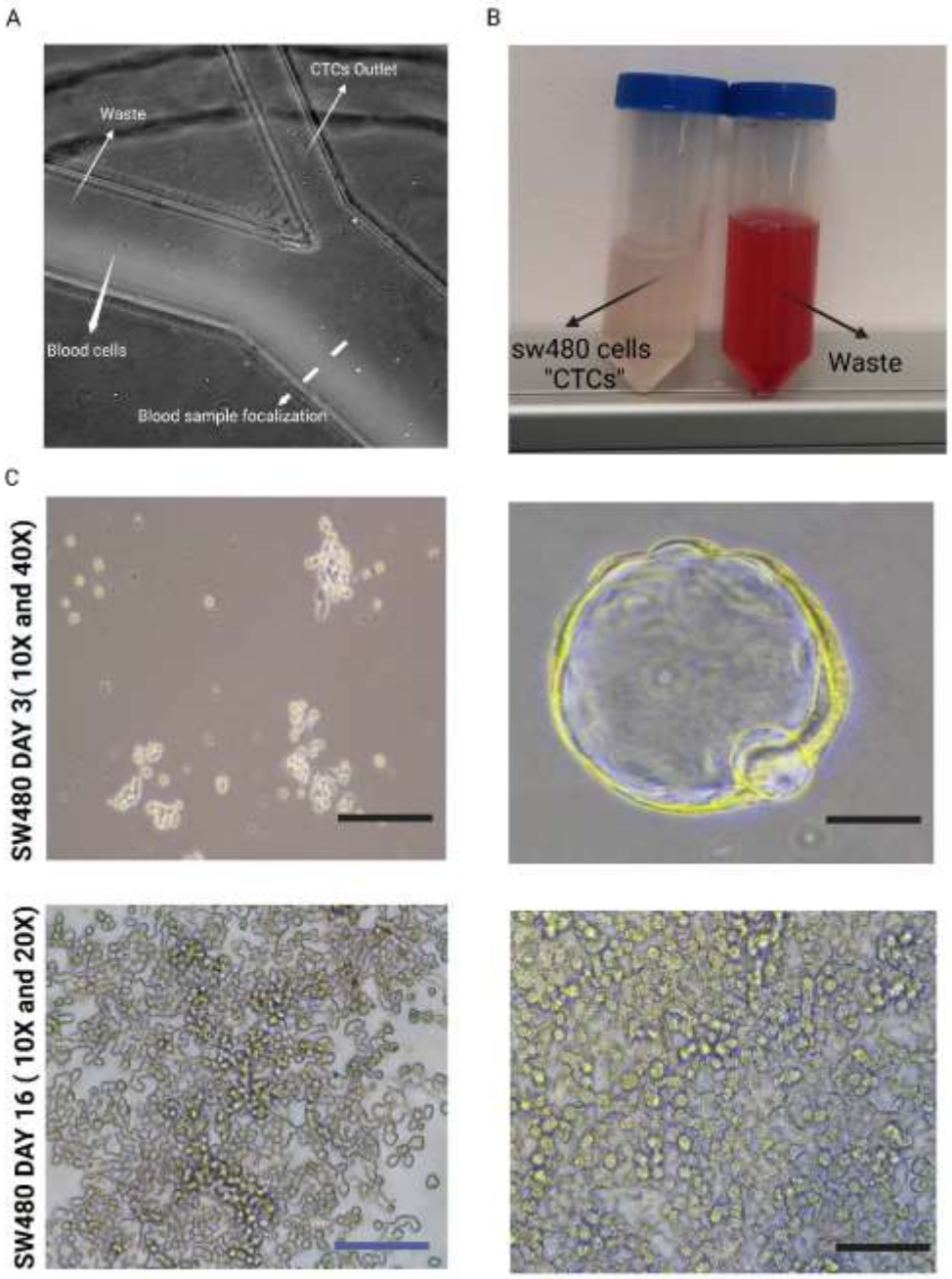

Figure 70. A) Focalization of the blood sample spiked with SW480 colon cancer cells. B)Sample collected from the chip outputs. CTCs output: “SW480 cancer cells”. Waste output: “Blood cells “. C) SW480 cancer cells collected from the chip, 3 and 16 days post-culture. Scale bars 100µm (10X), (20X) and (40X).

9.3 Processing of first blood sample from CRC patient

Following the same procedure previously optimized, the first sample from CRC samples was processed through the spiral device. As result, the sample was successfully processed though the spiral device, the focalization of the blood sample was guaranteed and checked by microscopy (Figure 84A, Supplementary video 2). Moreover, the sample collected from each outlet revealed clear differences (Figure 84B).

Although the key steps during the separation process were verified and guaranteed such as the targeting of the sample through the "Waste chip outlet" and the clear difference in appearance of the samples collected by each outlet was observed; the culture of the collected CTCs did not yield conclusive results. After 3 days of culture in Matrigel, some potential spheroids were observed, however, their growth was not observed in the following days.

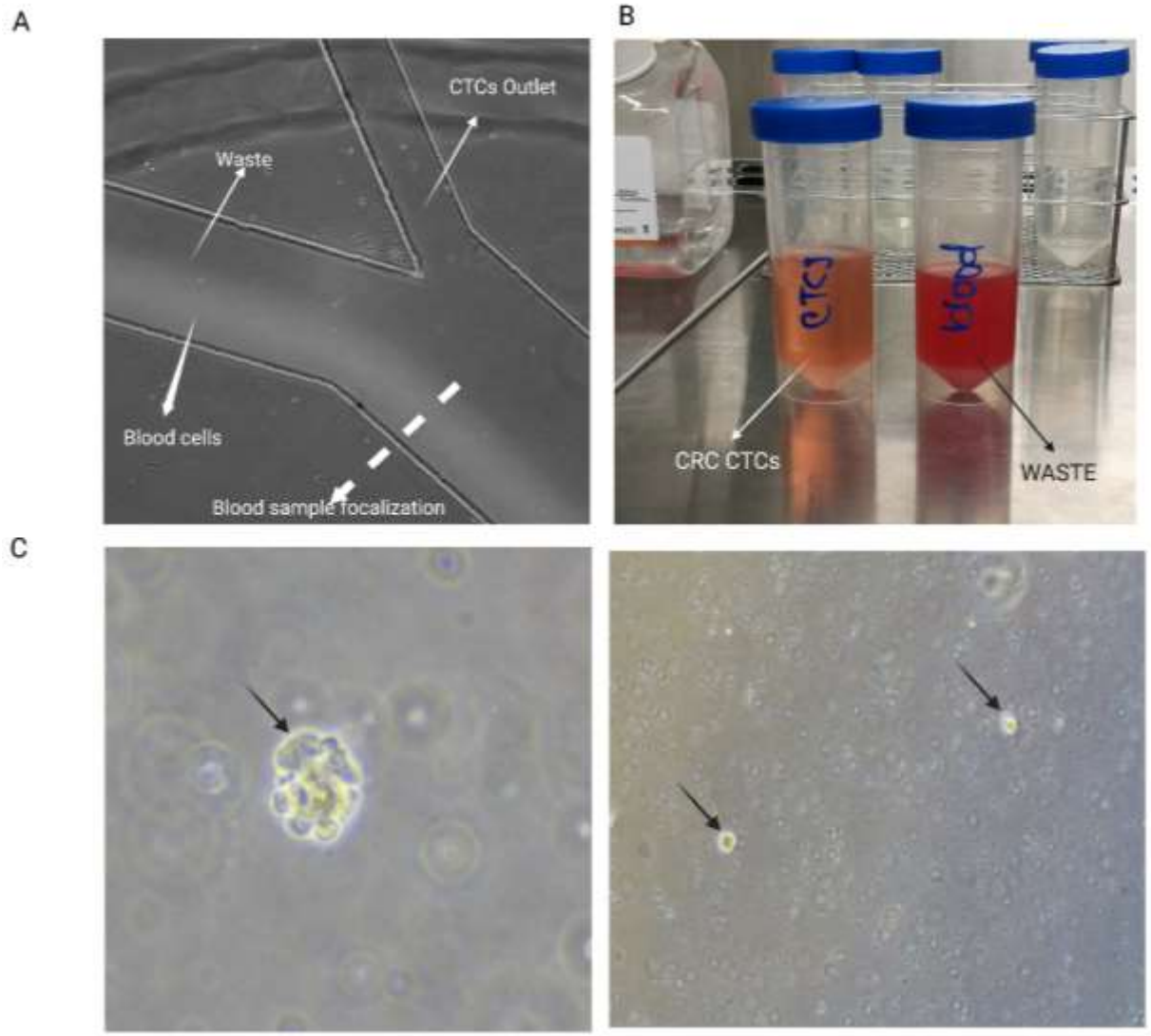

Figure 71.A) Focalization of the blood sample from CRC patient. B)Sample collected from the chip outputs. CTCs output: “CRC CTCs”. Waste output: “Blood cells “. C) Potential Spheroids formed by circulating tumour cell from CRC patient sample (black arrows).

9.4 Discussion

Prior studies have noted the importance of the cultivation of CTCs from the clinical perspective, highlighting that can be useful in predicting drug sensitivity for each patient, and treatment resistant. Moreover, the evidence suggest that the cell lines derived from CTCs display phenotypical characteristics that match with those cells present in tumor tissues, as well as these population express molecular features related to metastatic competency,

stemness properties [375] . Unfortunately, the expansion of CTCs in vitro is complicated and currently represents a big challenge to establish long-term CTC cultures.

Despite the absence of conclusive results regarding the spheroids formed by CTCs from the first CRC sample patient during this study. It was possible to establish a global workflow for the processing of the samples, correct handling, and transportation under optimal conditions for guaranteeing the cell viability using cell lines.

However, it is important to consider that this study has some limiting factors such as the availability of samples that meet the established requirements and the limited sample volume per patient. To develop a complete picture of the potential establishment of CTC lines derived from the different phenotypes of CRC patients, it will be necessary to complete the study with the remaining 14 patients. Moreover, could be crucial to compare the method developed in this thesis with the standard CellSearch®, to enumerate the CTCs recovered as an intermediate check point prior to the sample cultivation. Other studies suggested that more than 300 CTCs are required for successful culture[376], therefore, this is a parameter that could be considered for the following tests.

In conclusion, the *ex-vivo* expansion of CTCs represent a big tool of providing more information to offer the best therapeutic option possible to cancer patients, detecting new biomarkers, potentially predict drug sensitivity and eventually leading to personalized treatment strategies. However, the establishment of CTC lines represents a tremendously challenging, which still requires further optimizations to allow the translation into the clinic. The future perspectives of the Nanobioengineering research group will involve finalizing the present study and hopefully develop one method for the establishment of CTCs lines from CRC patients with different phenotypes.

Chapter 10

Discussion

Since liquid biopsies have emerged as a remarkable technology, researchers have shed light on CTCs as biomarkers for cancer diagnosis, prognosis and monitoring[377,378]. Nonetheless, there are a lot of challenges raised by their isolation, given their phenotypic, size heterogeneities, rarity among the blood cells and the need to preserve their viability for subsequent downstream analysis. In order to overcome the challenges previous exposed, microfluidic devices have emerged as promising tools for their isolation. As mentioned in the literature review, there is only one CTC test approved by the FDA, the CellSearch® system by Menarini Silicon Biosystems[300] .This system uses for quantifying the CTCs based on the EpCAM expression, considered as universal biomarker for epithelial-derived cancer types[302]. Nevertheless, the discovery of the CTCs heterogeneity and the existence of EpCAM-negative cancer cells[303] has revealed one of the major limitations of this method. To overcome these limitations, this work proposed the design and development of microfluidic technologies based on different approaches and fabrication methods with the final goal of obtaining a purified CTCs samples viable for subsequent analysis.

The current research was able to recreate a biomodel based on the formation of multicellular tumor spheroid by the cyclo-rgDfK(TPP) peptide as CTCs model. The results demonstrated that our model successfully recreates the key features of the CTCs related to the E-cadherin expression, and the loss of its expression in association with the epithelial-mesenchymal transition (EMT) that occurs during tumor metastasis[304]. Another important finding was the cell viability higher than 90%. The implementation of this model for the characterization and optimization of the microfluidic devices allowed to reduce the vias in the results caused by the tendency of attachment of the cancer cell lines to the microfluidic device surfaces. This model represents a significant advantage over previous studies, since the use of an appropriate cellular model in the early stages of characterization of devices such as the Herringbone has not been reported [142,149,201,310,379].

An initial objective of this study was to perform the design and the numerical simulation in COMSOL MULTIPHYSICS of a microfluidic device based in the inertial separation of CTCs from leukocytes and erythrocytes in a spiral microchannel. Thus, we successfully determine the trajectories of different size particles and the optimal microchannel height by the numerical simulation which were successfully compared and validated with images obtained with a microscope in an experimental set up using fluorescent beads with different sizes as CTCs and blood cells (6 µm, 10 µm, 15 µm and 20 µm). Moreover, the computational model was validated by experiments with blood samples from healthy donors spiked with breast cancer (MCF-7, 20µm) and different non-small lung cancer cells (A549 and H1437 cells). One interesting finding was the validation and confirmation of the results from the computational simulation with the experiments, which revealed a higher CTCs recovery rate (93.7±8.6%, 92.9±9.8% and 96.7±3% for MCF-7 (20µm), A549 (15 µm) and H1437 (15.7 µm) cells, respectively) under flow rates of 900 µL/min for PBS 1X and 100 µL/min from 10x diluted sample. Moreover, the experiments with fluorescent particles of 15 µm and 20 µm as the CTCs model demonstrated high recovery rates of 94% and 96%, which is similar to the rates obtained with cancer cells. The findings exposed in this study broadly supports the work of other studies performed by Warkiani et al [267], who based on FACS analysis of the samples recovered from the spiral microfluidic device, reported a high cancer cell recovery (>85%), enrichment ratio of 10^9 fold (over RBCs) ,10^3 fold (over leukocytes) and high cell viability (98%) [278] .In contrast, our findings reveal an improvement in the throughput (6ml/hr) compared to the of 3mL/hr reported by them. Thus, we successfully introduced a high throughput blood separation method based on ‘‘Dean Flow Fractionation (DFF)’’, where the use of an additional sheath buffer in our spiral device facilitates the Dean migration of RBCs in a controlled manner under a haematocrit of 4%, which differs from other reported to be 20-25%[266] .

In contrast, a high throughput could be achieve including a blood lysis as a previous step to the separation in the spiral microfluidic device. Nevertheless, this leads to losing up to 7% of the target cancer cells, which could be compensated by an increase in leukocyte depletion. . These results are consistent with the total cell loss due to lysis and centrifugation reported by Warkani et al (8%)[278,279].In addition, the use of this device displays a big potential as a label free isolation method with high erythrocytes and leukocytes depletion of 99.9±0.01% and 84±1.87% respectively. We also demonstrate that the 4% of haematocrit is required to achieve a higher cancer cell recovery and blood cells depletion rates

Our results are consistent previous studies demonstrated how the extremely high cell concentration of undiluted blood make the cell separation impossible caused by the intense cell-cell interactions[276] .Moreover, the relatively high viscosity of undiluted blood would

increase the difficulty of sample transportation and introduction. Despite, a higher degree of dilution would lead to better separation, this results in an increase of processing time[276] . Di Huang and colleagues reported a dilution of blood 100x in their experimental characterization and a throughput of 400 µL/min. In contrast, our study demonstrated that extremely higher dilution is not necessary to achieve optimal results, since a blood dilution of 10x lead a proper cell separation and blood cells depletion with a throughput of 100µL/min. Finally, our findings are consistent with the previous work of Bo-Wen Li et al, where 4% of haematocrit (10 fold dilution) was required for guarantee a correct cell distribution in the channel, and in consequence a higher cancer cell recovery and blood cells depletion rates[277]

Considering the results exposed in this thesis, we demonstrated how the computational modelling of spiral microfluidic devices for CTCs separation could be applied to define the best geometry of the device and operational conditions to achieve the highest efficiency depending on the target cell population. In addition, this device could be used to isolate even small CTCs that do not express EpCAM, and otherwise could not be separated in CTC label-dependent commercial approaches.

The findings exposed in this study broadly supports the work of other studies performed by Warkiani et al [267], who based on FACS analysis of the samples recovered from the spiral microfluidic device, reported a high cancer cell recovery (>85%), enrichment ratio of 10^9 fold (over RBCs) ,10^3 fold (over leukocytes) and high cell viability (98%) [278] .In contrast, our findings reveal an improvement in the throughput (6ml/hr) compared to the of 3mL/hr reported by them. Thus, we successfully introduced a high throughput blood separation method based on ‘‘Dean Flow Fractionation (DFF)’’, where the use of an additional sheath buffer in our spiral device facilitates the Dean migration of RBCs in a controlled manner under a haematocrit of 4%, which differs from other reported to be 20-25%[266] .

With respect to the second research question, we successfully design and manufacture an affinity-binding microfluidic device to selectively capture white blood cells. In our particular application, we achieved to implemented a chemical surfaces functionalization with a mix-SAM composed by organosilanes with poly(ethylene glycol) (PEG). In fact, the presence of Silane-PEG-OH was used to reduce the non-specific binding of the CTCs. Moreover, the results of the computational study demonstrated the impact of the grooves structures creating the localized mixing with an increase in the velocity profile when the flow rate increase from 10µL/min to 20 µL/min, which can be translate in an improvement of the probability of capturing leukocytes in the chip surface. The key role of the grooves in the leukocytes capture was ratified experimentally where in absence of the 76 set of grooves in a channel functionalized with a mix-SAM the cells tended to go straight and only 6±8.4% of leukocytes were capture in the chip surfaces.

Another finding that stands out from the results reported earlier is the recovery rate of CTCs from the chip outlet in solution between 80±3.6% and 85±7% (1000 cells/mL), which demonstrated the potential of the silane-PEG-OH in reduce the unspecific binding in 76 set of grooves under a flow rate of 20µL/min as well as the capability of this device of providing viable cancer cells in solution for further analysis (>90%).Therefore it is not necessary to carry out extra steps for the collection of CTCs from the chip surfaces, and can be used for all types of cancer regardless of EpCAM expression levels. These results highlight the advantages of our system compared to other previously reported technologies such as the microvortex-generating herringbone-chip developed by Shannon L. Stott, where 79% ± 4.5% of 5000 PC3 prostate cancer cells per milliliter were captured in the device surfaces, which implies that subsequent trypsinization or lysis must be done to collect the cells[310].In addition to being limited to capturing CTCs based on EpCAM expression levels.

In addition, the computational model supported together with the experimental characterization, allows us to estimate the number of grooves required to guarantee the capture of the total population of leukocytes that contaminate the sample of CTCs that are collected at the output chip. In this way, our results reveal that to eliminate all the leukocytes that contaminate a sample of blood spiked with CTCs model previously diluted and preprocesses to remove the erythrocytes, 228 sets of grooves are required, which is equivalent to 3 herringbone chips. In fact, two different factors were calculated experimentally in this study, one from cell lines (14.30) and the other from a blood sample (20.3). These factors could serve as support for the computational model to achieve a real approximation of captured cells using a certain amount of set of grooves from different types of samples as a source (cell lines or blood). It is worth noting that the difference between these two factors may be associated with the different characteristics of the samples that may influence the results of the capture efficiency. Since, in the first part of this study cell lines were used to recreate the targeted model (Leukocytes), with which there is a more homogeneous population in the expression levels of CD45 (Kasumi-1). Meanwhile, when leukocytes from blood samples are used, there is a heterogeneous population in terms of CD45 expression levels. This fact has been supported by previous studies, where it was demonstrated that the expression of CD45 was the highest on lymphocytes (279.3±101,4), intermediate on monocytes (52.3±15.1), and the lowest on granulocytes (26.8±7.8)[311]

Finally, the depletion obtained from 76 set of grooves employing a blood sample, can be translate into CTCs sample purity of 50%. Comparing this results with those ones obtained by Shunqiang Wang and colleagues, who reported a purity with the grooved-HB chip and the wavy-HB chip of 36.7% ± 2.2% vs. 25.6% ± 1.7% and 39.4% ± 4.3% vs. 25.7% ± 2.1%,respectively under different shear rates conditions[312] ,with our method is possible to

improve the purity over 10%. In fact, we provide a strategy for potentially achieve a complete depletion of leukocytes and in consequence have more chance of increasing the purity of the CTCs sample.

On the other hand, the results of this study showed the potential application of the 3D printing in the fabrication of functional microfluidic devices based on the principle of inertial forces and applied the negative enrichment principle for capturing leukocytes on beads surfaces, and subsequently separate them from the CTCs using a spiral microfluidic device. The most important finding was the validation of the computational model with particles of 70µm and 20µm as target models in the 3D device, where up to 75±17% of bigger particles functionalized with CD45 antibodies were separated and 100% of small particles as CTCs model were recovered. In addition, the preliminary evaluation of the method for anchoring leukocytes in particles with CD45 antibodies could open new approaches for leukocyte depletion from CTC populations using microfluidic spiral devices. However, the results revealed a maximum leukocyte capture efficiency of 48%, which is why future work requires an improvement in the optimization of the leukocytes capture method, such as the incubation time and sample conditions.

In Overall, if we consider all the results from the two different spiral microfluidic devices, we propose that it could be possible achieve a total leukocyte depletion up to 91% and a maximum cancer cells recovery up to 95%, which would represent an increase in the cancer recovery rate compared to the results reported by Warkiani et al ([323]).

The negative enrichment approaches previously exposed are advantageous not only because it leads to unbiased detection of CTCs regardless of EpCAM expression levels, but also produces intact tumor cells free of attached biomarkers, eliminating potential artifacts in subsequent studies. Although, the depletion of leukocytes through immunocapture on functionalized surfaces is not practical to be used in high blood volumes directly. The use of negative enrichment methods accompanied by the prior depletion of red blood cells opens new avenues for their potential application in clinical practice.

Moreover, this study set out with the aim to overcome the limitations of the traditional microfluidic set ups composed by syringe pumps and bigger microscopes with the invention of a low-cost fluidic platform using micropumps, Raspberry Pi and coding in open-source software (Python). This platform offers multiple advantages over traditional syringe-based perfusion systems, such as the processing of large sample volumes, it allows the creation of closed flow circuits for sample recirculation, and it is a compact and portable system that does not require the use of large microscopes.

The most interesting finding using this platform was the increase in sample processing performance at 3.3mL/10min compared to previously reported studies 3mL/h[142] , or using the traditional microfluidic set up previously reported in chapter 5 (∼1mL/10min). Another important finding was the high depletion rates of erythrocytes and leukocytes cells equivalent to those obtained using syringe pumps (97.5±1.89% and 83.4±3.6%), which reveal not only the potential application of this compact system, but also offer the advantage of speeding up the processing of real blood samples from cancer patient.

One of the biggest challenges of this study was validate the microfluidic devices with real samples from colon cancer patients. Particularly, the possibility of their cultivation which can be useful in predicting drug sensitivity in personalize medicine as well as treatment resistant. In our particular case and due to the impossibility of constantly accessing patient samples, it was only possible to process 1 sample from a patient with colon cancer through the spiral device. Unfortunately, no conclusive results of spheroid formation were obtained after 3 days of culture in Matrigel. This confirms the complexity of selecting the most appropriate technique and culture conditions for CTCs that allow their expansion as has been previously reported in the literature. In this context, the critical challenge is related to the high rate of heterogeneity of the CTCs, which overcomplicate the implementation of certain culturing options and in consequence affect the succeeding of the ex vivo CTC propagation[380]. In fact, previous investigations reported that in few samples was possible to obtain a long-term CTCs cultures (ref). In contrast, others reports that in most cases the CTCs were efficiently maintained in culture for a short period of 14 days with rare exceptions up to 50 days [380–385].In 2018 were able to establish durable CTCs cultures and permanent CTC lines from colorectal cancer patients[386,387]. Despite the absence of conclusive results regarding the spheroids formed by CTCs from the first CRC sample patient during this study. It was possible to establish a global workflow for the processing of the samples, correct handling, and transportation under optimal conditions for guaranteeing the cell viability using cell lines. Moreover, other studies suggested that more than 300 CTCs are required for successful culture[376], therefore, this is a parameter that could be considered for the following tests.

Therefore, considering the results previously reported in the literature, we will have a great challenge for the successful processing and culture of the CTCs of the remaining 14 patients included in this study. Moreover, could be crucial to compare the method developed in this thesis with the standard CellSearch®, to enumerate the CTCs recovered as an intermediate check point prior to the sample cultivation. The future perspectives of the Nanobioengineering research group will involve finalizing the present study and hopefully develop one method for the establishment of CTCs lines from CRC patients with different phenotypes.

In overall, the limitations of this work are related, first of all, to the poor accessibility of samples from patients with colon cancer due to multiple factors such as the required patient profile, since they had to be patients who had not previously received treatment. . Furthermore, the pandemic situation completely blocked access to blood samples from both healthy patients and cancer patients. Regarding the quantification of low concentrations of the CTCs biomodel, limitations were faced such as the impossibility of doing so with flow cytometry due to the limitations of the method and the risk of losing CTCs in subsequent centrifugation steps. Furthermore, in the case of the spiral microfluidic device, high volumes of blood were obtained at the outlet due to the need to dilute the sample; likewise, a high volume of blood could not be processed in a short time in the stages. However, the implementation of blood sample lysis and the invention of the low-cost electronic platform previously presented made it possible to solve these limitations during the study. Finally, regarding the complexity of modelling microfluidic devices in COMSOL, they were limited to the available computing resources.

Despite the promising results regarding the high rate of CTC isolation using the proposed biomodel, the maximum rate of red and white blood cell depletion combining the different approaches developed during this work, as well as the development of a low-cost platform that allow overcoming the barriers of microfluidic configurations to process large volumes of blood; questions still remain regarding the efficiency of those approaches in isolating CTCs from real cancer patients and their subsequent expansion in culture, which are expected to be answered in future work in the Nanobioengineering research group when the remaining 14 patient samples from colon cancer will be processed using the microfluidic devices developed during this thesis.

Chapter 11

Conclusions

- Size-based separation microfluidic module was successfully designed and fabricated for isolating CTCs bigger than 12 µm. The numerical simulations developed allowed to stablish the parameters for achieving the optimal device performance for this particular case, such as flow rate of 900 µL/min for the sheath-flow and 100 µL/min for the blood sample, as well as channel height of 152µm. In fact, we demonstrated how the computational modeling of spiral microfluidic devices for CTCs separation could be applied to define the best geometry of the device and operational conditions to achieve the highest efficiency depending on the target cell population. In addition, this device could be used to isolate even small CTCs (10 µm) that do not express EpCAM, and otherwise could not be separated in CTC label-dependent commercial approaches. Moreover, 4% of hematocrit is required for guarantee a higher cancer cell recovery from 93.7±8.6% to 96.7±3% and blood cells depletion rates of 99.9±0.01% and 84±1.87% for erythrocytes and leukocytes, respectively.

- Two different modules were successfully manufactured to achieve the selective isolation of CTC from remaining white blood cells. First, the Herringbone chip was designed, and the computational model allowed to stablish as an optimal flow rate of 20 µL/min for creating the focalization mixing in the grooves structure. Moreover, we successfully implemented a chemical surfaces functionalization in the Herringbone chip with a mix-SAM for capturing the leukocytes. Thus, one device composed by 76 sets of grooves allowed effectively recover up to 85±7% of CTCs, the depletion of leukocytes up to 43±0.90% and purity of 50%. In addition, this study provides two different factors which could serve as support for the computational model to achieve a real approximation of captured cells using a certain amount of set of grooves from different types of samples as a source (cell lines or blood).

- For the second module, an 3D printing spiral device was successfully designed, simulating in COMSOL and fabricated, generating a modular system that allow to collect cancer cells from blood samples and reduce the leukocytes contamination from the samples obtained. We successfully implemented a method for immobilize up to 48% of leukocytes in the surface of 70 µm particles, and its subsequent separation

using 3D printed spirals with a depletion efficiency of 70% and achieved a 100% recovery of the CTC model. Finally, these devices of providing viable cancer cells in solution for further analysis (>90%) and can be used for all types of cancer regardless of EpCAM expression levels.

- We successfully recreate a in-vitro biological model of CTCs based on the formation of multicellular tumor spheroid by the cyclo-rgDfK(TPP) peptide, guaranteeing cell viability higher than 90% and recapitulating one of the key features of the CTCs related to the loss of E-cadherin expression during the tumor metastasis .The implementation of this model for the characterization and optimization of the herringbone chip with cancer cell lines, allowed to reduce the bias in the results caused by the tendency of attachment of the cancer cell lines to the PDMS microfluidic device surfaces.

- We successfully developed a low-cost, portable, and scalable flow read-out platform that is easy to use and fully programmable. This platform can be used together with spiral microfluidic devices for cancer cell isolation and can also be adapted to other fluidic applications as well as, has the potential of being use in clinical settings. The results have demonstrated the feasibility of using micropumps for isolating viable cancer cells (>90%), and the ability to replace traditional syringe pumps with high-efficiency cancer cells separation using microfluidic spiral devices (>80%).

- It was possible to establish a global workflow for the clinical proof of concept for the processing of blood samples from colon cancer patients considering 3 different phenotypes: microsatellite instability (MSI), BRAF mutation (V600E) and KRAS mutation (G12C). Sample management protocols were successfully established during processing and transportation, guaranteeing its viability. However, given the limitations for the availability of the samples, it was not possible to conclude the successful cell culture after the application of the optimized workflow during this investigation.

References

1. Global Cancer Observatory: Cancer Today.
2. International Agency for Research on Cancer, GLOBOCAN 2020.
3. Promoting cancer early diagnosis.
4. Understanding What Cancer Is: Ancient Times to Present.
5. Bethesda (MD): National Institutes of Health (US). National Institutes of Health (US); Biological Sciences Curriculum Study. NIH Curriculum Supplement Series. (2007).
6. Welch, D. R. & Hurst, D. R. Defining the Hallmarks of Metastasis. *Cancer Res* **79**, 3011–3027 (2019).
7. Effect of O-GlcNAcylation on tamoxifen sensitivity in breast cancer derived MCF-7 cells. . (2013).
8. Hanahan, D. Hallmarks of Cancer: New Dimensions. *Cancer Discov* **12**, 31–46 (2022).
9. Bhowmick, N. A., Neilson, E. G. & Moses, H. L. Stromal fibroblasts in cancer initiation and progression. *Nature* **432**, 332–337 (2004).
10. Cheng, N., Chytil, A., Shyr, Y., Joly, A. & Moses, H. L. Transforming Growth Factor-β Signaling–Deficient Fibroblasts Enhance Hepatocyte Growth Factor Signaling in Mammary Carcinoma Cells to Promote Scattering and Invasion. *Molecular Cancer Research* **6**, 1521–1533 (2008).
11. Steeg, P. S. Tumor metastasis: mechanistic insights and clinical challenges. *Nat Med* **12**, 895–904 (2006).
12. van Zijl, F., Krupitza, G. & Mikulits, W. Initial steps of metastasis: Cell invasion and endothelial transmigration. *Mutation Research/Reviews in Mutation Research* **728**, 23–34 (2011).
13. Fares, J., Fares, M. Y., Khachfe, H. H., Salhab, H. A. & Fares, Y. Molecular principles of metastasis: a hallmark of cancer revisited. *Signal Transduct Target Ther* **5**, 28 (2020).
14. Friedl, P. & Wolf, K. Tumour-cell invasion and migration: diversity and escape mechanisms. *Nat Rev Cancer* **3**, 362–374 (2003).

15. Wu, J. *et al.* Plasticity of cancer cell invasion: Patterns and mechanisms. *Transl Oncol* **14**, 100899 (2021).

16. Lamouille, S., Xu, J. & Derynck, R. Molecular mechanisms of epithelial–mesenchymal transition. *Nat Rev Mol Cell Biol* **15**, 178–196 (2014).

17. Debnath, P., Huirem, R. S., Dutta, P. & Palchaudhuri, S. Epithelial–mesenchymal transition and its transcription factors. *Biosci Rep* **42**, (2022).

18. Friedl, P. & Wolf, K. Plasticity of cell migration: a multiscale tuning model. *Journal of Cell Biology* **188**, 11–19 (2010).

19. Hernandez-Caballero, M. E. Molecular Mechanisms of Metastasis: Epithelial-Mesenchymal Transition, Anoikis and Loss of Adhesion. in *Carcinogenesis* (InTech, 2013). doi:10.5772/55399.

20. Friedl, P. Prespecification and plasticity: shifting mechanisms of cell migration. *Curr Opin Cell Biol* **16**, 14–23 (2004).

21. van Zijl, F., Krupitza, G. & Mikulits, W. Initial steps of metastasis: Cell invasion and endothelial transmigration. *Mutation Research/Reviews in Mutation Research* **728**, 23–34 (2011).

22. Friedl, P., Hegerfeldt, Y. & Tusch, M. Collective cell migration in morphogenesis and cancer. *Int J Dev Biol* **48**, 441–449 (2004).

23. Hegerfeldt, Y., Tusch, M., Bröcker, E.-B. & Friedl, P. Collective Cell Movement in Primary Melanoma Explants: Plasticity of Cell-Cell Interaction, β1-Integrin Function, and Migration Strategies1,2. *Cancer Res* **62**, 2125–2130 (2002).

24. Wolf, K. *et al.* Multi-step pericellular proteolysis controls the transition from individual to collective cancer cell invasion. *Nat Cell Biol* **9**, 893–904 (2007).

25. Gray, R. S., Cheung, K. J. & Ewald, A. J. Cellular mechanisms regulating epithelial morphogenesis and cancer invasion. *Curr Opin Cell Biol* **22**, 640–650 (2010).

26. Huttenlocher, A. & Horwitz, A. R. Integrins in Cell Migration. *Cold Spring Harb Perspect Biol* **3**, a005074–a005074 (2011).

27. Walker, C., Mojares, E. & del Río Hernández, A. Role of Extracellular Matrix in Development and Cancer Progression. *Int J Mol Sci* **19**, 3028 (2018).

28. Trelstad, R. L., Hay, E. D. & Revel, J.-P. Cell contact during early morphogenesis in the chick embryo. *Dev Biol* **16**, 78–106 (1967).

29. Greenburg, G. & Hay, E. D. Epithelia suspended in collagen gels can lose polarity and express characteristics of migrating mesenchymal cells. *J Cell Biol* **95**, 333–339 (1982).

30. Christofori, G. New signals from the invasive front. *Nature* **441**, 444–450 (2006).

31. Grünert, S., Jechlinger, M. & Beug, H. Diverse cellular and molecular mechanisms contribute to epithelial plasticity and metastasis. *Nat Rev Mol Cell Biol* **4**, 657–665 (2003).

32. Thiery, J. P. Epithelial–mesenchymal transitions in tumour progression. *Nat Rev Cancer* **2**, 442–454 (2002).

33. Gotzmann, J. *et al.* Molecular aspects of epithelial cell plasticity: implications for local tumor invasion and metastasis. *Mutation Research/Reviews in Mutation Research* **566**, 9–20 (2004).

34. Brabletz, T. *et al.* Variable β-catenin expression in colorectal cancers indicates tumor progression driven by the tumor environment. *Proceedings of the National Academy of Sciences* **98**, 10356–10361 (2001).

35. Peinado, H., Olmeda, D. & Cano, A. Snail, Zeb and bHLH factors in tumour progression: an alliance against the epithelial phenotype? *Nat Rev Cancer* **7**, 415–428 (2007).

36. Kim, D. *et al.* Epithelial Mesenchymal Transition in Embryonic Development, Tissue Repair and Cancer: A Comprehensive Overview. *J Clin Med* **7**, 1 (2017).

37. Kalluri, R. EMT: When epithelial cells decide to become mesenchymal-like cells. *Journal of Clinical Investigation* **119**, 1417–1419 (2009).

38. Son, H.-J. & Moon, A. Epithelial-mesenchymal Transition and Cell Invasion. *Toxicol Res* **26**, 245–252 (2010).

39. Kim, D. *et al.* Epithelial Mesenchymal Transition in Embryonic Development, Tissue Repair and Cancer: A Comprehensive Overview. *J Clin Med* **7**, 1 (2017).

40. Krakhmal, N. V, Zavyalova, M. V, Denisov, E. V, Vtorushin, S. V & Perelmuter, V. M. Cancer Invasion: Patterns and Mechanisms. *Acta Naturae* **7**, 17–28 (2015).

41. Friedl, P. & Alexander, S. Cancer Invasion and the Microenvironment: Plasticity and Reciprocity. *Cell* **147**, 992–1009 (2011).

42. Spano, D., Heck, C., De Antonellis, P., Christofori, G. & Zollo, M. Molecular networks that regulate cancer metastasis. *Semin Cancer Biol* **22**, 234–249 (2012).

43. Scott, R. W., Crighton, D. & Olson, M. F. Modeling and Imaging 3-Dimensional Collective Cell Invasion. *Journal of Visualized Experiments* (2011) doi:10.3791/3525.

44. Paňková, K., Rösel, D., Novotný, M. & Brábek, J. The molecular mechanisms of transition between mesenchymal and amoeboid invasiveness in tumor cells. *Cellular and Molecular Life Sciences* **67**, 63–71 (2010).

45. Synek, L., Sekereš, J. & Žárský, V. The exocyst at the interface between cytoskeleton and membranes in eukaryotic cells. *Front Plant Sci* **4**, (2014).

46. Lash, L. L. *et al.* Small-Molecule Intramimics of Formin Autoinhibition: A New Strategy to Target the Cytoskeletal Remodeling Machinery in Cancer Cells. *Cancer Res* **73**, 6793–6803 (2013).

47. Friedl, P. & Wolf, K. Plasticity of cell migration: a multiscale tuning model. *Journal of Cell Biology* **188**, 11–19 (2010).

48. Yilmaz, M. & Christofori, G. Mechanisms of Motility in Metastasizing Cells. *Molecular Cancer Research* **8**, 629–642 (2010).

49. Russnes, H. G., Navin, N., Hicks, J. & Borresen-Dale, A.-L. Insight into the heterogeneity of breast cancer through next-generation sequencing. *Journal of Clinical Investigation* **121**, 3810–3818 (2011).

50. Fisher, R., Pusztai, L. & Swanton, C. Cancer heterogeneity: implications for targeted therapeutics. *Br J Cancer* **108**, 479–485 (2013).

51. Navin, N. E. & Hicks, J. Tracing the tumor lineage. *Mol Oncol* **4**, 267–283 (2010).

52. Nowell, P. C. The Clonal Evolution of Tumor Cell Populations. *Science (1979)* **194**, 23–28 (1976).

53. Sprouffske, K., Merlo, L. M. F., Gerrish, P. J., Maley, C. C. & Sniegowski, P. D. Cancer in Light of Experimental Evolution. *Current Biology* **22**, R762–R771 (2012).

54. Nickel, G. C. *et al.* Characterizing Mutational Heterogeneity in a Glioblastoma Patient with Double Recurrence. *PLoS One* **7**, e35262 (2012).

55. Inda, M.-M. *et al.* Tumor heterogeneity is an active process maintained by a mutant EGFR-induced cytokine circuit in glioblastoma. *Genes Dev* **24**, 1731–1745 (2010).

56. Bonavia, R., Inda, M.-M., Cavenee, W. K. & Furnari, F. B. Heterogeneity Maintenance in Glioblastoma: A Social Network. *Cancer Res* **71**, 4055–4060 (2011).

57. Pietras, A. Cancer Stem Cells in Tumor Heterogeneity. in 255–281 (2011). doi:10.1016/B978-0-12-387688-1.00009-0.

58. Croker, A. K. & Allan, A. L. Cancer stem cells: implications for the progression and treatment of metastatic disease. *J Cell Mol Med* **12**, 374–390 (2008).

59. Al-Hajj, M., Wicha, M. S., Benito-Hernandez, A., Morrison, S. J. & Clarke, M. F. Prospective identification of tumorigenic breast cancer cells. *Proceedings of the National Academy of Sciences* **100**, 3983–3988 (2003).

60. Eramo, A. *et al.* Identification and expansion of the tumorigenic lung cancer stem cell population. *Cell Death Differ* **15**, 504–514 (2008).

61. Schatton, T. *et al.* Identification of cells initiating human melanomas. *Nature* **451**, 345–349 (2008).

62. Ayob, A. Z. & Ramasamy, T. S. Cancer stem cells as key drivers of tumour progression. *J Biomed Sci* **25**, 20 (2018).

63. Magee, J. A., Piskounova, E. & Morrison, S. J. Cancer Stem Cells: Impact, Heterogeneity, and Uncertainty. *Cancer Cell* **21**, 283–296 (2012).

64. Magee, J. A., Piskounova, E. & Morrison, S. J. Cancer Stem Cells: Impact, Heterogeneity, and Uncertainty. *Cancer Cell* **21**, 283–296 (2012).

65. Jabbari, E., Kim, D., Lee, L. P., Ghaemmaghami, A. & Khademhosseini, A. *Handbook of Biomimetics and Bioinspiration*. vol. 9 (WORLD SCIENTIFIC, 2014).

66. Perrot-Applanat, M. & Di Benedetto, M. Autocrine functions of VEGF in breast tumor cells. *Cell Adh Migr* **6**, 547–553 (2012).

67. 25806217.

68. Guan, X. Cancer metastases: challenges and opportunities. *Acta Pharm Sin B* **5**, 402–418 (2015).

69. Li, S. *et al.* Shear stress promotes anoikis resistance of cancer cells via caveolin-1-dependent extrinsic and intrinsic apoptotic pathways. *J Cell Physiol* **234**, 3730–3743 (2019).

70. Chaffer, C. L. & Weinberg, R. A. A Perspective on Cancer Cell Metastasis. *Science (1979)* **331**, 1559–1564 (2011).

71. Aktas, B. *et al.* Stem cell and epithelial-mesenchymal transition markers are frequently overexpressed in circulating tumor cells of metastatic breast cancer patients. *Breast Cancer Research* **11**, R46 (2009).

72. Fabisiewicz, A. & Grzybowska, E. CTC clusters in cancer progression and metastasis. *Medical Oncology* **34**, 12 (2017).

73. Geethadevi, A., Parashar, D., Bishop, E., Pradeep, S. & Chaluvally-Raghavan, P. ERBB signaling in CTCs of ovarian cancer and glioblastoma. *Genes Cancer* **8**, 746–751 (2017).

74. DESITTER, I. *et al.* A New Device for Rapid Isolation by Size and Characterization of Rare Circulating Tumor Cells. *Anticancer Res* **31**, 427–441 (2011).

75. Vona, G. *et al.* Isolation by Size of Epithelial Tumor Cells. *Am J Pathol* **156**, 57–63 (2000).

76. Chaffer, C. L. & Weinberg, R. A. A Perspective on Cancer Cell Metastasis. *Science (1979)* **331**, 1559–1564 (2011).

77. Qiu, J. *et al.* Refining Cancer Management Using Integrated Liquid Biopsy. *Theranostics* **10**, 2374–2384 (2020).

78. Woestemeier, A. *et al.* Clinical Relevance of Circulating Tumor Cells in Esophageal Cancer Detected by a Combined MACS Enrichment Method. *Cancers (Basel)* **12**, 718 (2020).

79. Gerlinger, M. *et al.* Intratumor Heterogeneity and Branched Evolution Revealed by Multiregion Sequencing. *New England Journal of Medicine* **366**, 883–892 (2012).

80. Hyun, K.-A. & Jung, H.-I. Advances and critical concerns with the microfluidic enrichments of circulating tumor cells. *Lab Chip* **14**, 45–56 (2014).

81. Sun, J. *et al.* Double spiral microchannel for label-free tumor cell separation and enrichment. *Lab Chip* **12**, 3952 (2012).

82. Menairini Silicon Biosystems, "CellSearch - Circulating Tumor Cell Test," https://www.cellsearchctc.com/, 2022.

83. Miller, M. C., Doyle, G. V. & Terstappen, L. W. M. M. Significance of Circulating Tumor Cells Detected by the CellSearch System in Patients with Metastatic Breast Colorectal and Prostate Cancer. *J Oncol* **2010**, 1–8 (2010).

84. Eslami-S, Z., Cortés-Hernández, L. E. & Alix-Panabières, C. Epithelial Cell Adhesion Molecule: An Anchor to Isolate Clinically Relevant Circulating Tumor Cells. *Cells* **9**, 1836 (2020).

85. Woo, D. & Yu, M. Circulating tumor cells as "liquid biopsies" to understand cancer metastasis. *Translational Research* **201**, 128–135 (2018).

86. Mikolajczyk, S. D. *et al.* Detection of EpCAM-Negative and Cytokeratin-Negative Circulating Tumor Cells in Peripheral Blood. *J Oncol* **2011**, 1–10 (2011).

87. Wit, S. de *et al.* The detection of EpCAM+ and EpCAM– circulating tumor cells. *Sci Rep* **5**, 12270 (2015).

88. Gabriel, M. T., Calleja, L. R., Chalopin, A., Ory, B. & Heymann, D. Circulating Tumor Cells: A Review of Non–EpCAM-Based Approaches for Cell Enrichment and Isolation. *Clin Chem* **62**, 571–581 (2016).

89. Pantel, K. & Alix-Panabières, C. Liquid biopsy and minimal residual disease — latest advances and implications for cure. *Nat Rev Clin Oncol* **16**, 409–424 (2019).

90. Ignatiadis, M., Sledge, G. W. & Jeffrey, S. S. Liquid biopsy enters the clinic — implementation issues and future challenges. *Nat Rev Clin Oncol* **18**, 297–312 (2021).

91. Matikas, A. *et al.* Detection of circulating tumour cells before and following adjuvant chemotherapy and long-term prognosis of early breast cancer. *Br J Cancer* **126**, 1563–1569 (2022).

92. Strati, A., Nikolaou, M., Georgoulias, V. & Lianidou, E. Prognostic Significance of TWIST1, CD24, CD44, and ALDH1 Transcript Quantification in EpCAM-Positive Circulating Tumor Cells from Early Stage Breast Cancer Patients. *Cells* **8**, 652 (2019).

93. Kasimir-Bauer, S. *et al.* Circulating Tumor Cells Expressing the Prostate Specific Membrane Antigen (PSMA) Indicate Worse Outcome in Primary, Non-Metastatic Triple-Negative Breast Cancer. *Front Oncol* **10**, (2020).

94. Papadaki, M. A. *et al.* Clinical Relevance of Immune Checkpoints on Circulating Tumor Cells in Breast Cancer. *Cancers (Basel)* **12**, 376 (2020).

95. Strati, A., Zavridou, M., Bournakis, E., Mastoraki, S. & Lianidou, E. Expression pattern of androgen receptors, *AR-V7* and *AR-567es* , in circulating tumor cells and paired plasma-derived extracellular vesicles in metastatic castration resistant prostate cancer. *Analyst* **144**, 6671–6680 (2019).

96. Sperger, J. M. *et al.* Prospective Evaluation of Clinical Outcomes Using a Multiplex Liquid Biopsy Targeting Diverse Resistance Mechanisms in Metastatic Prostate Cancer. *Journal of Clinical Oncology* **39**, 2926–2937 (2021).

97. Sperger, J. M. *et al.* Prospective Evaluation of Clinical Outcomes Using a Multiplex Liquid Biopsy Targeting Diverse Resistance Mechanisms in Metastatic Prostate Cancer. *Journal of Clinical Oncology* **39**, 2926–2937 (2021).

98. Giordano, A. *et al.* Circulating tumor cells in immunohistochemical subtypes of metastatic breast cancer: lack of prediction in HER2-positive disease treated with targeted therapy. *Annals of Oncology* **23**, 1144–1150 (2012).

99. Paoletti, C. *et al.* Circulating Tumor Cell Clusters in Patients with Metastatic Breast Cancer: a SWOG S0500 Translational Medicine Study. *Clinical Cancer Research* **25**, 6089–6097 (2019).

100. Larsson, A.-M. *et al.* Longitudinal enumeration and cluster evaluation of circulating tumor cells improve prognostication for patients with newly diagnosed metastatic breast cancer in a prospective observational trial. *Breast Cancer Research* **20**, 48 (2018).

101. Marrinucci, D. *et al.* Fluid biopsy in patients with metastatic prostate, pancreatic and breast cancers. *Phys Biol* **9**, 016003 (2012).

102. Ting, D. T. *et al.* Single-Cell RNA Sequencing Identifies Extracellular Matrix Gene Expression by Pancreatic Circulating Tumor Cells. *Cell Rep* **8**, 1905–1918 (2014).

103. Aceto, N. *et al.* Circulating Tumor Cell Clusters Are Oligoclonal Precursors of Breast Cancer Metastasis. *Cell* **158**, 1110–1122 (2014).

104. Yu, M. *et al.* Ex vivo culture of circulating breast tumor cells for individualized testing of drug susceptibility. *Science (1979)* **345**, 216–220 (2014).

105. Yu, T. *et al.* Heterogeneity of CTC contributes to the organotropism of breast cancer. *Biomedicine & Pharmacotherapy* **137**, 111314 (2021).

106. Diehl, F. *et al.* Circulating mutant DNA to assess tumor dynamics. *Nat Med* **14**, 985–990 (2008).

107. Marrugo-Ramírez, J., Mir, M. & Samitier, J. Blood-Based Cancer Biomarkers in Liquid Biopsy: A Promising Non-Invasive Alternative to Tissue Biopsy. *Int J Mol Sci* **19**, 2877 (2018).

108. Kalli, M. & Stylianopoulos, T. Defining the Role of Solid Stress and Matrix Stiffness in Cancer Cell Proliferation and Metastasis. *Front Oncol* **8**, (2018).

109. Gerlinger, M. *et al.* Intratumor Heterogeneity and Branched Evolution Revealed by Multiregion Sequencing. *New England Journal of Medicine* **366**, 883–892 (2012).

110. Robertson, E. G. & Baxter, G. Tumour seeding following percutaneous needle biopsy: The real story! *Clin Radiol* **66**, 1007–1014 (2011).

111. Alix-Panabières, C. & Pantel, K. Clinical Applications of Circulating Tumor Cells and Circulating Tumor DNA as Liquid Biopsy. *Cancer Discov* **6**, 479–491 (2016).

112. Alix-Panabières, C. & Pantel, K. Challenges in circulating tumour cell research. *Nat Rev Cancer* **14**, 623–631 (2014).

113. Crowley, E., Di Nicolantonio, F., Loupakis, F. & Bardelli, A. Liquid biopsy: monitoring cancer-genetics in the blood. *Nat Rev Clin Oncol* **10**, 472–484 (2013).

114. Satelli, A. *et al.* Epithelial–Mesenchymal Transitioned Circulating Tumor Cells Capture for Detecting Tumor Progression. *Clinical Cancer Research* **21**, 899–906 (2015).

115. Thiery, J. P. Epithelial–mesenchymal transitions in tumour progression. *Nat Rev Cancer* **2**, 442–454 (2002).

116. Haber, D. A. & Velculescu, V. E. Blood-Based Analyses of Cancer: Circulating Tumor Cells and Circulating Tumor DNA. *Cancer Discov* **4**, 650–661 (2014).

117. Alix-Panabières, C. & Pantel, K. Circulating Tumor Cells: Liquid Biopsy of Cancer. *Clin Chem* **59**, 110–118 (2013).

118. Bardelli, A. & Pantel, K. Liquid Biopsies, What We Do Not Know (Yet). *Cancer Cell* **31**, 172–179 (2017).

119. Bardelli, A. & Pantel, K. Liquid Biopsies, What We Do Not Know (Yet). *Cancer Cell* **31**, 172–179 (2017).

120. Zhang, Z., Ramnath, N. & Nagrath, S. Current Status of CTCs as Liquid Biopsy in Lung Cancer and Future Directions. *Front Oncol* **5**, (2015).

121. Yu, M., Stott, S., Toner, M., Maheswaran, S. & Haber, D. A. Circulating tumor cells: approaches to isolation and characterization. *Journal of Cell Biology* **192**, 373–382 (2011).

122. Wan, J. C. M. *et al.* Liquid biopsies come of age: towards implementation of circulating tumour DNA. *Nat Rev Cancer* **17**, 223–238 (2017).

123. Siravegna, G., Marsoni, S., Siena, S. & Bardelli, A. Integrating liquid biopsies into the management of cancer. *Nat Rev Clin Oncol* **14**, 531–548 (2017).

124. Heitzer, E., Ulz, P., Geigl, J. B. & Speicher, M. R. Non-invasive detection of genome-wide somatic copy number alterations by liquid biopsies. *Mol Oncol* **10**, 494–502 (2016).

125. Diaz, L. A. & Bardelli, A. Liquid Biopsies: Genotyping Circulating Tumor DNA. *Journal of Clinical Oncology* **32**, 579–586 (2014).

126. Perakis, S. & Speicher, M. R. Emerging concepts in liquid biopsies. *BMC Med* **15**, 75 (2017).

127. Bach, D.-H., Hong, J.-Y., Park, H. J. & Lee, S. K. The role of exosomes and miRNAs in drug-resistance of cancer cells. *Int J Cancer* **141**, 220–230 (2017).

128. Ulz, P., Heitzer, E., Geigl, J. B. & Speicher, M. R. Patient monitoring through liquid biopsies using circulating tumor DNA. *Int J Cancer* **141**, 887–896 (2017).

129. Tian, W., Liu, S. & Li, B. Potential Role of Exosomes in Cancer Metastasis. *Biomed Res Int* **2019**, 1–12 (2019).

130. Becker, A. *et al.* Extracellular Vesicles in Cancer: Cell-to-Cell Mediators of Metastasis. *Cancer Cell* **30**, 836–848 (2016).

131. Lone, S. N. *et al.* Liquid biopsy: a step closer to transform diagnosis, prognosis and future of cancer treatments. *Mol Cancer* **21**, 79 (2022).

132. Sajeesh, P. & Sen, A. K. Particle separation and sorting in microfluidic devices: a review. *Microfluid Nanofluidics* **17**, 1–52 (2014).

133. Mark, D., Haeberle, S., Roth, G., von Stetten, F. & Zengerle, R. Microfluidic lab-on-a-chip platforms: requirements, characteristics and applications. *Chem Soc Rev* **39**, 1153 (2010).

134. Warkiani, M. E., Wu, L., Tay, A. K. P. & Han, J. Large-Volume Microfluidic Cell Sorting for Biomedical Applications. *Annu Rev Biomed Eng* **17**, 1–34 (2015).

135. Di Carlo, D., Irimia, D., Tompkins, R. G. & Toner, M. Continuous inertial focusing, ordering, and separation of particles in microchannels. *Proceedings of the National Academy of Sciences* **104**, 18892–18897 (2007).

136. Vona, G. *et al.* Isolation by Size of Epithelial Tumor Cells. *Am J Pathol* **156**, 57–63 (2000).

137. Jiang, X. *et al.* Microfluidic isolation of platelet-covered circulating tumor cells. *Lab Chip* **17**, 3498–3503 (2017).

138. Warkiani, M. E., Wu, L., Tay, A. K. P. & Han, J. Large-Volume Microfluidic Cell Sorting for Biomedical Applications. *Annu Rev Biomed Eng* **17**, 1–34 (2015).

139. Lin, Z. *et al.* Recent Advances in Microfluidic Platforms Applied in Cancer Metastasis: Circulating Tumor Cells' (CTCs) Isolation and Tumor-On-A-Chip. *Small* **16**, 1903899 (2020).

140. Wang, S. *et al.* Highly efficient and selective isolation of rare tumor cells using a microfluidic chip with wavy-herringbone micro-patterned surfaces. *Analyst* **141**, 2228–2237 (2016).

141. Al-Faqheri, W. *et al.* Particle/cell separation on microfluidic platforms based on centrifugation effect: a review. *Microfluid Nanofluidics* **21**, 102 (2017).

142. Xue, P., Zhang, L., Guo, J., Xu, Z. & Kang, Y. Isolation and retrieval of circulating tumor cells on a microchip with double parallel layers of herringbone structure. *Microfluid Nanofluidics* **20**, 169 (2016).

143. LeValley, P. J. *et al.* Immunofunctional photodegradable poly(ethylene glycol) hydrogel surfaces for the capture and release of rare cells. *Colloids Surf B Biointerfaces* **174**, 483–492 (2019).

144. Zhang, X., Ju, S., Wang, X. & Cong, H. Advances in liquid biopsy using circulating tumor cells and circulating cell-free tumor DNA for detection and monitoring of breast cancer. *Clin Exp Med* **19**, 271–279 (2019).

145. Zhou, J. *et al.* Isolation of circulating tumor cells in non-small-cell-lung-cancer patients using a multi-flow microfluidic channel. *Microsyst Nanoeng* **5**, 8 (2019).

146. Kulasinghe, A. *et al.* Enrichment of circulating head and neck tumour cells using spiral microfluidic technology. *Sci Rep* **7**, 42517 (2017).

147. Nagrath, S. *et al.* Isolation of rare circulating tumour cells in cancer patients by microchip technology. *Nature* **450**, 1235–1239 (2007).

148. Stott, S. L. *et al.* Isolation of circulating tumor cells using a microvortex-generating herringbone-chip. *Proceedings of the National Academy of Sciences* **107**, 18392–18397 (2010).

149. Xue, P. *et al.* Isolation and elution of Hep3B circulating tumor cells using a dual-functional herringbone chip. *Microfluid Nanofluidics* **16**, 605–612 (2014).

150. Xue, P., Wu, Y., Guo, J. & Kang, Y. Highly efficient capture and harvest of circulating tumor cells on a microfluidic chip integrated with herringbone and micropost arrays. *Biomed Microdevices* **17**, 39 (2015).

151. Wang, S. *et al.* Highly efficient and selective isolation of rare tumor cells using a microfluidic chip with wavy-herringbone micro-patterned surfaces. *Analyst* **141**, 2228–2237 (2016).

152. Kim, H. U., Lim, Y. J., Lee, H. J., Lee, N. J. & Bong, K. W. Degassed micromolding lithography for rapid fabrication of anisotropic hydrogel microparticles with high-resolution and high uniformity. *Lab Chip* **20**, 74–83 (2020).

153. Lee, N. J. *et al.* Affinity-Enhanced CTC-Capturing Hydrogel Microparticles Fabricated by Degassed Mold Lithography. *J Clin Med* **9**, 301 (2020).

154. Gleghorn, J. P. *et al.* Capture of circulating tumor cells from whole blood of prostate cancer patients using geometrically enhanced differential immunocapture (GEDI) and a prostate-specific antibody. *Lab Chip* **10**, 27–29 (2010).

155. Turetta, M. *et al.* Emerging Technologies for Cancer Research: Towards Personalized Medicine with Microfluidic Platforms and 3D Tumor Models. *Curr Med Chem* **25**, 4616–4637 (2018).

156. Hou, S. *et al.* Polymer Nanofiber-Embedded Microchips for Detection, Isolation, and Molecular Analysis of Single Circulating Melanoma Cells. *Angewandte Chemie International Edition* **52**, 3379–3383 (2013).

157. Wang, S. *et al.* Highly efficient and selective isolation of rare tumor cells using a microfluidic chip with wavy-herringbone micro-patterned surfaces. *Analyst* **141**, 2228–2237 (2016).

158. Yu, M. *et al.* Circulating Breast Tumor Cells Exhibit Dynamic Changes in Epithelial and Mesenchymal Composition. *Science (1979)* **339**, 580–584 (2013).

159. Lin, Z. *et al.* Recent Advances in Microfluidic Platforms Applied in Cancer Metastasis: Circulating Tumor Cells' (CTCs) Isolation and Tumor-On-A-Chip. *Small* **16**, 1903899 (2020).

160. Desitter, I. *et al.* A new device for rapid isolation by size and characterization of rare circulating tumor cells. *Anticancer Res* **31**, 427–41 (2011).

161. Ferreira, M. M., Ramani, V. C. & Jeffrey, S. S. Circulating tumor cell technologies. *Mol Oncol* **10**, 374–394 (2016).

162. Ozkumur, E. *et al.* Inertial Focusing for Tumor Antigen–Dependent and –Independent Sorting of Rare Circulating Tumor Cells. *Sci Transl Med* **5**, (2013).

163. Hyun, K.-A., Lee, T. Y. & Jung, H.-I. Negative Enrichment of Circulating Tumor Cells Using a Geometrically Activated Surface Interaction Chip. *Anal Chem* **85**, 4439–4445 (2013).

164. Blagosklonny, M. & Gudkov, A. Introducing, OncoTarget. *Oncotarget* **1**, 2–2 (2010).

165. Qasaimeh, M. A. *et al.* Isolation of Circulating Plasma Cells in Multiple Myeloma Using CD138 Antibody-Based Capture in a Microfluidic Device. *Sci Rep* **7**, 45681 (2017).

166. Turetta, M. *et al.* Emerging Technologies for Cancer Research: Towards Personalized Medicine with Microfluidic Platforms and 3D Tumor Models. *Curr Med Chem* **25**, 4616–4637 (2018).

167. Keefe, A. D., Pai, S. & Ellington, A. Aptamers as therapeutics. *Nat Rev Drug Discov* **9**, 537–550 (2010).

168. Di Carlo, D., Irimia, D., Tompkins, R. G. & Toner, M. Continuous inertial focusing, ordering, and separation of particles in microchannels. *Proceedings of the National Academy of Sciences* **104**, 18892–18897 (2007).

169. Gascoyne, P. & Shim, S. Isolation of Circulating Tumor Cells by Dielectrophoresis. *Cancers (Basel)* **6**, 545–579 (2014).

170. Sung, H. *et al.* Global Cancer Statistics 2020: GLOBOCAN Estimates of Incidence and Mortality Worldwide for 36 Cancers in 185 Countries. *CA Cancer J Clin* **71**, 209–249 (2021).

171. Hirz, T. & Dumontet, C. Neutrophil Isolation and Analysis to Determine their Role in Lymphoma Cell Sensitivity to Therapeutic Agents. *Journal of Visualized Experiments* (2016) doi:10.3791/53846.

172. Jin, C. *et al.* Technologies for label-free separation of circulating tumor cells: from historical foundations to recent developments. *Lab Chip* **14**, 32–44 (2014).

173. Gerhardt, T., Woo, S. & Ma, H. Chromatographic behaviour of single cells in a microchannel with dynamic geometry. *Lab Chip* **11**, 2731 (2011).

174. Inglis, D. W. Efficient microfluidic particle separation arrays. *Appl Phys Lett* **94**, (2009).

175. Harouaka, R. A., Nisic, M. & Zheng, S.-Y. Circulating Tumor Cell Enrichment Based on Physical Properties. *SLAS Technol* **18**, 455–468 (2013).

176. Mohamed, H., Murray, M., Turner, J. N. & Caggana, M. Isolation of tumor cells using size and deformation. *J Chromatogr A* **1216**, 8289–8295 (2009).

177. Lee, Y., Guan, G. & Bhagat, A. A. ClearCell® FX, a label-free microfluidics technology for enrichment of viable circulating tumor cells. *Cytometry Part A* **93**, 1251–1254 (2018).

178. Roumeliotou, A. *et al.* Phenotypic Characterization of Circulating Tumor Cells Isolated from Non-Small and Small Cell Lung Cancer Patients. *Cancers (Basel)* **15**, 171 (2022).

179. Drucker, A. *et al.* Comparative performance of different methods for circulating tumor cell enrichment in metastatic breast cancer patients. *PLoS One* **15**, e0237308 (2020).

180. Mohamed, H., Murray, M., Turner, J. N. & Caggana, M. Isolation of tumor cells using size and deformation. *J Chromatogr A* **1216**, 8289–8295 (2009).

181. Warkiani, M. E., Tay, A. K. P., Guan, G. & Han, J. Membrane-less microfiltration using inertial microfluidics. *Sci Rep* **5**, 11018 (2015).

182. Di Carlo, D. Inertial microfluidics. *Lab Chip* **9**, 3038 (2009).

183. Zhang, J. *et al.* Fundamentals and applications of inertial microfluidics: a review. *Lab Chip* **16**, 10–34 (2016).

184. Amini, H., Lee, W. & Di Carlo, D. Inertial microfluidic physics. *Lab Chip* **14**, 2739 (2014).

185. Di Carlo, D., Edd, J. F., Humphry, K. J., Stone, H. A. & Toner, M. Particle segregation and dynamics in confined flows. *Phys Rev Lett* **102**, 94503 (2009).

186. Kuntaegowdanahalli, S. S., Bhagat, A. A. S., Kumar, G. & Papautsky, I. Inertial microfluidics for continuous particle separation in spiral microchannels. *Lab Chip* **9**, 2973 (2009).

187. Warkiani, M. E. *et al.* An ultra-high-throughput spiral microfluidic biochip for the enrichment of circulating tumor cells. *Analyst* **139**, 3245–3255 (2014).

188. Zhang, Y., Zhang, J., Tang, F., Li, W. & Wang, X. Design of a Single-Layer Microchannel for Continuous Sheathless Single-Stream Particle Inertial Focusing. *Anal Chem* **90**, 1786–1794 (2018).

189. Sun, J. *et al.* Double spiral microchannel for label-free tumor cell separation and enrichment. *Lab Chip* **12**, 3952 (2012).

190. Warkiani, M. E. *et al.* Slanted spiral microfluidics for the ultra-fast, label-free isolation of circulating tumor cells. *Lab Chip* **14**, 128–137 (2014).

191. Abdulla, A., Liu, W., Gholamipour-Shirazi, A., Sun, J. & Ding, X. High-Throughput Isolation of Circulating Tumor Cells Using Cascaded Inertial Focusing Microfluidic Channel. *Anal Chem* **90**, 4397–4405 (2018).

192. Abdulla, A. *et al.* Integrated microfluidic single-cell immunoblotting chip enables high-throughput isolation, enrichment and direct protein analysis of circulating tumor cells. *Microsyst Nanoeng* **8**, 13 (2022).

193. Khoo, B. L. *et al.* Liquid biopsy for minimal residual disease detection in leukemia using a portable blast cell biochip. *NPJ Precis Oncol* **3**, 30 (2019).

194. Chen, H. A Triplet Parallelizing Spiral Microfluidic Chip for Continuous Separation of Tumor Cells. *Sci Rep* **8**, 4042 (2018).

195. Abd Rahman, N., Ibrahim, F. & Yafouz, B. Dielectrophoresis for Biomedical Sciences Applications: A Review. *Sensors* **17**, 449 (2017).

196. Low, W. S. & Wan Abas, W. A. B. Benchtop Technologies for Circulating Tumor Cells Separation Based on Biophysical Properties. *Biomed Res Int* **2015**, 1–22 (2015).

197. Alazzam, A., Stiharu, I., Bhat, R. & Meguerditchian, A.-N. Interdigitated comb-like electrodes for continuous separation of malignant cells from blood using dielectrophoresis. *Electrophoresis* **32**, 1327–1336 (2011).

198. Liao, C.-J. *et al.* An Optically Induced Dielectrophoresis (ODEP)-Based Microfluidic System for the Isolation of High-Purity CD45neg/EpCAMneg Cells from the Blood Samples of Cancer Patients—Demonstration and Initial Exploration of the Clinical Significance of These Cells. *Micromachines (Basel)* **9**, 563 (2018).

199. Tietze, U., Schenk, C. & Gamm, E. Field Effect Transistor. in *Electronic Circuits* 169–268 (Springer Berlin Heidelberg, 2008). doi:10.1007/978-3-540-78655-9_3.

200. Han, K.-H., Han, A. & Frazier, A. B. Microsystems for isolation and electrophysiological analysis of breast cancer cells from blood. *Biosens Bioelectron* **21**, 1907–1914 (2006).

201. Wang, M. *et al.* A microfluidic chip with double-sided herringbone microstructures for enhanced capture of rare tumor cells. *J Mater Chem B* **5**, 9114–9120 (2017).

202. Stott, S. L. *et al.* Isolation of circulating tumor cells using a microvortex-generating herringbone-chip. *Proceedings of the National Academy of Sciences* **107**, 18392–18397 (2010).

203. Chen, Y.-H., Pulikkathodi, A. K., Ma, Y.-D., Wang, Y.-L. & Lee, G.-B. A microfluidic platform integrated with field-effect transistors for enumeration of circulating tumor cells. *Lab Chip* **19**, 618–625 (2019).

204. Pulikkathodi, A. K. *et al.* Enumeration of circulating tumor cells and investigation of cellular responses using aptamer-immobilized AlGaN/GaN high electron mobility transistor sensor array. *Sens Actuators B Chem* **257**, 96–104 (2018).

205. Gu, W. & Zhao, Y. Cellular electrical impedance spectroscopy: an emerging technology of microscale biosensors. *Expert Rev Med Devices* **7**, 767–779 (2010).

206. Nguyen, N.-V. & Jen, C.-P. Impedance detection integrated with dielectrophoresis enrichment platform for lung circulating tumor cells in a microfluidic channel. *Biosens Bioelectron* **121**, 10–18 (2018).

207. Kumeria, T., Kurkuri, M. D., Diener, K. R., Parkinson, L. & Losic, D. Label-free reflectometric interference microchip biosensor based on nanoporous alumina for detection of circulating tumour cells. *Biosens Bioelectron* **35**, 167–173 (2012).

208. Chiu, T.-K. *et al.* Development of a Microfluidic-Based Optical Sensing Device for Label-Free Detection of Circulating Tumor Cells (CTCs) Through Their Lactic Acid Metabolism. *Sensors* **15**, 6789–6806 (2015).

209. Mani, G. K. *et al.* ZnO-Based Microfluidic pH Sensor: A Versatile Approach for Quick Recognition of Circulating Tumor Cells in Blood. *ACS Appl Mater Interfaces* **9**, 5193–5203 (2017).

210. Nguyen, N.-V. & Jen, C.-P. Impedance detection integrated with dielectrophoresis enrichment platform for lung circulating tumor cells in a microfluidic channel. *Biosens Bioelectron* **121**, 10–18 (2018).

211. Christoffersson, J. & Mandenius, C.-F. Fabrication of a Microfluidic Cell Culture Device Using Photolithographic and Soft Lithographic Techniques. in 227–233 (2019). doi:10.1007/978-1-4939-9477-9_21.

212. Campo, A. del & Greiner, C. SU-8: a photoresist for high-aspect-ratio and 3D submicron lithography. *Journal of Micromechanics and Microengineering* **17**, R81–R95 (2007).

213. Whitesides, G. M. The origins and the future of microfluidics. *Nature* **442**, 368–373 (2006).

214. Araci, I. E. & Quake, S. R. Microfluidic very large scale integration (mVLSI) with integrated micromechanical valves. *Lab Chip* **12**, 2803 (2012).

215. Nguyen, T., Chidambara Vinayaka, A., Duong Bang, D. & Wolff, A. A Complete Protocol for Rapid and Low-Cost Fabrication of Polymer Microfluidic Chips Containing Three-Dimensional Microstructures Used in Point-of-Care Devices. *Micromachines (Basel)* **10**, 624 (2019).

216. Poulsen, C. E. *et al.* Laser ablated micropillar energy directors for ultrasonic welding of microfluidic systems. *Journal of Micromechanics and Microengineering* **26**, 067001 (2016).

217. Mohanty, S. *et al.* 3D Printed Silicone–Hydrogel Scaffold with Enhanced Physicochemical Properties. *Biomacromolecules* **17**, 1321–1329 (2016).

218. Mohanty, S. *et al.* 3D Printed Silicone–Hydrogel Scaffold with Enhanced Physicochemical Properties. *Biomacromolecules* **17**, 1321–1329 (2016).

219. Subirada, F. *et al.* Development of a Custom-Made 3D Printing Protocol with Commercial Resins for Manufacturing Microfluidic Devices. *Polymers (Basel)* **14**, 2955 (2022).

220. Moraes, C., Sun, Y. & Simmons, C. A. Solving the shrinkage-induced PDMS alignment registration issue in multilayer soft lithography. *Journal of Micromechanics and Microengineering* **19**, 065015 (2009).

221. Nguyen, T. *et al.* Multilayer Soft Photolithography Fabrication of Microfluidic Devices Using a Custom-Built Wafer-Scale PDMS Slab Aligner and Cost-Efficient Equipment. *Micromachines (Basel)* **13**, 1357 (2022).

222. Ng, J. M. K., Gitlin, I., Stroock, A. D. & Whitesides, G. M. Components for integrated poly(dimethylsiloxane) microfluidic systems. *Electrophoresis* **23**, 3461–3473 (2002).

223. Ng, J. M. K., Gitlin, I., Stroock, A. D. & Whitesides, G. M. Components for integrated poly(dimethylsiloxane) microfluidic systems. *Electrophoresis* **23**, 3461–3473 (2002).

224. Bernard, A., Michel, B. & Delamarche, E. Micromosaic Immunoassays. *Anal Chem* **73**, 8–12 (2001).

225. McDonald, J. C. *et al.* Prototyping of Microfluidic Devices in Poly(dimethylsiloxane) Using Solid-Object Printing. *Anal Chem* **74**, 1537–1545 (2002).

226. McDonald, J. C. & Whitesides, G. M. Poly(dimethylsiloxane) as a Material for Fabricating Microfluidic Devices. *Acc Chem Res* **35**, 491–499 (2002).

227. Ferrari, M., Cirisano, F. & Morán, M. C. Mammalian Cell Behavior on Hydrophobic Substrates: Influence of Surface Properties. *Colloids and Interfaces* **3**, 48 (2019).

228. Subirada, F. *et al.* Development of a Custom-Made 3D Printing Protocol with Commercial Resins for Manufacturing Microfluidic Devices. *Polymers (Basel)* **14**, 2955 (2022).

229. Schmidleithner, C. & Kalaskar, D. M. Stereolithography. in *3D Printing* (InTech, 2018). doi:10.5772/intechopen.78147.

230. Schönberger, M. & Hoffstetter, M. Generative Manufacturing Technologies—The Future? in *Emerging Trends in Medical Plastic Engineering and Manufacturing* 107–174 (Elsevier, 2016). doi:10.1016/B978-0-323-37023-3.00004-X.

231. Gong, H., Woolley, A. T. & Nordin, G. P. High density 3D printed microfluidic valves, pumps, and multiplexers. *Lab Chip* **16**, 2450–2458 (2016).

232. Malinauskas, M., Jonušauskas, L., Gailevičius, D., Rekštyte, S. & Juodkazis, S. Optical 3D printing in mesoscale. in *Laser 3D Manufacturing V* (eds. Helvajian, H., Piqué, A. & Gu, B.) 36 (SPIE, 2018). doi:10.1117/12.2287669.

233. Gong, H., Bickham, B. P., Woolley, A. T. & Nordin, G. P. Custom 3D printer and resin for 18 µm × 20 µm microfluidic flow channels. *Lab Chip* **17**, 2899–2909 (2017).

234. Beauchamp, M. J., Nielsen, A. V., Gong, H., Nordin, G. P. & Woolley, A. T. 3D Printed Microfluidic Devices for Microchip Electrophoresis of Preterm Birth Biomarkers. *Anal Chem* **91**, 7418–7425 (2019).

235. Parker, E. K. *et al.* 3D printed microfluidic devices with immunoaffinity monoliths for extraction of preterm birth biomarkers. *Anal Bioanal Chem* **411**, 5405–5413 (2019).

236. Gong, H., Woolley, A. T. & Nordin, G. P. 3D printed selectable dilution mixer pumps. *Biomicrofluidics* **13**, (2019).

237. Hou, H. W. *et al.* Isolation and retrieval of circulating tumor cells using centrifugal forces. *Sci Rep* **3**, 1259 (2013).

238. Ma, Y., Thiele, J., Abdelmohsen, L., Xu, J. & Huck, W. T. S. Biocompatible macro-initiators controlling radical retention in microfluidic on-chip photo-polymerization of water-in-oil emulsions. *Chem. Commun.* **50**, 112–114 (2014).

239. Stroock, A. D. *et al.* Chaotic Mixer for Microchannels. *Science (1979)* **295**, 647–651 (2002).

240. Stott, S. L. *et al.* Isolation of circulating tumor cells using a microvortex-generating herringbone-chip. *Proceedings of the National Academy of Sciences* **107**, 18392–18397 (2010).

241. Jacobson, S. C. & Ramsey, J. M. Integrated Microdevice for DNA Restriction Fragment Analysis. *Anal Chem* **68**, 720–723 (1996).

242. Yuen, P. K. *et al.* Microchip Module for Blood Sample Preparation and Nucleic Acid Amplification Reactions. *Genome Res* **11**, 405–412 (2001).

243. Tigner A, I. S. M. I. Histology, White Blood Cell. *https://www.ncbi.nlm.nih.gov/books/NBK563148/* (2022).

244. Zhang, X. *et al.* Fluorescence Analysis of Vitamin D Receptor Status of Circulating Tumor Cells (CTCS) in Breast Cancer: From Cell Models to Metastatic Patients. *Int J Mol Sci* **18**, 1318 (2017).

245. Mendelaar, P. A. J. *et al.* Defining the dimensions of circulating tumor cells in a large series of breast, prostate, colon, and bladder cancer patients. *Mol Oncol* **15**, 116–125 (2021).

246. Fachin, F. *et al.* Monolithic Chip for High-throughput Blood Cell Depletion to Sort Rare Circulating Tumor Cells. *Sci Rep* **7**, 10936 (2017).

247. Zhao, W. *et al.* Tumor antigen-independent and cell size variation-inclusive enrichment of viable circulating tumor cells. *Lab Chip* **19**, 1860–1876 (2019).

248. Zhao, W. *et al.* Tumor antigen-independent and cell size variation-inclusive enrichment of viable circulating tumor cells. *Lab Chip* **19**, 1860–1876 (2019).

249. Yeh, P. Y. *et al.* An efficient spiral microchannel for continuous small particle separations. *Sens Actuators B Chem* **252**, 606–615 (2017).

250. Wu, Z., Willing, B., Bjerketorp, J., Jansson, J. K. & Hjort, K. Soft inertial microfluidics for high throughput separation of bacteria from human blood cells. *Lab Chip* **9**, 1193 (2009).

251. Palumbo, J., Navi, M., Tsai, S. S. H., Spelt, J. K. & Papini, M. Inertial particle separation in helical channels: A calibrated numerical analysis. *AIP Adv* **10**, (2020).

252. Mashhadian, A. & Shamloo, A. Inertial microfluidics: A method for fast prediction of focusing pattern of particles in the cross section of the channel. *Anal Chim Acta* **1083**, 137–149 (2019).

253. Saha, S. C., Francis, I. & Nassir, T. Computational Inertial Microfluidics: Optimal Design for Particle Separation. *Fluids* **7**, 308 (2022).

254. “Plasma Cleaning| Plasma Cleaner| Oxygen Argon Plasma| Plasma Etch, Inc”.

255. “Processing guidelines for: SU8 2100 and SU8 2150,”.

256. Subirada, F. *et al.* Development of a Custom-Made 3D Printing Protocol with Commercial Resins for Manufacturing Microfluidic Devices. *Polymers (Basel)* **14**, 2955 (2022).

257. Xue, P., Zhang, L., Guo, J., Xu, Z. & Kang, Y. Isolation and retrieval of circulating tumor cells on a microchip with double parallel layers of herringbone structure. *Microfluid Nanofluidics* **20**, 169 (2016).

258. Sajeesh, P. & Sen, A. K. Particle separation and sorting in microfluidic devices: a review. *Microfluid Nanofluid* **17**, 1–52 (2014).

259. Al-Faqheri, W. *et al.* Particle/cell separation on microfluidic platforms based on centrifugation effect: a review. *Microfluid Nanofluidics* **21:102**, (2017).

260. Zhang, J. *et al.* Fundamentals and applications of inertial microfluidics: a review. *Lab Chip* **16**, 10–34 (2016).

261. Kulasinghe, A. *et al.* Enrichment of circulating head and neck tumour cells using spiral microfluidic technology. *Sci Rep* **7**, 42517 (2017).

262. Warkiani, M. E., Wu, L., Kah, A., Tay, P. & Han, J. Large-Volume Microfluidic Cell Sorting for Biomedical Applications. *Annu. Rev. Biomed. Eng* **17**, 1–34 (2015).

263. Sun, J. *et al.* Double spiral microchannel for label-free tumor cell separation and enrichment. *Lab Chip* **12**, 3952–3960 (2012).

264. Hug, S. *et al.* Activation of Neutrophil Granulocytes by Platelet-Activating Factor Is Impaired During Experimental Sepsis. *Front Immunol* **12**, (2021).

265. Di Carlo, D., Irimia, D., Tompkins, R. G. & Toner, M. Continuous inertial focusing, ordering, and separation of particles in microchannels. *PNAS* **104**, 18892–18897 (2007).

266. Hou, H. W. *et al.* Isolation and retrieval of circulating tumor cells using centrifugal forces. *Sci Rep* **3**, 1259 (2013).

267. Warkiani, M. E. *et al.* Ultra-fast, label-free isolation of circulating tumor cells from blood using spiral microfluidics. *Nat Protoc* **11**, 134–148 (2016).

268. Amini, H., Lee, W. & Di Carlo, D. Inertial microfluidic physics. *Lab Chip* **14**, 2739–2761 (2014).

269. Ying, Y. & Lin, Y. Inertial Focusing and Separation of Particles in Similar Curved Channels. *Sci Rep* **9**, 16575 (2019).

270. Saffman, P. G. The lift on a small sphere in a slow shear flow. *Fluid Mech.* **22**, 385–400 (1965).

271. ASMOLOV, E. S. The inertial lift on a spherical particle in a plane Poiseuille flow at large channel Reynolds number. *J Fluid Mech* **381**, 63–87 (1999).

272. Asmolov, E. S. *et al.* Inertial focusing of finite-size particles in microchannels. *J. Fluid Mech* **840**, 613–630 (2018).

273. Bazaz, S. R. *et al.* Computational inertial microfluidics: a review. *Lab Chip* **20**, 1023–1048 (2020).

274. Ho, B. P. & Leal, L. G. Inertial migration of rigid spheres i n two-dimensional unidirectional flows. *J Fluid Mech* **65**, 365–400 (1974).

275. Beris, A. N., Horner, J. S., Jariwala, S., Armstrong, M. J. & Wagner, N. J. Recent advances in blood rheology: a review. *Soft Matter* **17**, 10591–10613 (2021).

276. Huang, D. *et al.* Rapid separation of human breast cancer cells from blood using a simple spiral channel device. *Analytical Methods* **8**, 5940–5948 (2016).

277. Li, B.-W. *et al.* Enhanced Separation Efficiency and Purity of Circulating Tumor Cells Based on the Combined Effects of Double Sheath Fluids and Inertial Focusing. *Front Bioeng Biotechnol* **9**, (2021).

278. Khoo, B. L. *et al.* Ultra-High Throughput Enrichment of Viable Circulating Tumor Cells. in 1–4 (2014). doi:10.1007/978-3-319-02913-9_1.

279. Warkiani, M. E. *et al.* Ultra-fast, label-free isolation of circulating tumor cells from blood using spiral microfluidics. *Nat Protoc* **11**, 134–148 (2016).

280. Jiang, J. *et al.* An integrated microfluidic device for rapid and high-sensitivity analysis of circulating tumor cells. *Sci Rep* **7**, 42612 (2017).

281. Ribeiro-Samy, S. *et al.* Fast and efficient microfluidic cell filter for isolation of circulating tumor cells from unprocessed whole blood of colorectal cancer patients. *Sci Rep* **9**, 8032 (2019).

282. Nagrath, S. *et al.* Isolation of rare circulating tumour cells in cancer patients by microchip technology. *Nature* **450**, 1235–1239 (2007).

283. Adams, A. A. *et al.* Highly Efficient Circulating Tumor Cell Isolation from Whole Blood and Label-Free Enumeration Using Polymer-Based Microfluidics with an Integrated Conductivity Sensor. *J Am Chem Soc* **130**, 8633–8641 (2008).

284. Stroock, A. D. *et al.* Chaotic Mixer for Microchannels. *Science (1979)* **295**, 647–651 (2002).

285. Santos, A. Fundamentals and Applications of Impedimetric and Redox Capacitive Biosensors. *J Anal Bioanal Tech* **S7**, (2014).

286. Hyun, K.-A., Lee, T. Y. & Jung, H.-I. Negative Enrichment of Circulating Tumor Cells Using a Geometrically Activated Surface Interaction Chip. *Anal Chem* **85**, 4439–4445 (2013).

287. Hermanson, G. T. (Strept)avidin–Biotin Systems. in *Bioconjugate Techniques* 465–505 (Elsevier, 2013). doi:10.1016/B978-0-12-382239-0.00011-X.

288. Santos, A. Fundamentals and Applications of Impedimetric and Redox Capacitive Biosensors. *J Anal Bioanal Tech* **S7**, (2014).

289. Singh, M., Kaur, N. & Comini, E. The role of self-assembled monolayers in electronic devices. *J Mater Chem C Mater* **8**, 3938–3955 (2020).

290. Watcharinyanon, S. Structure of Self-Assembled Monolayers on Gold Studied by NEXAFS and Photoelectron Spectroscopy . (Karlstads universitet, 2008).

291. Noel, J. A., Teizer, W. & Hwang, W. Surface Manipulation of Microtubules Using Self-Assembled Monolayers and Electrophoresis. *ACS Nano* **3**, 1938–1946 (2009).

292. Ghosh, U. Quantifying formations of Neutravidin clusters on biotinylated mixed silane Self-Assembled Monolayers. *bioRxiv* 2022.03.21.485091 (2022) doi:10.1101/2022.03.21.485091.

293. Kim, D. & Herr, A. E. Protein immobilization techniques for microfluidic assays. *Biomicrofluidics* **7**, 041501 (2013).

294. Akasov, R. *et al.* 3D in vitro co-culture models based on normal cells and tumor spheroids formed by cyclic RGD-peptide induced cell self-assembly. *Biotechnol Lett* **39**, 45–53 (2017).

295. Akasov, R. *et al.* Sialylation transmogrifies human breast and pancreatic cancer cells into 3D multicellular tumor spheroids using cyclic RGD-peptide induced self-assembly. *Oncotarget* **7**, 66119–66134 (2016).

296. Nimse, S., Song, K., Sonawane, M., Sayyed, D. & Kim, T. Immobilization Techniques for Microarray: Challenges and Applications. *Sensors* **14**, 22208–22229 (2014).

297. Nora Dickson, M. *et al.* Efficient capture of circulating tumor cells with a novel immunocytochemical microfluidic device. *Biomicrofluidics* **5**, 034119 (2011).

298. Cai, H. & Wind, S. J. Improved Glass Surface Passivation for Single-Molecule Nanoarrays. *Langmuir* **32**, 10034–10041 (2016).

299. Wadu-Mesthrige, K., Amro, N. A. & Liu, G.-Y. Immobilization of proteins on self-assembled monolayers. *Scanning* **22**, 380–388 (2006).

300. Sierra-Agudelo, J., Rodriguez-Trujillo, R. & Samitier, J. Microfluidics for the Isolation and Detection of Circulating Tumor Cells. in 389–412 (2022). doi:10.1007/978-3-031-04039-9_16.

301. Miller, M. C., Doyle, G. V. & Terstappen, L. W. M. M. Significance of Circulating Tumor Cells Detected by the CellSearch System in Patients with Metastatic Breast Colorectal and Prostate Cancer. *J Oncol* **2010**, 1–8 (2010).

302. Miller, M. C., Doyle, G. V. & Terstappen, L. W. M. M. Significance of Circulating Tumor Cells Detected by the CellSearch System in Patients with Metastatic Breast Colorectal and Prostate Cancer. *J Oncol* **2010**, 1–8 (2010).

303. Agnoletto, C. *et al.* Heterogeneity in Circulating Tumor Cells: The Relevance of the Stem-Cell Subset. *Cancers (Basel)* **11**, 483 (2019).

304. Jie, X.-X., Zhang, X.-Y. & Xu, C.-J. Epithelial-to-mesenchymal transition, circulating tumor cells and cancer metastasis: Mechanisms and clinical applications. *Oncotarget* **8**, 81558–81571 (2017).

305. Stott, S. L. *et al.* Isolation of circulating tumor cells using a microvortex-generating herringbone-chip. *Proceedings of the National Academy of Sciences* **107**, 18392–18397 (2010).

306. Schmolke, H. *et al.* Polyelectrolyte multilayer surface functionalization of poly(dimethylsiloxane) (PDMS) for reduction of yeast cell adhesion in microfluidic devices. *Biomicrofluidics* **4**, (2010).

307. Boozer, C. *et al.* Surface functionalization for self-referencing surface plasmon resonance (SPR) biosensors by multi-step self-assembly. *Sens Actuators B Chem* **90**, 22–30 (2003).

308. Glass, N. R., Tjeung, R., Chan, P., Yeo, L. Y. & Friend, J. R. Organosilane deposition for microfluidic applications. *Biomicrofluidics* **5**, (2011).

309. Peterson, A. W. The effect of surface probe density on DNA hybridization. *Nucleic Acids Res* **29**, 5163–5168 (2001).

310. Stott, S. L. *et al.* Isolation of circulating tumor cells using a microvortex-generating herringbone-chip. *Proceedings of the National Academy of Sciences* **107**, 18392–18397 (2010).

311. Im, M. *et al.* Comparative Quantitative Analysis of Cluster of Differentiation 45 Antigen Expression on Lymphocyte Subsets. *Ann Lab Med* **31**, 148–153 (2011).

312. Wang, S. *et al.* Highly efficient and selective isolation of rare tumor cells using a microfluidic chip with wavy-herringbone micro-patterned surfaces. *Analyst* **141**, 2228–2237 (2016).

313. Behrens, M. R. *et al.* Open-source, 3D-printed Peristaltic Pumps for Small Volume Point-of-Care Liquid Handling. *Sci Rep* **10**, 1543 (2020).

314. Zeng, W., Li, S. & Wang, Z. Characterization of syringe-pump-driven versus pressure-driven microfluidic flows. in *2015 International Conference on Fluid Power and Mechatronics (FPM)* 711–715 (IEEE, 2015). doi:10.1109/FPM.2015.7337207.

315. Gu, W., Zhu, X., Futai, N., Cho, B. S. & Takayama, S. Computerized microfluidic cell culture using elastomeric channels and Braille displays. *Proceedings of the National Academy of Sciences* **101**, 15861–15866 (2004).

316. Mosadegh, B. *et al.* Control of soft machines using actuators operated by a Braille display. *Lab Chip* **14**, 189–199 (2014).

317. Lake, J. R., Heyde, K. C. & Ruder, W. C. Low-cost feedback-controlled syringe pressure pumps for microfluidics applications. *PLoS One* **12**, e0175089 (2017).

318. Wijnen, B., Hunt, E. J., Anzalone, G. C. & Pearce, J. M. Open-Source Syringe Pump Library. *PLoS One* **9**, e107216 (2014).

319. Garcia, V. E., Liu, J. & DeRisi, J. L. Low-cost touchscreen driven programmable dual syringe pump for life science applications. *HardwareX* **4**, e00027 (2018).

320. Kassis, T. *et al.* PiFlow: A biocompatible low-cost programmable dynamic flow pumping system utilizing a Raspberry Pi Zero and commercial piezoelectric pumps. *HardwareX* **4**, e00034 (2018).

321. Micropumps | EnSense. *http://www.ensensetech.com/micropumps/* (2022).

322. Zhang, J., Chen, K. & Fan, Z. H. Circulating Tumor Cell Isolation and Analysis. in 1–31 (2016). doi:10.1016/bs.acc.2016.03.003.

323. Warkiani, M. E. *et al.* Ultra-fast, label-free isolation of circulating tumor cells from blood using spiral microfluidics. *Nat Protoc* **11**, 134–148 (2016).

324. Guzniczak, E. *et al.* Deformability-induced lift force in spiral microchannels for cell separation. *Lab Chip* **20**, 614–625 (2020).

325. Lake, M. *et al.* Microfluidic device design, fabrication, and testing protocols. *Protoc Exch* (2015) doi:10.1038/protex.2015.069.

326. Onoshima, D. *et al.* Leukocyte Depletion and Size-Based Enrichment of Circulating Tumor Cells Using a Pressure-Sensing Microfiltration Device. *ACS Measurement Science Au* **3**, 113–119 (2023).

327. Diéguez, L., Winter, M. A., Pocock, K. J., Bremmell, K. E. & Thierry, B. Efficient microfluidic negative enrichment of circulating tumor cells in blood using roughened PDMS. *Analyst* **140**, 3565–3572 (2015).

328. Peterson, A. W. The effect of surface probe density on DNA hybridization. *Nucleic Acids Res* **29**, 5163–5168 (2001).

329. Nouni-García, R. *et al.* Factors Associated with Colorectal Cancer Screening in Spain: Results of the 2017 National Health Survey. *Int J Environ Res Public Health* **19**, 5460 (2022).

330. International Agency for Research on Cancer. World health organization. https://gco.iarc.fr/today/home.

331. Morgan, E. *et al.* Global burden of colorectal cancer in 2020 and 2040: incidence and mortality estimates from GLOBOCAN. *Gut* **72**, 338–344 (2023).

332. Caputo *et al.* BRAF-Mutated Colorectal Cancer: Clinical and Molecular Insights. *Int J Mol Sci* **20**, 5369 (2019).

333. Guinney, J. *et al.* The consensus molecular subtypes of colorectal cancer. *Nat Med* **21**, 1350–1356 (2015).

334. Boland, C. R. & Goel, A. Microsatellite Instability in Colorectal Cancer. *Gastroenterology* **138**, 2073-2087.e3 (2010).

335. de la Chapelle, A. & Hampel, H. Clinical Relevance of Microsatellite Instability in Colorectal Cancer. *Journal of Clinical Oncology* **28**, 3380–3387 (2010).

336. de la Chapelle, A. & Hampel, H. Clinical Relevance of Microsatellite Instability in Colorectal Cancer. *Journal of Clinical Oncology* **28**, 3380–3387 (2010).

337. Tieng, F. Y. F., Abu, N., Lee, L.-H. & Ab Mutalib, N.-S. Microsatellite Instability in Colorectal Cancer Liquid Biopsy—Current Updates on Its Potential in Non-Invasive Detection, Prognosis and as a Predictive Marker. *Diagnostics* **11**, 544 (2021).

338. Borrebaeck, C. A. K. Precision diagnostics: moving towards protein biomarker signatures of clinical utility in cancer. *Nat Rev Cancer* **17**, 199–204 (2017).

339. Ahn, S. B. *et al.* Potential early clinical stage colorectal cancer diagnosis using a proteomics blood test panel. *Clin Proteomics* **16**, 34 (2019).

340. Kuppusamy, P., Govindan, N., Yusoff, M. M. & Ichwan, S. J. A. Proteins are potent biomarkers to detect colon cancer progression. *Saudi J Biol Sci* **24**, 1212–1221 (2017).

341. Chen, B. *et al.* Emerging microRNA biomarkers for colorectal cancer diagnosis and prognosis. *Open Biol* **9**, (2019).

342. Abedini, P. *et al.* Expression analysis of circulating plasma long noncoding RNAs in colorectal cancer: The relevance of lncRNAs ATB and CCAT1 as potential clinical hallmarks. *J Cell Physiol* **234**, 22028–22033 (2019).

343. Luo, X., Burwinkel, B., Tao, S. & Brenner, H. MicroRNA Signatures: Novel Biomarker for Colorectal Cancer? *Cancer Epidemiology, Biomarkers & Prevention* **20**, 1272–1286 (2011).

344. Mohd Yunos, R. I., Ab Mutalib, N. S., Tieng, F. Y. F., Abu, N. & Jamal, R. Actionable Potentials of Less Frequently Mutated Genes in Colorectal Cancer and Their Roles in Precision Medicine. *Biomolecules* **10**, 476 (2020).

345. Loktionov, A. Biomarkers for detecting colorectal cancer non-invasively: DNA, RNA or proteins? *World J Gastrointest Oncol* **12**, 124–148 (2020).

346. Van Lier, M. G. F. *et al.* Underutilization of microsatellite instability analysis in colorectal cancer patients at high risk for Lynch syndrome. *Scand J Gastroenterol* **44**, 600–604 (2009).

347. Silveira, A. B. *et al.* High-Accuracy Determination of Microsatellite Instability Compatible with Liquid Biopsies. *Clin Chem* **66**, 606–613 (2020).

348. Willis, J. *et al.* Validation of Microsatellite Instability Detection Using a Comprehensive Plasma-Based Genotyping Panel. *Clinical Cancer Research* **25**, 7035–7045 (2019).

349. Mohamed Suhaimi, N.-A. *et al.* Non-invasive sensitive detection of *KRAS* and *BRAF* mutation in circulating tumor cells of colorectal cancer patients. *Mol Oncol* **9**, 850–860 (2015).

350. Burz, C. *et al.* Circulating tumor cells in clinical research and monitoring patients with colorectal cancer. *Oncotarget* **9**, 24561–24571 (2018).

351. Allen-Mersh, T. G. *et al.* Role of circulating tumour cells in predicting recurrence after excision of primary colorectal carcinoma. *British Journal of Surgery* **94**, 96–105 (2007).

352. Toh, J. W. T. *et al.* Association between Microsatellite Instability Status and Peri-Operative Release of Circulating Tumour Cells in Colorectal Cancer. *Cells* **9**, 425 (2020).

353. Tan, C. R. C., Zhou, L. & El-Deiry, W. S. Circulating Tumor Cells Versus Circulating Tumor DNA in Colorectal Cancer: Pros and Cons. *Curr Colorectal Cancer Rep* **12**, 151–161 (2016).

354. Steinert, G. *et al.* Immune Escape and Survival Mechanisms in Circulating Tumor Cells of Colorectal Cancer. *Cancer Res* **74**, 1694–1704 (2014).

355. Messaritakis, I. *et al.* Circulating tumor cell detection and microsatellite instability status in predicting outcomes of advanced CRC patients. *Annals of Oncology* **30**, iv21 (2019).

356. Motta Guerrero, R. *et al.* Targeting BRAF V600E in metastatic colorectal cancer: where are we today? *Ecancermedicalscience* **16**, (2022).

357. Taieb, J., Lapeyre-Prost, A., Laurent Puig, P. & Zaanan, A. Exploring the best treatment options for BRAF-mutant metastatic colon cancer. *Br J Cancer* **121**, 434–442 (2019).

358. Zhu, G., Pei, L., Xia, H., Tang, Q. & Bi, F. Role of oncogenic KRAS in the prognosis, diagnosis and treatment of colorectal cancer. *Mol Cancer* **20**, 143 (2021).

359. Buim, M. E. *et al.* Detection of KRAS mutations in circulating tumor cells from patients with metastatic colorectal cancer. *Cancer Biol Ther* **16**, 1289–1295 (2015).

360. Kondo, Y. *et al.* KRAS mutation analysis of single circulating tumor cells from patients with metastatic colorectal cancer. *BMC Cancer* **17**, 311 (2017).

361. Buim, M. E. *et al.* Detection of KRAS mutations in circulating tumor cells from patients with metastatic colorectal cancer. *Cancer Biol Ther* **16**, 1289–1295 (2015).

362. Cheng, Y. *et al.* Diagnostic Value of Different Phenotype Circulating Tumor Cells in Hepatocellular Carcinoma. *Journal of Gastrointestinal Surgery* **23**, 2354–2361 (2019).

363. Ha, Y. *et al.* Circulating tumor cells are associated with poor outcomes in early-stage hepatocellular carcinoma: a prospective study. *Hepatol Int* **13**, 726–735 (2019).

364. Zhu, G., Pei, L., Xia, H., Tang, Q. & Bi, F. Role of oncogenic KRAS in the prognosis, diagnosis and treatment of colorectal cancer. *Mol Cancer* **20**, 143 (2021).

365. Liu, Y., Meucci, S., Sheng, L. & Keilholz, U. Meta-analysis of the mutational status of circulation tumor cells and paired primary tumor tissues from colorectal cancer patients. *Oncotarget* **8**, 77928–77941 (2017).

366. Kidess-Sigal, E. *et al.* Enumeration and targeted analysis of *KRAS* , *BRAF* and *PIK3CA* mutations in CTCs captured by a label-free platform: Comparison to ctDNA and tissue in metastatic colorectal cancer. *Oncotarget* **7**, 85349–85364 (2016).

367. Yang, C., Zhuang, W., Hu, Y. & Zhu, L. Clinical significance of peripheral circulating tumor cell counts in colorectal polyps and non-metastatic colorectal cancer. *World J Surg Oncol* **16**, 13 (2018).

368. Jiang, M. *et al.* Detection and clinical significance of circulating tumor cells in colorectal cancer. *Biomark Res* **9**, 85 (2021).

369. Grillet, F. *et al.* Circulating tumour cells from patients with colorectal cancer have cancer stem cell hallmarks in *ex vivo* culture. *Gut* **66**, 1802–1810 (2017).

370. Mackenzie, C. G., Mackenzie, J. B. & Beck, P. THE EFFECT OF pH ON GROWTH, PROTEIN SYNTHESIS, AND LIPID-RICH PARTICLES OF CULTURED MAMMALIAN CELLS. *J Biophys Biochem Cytol* **9**, 141–156 (1961).

371. Eagle, H. The effect of environmental pH on the growth of normal and malignant cells. *J Cell Physiol* **82**, 1–8 (1973).

372. Kurosawa, H. Application of Rho-associated protein kinase (ROCK) inhibitor to human pluripotent stem cells. *J Biosci Bioeng* **114**, 577–581 (2012).

373. Lee, W. *et al.* Effect of Rho-kinase Inhibitor, Y27632, on Porcine Corneal Endothelial Cell Culture, Inflammation and Immune Regulation. *Ocul Immunol Inflamm* **24**, 579–593 (2016).

374. Haga, R. B. & Ridley, A. J. Rho GTPases: Regulation and roles in cancer cell biology. *Small GTPases* **7**, 207–221 (2016).

375. De Renzi, G. *et al.* In vitro cultures of circulating tumor cells: a potential tool to unravel drug sensitivity. *Cancer Drug Resistance* (2022) doi:10.20517/cdr.2021.121.

376. Cayrefourcq, L. *et al.* Establishment and Characterization of a Cell Line from Human Circulating Colon Cancer Cells. *Cancer Res* **75**, 892–901 (2015).

377. Descamps, L., Le Roy, D. & Deman, A.-L. Microfluidic-Based Technologies for CTC Isolation: A Review of 10 Years of Intense Efforts towards Liquid Biopsy. *Int J Mol Sci* **23**, 1981 (2022).

378. Nikanjam, M., Kato, S. & Kurzrock, R. Liquid biopsy: current technology and clinical applications. *J Hematol Oncol* **15**, 131 (2022).

379. Forbes, T. P. & Kralj, J. G. Engineering and analysis of surface interactions in a microfluidic herringbone micromixer. *Lab Chip* **12**, 2634 (2012).

380. Guo, T. Culture of Circulating Tumor Cells - Holy Grail and Big Challenge. *Int J Cancer Clin Res* **3**, (2016).

381. Kulasinghe, A. *et al.* Short term *ex-vivo* expansion of circulating head and neck tumour cells. *Oncotarget* **7**, 60101–60109 (2016).

382. Cegan, M. *et al.* In vitro culturing of viable circulating tumor cells of urinary bladder cancer. *Int J Clin Exp Pathol* **7**, 7164–71 (2014).

383. Bobek, V. *et al.* Cultivation of circulating tumor cells in esophageal cancer. *Folia Histochem Cytobiol* **52**, 171–177 (2014).

384. Zhang, Z. *et al.* Expansion of CTCs from early stage lung cancer patients using a microfluidic co-culture model. *Oncotarget* **5**, 12383–12397 (2014).

385. BOBEK, V., KACPRZAK, G., RZECHONEK, A. & KOLOSTOVA, K. Detection and Cultivation of Circulating Tumor Cells in Malignant Pleural Mesothelioma. *Anticancer Res* **34**, 2565 (2014).

386. Soler, A. *et al.* Autologous cell lines from circulating colon cancer cells captured from sequential liquid biopsies as model to study therapy-driven tumor changes. *Sci Rep* **8**, 15931 (2018).

387. Cayrefourcq, L. *et al.* Establishment and Characterization of a Cell Line from Human Circulating Colon Cancer Cells. *Cancer Res* **75**, 892–901 (2015).

388. COMSOL Multiphysics Modeling guide . in vol. COMSOL 3.4 130–155 (2007).

389. Berney, H., Roseingrave, P., Alderman, J., Lane, W. & Collins, J. K. Biosensor surface characterisation: confirming multilayer immobilisation, determining coverage of the biospecies and establishing detection limits. *Sens Actuators B Chem* **44**, 341–349 (1997).

APPENDIX A

Numerical modelling of spiral microfluidic device: Discretization methods

Supplementary Figure 45B-E show the simulations performed with the two different discretization methods and the result particle trajectory for a particle size of 20 µm. The velocity magnitude has the standard parabolic profile of a laminar flow in a channel (Poiseuille Flow) with higher velocities in the centre that decrease as it approaches the walls, where the velocity is zero (no slip condition) (Figure 45B,D).

In Figures 45B and D is shown that the profiles of the velocity and the shear stress were smoother on the solutions obtained with a higher-order discretization for the fluid (P2+P1). An accurate solution of velocity and pressure is essential for the correct calculation of the particles trajectories, as the local velocity is used to calculate the Drag force , (equation 5) and the shear stress is used to calculate the wall-induced lift force (equations 6 to 9)[388]. The simulations using P2+P1 discretization indicate that 20 µm particles took the CTC outlet (Figure 45C), while with P1+P1 discretization the 20 µm particles took the waste outlet (Figure 45D). This demonstrates the importance to increase the discretization in this kind of models for avoiding wrong assumptions and successfully predict the trajectories of the particles.

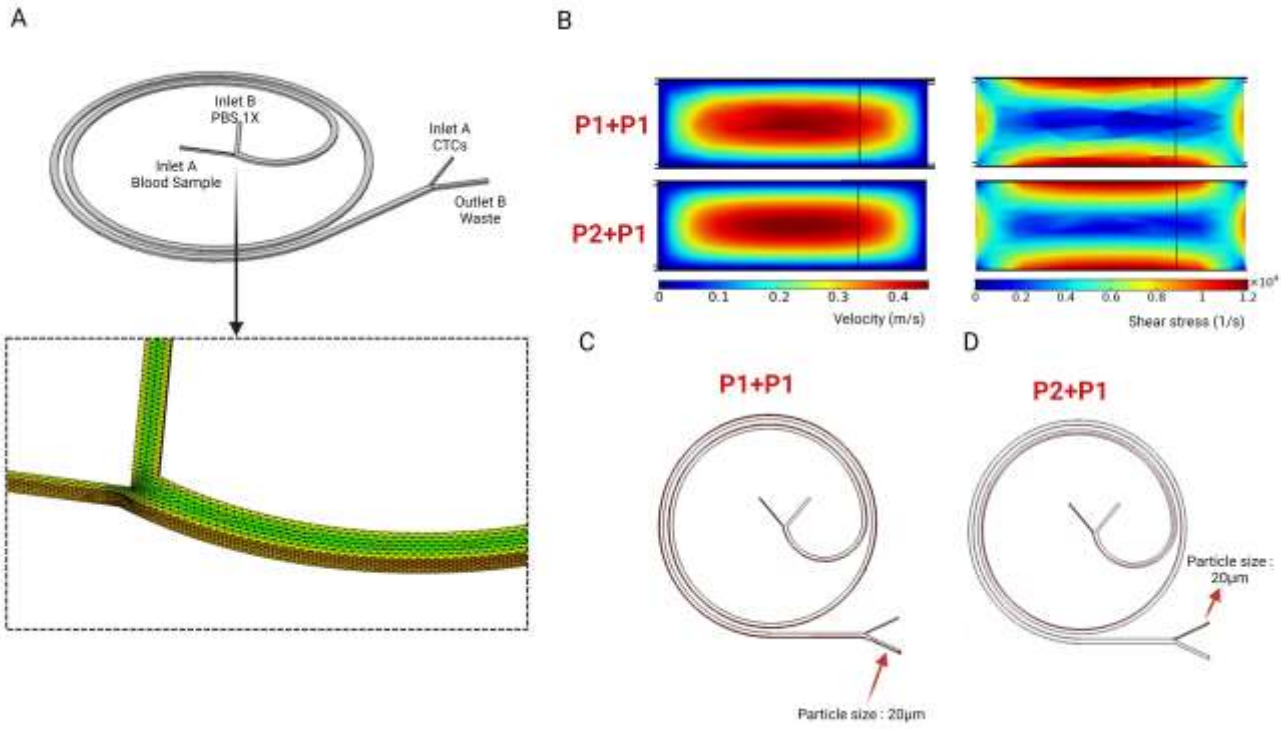

Supplementary Figure 72. **A).** Geometry of the simulated spiral with a detail of the mesh built**. B)** Simulations with fluid discretization P1+P1 and P2+P1 for a sheath flow rate of 900 µL/min and inlet sample flow rate of 100 µL/min. Velocity profile (left pictures), Shear stress profile (right pictures). **C)** 20 µm particles trajectories with fluid discretization P1+P1. D) 20 µm particles trajectories with fluid discretization P2+P1.

Numerical modelling of spiral microfluidic device: Isolation of 10µm CTCs

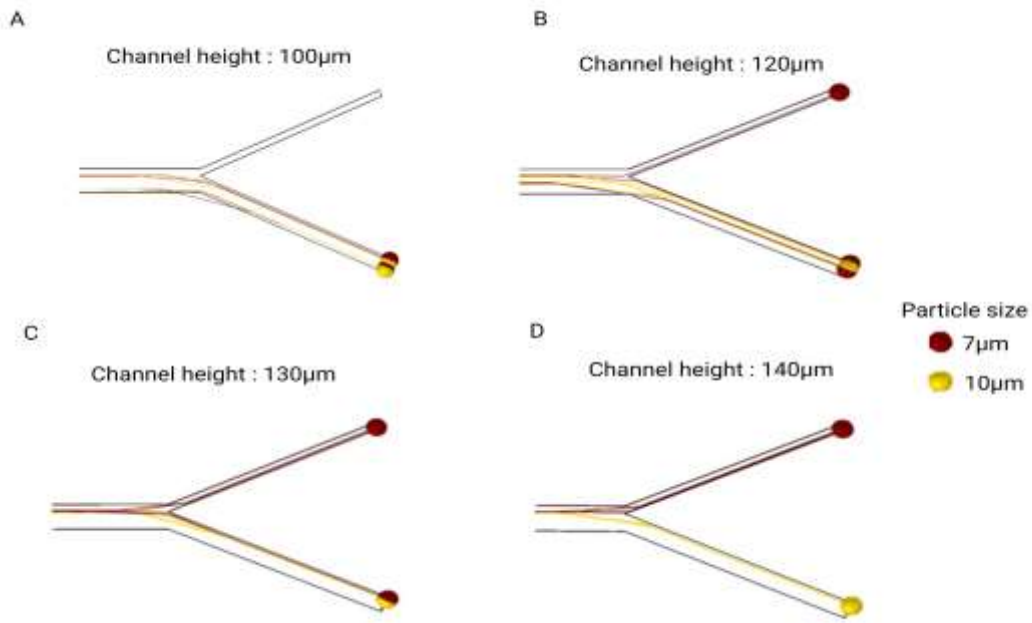

Supplementary Figure 73. Spiral microfluidic device for isolation of small CTCs (~10 µm). Particles of 7 µm were considered as erythrocytes and 10 µm as CTCs model. The figure shows the Particles trajectories in the output of the spiral (Left images) and particles position plotted in a transversal plane 0.5 mm before the bifurcation for inlet sample flow rate of 100 µL/min and sheath flow rate of 900 µL/min according to the channel height (right images): 100 µm **(A),** 120 µm **(B),** 130 µm **(C)** and 140 µm **(D).**

APPENDIX C

A time-dependent study was conducted to analyze particle trajectories within the device designed for white blood cell capture, focusing on leukocytes. The simulation, however, did not consider binding reactions between cells and the functionalized surface. To simulate binding positions, a freeze condition was applied to the device walls, capturing any particles contacting them .

Trajectories were calculated for 40 seconds at an inlet condition of 2.5 µL/min and for 20 seconds at 5 µL/min, ensuring all particles not captured exited the simulated domain. Results in Figure 47 show particle positions at the end of the simulation, with dark blue particles captured on the bottom wall, green ones on the channel surface between grooves, yellow/orange ones on groove walls, and red ones on top of the grooves.

Simulation results indicate that most cells would be captured in the grooves region. The number of cells attached to device walls remained similar for both tested conditions (44% at 2.5 µL/min and 46% at 5 µL/min) due to unchanged hydrodynamic profiles and only differing velocity magnitudes. Thus, the flow rate increase from 2.5 to 5 µL/min had minimal impact on the number of particles reaching the walls.

Considering a similar capture efficiency throughout the device as observed in the simulated section, the total capture efficiency across the entire device was estimated at approximately 95% of entering leukocytes. This aligns with experimental results reported by Hyun et al for similar devices[286]. The simulations also revealed that most cells would be captured on the channel surface between grooves and groove side walls, consistent with Forbes and Kralj's findings[379].

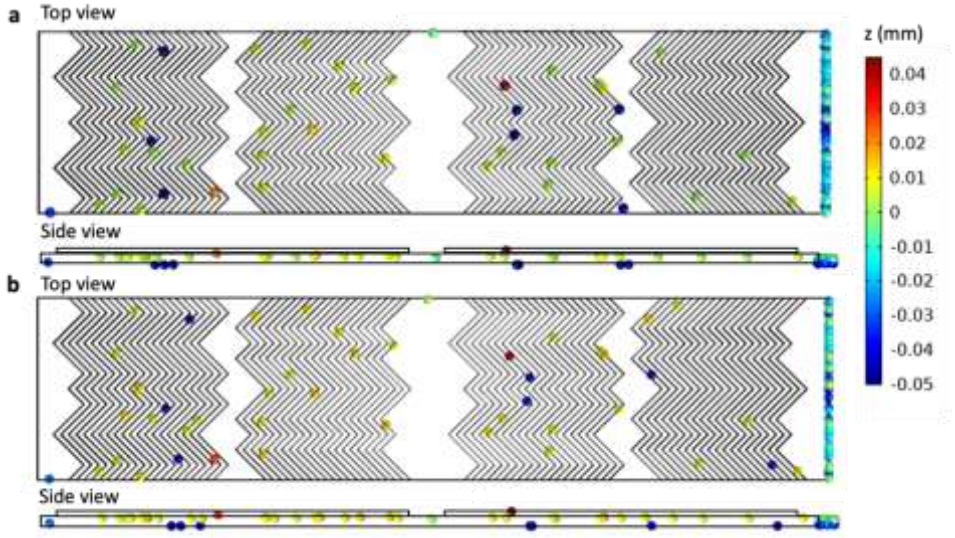

Supplementary Figure 74. Position of the leukocytes captured in the functionalized wall of the device for an inlet flow rate of **A)** 2.5 µL/min and **B)** 5 µL/min. The colors indicate the z position.

APPENDIX D

Fluorescent polystyrene particles of different sizes (Experiment 1): Fluorescent particles trajectories

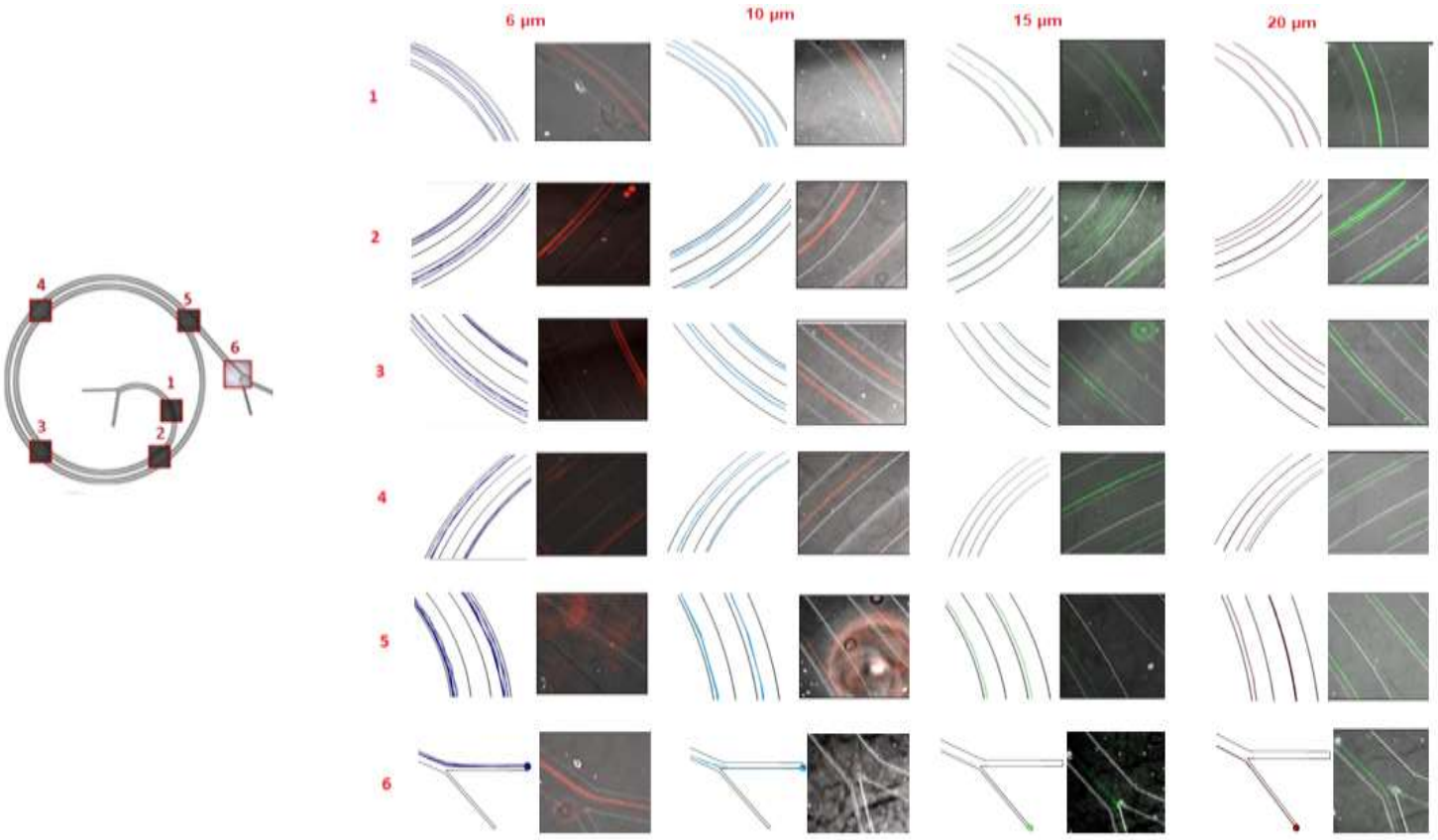

Supplementary Figure 75. Comparison of particle trajectories between COMSOL Multiphysics simulation and experiment with fluorescent particles of 6 µm and 10 µm as blood cells model, 15 µm and 20 µm as CTCs model. The figures show the trajectories in 6 different points of the spiral chip and with inlet sample flow rate of 100 µL/min and sheath flow rates of 900 µL/min.

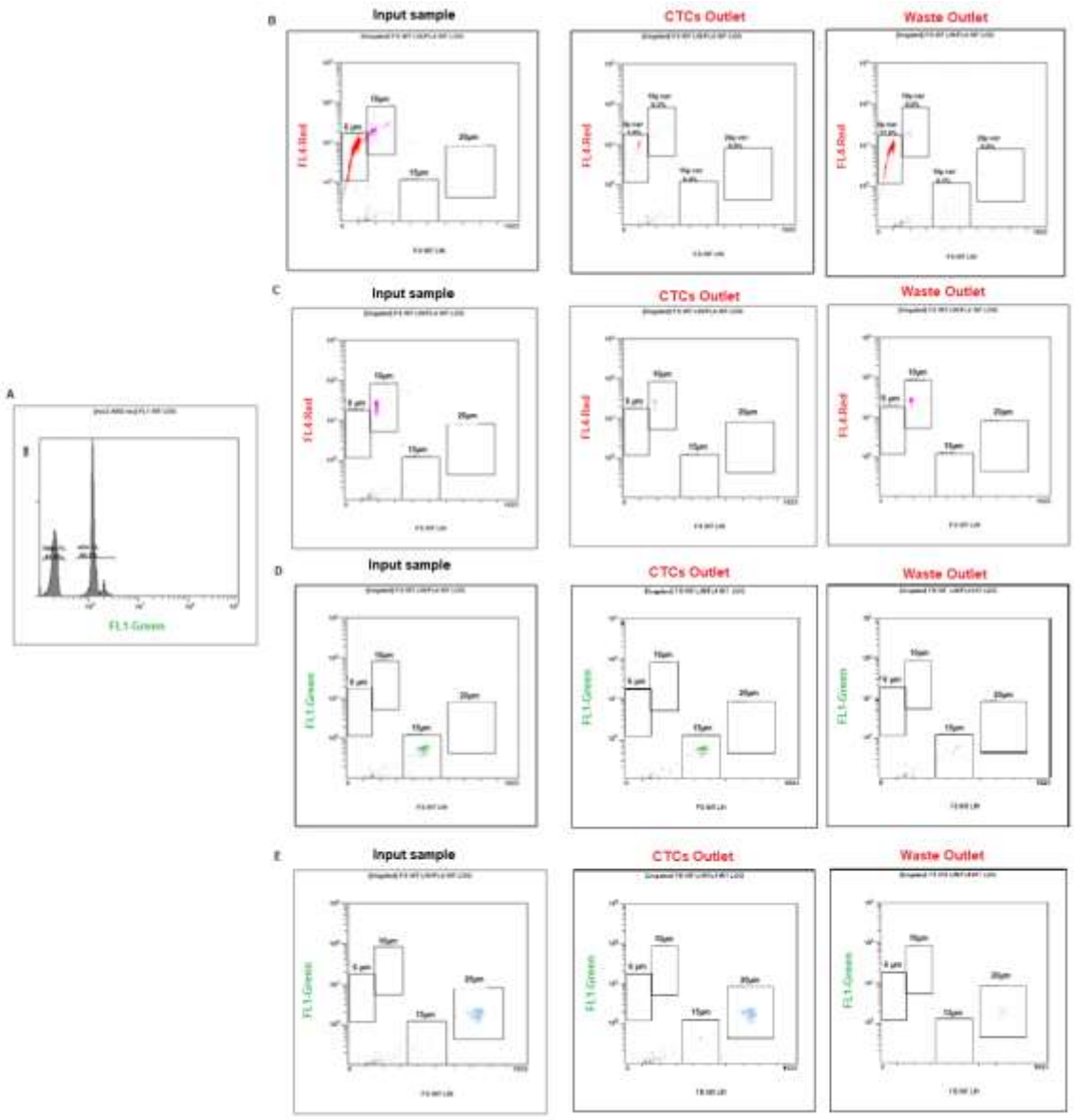

Supplementary Figure 76. Flow cytometry analysis of CTCs outlet and waste Outlet with fluorescent particles. **A)** AccuCheck counting beads for count the cells **B,C)** Analysis of 6 µm and 10 µm Particles from input sample, CTCs Outlet and Waste Outlet. A High particle concentration is observed in the waste Outlet image. **D,E)** Analysis of 15 µm and 20 µm particles from input sample, CTCs Outlet and Waste Outlet. A High particle concentration is observed in the CTCs Outlet.

APPENDIX E

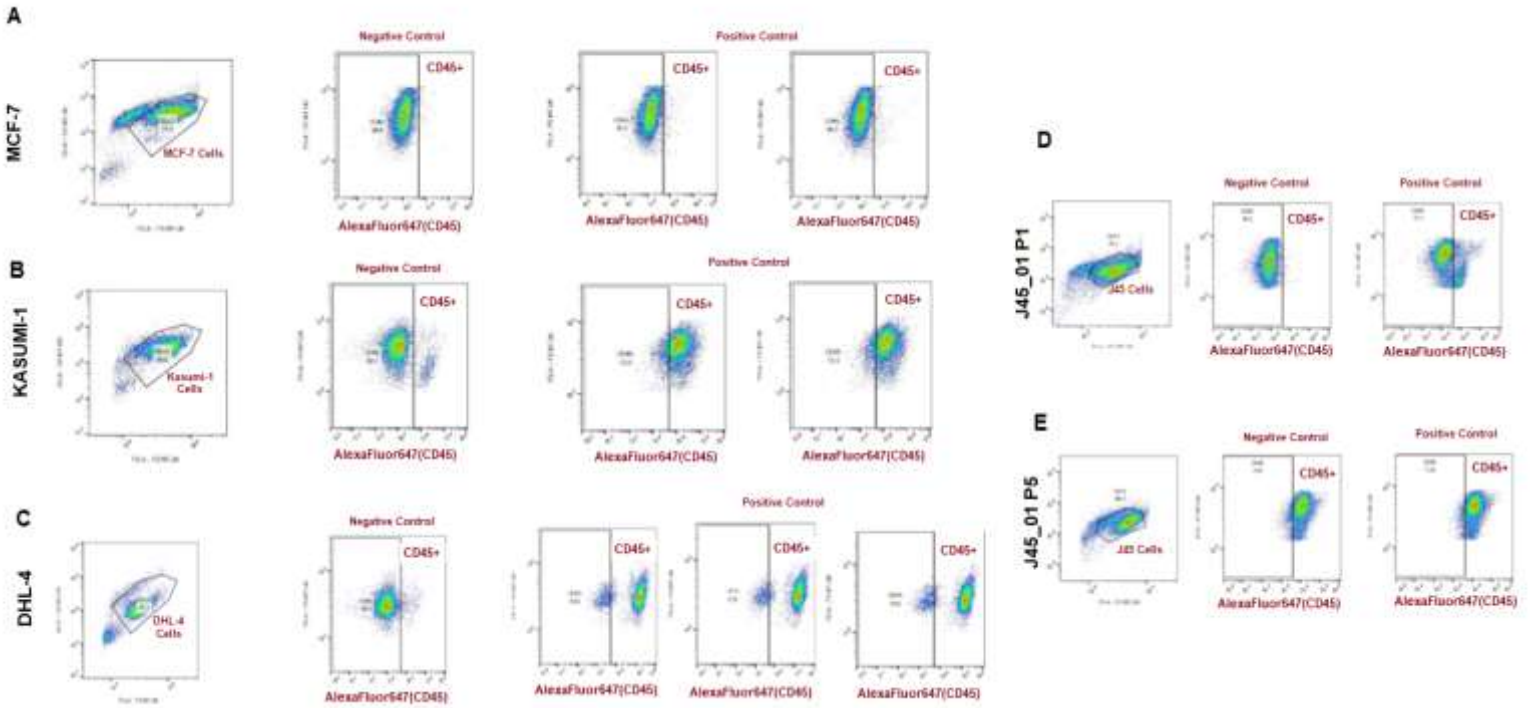

Supplementary Figure 77. The first image on the left represent the gate selected for the cell population and the negative control for the biomarker AlexaFluor 647 CD45, and images on the right represent the positive controls for AlexaFluor 647 CD45(The expression levels increase from left to right at X axis . **A)** Flow cytometry analysis shows very low expression levels of CD45 in MCF-7. **B)** The results show the high expression levels of CD45 in Kaumi-1 **C).** DHL-4 cells display a clear negative subpopulation for CD45 and another cell population CD45+. J45_01 cells change the expression levels of CD45 depends on the pass number. **D)** J45_01P1 represents cells in pass 1 and show low expression levels of CD45, meanwhile cells in pass 5 display high expression levels for CD45 **€**

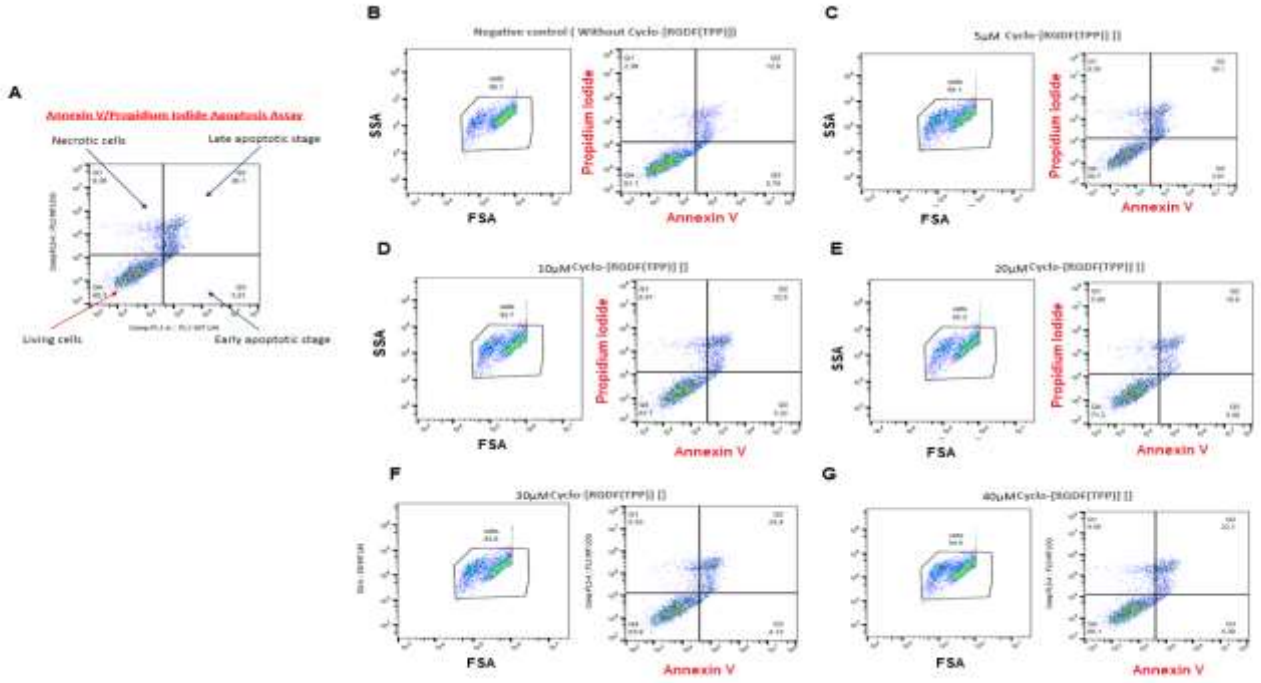

Supplementary Figure 78. Annexin V/ Propidium Iodide apoptosis assay for cell viability in RGD Tumor cell model. **A)** Flow cytometry analysis shows the cells considered as living cells (third quadrant), Early apoptotic cells (fourth quadrant), late apoptotic cells (second quadrant) and Necrotic cells (First quadrant). **B)** Negative control MCF-7 cells without cyclo-[RGDF(TPP)]. **C)** MCF-7 cells incubated with 5µM of cyclo-[RGDF(TPP)]. **D)** MCF-7 cells incubated with 10µM of cyclo-[RGDF(TPP)]. **E)** MCF-7 cells incubated with 20µM of cyclo-[RGDF(TPP)]. **F)** MCF-7 cells incubated with 30µM of cyclo-[RGDF(TPP)]. **G)** MCF-7 cells incubated with 40µM of cyclo-[RGDF(TPP)]. All the conditions display a high percentage of living cells.

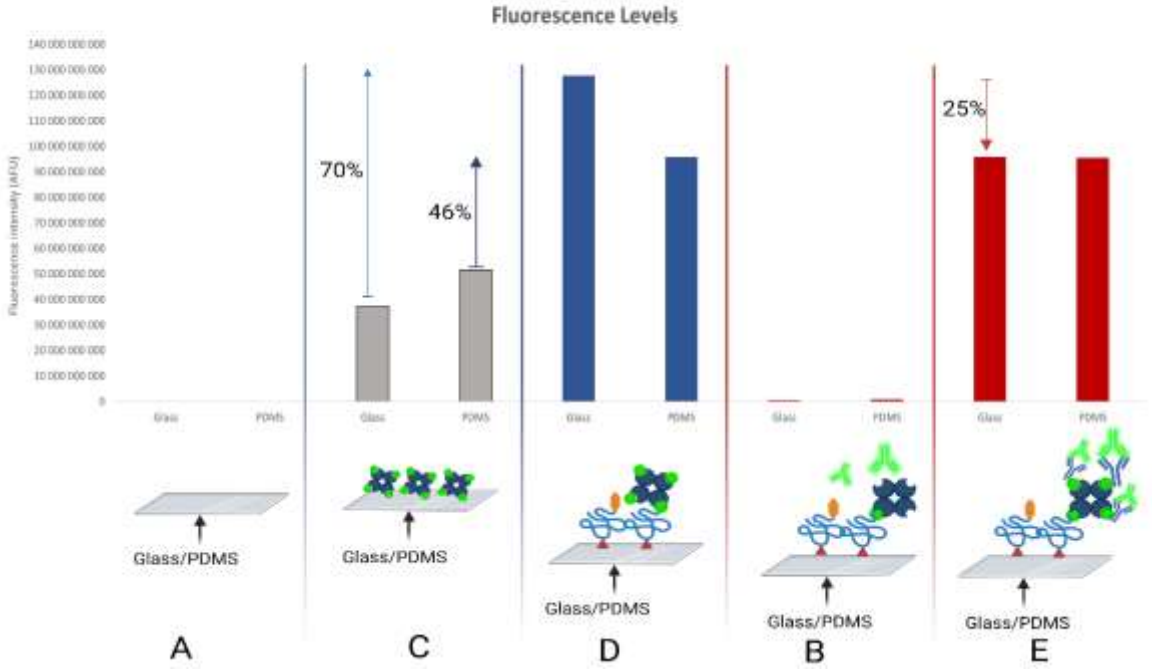

Supplementary Figure 79.Quantification of Fluorescence intensity (AFU) in surfaces immobilized by mixed-SAM. **A)** Negative control herrringbone chip surfaces (glass and PDMS) without SAM. **C)** Herrringbone chip surfaces (glass and PDMS) immobilized with Neutravidin Oregon green 488. D) Herrringbone chip surfaces (glass and PDMS) immobilized with Silane-PEG-Biotin,Silane-PEG-OH, Neutravidin Oregon green 488.B) Herrringbone chip surfaces (glass and PDMS) immobilized with Silane-PEG-Biotin,Silane-PEG-OH, Neutravidin and secondary antibody Goat Anti-Mouse IgG H&L Alexa Fluor 488.E) Herrringbone chip surfaces (glass and PDMS) immobilized with Silane-PEG-Biotin,Silane-PEG-OH, Neutravidin, Biotinylated CD45 antibody and secondary antibody Goat Anti-Mouse IgG H&L Alexa Fluor 488

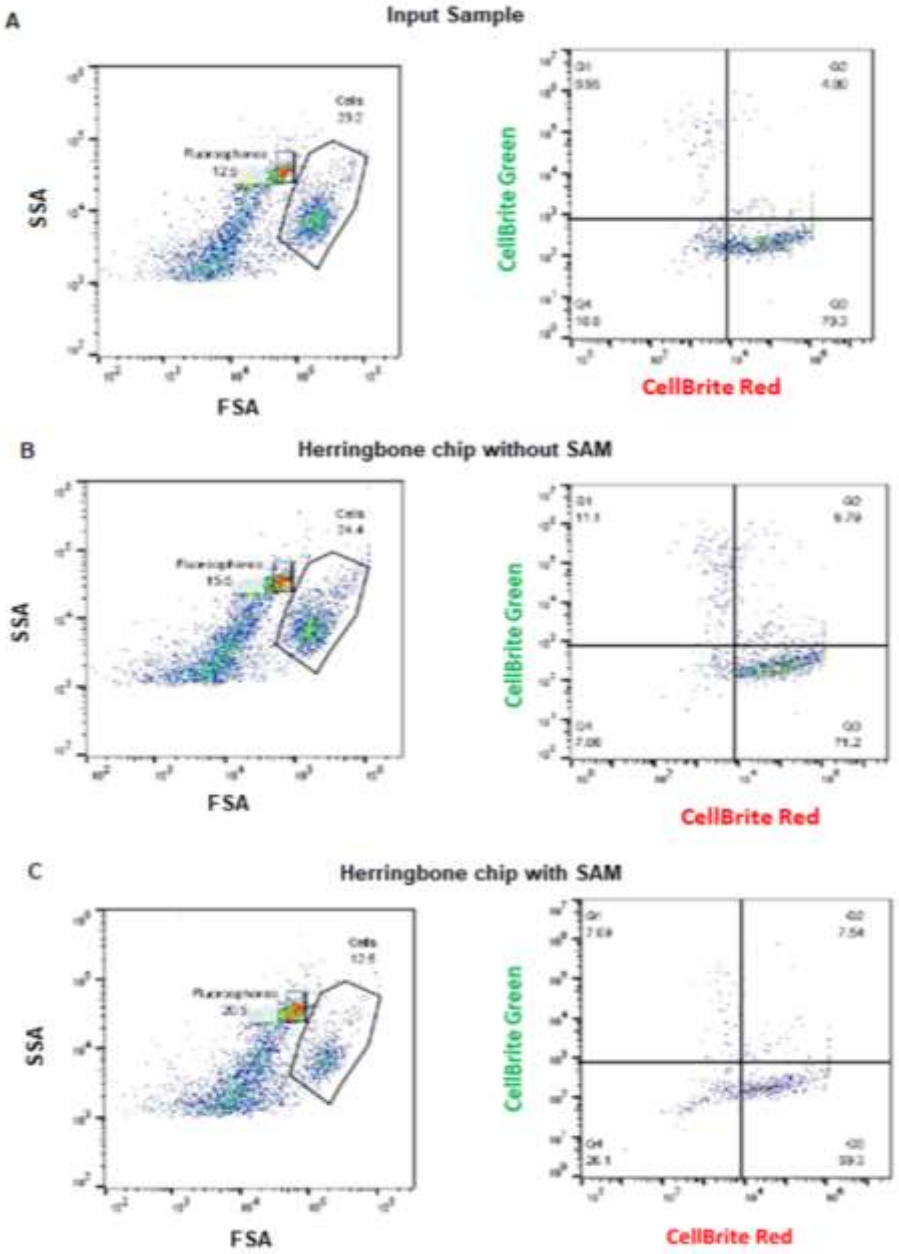

Supplementary Figure 80. Flow cytometry analysis of herringbone chip characterization with cell lines. A) Flow cytometry analysis of input sample.. Kasumi-1 and MCF-7 cells were stained with Cellbrite Red (X axis) and Cellbrite Green (Y axis), respectively. B,C) Chip output without SAM and with SAM. Kasumi-1 and MCF-7 cells were stained with Cellbrite Red (X axis) and Cellbrite Green (Y axis), respectively

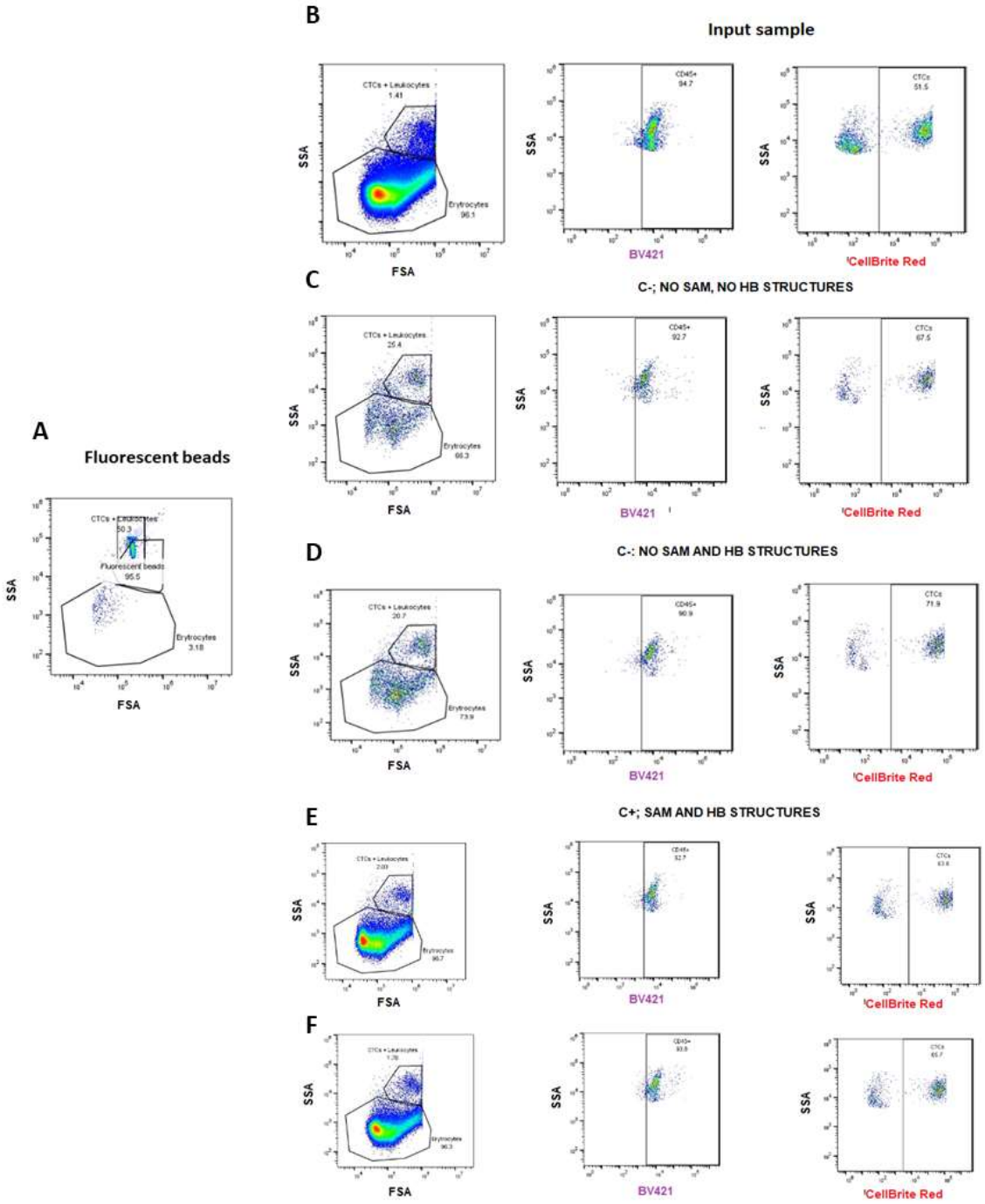

Supplementary Figure 81. Flow cytometry analysis of Herringbone chip characterization with output sample from spiral microfluidic device tested with blood. A) Flow cytometry analysis of AccuCheck counting beads for count the cells. B) Flow cytometry analysis of Input sample where MCF-7 cells were stained with Cellbrite Red (X axis-Right image) and Leukocytes with BV421 CD45 (X axis-left image). C) Negative control. Output sample from Herringbone chip without structures (grooves) neither SAM

surface modification. D) Negative control. Output sample from Herringbone chip with structures (grooves) and without SAM surface modification. E) Positive control. Output sample from Herringbone chip with structures (grooves) and with SAM surface modification. In all the conditions MCF-7 cells were stained with Cellbrite Red (X axis-Right image) and Leukocytes with BV421 CD45 (X axis-left image).

APPENDIX F

Supplementary Equation (1)- Surface coverage

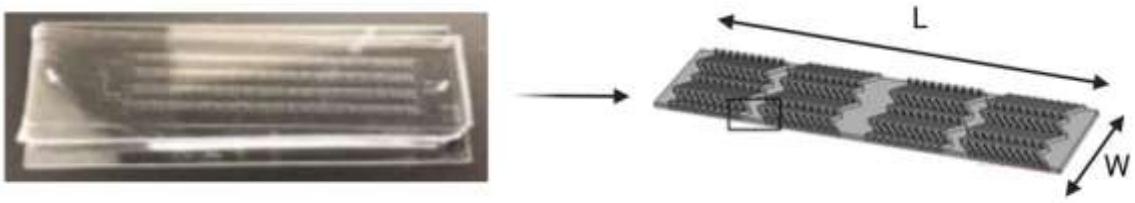

Where L is the channel length and W is the channel width

$A1=L1*W1$

$A1=3000\mu m*2000\mu m$

$A1=6'\,000.000\ 〖\mu m〗\ ^2$

$A2=((a*b)*(L1/a)*W1$

$A2=((60\mu m*45\mu m)*((3000\mu m)/(60\mu m)))*2000\mu m$

$A2=2700\mu m*50*2000\mu m$

$A2=270.000.000\ 〖\mu m〗\ ^2$

$A3=((a*b)*(W1/a)*b$

$A3=((60\mu m*45\mu m)*((2000\mu m)/(60\mu m)))*45\mu m$

$A3=2700\mu m*33{,}3*45\mu m$

$A3=2700\mu m*40*45\mu m$

$A3=4.045.950\ 〖\mu m〗\ ^2*2$

$A3=〖8.0.000\mu m〗\ ^2$

$A4=W1*d$

$A4$=(2000µm∗60µm)∗2

$A4$=240.000〖µm〗^2

A_Total=$A1$+$A2$+$A3$+$A4$

A_Total=(6.000.000+270.000.000+8.100.000+240.000) 〖µm〗^2

A_Total=284.340.000 〖µm〗^2

$$A = \frac{A_{Total}}{Cell\ diameter}$$

$$A = \frac{284.340.000}{20}$$

$$A = 14.217.000 * 30\%$$

$$A = 4.265.100\ cells$$

APPENDIX G

Python script

Raspberry Pi Zero was used to control the mp-Lowdriver through a python code along with GPIO library. Which allows controlling a PWM signal. Thus, the frequency of the PWM was modulated to control the flow rate. In addition, it is possible to specify the duration and turn on first the pump that controls the PBS 1x meanwhile the flow is stabilized, subsequently the pump connected to the blood sample is activated during the desired time.

To validate the flow rates, cell culture media was employed, and measurements were taken at 60-minute intervals. The obtained experimental curve was then compared to the reference values provided by the manufacturer of the pump. Typically, it can be assumed that the flow rate decreases in a linear fashion as the driving voltage decreases. Additionally, reducing the frequency also leads to an approximate linear decrease in the flow rate [43]. The calibration equation derived from these observations was incorporated into the code for further calculations and adjustments.

On the other hand, the python script controls the Raspberry Pi camera connected to the small microscope XPD-101 expedition Bresser, with the camera is possible to record the correct blood focalization through the spiral microfluidic device and check in real time the correct microfluidic device functionality. Finally, the PCB is composed by two-layer board designed in Autodesk EAGLE

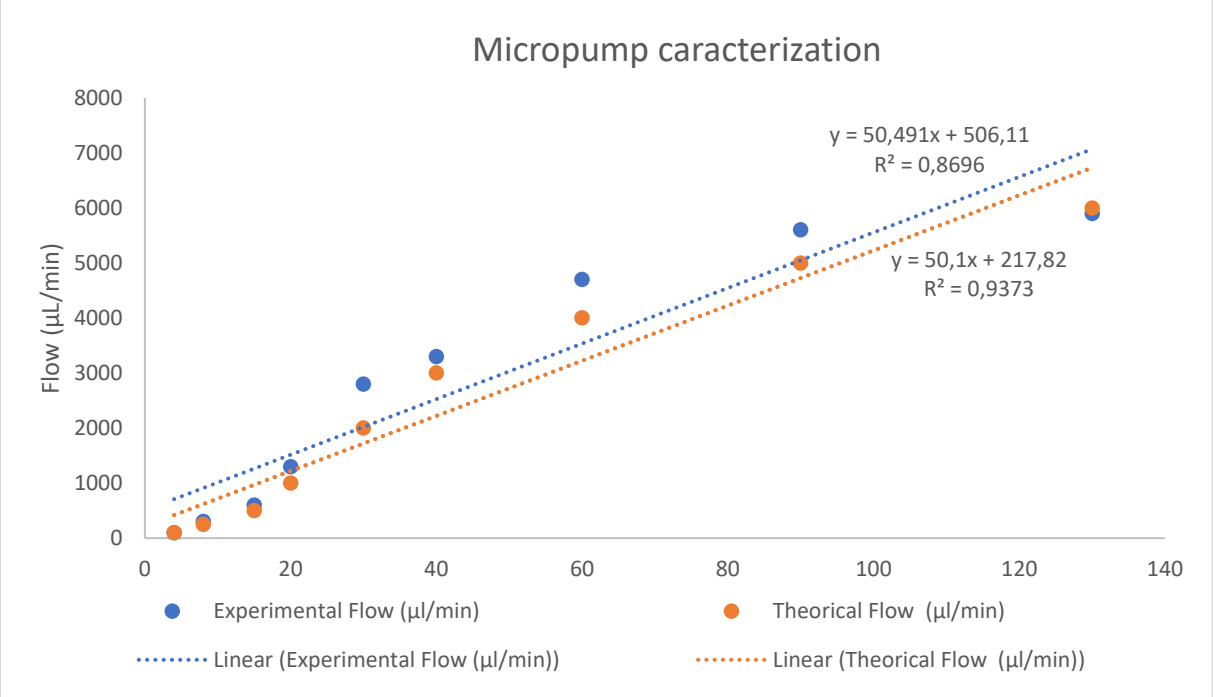

Supplementary Figure 82.Calibration curve for biocompatible flow platform by measuring the cell media displacement at given frequencies from 0 to 130Hz. The equation of line was used in the code for the selection of the desired flow rate.

	Experimental Value	**Theoretical value**
Frequency (Hz) min	Experimental Flow (µl/min)	Theorical Flow (µl/min)
130	5900	6000
90	5600	5000
60	4700	4000
40	3300	3000
30	2800	2000
20	1300	1000
15	600	500
8	300	250
4	100	100

Table 12. Flow rates were measured under different frequency (Hz) values. Experimental values were compared with the theorical values from micropumps manufacture.

Microfluidic Devices Fabrication Using 3D Printed Molds or Assembling 3D Printed Parts

Thanks to the technological development in 3D printing carried out in the Nanobioengineering group at IBEC. We designed and developed 3D printed molds for creating microfluidic spiral devices molds using different biocompatible resins such as Detax resin. Figure 73A shows the embossed extrusion to create an open channel, which is used for creating PDMS replicas. Figure 73B shows the PDMS replica bonded to glass and tested with dyes for further confirmation of the absence of leakage between the channels [256]

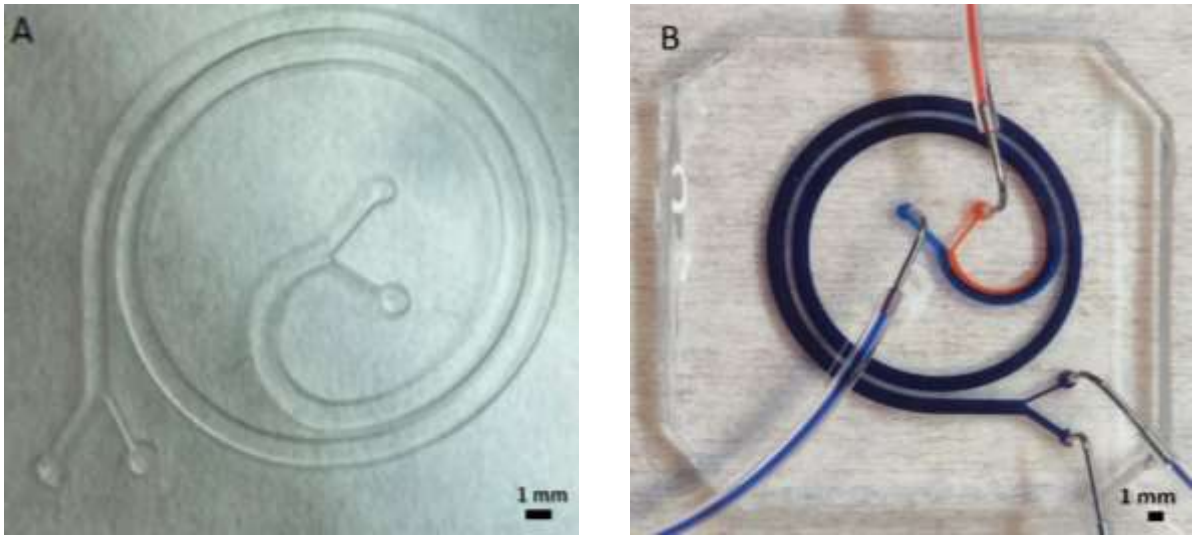

Supplementary Figure 83. A) 3D printed result with Detax resin of the extruded spiral, with a designed channel width of 1 mm and height of 600 µm. B) Picture of the microfluidic system created with the PDMS replica based on the 3D printed.

Recently, closed microfluidic spirals were successfully developed, using transparent biocompatible resins that allow correct visualization under the microscope, making it suitable for use in biological experiments (Figure 74). The dimensions of the channel are 1.4 mm in width, 0.4 mm for the smaller input and output which will contain the blood sample and therefore the CTCs, and 1mm for the wider inputs and outputs which are used for PBS 1X and waste respectively. The aim is to perform separation of CTCs with increased purity and reduced contamination. The influence of channel height has been tested between 600 µm and 800 µm and optimized accordingly. This channel dimensions were chosen due to the capabilities of the 3D printer developed by Subirada et. al.

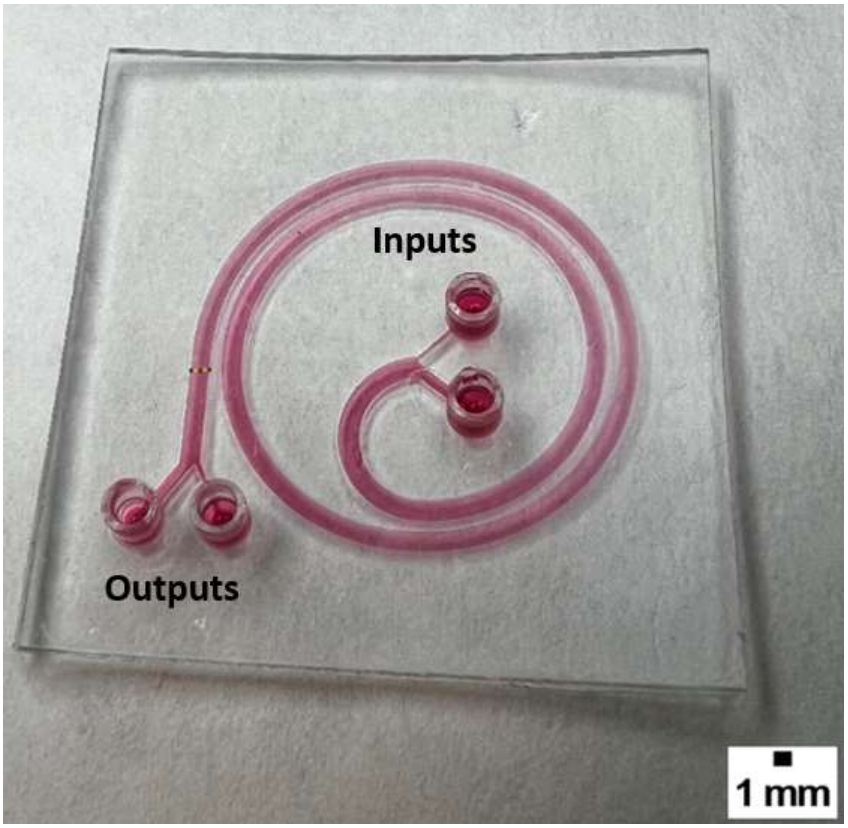

Supplementary Figure 84.The picture shows a 3D printed device, which consists in a spiral with a channel of 1.4 mm width and 600 µm height.

APPENDIX H

Surface particle coverage for leukocytes capture

The sensor behavior is strongly influence by the surface geometry and morphology of the immobilized biolayer[389]. In addition, the detection limits are primarily determined by the number of active biomolecules immobilized on the transducer. In this particular case, the surface particle coverage with the CD45 antibodies was calculated in order to determine the number of particles for capturing the total amount of leukocytes that contaminate the sample based on the antibody capture efficiency.

Leukocyte sample:

$$900.000\,\frac{\text{Leukocytes}}{\text{mL}} \qquad \text{Size: } 12-20\mu\text{m} \qquad \text{Approximate volume: } 15\text{ mL}$$

Polystyrene particles parameters:

Nominal size: 74.5 μm

Density: $1.05\ \frac{\text{g}}{\text{cm}^3}$

Concentration: $1\% = \frac{1\text{g}}{100\text{mL}} = 10\frac{\text{mg}}{\text{mL}}$

Total volumen of particles : 4mL

Binding capacity (Streptavidin): $0.01\,\frac{\text{nmol}}{1\text{mg of particles}}$

MW of polystyrene particle: $1 * 10^6\,\frac{\text{g}}{\text{mol}}$

Leukocyte surface area (La): $4 * \pi * r^2 = \frac{(4*\pi*(10)^2)}{2} = 628\ \mu m^2$

Particle surface area (Lp): $4 * \pi * r^2 = 4 * \pi * (37.25)^2 = 17.437\ \mu m^2$

Amount of leukocytes that can be anchored per particle

$$\frac{\text{Lp}}{\text{La}} = \frac{17.437\ \mu m^2}{628\ \mu m^2} = 28\ \text{Particles}$$

Number of particles in 1 mg

$$\text{Volumen of particle (V)} = \frac{\pi}{6} * d^3 * 10^{-12}\ \frac{cm^3}{\text{particle}} \quad d = \text{diameter of particles}$$

$$V = \frac{\pi}{6} * (74.5)^3 * 10^{-12}\ \frac{cm^3}{\text{particle}} = 216 * 10^{-12}\ \frac{cm^3}{\text{particle}}$$

$$\text{mass} = \text{Volume} * \text{density} = 216 * 10^{-12}\ \frac{cm^3}{\text{particle}} * 1.05\ \frac{g}{cm^3} = 227 * 10^{-12}\ \frac{g}{\text{particle}}$$

$$m = 227 * 10^{-12}\ \frac{g}{\text{particle}}$$

Number of particles in 1 mg= $\frac{0.001}{227*10^{-12}}\ \frac{g}{\frac{g}{\text{particle}}}$ = 440.529 particles in 1mg

In 1 Particle we can capture 28 leukocytes. We have to catch 900.000 Leukocytes/mL. So, we need 32.143 particles (0.072mg/mL).

$$Ci * Vi = Cf * Vf$$

$$Vi = \frac{Cf*Vf}{Ci} = \frac{0.072*15mL}{10\frac{mg}{mL}} = 108\ \mu L \text{ from stock}$$

Where Ci is the initial concentration, Vi corresponds to the initial volume, Cf is the final concentration and Vf represent the final volume

Publications

- Subirada, F.; Paoli, R.; Sierra-Agudelo, J.; Lagunas, A.; Rodriguez-Trujillo, R.; Samitier, J. Development of aCustom-Made 3D Printing Protocol with Commercial Resins for Manufacturing MicrofluidicDevices. *Polymers* **2022**, *14*, 2955. https://doi.org/10.3390/polym14142955

- Sierra-Agudelo, J., Rodriguez-Trujillo, R., Samitier, J. (2022). Microfluidics for the Isolation and Detection of Circulating Tumor Cells. In: Caballero, D., Kundu, S.C., Reis, R.L. (eds) Microfluidics and Biosensors in Cancer Research. Advances in Experimental Medicine and Biology, vol 1379. Springer, Cham. https://doi.org/10.1007/978-3-031-04039-9_16

- Sierra, J.; Marrugo-Ramírez, J.; Rodriguez-Trujillo, R.; Mir, M.; Samitier, J. Sensor-Integrated Microfluidic Approaches for Liquid Biopsies Applications in EarlyDetection of Cancer. Sensors 2020, 20, 1317. https://doi.org/10.3390/s20051317

- Sierra, J.; Subirada, F.; Rodriguez-Trujillo, R.; Mir, M.; Samitier, J. Low-cost 3D printed inertial flow microfluidic devices for cells isolation in liquid biopsies. Frontiers in Lab on a Chip Technologies “Under revision”

- Sierra, J. Borges, B, Rodriguez-Trujillo, R.; Samitier, J. Assessment of a microfluidic spiral device for circulating tumour cell isolation based on computational modelling and in-vitro biomodel . Royal Society of Chemistry. Lab on a chip “Under preparation”.

- Sierra, J. Borges, B, Alcon, C, Mir, M, Rodriguez-Trujillo, R.; Samitier, J. Enrichment of circulating tumor cells in liquid biopsies using an enhanced Herringbone chip Mir, M. International journal of molecular science. “Under preparation”.